SYNTHESIS AND CHARACTERIZATION OF CHROMIUM BASED HARD COATINGS

A THESIS

Submitted in partial fulfilment of the requirements for the award of the degree of

DOCTOR OF PHILOSOPHY

in

METALLURGICAL AND MATERIALS ENGINEERING

by

HETAL NAGINBHAI SHAH

DEPARTMENT OF METALLURGICAL AND MATERIALS ENGINEERING
INDIAN INSTITUTE OF TECHNOLOGY ROORKEE
ROORKEE-247 667 (INDIA)

OCTOBER, 2010

INDIAN INSTITUTE OF TECHNOLOGY ROORKEE
ROORKEE

CANDIDATE'S DECLARATION

I hereby certify that the work which is being presented in the thesis entitled "**Synthesis and Characterization of Chromium Based Hard Coatings**" in partial fulfilment of the requirement for the award of the Degree of Doctor of Philosophy and submitted in the Department of Metallurgical and Materials Engineering of the Indian Institute of Technology Roorkee, Roorkee is an authentic record of my own work carried out during a period from July 2007 to October 2010 under the supervision of Dr. R. Jayaganthan, Associate Professor, Department of Metallurgical and Materials Engineering and Dr. Davinder Kaur, Associate Professor, Department of Physics, Indian Institute of Technology Roorkee, Roorkee.

The matter presented in this thesis has not been submitted by me for the award of any other degree of this or any other Institute.

(HETAL NAGINBHAI SHAH)

This is to certify that the above statement made by the candidate is correct to the best of our knowledge.

(Davinder Kaur)
Supervisor

(R. Jayaganthan)
Supervisor

Date: 21/10/2010

The Ph. D. Viva-Voce Examination of **Mr. Hetal Naginbhai Shah**, Research Scholar, has been held on .....

Signature of Supervisors

Signature of External Examiner

ABSTRACT

Hard coatings of transition metal nitride materials (TiN, CrN, TiSiN, CrSiN, etc) are used in tribological applications due to their remarkable physical and mechanical properties such as high hardness, high melting point, excellent wear resistance, chemical inertness, and good thermodynamic stability. Development of hard coatings with superior tribological properties, through various physical and chemical vapor deposition techniques, is ever growing to provide protection and extend service life of the equipments/components used in the actual engineering applications such as in machining and forming tools.

The fabrication of transition metal nitride coatings such as CrN, CrSiN, and CrAlN with desirable microstructural characteristics in terms of grain size, crystallographic orientations, lattice defects, and surface morphology as well as phase composition is very important in realizing the improved tribological properties hitherto unachieved in the literature. It is possible only through the thorough understanding of the influence of process variables, in the physical/chemical vapor deposition techniques, used for the fabrication of hard coatings. Although literature is available on sputter deposited Cr based transition metal nitride coatings, there is no single processing window with the optimized process conditions for achieving the desired microstructural morphology of the hard coatings, probably due to their high sensitivity/complexity of the environmental factors manifested in the vacuum chamber employed in various physical vapor deposition techniques. Therefore, it is essential to investigate the influence of sputtering process parameters for achieving the desirable microstructural characteristics with enhanced tribological properties in Cr based metal nitrides coatings. The main objectives of the present work were i) To synthesize CrN, CrSiN, and CrAlN coatings on stainless steel and Si substrates by DC/RF magnetron sputtering technique, ii) To study the effect of various sputtering process parameters on the phase formation and microstructural characteristics of these coatings by XRD, FE-SEM/EDS, and AFM, and iii) To measure the mechanical and tribological properties of CrN, CrSiN, and CrAlN by microhardness, nanoindenter, and pin-on-disc tribotester, respectively. A detailed description of the present work is presented in seven Chapters and it is briefly discussed below.

Chapter 1 gives an overview of hard coatings and nanostructured coatings. The growth mechanisms, structural properties of films, and mechanical properties of nanostructured

coatings are discussed in this . A brief description of properties of CrN compound and review of the literature on transition metal nitrides coatings such as CrSiN and CrAlN are presented in **Chapter 2**. It is well reported in the literature that the mechanical and tribological properties of coatings depend on their microstructural characteristics and surface topography. The hardness of CrN coatings deposited under different process conditions varies between 13 to 25 GPa as reported in the literature. The hardness of CrSiN and CrAlN, coatings vary between 20 to 35 GPa, depending upon the deposition techniques and different process parameters selected during deposition. Very few research groups have reported hardness values above the given range. In CrSiN system, an addition of Si leads to the formation of two-phases containing CrN_x nanocrystallites surrounded by the SiN_x, which obstructs the dislocation movement. The surface roughness, grain size, hardness, and coefficient of friction (COF) of CrSiN coatings decrease with increasing Si contents.

Chapter 3 describes the experimental technique, i.e., physical vapor deposition (Magnetron sputtering) technique used for deposition of CrN, CrSiN, and CrAlN coatings on stainless steel and Si substrate. The characterization techniques such as XRD, AFM, FESEM, stylus profilometer, and TEM employed for investigating the microstructural features and phase formation of these coatings are discussed.

The principles of measurement techniques such as Microhardness, Nanoindentation, and Pin on Disc used for investigating the mechanical properties of the coatings are discussed. The procedures of sample preparations, critical for characterizing the coatings are briefly described.

Chapter 4 describes the synthesis and characterization of magnetron sputtered chromium nitride coatings and it is divided into two Sections. The **Section 4.1** mainly describes effect of working pressure (1.33 / 1.99 / 2.66 Pa), temperature (473 K / 573 K / 673 K), and target power (75 W / 100 W) on DC magnetron sputtered CrN coatings deposited on silicon Si(100) and stainless steel (SA304) substrate. The experimental results have shown that CrN coatings deposited on Si(100) and SA304 substrates at lower temperature (473K) exhibit (111) preferred orientation and it transforms into (200) orientation with the increasing working pressure due to decrease of deposition rate. The preferential growth of the coatings along (200) orientation occurs to due its lower surface free energy as compared to (111) plane. The coatings deposited at lower working pressure on the both substrates show a large grain size with higher crystallinity but the grain size is reduced with increasing working pressure. The microstrain in the CrN coatings is decreasing with increasing working pressure for the low

deposition temperature (473K) as observed in the present work. The coatings exhibit columnar grain morphology for the chosen deposition conditions. The microhardness of CrN coatings has been measured and it shows an increasing trend with increase in the combined effect of temperature, working pressure, and power density. **Section 4.2** describes the influence of process conditions such as nitrogen contents, substrate temperature (473 K, 573 K and 673 K) in pure N_2 gaseous environment, and different sputtering gases (a mixture of $Ar+N_2$, $He+N_2$ and pure N_2) on CrN coatings deposited on stainless steel (SA-304) substrate by using DC reactive magnetron sputtering. The following conclusions are made based on the present study. The grain size of CrN thin coatings is decreasing and the coatings become denser at higher nitrogen percentage in the gas mixture. The surface roughness of CrN coatings decreases with increasing nitrogen content and substrate temperature. The coatings deposited in ($He+N_2$) atmosphere lead to lower coatings thickness and grain size as compared to coatings deposited in $Ar+N_2$ atmosphere due to lower sputtering yield of helium ions than argon ions. A mixture of different gases affects the surface morphology, grain size, and microhardness of CrN thin coatings.

The hardness value of CrN +Cr_2N (at 30% N_2 content in the chamber) phase is higher than the CrN (> 40% N_2 content) phase. The hardness and modulus of the thin coatings are influenced by the factors such as grain size, grain morphology, film defects, density, and surface roughness of the coatings. The CrN coatings deposited, at 60:40 Ar:N_2 content, exhibit high hardness value of 21 GPa, which is attributed mainly to the mixture of Cr_2N and CrN phases present in the thin coatings, in which Cr_2N phase (hcp structure) is more pronounced. The enhancement of hardness may also be due to reduction in surface roughness (RMS) and low film defects (porosity), which increase density of the coatings. The CrN coatings deposited in pure N_2 exhibits a high hardness (27 GPa) and modulus (253 GPa) as compared to that of the coatings deposited in Ar:N_2 environment, mainly due to solid solution hardening. The COF of the coatings is found to be in the range of 0.63 -0.68. The coatings deposited in pure N_2 environment show comparatively lower COF (0.64) than CrN coatings deposited under different Ar:N_2 proportions (0.68). The SEM analysis of coated pins revealed that an adhesive wear mechanism is promoted in the contact area during the test. During wear test, the transferred materials from the counter material get compacted and mechanically mixed with the coating material. Subsequently, the mixture of debris has formed layers, which stick to the coated surface contributing to the reduction in wear.

Chapter 5 describes the chromium silicon nitride (CrSiN) coatings synthesized by reactive magnetron sputtering, in which the influence of process parameters such as power density, substrate temperature, working pressure, deposition time, and gas proportion on microstructural and mechanical properties of the coatings was investigated. The effect of Si content on structural and mechanical properties of CrSiN coatings deposited on SA304 coatings is discussed in **Section 5.1**. The surface roughness and grain size of CrSiN coatings decrease with increasing Si content as observed in the present work. The coatings exhibit a triangular needle-shaped columnar morphology, which transforms into a finer columnar morphology at higher Si contents of 14.88 at.%. The maximum nanohardness and modulus of CrSiN coatings is found to be 28 GPa and 246 GPa, respectively. The maximum hardness of 28 GPa is observed with 6.33at % Si in the coatings, which is due to size effect caused by grain refinement. However, with the further increase in Si content, the hardness is reduced due to high volume fraction of a-Si_3N_4. The tribological properties of the CrSiN coatings were evaluated by pin-on-disc test. The COF and wear loss of the coatings are found to be 0.49 and $1.93x10^{-6}$ mm^3/Nm, respectively. The formation of amorphous SiN_x phase and the oxide layers (silica and chromia) formed due to tribooxidation contribute to the improved wear resistance and reduction in COF of the CrSiN coatings.

The influence of process parameters such as substrate temperature, working pressure, deposition time, and argon: nitrogen gas proportion on the structural and mechanical properties of CrSiN coatings was analyzed and reported in **Section 5.2**. The coatings deposited under equal proportion of Ar+N_2 atmosphere exhibit a (111) preferred orientation with increasing deposition time. The crystallite size of the coatings is increased with increasing deposition time. It is observed from the FE-SEM results that, with increasing mode of RF power on Si target during the CrSiN deposition, the triangular needle-shaped columnar morphology has transformed into a finer columnar morphology. The coating with comparatively low nitrogen content, 40% N_2, during deposition, formed a crystalline structure consisting of nano-crystalline CrN, which is separated by an amorphous SiN_x phase, as evident from X-ray diffraction (XRD) and Transmission Electron Microscopy (TEM), respectively. A less columnar growth is observed in CrSiN coatings deposited at low argon content, Ar: N_2 (20:80), and with 3.67 at% Si in the coatings. However, it becomes dense with increasing nitrogen content and temperature. The XRD analysis shows that the intensity of a dominating peak (111) is decreasing from (80:20) to (60:40) argon: nitrogen environment. With a further increase of nitrogen content, from (60:40) to (40:60) argon-nitrogen, there is a sudden increase

in (111) peak and above (40:60), the peak reduction rate is very slow than the previous one. The (111) and (200) peak intensity variations are very limited due to high nitrogen content, (>50%), and considerable amount of Si atoms (3.67at%) present in the CrN coatings.

CrAlN coatings with different Al content (Phase I: < 10% and Phase II: 10% < Al < 35%) were deposited on SA304 and Si substrates by a reactive magnetron sputtering technique and they are described in **Chapter 6**. The deposited coatings on SA304 substrate are highly textured with dominating peak of CrAlN(111), with position being shifted to higher 2θ angle with increasing Al contents in the coatings. There is no appreciable peak separation found within the range of applied power to the Al target up to 20.77 at% Al. The grain size is reduced to 22 nm at 30.06 at% Al content, which is minimum in all the experiments and then, it increases to 48 nm with further increase in Al contents up to 34.72%. The surface roughness is comparatively low, between 2 to 10 nm in all the coatings with varying Al content. The low surface roughness and high density of the coatings may be due to increasing applied voltage to Al target, which increases mobility of the atoms and results in higher nucleation density leading to denser coatings. The linear relationship is observed between microhardness and Al content (at%) in the CrAlN coatings. The minimum and maximum hardness measured were 15.28 GPa and 27.90 GPa, respectively, which is quite higher than CrN coatings (13.93 GPa) deposited under similar conditions. The wear resistance of all the CrAlN coatings is better than that of pure CrN coating deposited under similar conditions, and it is improved gradually with the increase of aluminum incorporation in the coatings. The increase in hardness and reduction in wear rate is observed with increasing Al content of the coatings. The mean COF and wear rate of CrAlN coatings is found to be to 0.40 and 1.38×10^{-6} mm^3/Nm, respectively, which is less than the CrN coatings, where it is found to be 0.644 and 1.40×10^{-4} mm^3/Nm, respectively. The hardness difference and friction generated in the kinetic pair of pin-on-disc, during dry sliding wear test, leads to increase in temperature. As a result, the soft element mainly Fe in EN32 material reacts with atmospheric oxygen and gets oxidized, the process is called tribo-oxidation, which results in the formation of a thin layer between sliding pair. The formation of transfer layer, due to tribo oxidation, in the coating sample with increase in Al content has contributed to the reduced wear rate.

The summary and conclusions are given in **Chapter 7**. The scope for future work in Cr based hard coatings is incorporated in this Chapter.

ACKNOWLEDGEMENTS

The thesis in present format is a result of three years of research work carried out at Department of Metallurgical and Materials Engineering, Indian Institute of Technology – Roorkee. By that time, I have worked with number of people whose contribution in assorted ways to the research and the making of the thesis. It is now a matter of immense pleasure for me to acknowledge all of them.

At the outset, let me thank the almighty God, who is the most graceful and generous for his blessing that given me courage and strength for the successful accomplishment of this work.

I would like to express my sincere thanks and deepest respect to my research supervisor Dr. R. Jayaganthan, for his inspiring guidance, advise and supervision from the very early stage of this research. He was always there to listen with endless patience, and to give proper advice. Above all, he provides me a support and encouragement during my hard time. He helps me in examining and shaping the manuscript in spite of his enormous academic preoccupation. The thesis would not have been possible without his constant monitoring and the insight provided by him in the subject matter which was totally nerve for me. As my supervisor, he has constantly forced me to remain focused on achieving my goal. His guidance, observations and precious suggestions helped me to establish the overall direction of the research and played a vital source of inspiration for bringing the present work in the final shape. Apart from all, his suggestions and solutions regarding experimental part of my research and critical remarks on the results are highly acknowledged. He definitely has been a source of inspiration and encouragement for me. I thank him for the interest he has shown in my academic and personal well-being. What I learned from him will benefit my whole life.

At the same time I would like to heartily acknowledge my research co-supervisor Dr. Davinder Kaur for her support, encouragement, and guidance during the course of this research work. She has given useful ideas and relevant discussions that have become an integral part of my learning and research.

I am deeply grateful to Dr. Ramesh Chandra, Associate Professor, Institute Instrumentation Center, for having provided the experimental facilities for the present work in the Nano-Science Laboratory. Also he has constantly motivate and giving his valuable suggestions from the beginning of this research work.

I am also thankful to the members of my doctoral research committee (SRC), Prof. Satya Prakash (Chairman), Prof. Surendra Singh (Internal member) for their useful suggestions and critical evaluation of the progress of my thesis.

I am thankful to Prof. P K Ghosh, Head of the Department, and other faculty members of the department for their support in this work. I am highly obliged and express my sincere thanks to the officials & technical staff of the Department of Metallurgical and Materials Engineering and Institute Instrumentation Center, especially Mr. Rajendra Sharma, Mr. T K Sharma, Mr. R K Sharma, Mr. Dherampalji, Mr. Narendra Kumar, Mr. M Aslam, Mr. S.D.Sharma (SEM), Mr. Birendra Dutt (AFM) and Mr. Shivkumar (XRD) who have rendered their help in all possible ways during the research work.

I owe my most sincere thanks to Prof. A C Pandey, Department of physics, Allahabad University, who rendered me an opportunity for performing the nanoindentation measurements in their Nanophosphorous Application Lab. Also I am thankful to Mr. Prashant K. Sharma and Mr. Ragvendra Yadav for their help during the experimental work at Allahabad.

I am grateful to Prof. C R Lin, Head of Mechanical Engineering Department – NTUT, Taiwan, Prof. Yin Yu Chang, Department of Materials Science and Engineering, Mingdao University, Taiwan, Prof Kevin Chou, Department of Mechanical Engineering, Alabana University, USA, and Dr. Indrani Banerjee, Department of Physics, BITS, Ranchi for their interactive discussion during the conference (TACT-2009) at Taiwan.

I greatly enjoyed working with my lab buddy Dr. Amit Kumar Chawla, Dr. Vipin Chawla, Gautam, Mukesh, Rajan, Sushant, Archana, Sonal, Paritosh and Mr Yeshpal Singh at Nano-Science Lab made it a convivial place to work. I also got a good support from Dr. Preetam Singh, Dr. Ashwani Kumar, Dr. Ashish Pandey, Deepak, Ajay, Nitin, Ritu in Physics lab and Dr. Sushanta Panighrahi, Nageshwar Rao, Atikur, Nidhi, Sankulp and Dharmendra, in Metallurgical Analysis lab. I thank them all for their full cooperation and ever needed help throughout to carry out this work and also for being around all the time, be it while partying, playing cricket or discussing academics or doing other crazy things. Also I am thanks to my department friends Bansi Agrawal, Kuntal Maiti, Sachin Tyagi, Amrendra and all other fellows who helped me directly or indirectly during the entire period of my research work.

I feel greatly obliged to my friends Anil Gonde and Dinesh Rajoriya at MRC Bhavwan. I wish to thank my close friends Bhavesh, Prashant, Bhadresh, Jayesh and Krutin for their constant support during my hard times. The everlasting support from my colleague Mr. Vijay Choudhary and Mr. Rajesh Patel is highly acknowledged. Also I am thankful to my college friends Mr. Mukesh Inamdar, Ms. Sudhikala, Ms. Vinita Nair for their constant encouragement and mental support.

I am especially grateful to the management of Charotar University of Science and Technology – Changa for giving me a permission to pursue the PhD at Indian Institute of Technology Roorkee for three years. I personally thanks to Principal Dr. Y P Kosta, Prof. S G Shah, Dr. T K Choudhary and Mr. Devang Joshi for their everlasting support for this research and administrative work.

The financial support from Department of Science and Technology – New Delhi for an international conference (TACT 2009) at Taiwan in December 2009 is remarkably acknowledged.

Where would I be without my family? I am really grateful to my family members including my mother, Late Smt. Madhukanta and father, Mr. Naginbhai Shah, in-laws, Smt. Kokilaben Shah and Mr. Manharbhai Shah, two elder brothers and sisters, Bhabhi, Jijaji, my aunty Sumitraben Shah and Vinaben Rawal for their unflagging love and support throughout my life. Without their support and help over the years towards my education, all this would not have been possible. I have gained great strength from them. Their ultimate patience in the extremely tough conditions gave me continuous inspiration and made my dreams true so they deserve and receive my utmost respect and gratitude. And finally I wish to extend my heartfelt gratitude to my beloved partner, Ami Shah, whose love, support, patience and belief in me enabled this thesis to be completed despite of her own burden of PhD as well as family. We had extraordinarily fortunate to have our little princess Vaishvi, whose innocent love and always smiling face released my stress of PhD. I thank almighty for so precious and adoring child just before starting of our Ph.D.

I wish to thank all my teachers, from my school age in Jeevan Vikas, D.D Technical School and Basudiwala School to my college age in B P Polytechnic, S S Engineering College and BVM Engineering College for his special attention and care in making my carrier.

I am very thankful to everyone who has contributed directly or indirectly, but express my apology that I could not mention personally.

This thesis is dedicated to my parents and my family.

(Hetal Naginbhai Shah)

CONTENTS

LIST OF FIGURES

LIST OF TABLES

LIST OF PUBLICATIONS

Research publications (Published/Under review)

1. **Hetal N. Shah**, Vipin Chawla, R Jayaganthan, Davinder Kaur, "Microstructural Characterization of CrN thin films deposited on Stainless Steel substrate by DC reactive magnetron sputtering", **Bulletin of Material Science** 32 (2010) 103-110.

2. **Hetal N. Shah**, R Jayaganthan, Davinder Kaur, Ramesh Chandra, "Influence of Sputtering parameters and Reactive gases on Microstructure of Chromium Nitride thin films deposited on SS-304 substrates by DC-Reactive Magnetron Sputtering", **Thin Solid Films** 518 (2010) 5762-5768.

3. **Hetal N. Shah,** R. Jayaganthan, Davinder Kaur, "Influence of Silicon content on the Microstructure and Hardness of CrN coatings deposited by Reactive Magnetron Sputtering", **Materials Chemistry and Physics** 121 (2010) 567–571.

4. **Hetal N. Shah**, R Jayaganthan, Davinder Kaur "Effect of Sputtering Pressure and Temperature on DC Magnetron Sputtered CrN films", **Surface Engineering** 2009, In Press, DOI 10.1179 /174329409X389326.

5. **Hetal N. Shah**, R Jayaganthan, Davinder Kaur, "Synthesis and Characterization of CrSiN thin films deposited on Si (100) substrate", **Surface Engineering**, 2009, In Press, DOI: 10.1179/026708410 X12459349720097.

6. **Hetal N. Shah**, R. Jayaganthan, Davinder Kaur, "Influence of Reactive gas and Temperature on Structural properties of Magnetron Sputtered CrSiN coatings", **Applied Surface Science** (2010) (Provisionally Accepted).

7. **Hetal N. Shah**, R. Jayaganthan, Avinash C Pandey, "Nanoindentation study of Magnetron sputtered CrN and CrSiN thin films", **Materials and Design** (2010) (under review).

Conference Proceedings

8. **Hetal N. Shah**, R. Jayaganthan, Davinder Kaur, Ramesh Chandra, Avinash Pandey, "Structural and Mechanical characterization of nanocrystalline CrN hard coating on silicon substrate", Proc. of TACT 2009 in International Conference of Thin Films during 14 – 16 December 2009, Taiwan, 127-128.

9. **Hetal N. Shah**, R. Jayaganthan, Davinder Kaur, Ramesh Chandra, "Structural characterizations of CrN thin films deposited on glass substrate"; Proc. of TACT 2009 in International Conference of Thin Films during 14 – 16 December 2009, Taiwan, 142.

CHAPTER 1
HARD COATINGS

1.1 Introduction

Many efforts have been made to improve the performance of hard materials since the bronze-age. Subsequently, protective hard coatings were identified as one of the alternatives applied to iron tools. The development and evolution of hard coatings is strongly related to metallurgy. For example, the formation of hard carbides on the surface of Fe based alloys was possible at high temperature due to thorough understanding of diffusion kinetics in physical metallurgy.

Surface engineering or interfacial engineering has become one of the most important technologies to improve the life time and performance of many components. The interfacial engineering plays a vital role in improving mechanical properties of the bulk material such as high toughness and strength as well as to impart high hardness, corrosion and wear resistance to the surface of materials through a grain size/interface effect (Arzt *et al.* 1998). The lifetime of the component or tools could be increased more than ten times with application of surface modification techniques. For many years, hard chromium coatings, produced by electrochemical processes, have played an important role for wear-resistant surfacing of machinery components and tools (e.g. piston rings, valves, hydraulic pumps, dies, moulds), aerospace parts (landing gears), semiconductor integrated circuit packaging (Sun *et al.* 2006), and as decorative coatings (e.g. automobile trims, wheels, office furniture). Industrial applications of the CrN coatings synthesized by physical vapor deposition (PVD) are rapidly increasing due to its superior tribological properties (Chang *et al.* 2004). The development of wear-resistant hard coatings is ever growing due to the following facts. About 90% of all indexable inserts for metal cutting, based on cemented carbide substrates, are coated for wear protection by chemical vapor deposition (CVD) or Physical vapor deposition (PVD) techniques, with PVD being used in about 25% of the cases. **Figure 1.1** shows the CrN coatings applied to cutting tools of machining industries.

Similarly, metallic components like moulds, dies and machinery are subjected to degradation during plastic transformation processes, namely when working with abrasive fillers and corrosive components combined with relatively high processing temperatures. The important

issue for the future is not only to develop the suitable deposition technology but to achieve the desired properties of the hard coatings through microstructural design, substantiating the influence of process parameters on the microstructures. Also, due to design changes of automobiles components, (Yuji *et al.* 1998), emphasis has shifted to tribological approaches, owing to lifetime of the components caused by wear, which has a direct impact on process productivity and surface finish of the final products.

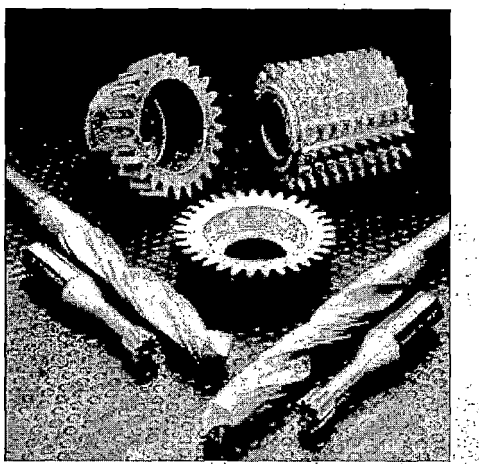

Figure 1.1 CrN coatings applied to cutting tools.

Hard coatings with modified properties are essential in many different areas of engineering applications. Deposition of hard coatings with a few microns in thickness is a common technology to improve the performance of tools, dies, and molds for many different applications (North *et al.* 1998). The most commonly used techniques, in industries, to deposit coatings on tools are thermally activated CVD and PVD (Hondros *et al.* 1992, Schneider *et al.* 2000).

In recent times, transition metal nitride coatings are widely used to improve lifetime and performance of tools. They provide high hardness, chemical inertness, good electrical conductivity and excellent wear resistance due to their bond structure, a mixture of covalent, metallic and ionic components; Also, nitride based hard coatings have proven their capability in increasing tool lifetime in abrasive and corrosive environments (Cunha *et al.* 1999, Gregor *et al.* 2006) like coatings for cutting tools under dry and high speed machining conditions, protective coatings for

turbine blades and engine parts to improve their durability (Chandra *et al.* 2006). In recent years, especially hard coatings based on CrN have been used to increase wear and corrosion resistance of working tools (Eiper *et al.* 2006) and for high temperature applications (Weblink 1). Also, CrN based hard coatings is more corrosion resistant than TiN, especially in aqueous solutions and therefore used as a direct substitute for chromium plating. The coating to substrate adhesion is an important factor for realizing the superior tribological properties as reported in literature (Srivastav *et al.* 1995).

1.2 Nanostructured Hard Coatings

Nanostructured transition metal nitride coatings, with grain size between 10-100 nm, exhibit superior hardness and wear resistance when compared to their conventional counter parts. There are two basic mechanisms that enhance hardness in alloys (Hauert 2000). The first one is the modification of the chemical bonding (CrN), either by altering composition of the alloy or by modifying the stoichiometry. The second mechanism involves the introduction of lattice distortions in to the nitrides (CrAlN, CrSiN, TiSiN), in terms of addition of minor impurities, grain boundaries, and fine precipitates, which restricts the propagation of dislocations through the solid. The hardness (H) enhancement in superhard material is achieved due to the minimized dislocation activity. The main factors responsible for the enhanced H of hard coatings are: (i) dislocation dominated plastic deformation, (ii) cohesion forces between atoms, (iii) nanostructure, and (iv) compressive macrostress 'σ' generated in the coatings during its growth. The grain boundaries in the two-phase materials introduce the lattice distortions, which increase hardness substantially for the nanometer sized grains in the coatings. In the case of polycrystalline solids, this hardening effect is expressed through the Hall-Petch relation (Hall 1951, Petch 1953).

$$\sigma_y = Kd^{-0.5} + \sigma_0 \qquad (1.1)$$

where the enhancement of the yield stress, σ_y, is connected to the grain size, d, by means of two constants, K and σ_0. According to this model, the high hardness of materials with smaller grain size, as shown in **Figure 1.2**, is ascribed to pileup of dislocations at grain boundaries. In fact, such defects act as obstacles for dislocation motion through the solid. If the embedded grains are nanoscaled, it is referred as nanocomposite for which the mechanical properties are improved by superlattice effects. A superlattice is a solid constructed by two or more superimposed patterns with similar scales. **Figure 1.3** shows a scheme of crystalline inclusions embedded in an

amorphous matrix as an example of composite material. Here, the grain size coincides with the crystallite size. The classification of hard nanocomposite coatings is generally made as a function of their structure and the elements therein. According to Musil (2000), two basic groups can be distinguished: crystalline/amorphous and crystalline/crystalline nanocomposites. Nanocrystalline coatings are characterized by broad, low-intensity X-ray reflections. In such coatings, called transition regions, where the film structure changes continuously. There are three groups of transitions such as (i) transition from crystalline to amorphous phase, (ii) transition between two phases of different material, and (iii) transition between two preferred orientations of grains of the same material, as shown in **Figure 1.3**.

Nanostructured and nanocomposite films with enhanced H can exhibit different nanostructure, as shown in **Figure 1.4**. The films of the first group produced in a smooth transition are composed either of (i) columns or (ii) nc-grains surrounded by a thin tissue phase (**Figure 1.4b**; a slightly higher amount of B in $A_{1-x}B_xN$ compound compared to **Figure 1.4a**). The columns are perpendicular to the substrate/film interface. The columnar nanostructure exhibits also nanocomposites of the 2nd and 3rd group produced at edges of sharp transitions. On the contrary, nanocomposites films of the 2nd and 3rd group produced between the sharp transitions composed of a mixture of small nanograins and exhibit dense globular microstructure (**Figure 1.4c**).

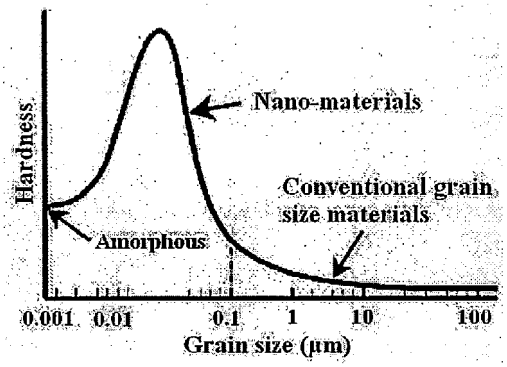

Figure 1.2 Hall–Petch effects.

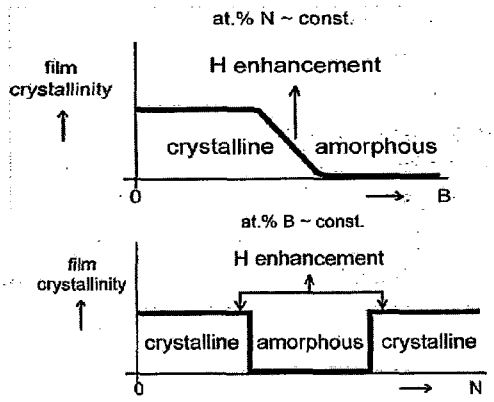

Figure 1.3 Schematic illustration of transition regions for $A_{1-x}B_xN$ compounds. a) transition region from crystalline to amorphous phase and b) transition region between two crystalline phases or two preferred crystallographic orientations of grains (Musil J. 2006, Musil J. 2006a).

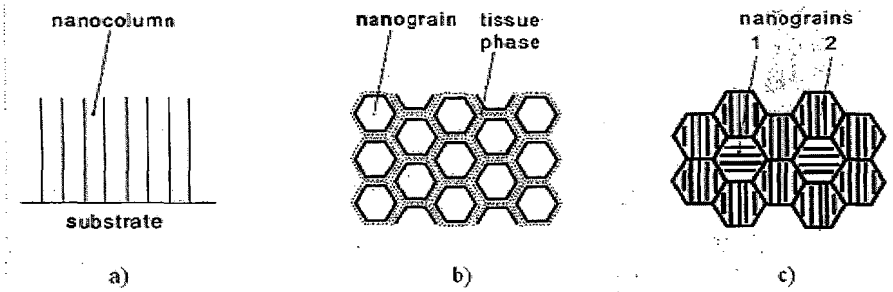

Figure 1.4 Schematic diagrams of different nanostructures of nanocomposites with enhanced *H*. a) columnar, b) nanograins surrounded by tissue phase and c) mixture of nanograins with different orientations (Musil J. 2006, Musil J. 2006a).

Nanostructured coatings offer the potential for significant improvements in physical and mechanical properties resulting from reducing their microstructural features from macro - micro to nano compared to current engineering materials. The potential benefits as shown in **Figure 1.5**,

include excellent hardness and strength in metals and ceramic resulting from reduced grain size and slip distance, respectively. In ceramics, high hardness and toughness may be achieved with reduced defect size and enhanced grain boundary stress relaxation, even at ambient temperature. Nowadays, nanostructured coatings are used in different industrial applications such as in machining, forming, stamping, and as thermal barrier coatings in turbines.

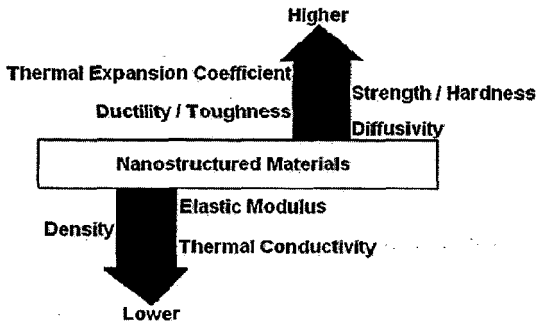

Figure 1.5 Properties of Nanostructured materials.

Coatings are very much essential to prevent wear, erosion, and corrosion, and to provide thermal insulation of bulk materials used in various engineering applications. The theoretical concept for the design of the hard nanocrystalline composites is associated with the preparation of a composite material consisting of nanocrystallites embedded within a very thin amorphous matrix (Gleiter *et al.* 1993, Veprek et *al.* 1995). Such multiphase materials often show higher hardness and toughness values than the single phase materials, due to the strong hindering of the crack formation and propagation in the thin amorphous phase between the crystallites. One of the most recent nanocomposite materials is nc-TiN/a-Si_3N_4 system, where a small TiN grains are embedded in a amorphous Si_3N_4 matrix (Veprek *et al.* 1995, Sun *et al.* 1997, Smith *et al.* 1997, Christiansen *et al.* 1998). This system revealed an extremely high hardness and Young's modulus (Niederhofer *et al.* 1999), and it could also be useful for future applications in ultra large scale integrated diffusion barriers(Reid *et al.* 1994, Smith *et al.* 1997, Niederhofer *et al.* 1999).

1.3 Introduction to Thin Film Growth and Mechanisms

1.3.1 General- Film Growths

A thin film is a thin coating with thickness ranging from fractions of a nanometer to several micrometers grown on substrates. The thin films growth starts with nucleation in the form of island, merging of island with coalescence phenomena and then subsequently thickness growth, all stages of which are influenced by deposition parameters. There are mainly three types of growth mode in the thin film technology, as shown in **Figure1.6**, are given below:

a) Island (Volmer – Weber)
b) Layer (Frank – Van der merve)
c) Island – Layer Mixed mode (Stranski – Krastanor)

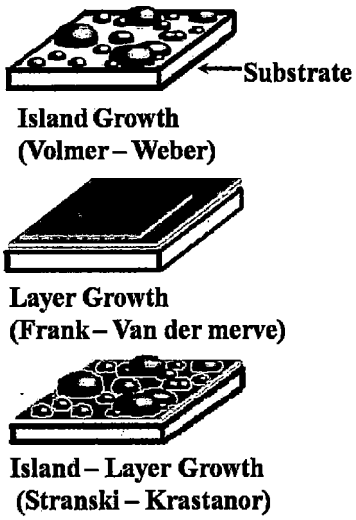

Figure 1.6 Types of growth mode in the formation of thin film.

a) Island Growth

When the atoms or molecules in the deposits are more strongly bound to each other than with the substrates, there is a possibility of island growth. Also, the smallest stable clusters nucleate on the substrate and grow in the three dimensions to form islands. The metal and semiconductor films deposited on oxide substrates are initially form such islands.

b) Layer Growth

When the atoms or molecule in the deposits are more strongly bound to the substrates than each other and nucleates in two dimensions form a layer on the substrate. Each new monolayer starts to grow on top of another layer, only when the last one is completed. The first monolayer is then covered with a somewhat less tightly bound layer **(Ohring M 2002).**

c) Island – Layer Mixed mode (S-K mode)

This is an intermediate combination of previous modes. In this growth mode, after forming one or more monolayers, the next subsequent layer growth becomes unfavorable and forms island. This kind of growth mode is fairly common and mainly observed in metal – metal or metal – semiconductor system.

The Young's equation can be used to explain three modes of film growth.

$$\gamma_c = \gamma_{fc} + \gamma_c Cos\theta \qquad (1.2)$$

Atoms at free surfaces are more energetic than atoms within the underlaying bulk because of fewer bonds with surrounding atoms and so they are less constrained. The surface energy is come into consideration because of the difference in interatomic energy of atoms at two locations. In the above **Eq. 1.2**, θ is a wetting angle of nucleus on substrate and subscript '*s*' indicates substrate and '*c*' indicates coating.

For island growth, $\theta > 0$ and in this case

$$\gamma_s < \gamma_{cs} + \gamma_c \qquad (1.3)$$

From the above relation, it can be deduced that the island growth occurs when the surface tension of the film goes above that of the substrate.

For layer growth, $\theta \approx 0$ and in this case

$$\gamma_s \geq \gamma_{cs} + \gamma_c \qquad (1.4)$$

The materials with low surface energy would wet the substrates with a higher surface energy. The layer growth occurs when the surface tension of the substrate is higher than the films. For S-K growth, initially the strain energy per unit area of the film is higher than γ_f, which is permitting nuclei to form above the initial layers. Initially,

$$\gamma_s > \gamma_{fs} + \gamma_f \qquad (1.5)$$

Film growth is a non-equilibrium process; grain size is determined by mobility of atoms on surface. The mobility depends mainly on substrate temperature, surface and bulk diffusion (*Tm*), energy supplied by ion bombardment and adsorption strength.

1.3.2 Film Structure

The influence of deposition variables on the structural features of thin films has been depicted in terms of structure zone diagrams (*SZD*). The condensation from the vapor involves incident atoms becoming bonded ad-atoms, which then diffuse on top surface of the film until they desorbs or they trapped at low energy lattice sites. The formation of film structure involves four basic processes: shadowing, surface diffusion, bulk diffusion, and desorption. The shadowing is a phenomena arising from the geometric constraint imposed by the roughness of the growing films and line of sight impingement of arriving atoms. The last three processes are quantified by the diffusion and sublimation activation energies, whose magnitude scale directly with the melting point of the condensate. The dominance of one or more of these four processes as a function of substrate temperature '*Ts*' is manifested by different structural morphologies. This is the basis of structure zone models (SZMs). The SZM is mainly used to the explain the formation of different morphology and growth mechanism at various normalized temperature (*Ts/Tm*) and energy transfer (atoms at high energy growth). It is applicable for several deposition techniques, like PVD and CVD, and for various materials such as metals, insulators, and semiconductors.

The SZM for sputtered films was introduced by Thornton (1977) with four different zones. This structure model is based on morphologies developed in 20 to 250 μm thick magnetron sputtered coatings of Ti, Cr, Fe, Cu, Mo and Al deposited at rates ranging from 50 to 20,000 Å/m. **Figure 1.7** shows the structure zone models for the sputtered deposited coatings.

Also, the **Figure 1.8** illustrates the effect of individual physical process on structure and how they depend on substrate temperature and sputtering gas pressure. Zone 1 structure, which appears in amorphous as well as cryatalline deposits, are the results of shadowing effects, which overcome restricted adatom surface diffusion. In the zone 2 region, structures are the result of surface diffusion controlled growth. Lattice and grain boundary diffusional process dominates at the higher substrate temperature giving rise to the equixed recrystallized grains of zone 3. The

zone T consisting of a dense array of poorly defined fibrous grains, which may be viewed as the transition region between zone 1 and 2.

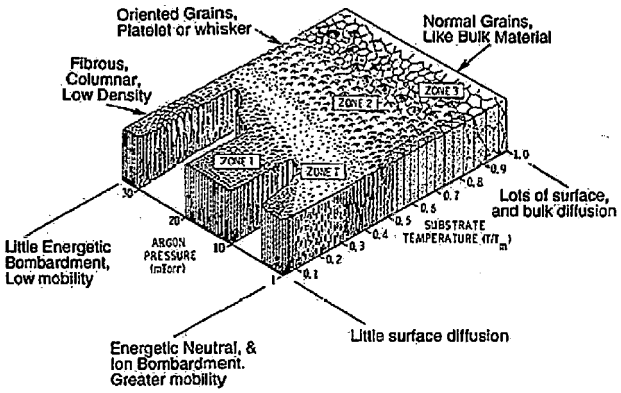

Figure 1.7 Structure Zone Model for sputtered deposited films.

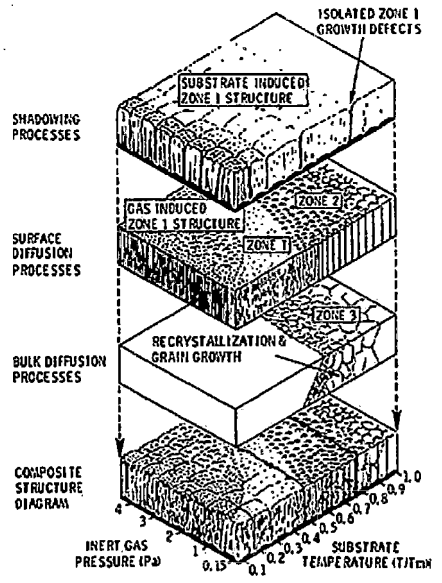

Figure 1.8 Influence of deposition parameters (T, P) on thin films structure.

1.4 Outline of Thesis

The contents of various chapters are summarized below:

The basic properties of CrN compound followed by exhaustive literature based on CrN, CrSiN and CrAlN coatings are summarized in **chapter 2.** The objectives were set based on literature survey and listed in section 2.5 of this chapter. The details of experimental techniques and methodologies pertaining to synthesis and characterization of the Cr based transition metal nitride coatings are discussed in **chapter 3.** The CrN, CrSiN and CrAlN coatings were deposited on different substrates like stainless steel (Grade SA304) and silicon wafer Si(100). The synthesis and characterizations of CrN coatings are described in the **chapter 4.** The influence of processes parameters such as substrate temperature, working pressure, target power, different sputtering and reactive gas environment, gas proportion, and gas flow rate on microstructural, mechanical and tribological properties of the CrN films are discussed.

CrSiN films deposited with various processes parameters such as target power, substrate temperature, working pressure, deposition time and gas proportion were investigated for their microstructural features and mechanical properties and discussed in detail in **Chapter 5.** The effect of Al concentration on structural, mechanical and tribological properties of CrAlN coatings are discussed in **chapter 6.** The final conclusions are summarized in **chapter 7** with future scope followed by references in the present work.

CHAPTER 2
LITERATURE REVIEW – TRANSITION METAL NITRIDE

2.1 Properties of CrN

The most common compounds employed in hardness applications are basically carbides, nitrides and borides of groups IV, V and VI of the periodic table, namely TiN, TiC, TiCN, TiAlN, and CrN. The transition metals form a variety of compounds when deposited in different proportion of nitrogen atmosphere. As mentioned in the Chapter 1, Section 1.1, the transition metal nitrides are widely used in the machining industries to retain the edges of the cutting tools and to enhance the corrosion resistance of single and multipoint cutting tools like milling, drill bit etc. for improving their cutting life by more than three times. The CrN finds their applications not only in the conventional machining industries but also in the nuclear industries as hard facing materials due to their excellent resistance to galling and high thermal stability. The CrN is a best substitute for TiN due to its less brittleness but still quite hard, makes it more suitable for surface protection application on comparatively soft materials like stainless steel and aluminum alloys. The use of plasma techniques for deposition of coatings ensures that only surface is coated, so high brittleness associated with integral nitriding of the samples is avoided. The structure (Weblink 2) of CrN is shown in **Figure 2.1** and main properties are tabulated in **Table 2.1**.

CrN coatings is an extremely hard and inert, applied primarily to precision metal parts. It offers higher temperature resistance than TiN and is an ideal choice for high temperature environments. It also performs well in corrosive environments and in sliding wear applications. A number of reports on the growth of chromium nitrides employing the PVD (Bertrand *et al.* 1997, Tu et *al.* 2000, Nam *et al.* 2000, Chen *et al.* 2004, Fornies *et al.* 2006, Barshilia *et al.* 2006a, Weng *et al.* 2008, Zhang *et al.* 2008, Lin *et al.* 2009, Shi *et al.* 2009) techniques are available in the literature. The main features of CrN coatings are:

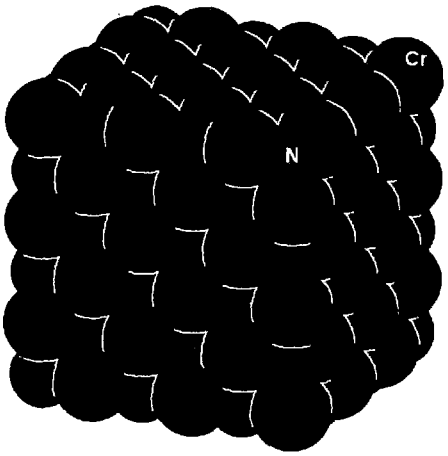

Figure 2.1: Structure of CrN compound.

Table 2.1 Basic properties of CrN compound.

Properties	Values / Description
Color	Grey
Appearance	Crystalline solid
Melting point	1353K
Density	5900 kg m^{-3}
Geometry of chromium	6 coordinate: octahedral
Prototypical structure	NaCl (rock salt)
Crystal Structure	Cubic
Toxicity	Non Toxic
Residual compressive stress	5.5 GPa

- Lower residual compressive stresses than TiN, thicker coatings can be grown.
- Dense and continuous coatings and can withstand elevated temperatures up to 973K in air.
- It can be easily deposited by environmentally safe, Physical Vapor Deposition (PVD) technique.
- It can be applied to most metals to provide enhanced surface characteristics as well as for some ceramics and plastics.
- It has the appearance of metallic silver and it is harder than hard chrome plating.
- Highly inert – excellent corrosion resistance and chemical stability.

- Non-toxic nature enables it for use in medical surgical devices and food processing equipments.
- Coating is dense and non-porous and exhibit uniform thickness that follows the contour of the part's surface. It forms an outstanding bond to the base material that will not blister, flake or chip.

2.2 Review of Hard coatings

2.2.1 CrN Hard coatings

Physical vapor deposited (PVD) Cr-N coatings have been investigated extensively in the last decade and have attracted attention as a possible replacement for electroplated coatings in a number of applications. The deposition techniques such as sputtering (Aubert *et al.* 1983, Rebholz *et al.* 1999), cathodic arc (Sue *et al.* 1995, Grant *et al.* 1996), and electron beam evaporation (Wang *et al.* 1990) enable the deposition of CrN hard coatings with good oxidation, corrosion and wear properties. Irrespective of the deposition techniques, Cr, Cr-N (with N in solid solution), Cr_2N, mixed Cr_2N/CrN and CrN phases have been identified in the coatings, depending upon on the partial pressure of the N_2 gas. Hardness values between 17 and 25 GPa have been reported for the coating over a composition range from $CrN_{0.1}$ to stoichiometric CrN (Hurkmans *et al.* 1996, **Chang *et al.* 2004**), compared to the values between 6 and 12 GPa for electrodeposited hard-chrome produced with different catalysts (Lausmann *et al.* 1996). In the 1980s, Aubert *et al.* (1983, 1985) studied the mechanical properties of magnetron-sputtered Cr coatings and the corresponding nitrogen and carbon containing alloys, and concluded that these coatings could be widely used for wear resistance applications. Terrat *et al.* (1991) have reported reactively sputtered wear-resistant coatings within the Cr-N system between a minimum pressure, at which the Cr phase was saturated with interstitial nitrogen, and a maximum pressure, at which hcp Cr_2N started to form. Cosset *et al.* (1996) have studied in detail the structure, corrosion, adhesion, hardness and wear behavior of magnetron sputtered $Cr_{1-x}N_x$ coating with x = 0 to 0.11 at temperatures between 473K to 773K and concluded that the properties of these coatings depend closely on both deposition temperature and nitrogen content. Hurkmans *et al.* (1996) and Demaree *et al.* (1996) reported structure, hardness and adhesion as a function of the nitrogen content up to 50 at.% for sputtered CrN coatings consisting of different phases. For pure Cr coatings, hardness value of around 7 GPa was observed, (Hurkmans *et al.* 1996, Bertrand *et al.* 1997, Rebholz *et al.* 1999).

With increasing nitrogen partial pressure, the amount of nitrogen in chromium lattice has increased. Hence, the increase in microhardness of CrN can be explained in terms of solid-solution strengthening of the chromium coatings by nitrogen atoms (Rebholz *et al.* 1999). A further increase in nitrogen led to an almost linear increase to 24 GPa for $Cr_{1-x}N_x$ coatings consisting of the Cr_2N phase (x= 0.29). Coatings containing the dual Cr_2N/CrN phase display hardness value of around 16 GPa. The similar trends in hardness values but different values were reported by other authors (Legg *et al.* 1996, Hurkmans *et al.* 1996, Bertrand *et al.* 1997, Hones *et al.* 1997) with increasing nitrogen flows rates for coatings deposited at substrate temperatures between 473K and 723K. However, in most cases, only limited data are available for coatings containing the expanded a-Cr phase. The different phases formed during CrN deposition were studied by Tu *et al* (2000) and reported in their work that the coatings with lower nitrogen contents exhibit Cr and Cr_2N phases, while the CrN phase is observed in films with nitrogen contents higher than 58 at.%. The microhardness of the deposited CrN coatings with different phases varied from 15 to 18 GPa at a load of 3 gf with a knoop indenter. Forniés *et al.* (2006) investigated CrN deposited by magnetron sputtering in an Ar+N_2 atmosphere at different bias substrate voltages. The hardness values without bias were found to be 20 GPa (40% N_2), with a maximum value of 21 GPa for films deposited in 100% nitrogen atmosphere as reported in their work. The hardness of the CrN coatings deposited in 40 %N_2 with bias (-160 to 20 V) showed maximum 22 GPa and minimum 16 GPa while hardness of the film deposited with 70 at.% N_2 with same bias range was found to be maximum 25 GPa and minimum 19 GPa. Weng *et. al* (2008) deposited chromium nitride coatings using a hybrid physical vapor deposition (PVD) system containing a filter arc deposition (FAD) and a metal plasma ion implantation source (MPII). They investigated the effect of implanting carbon on CrN films with and without implanted carbon. They observed that the implanted carbon increases ion bombardment energy and smoothens surface of the CrN macro particles. Also observed that the implanting carbon increased the compressive residual stress (-3.673 from -3.162 GPa) and hardness (24.83 from 21.68 GPa) compared with those for unimplanted CrN. The wear resistance was also improved by implanting carbon from 0.107 to 0.037 mm^3/m on CrN coatings. Kim and Cha (2004) deposited on tool steel by co-deposition of chromium nitride and MoS_2 by DC magnetron sputtering to increase the hardness and tribological properties. The coating worked as a solid lubricant coatings and the hardness value with -100 V bias were foung to be 28 GPa. The literature based on sputter deposited CrN hard coatings especially on mechanical and tribological properties are summarized in **Table 2.2.**

Table 2.2 Review of CrN coatings.

Research Group/s (year)	Hardness (GPa)	Modulus (GPa)	COF	Wear loss (mm^3/Nm)	Process and Variable Parameters	Remarks
Huang Z.P. *et al.* (1994)	16.50	--	3.5 to 6	--	Plasma-assisted PVD	
Gautier C. *et al.* (1996)	15 at 623K	--	--	Reduced with temp	Magnetron Sputtering and Vacuum arc evaporation	Influence of the substrate temperature
G. Bertrand *et al.* (1997)	25	--	--	--	RF Magnetron Sputtering	Influence of N_2
Hurkmans T. *et al.* (1999)	22 at −200 V bias	--	--	--	Reactive Unbalanced Magnetron Sputtering	Substrate bias voltage and substrate bias current density
Rebholz C. *et al.* (1999)	24	--	0.7 – 0.8	--	Magnetron Sputtering	Influence of nitrogen content
Wu F. B. *et al.* (2000)	24.5	400 to 510	--	Reduced with Ni interlayer	RF Magnetron Sputtering	Electroless Ni interlayer
Nam K H *et al.* (2000)	22.50				Pulsed DC Magnetron Sputtering	N_2 flow rate, substrate bias voltage, duty cycle and frequency
He X M *et al.* (2000)	31	--	0.2	--	Reactive DC Magnetron Sputtering	Negative bias voltage and the gas flow ratio of N_2
Tu J. N. *et al.* (2000)	15 to 18	--	--	--	Reactive Magnetron Sputtering	Various nitrogen content
Mayrhofer P.H *et al.* (2001)	38.4	--	--	--	Unbalanced DC Magnetron sputtering	Influence of nitrogen : argon flow rate ratio, ion energy and ion atom flux ratio
Nam K. H. *et al.* (2001)	23	--	--	--	Reactive Magnetron Sputtering	Films deposition rate
Seok J.W. *et al.* (2001)	12.70	--	--	--	Magnetron Sputter-Deposition	Various N_2 flows

Research Group/s (year)	Hardness (GPa)	Modulus (GPa)	COF	Wear loss (mm^3/Nm)	Process and Variable Parameters	Remarks
Han Z. *et al.* (2003)	26.8 (Single phase Cr_2N)	350	--	--	Reactive Magnetron Sputtering	Effect of N2 partial pressure
Olaya J.J. *et al.* (2005)	12 to 16	--	--	--	Unbalanced magnetron Sputtering	With and without substrate bias
Essen P V *et al.* (2006)	30	240	0.4	$170X10^{-16}$ m^3/Nm	Reactive Sputter Deposition	Various N_2 flows
Fornies E *et al.* (2006)	21at (30% N_2) 25 at (-100V)	--	0.4 – 0.48	Decreases (with negative bias)	Magnetron sputtering	Different bias substrate voltage
Mercs D *et al.* (2007)	26-27 (CrN),	--	375	--	Reactive Magnetron Sputtering	Constant RF bias voltage -200V
Zhang G A *et al.* (2007 and 2007a)	--	--	0.72	0.12 μm^3/Nμ	Magnetron Sputtering	N_2 content variations
Elangovan *et al.* (2010)	12±1.81	250±51	0.16	--	Pulsed DC Magnetron Sputtering	Different gas mixtures of argon and nitrogen and in the substrate temperature range 303–973 K
Lin J. *et al.* (2010)	26 (MPP)	--	0.36 (MPP)	--	DC Magnetron Sputtering (dcMS), Pulsed DC Magnetron Sputtering (PMS), and Modulated Pulse Power (MPP) Magnetron Sputtering	Effect of different types of power supply
Paulitsch J. *et al.* (2010)	23 (CrN_{HIPIMS}) 35 (TiN_{HIPIMS})	--	---	--	High Power Impulse Magnetron Sputtering (HIPIMS) and DC Magnetron Sputtering (DCMS)	Multi-fold substrate rotations during deposition
Feng Cai *et al.* (2010)	19.9±1.23 (CrN)	309.9±16.38 (CrN)	0.81	1.89×10−6	Plasma Enhanced Magnetron Sputtering	Effect of Si and C additions to CrN

2.2.2 CrSiN Hard Coatings

The addition of third element like Si, Al into the CrN, TiN and WN coating layer led to a significant increase in their structural and mechanical properties as reported in the literature (Veprek 1996, Kim *et.al.* 2002, Choi 2004). The addition of third element such as Si and/or Al into the CrN binary compound has shown improved properties such as high hardness, wear resistance, and high temperature oxidation resistance. Sandu *et al.* (2006) reported that in all M–X–N systems, the segregation of X (X = Si, Ge) to the grain boundaries limits the crystallite growth and involves the formation of a new phase. In the case of M–Si–N systems, the addition of Si leads to the formation of two-phases containing MN_x nanocrystallites, where M is (Cr, Ti, W) surrounded by the SiN_x amorphous phase (Holleck *et al.* 1986 , Hones *et al.* 2000, Vepreak *et.al.* 1996, Diserens *et al.* 1999, Cavalerio *et al.* 2002). Wang *et al.* (2009) studied the microstructural evaluation of CrSiN deposited by hybrid arc ion plating and magnetron sputtering process and reported that with increasing Si content, the morphology of films change from long and coarse crystallite to shorter and finer ones, further to nanoclusters get dispersed in an amorphous matrix, and finally to amorphous state. Lee *et al.* (2007) studied the microstructures and mechanical properties of CrSiN coatings deposited by pulsed DC reactive magnetron sputtering and observed that the surface roughness, grain size, hardness, and friction coefficient of CrSiN coatings decrease with increasing Si contents. It was found that the ternary system of X–Si–N (X= Ti, Cr) with about 5~10 at.% silicon content possessed high hardness (≧40 GPa), and better oxidation resistance than traditional binary TiN or CrN coatings (Yang *et al.* 2008). Mercs *et al.* (2005) deposited CrN and CrSiN coatings with different nitrogen flow rates, 6 and 10 sccm, for a constant argon flow rate of 20 sccm and found that the increase of the silicon content up to 2.5 at.% into the coating leads to a maximum hardness (H) (24.5 GPa) and a low Young's modulus (E) (298 GPa). A further increase of the Si content leads to the decrease of H and E (22 and 275 GPa) in both cases. It was reported in their further work (Mercs *et al.* 2007) on the CrN and CrSiN coatings produced with at.% Si ≤ 0.92, in Ar/N_2 mixture atmosphere, that the formation of amorphous silicon nitride phase has occurred at the grain boundaries of CrN. Martinez *et al.* (2004, 2004a) investigated the electrical, optical and mechanical properties of reactive magnetron sputtered CrN and CrSiN coatings as a function of N and Si contents and observed that the hardness of CrN coatings is influenced by the coating morphology. Benkahoul

et al. (2008) deposited CrSiN thin coatings by pulsed DC reactive dual magnetron sputtering and reported that the increasing Si content does not affect the grain size, but it leads to solid solution hardening. The film hardening is generated by the two cases that result from formation of solid solution and formation of nc-CrN/a-Si_3N_4 (Lee *et al.* 2005). The nanohardness values of (111) and (200) CrN are typically between 12–18 GPa. The addition of small amounts of Si increases the hardness values up to 24 GPa for CrSiN as reported in their work. The coatings containing 2.3 at.% of Si, corresponding to the solubility limit, exhibits the best mechanical and tribological performance (Benkahoul *et al.* 2009). Also, the Si addition to CrN-based coatings significantly increases their resistance to solid particle erosion as reported in literature (Bousser *et al.* 2008).

The systematic variation of the deposition parameters resulted in relative Si atomic concentrations Si/(Cr + Si) within 0 and 15 at.%, which affect significantly properties of the coatings, their phase stability, and oxidation resistance. Also, the hardness and Young's modulus of the coatings increase with increasing Si concentration (Castaldi *et al.* 2007, Lee et *al.* 2006). The films hardening occurs through two possible mechanisms, i.e., formation of a solid solution of X atoms in MN lattice or formation a nanocomposite material: nc-MN + amorphous phase containing X atoms (Sandu *et al.* 2006a). The increase in nanohardness was attributed to a solid solution hardening mechanism because Si atoms are soluble in the MN lattice in particular concentration range. It can also be attributed to the formation of a nanocomposite films (Sanjinés *et al.* 2005). The nanohardness of M-Si-N ternary coatings depends on Si content. For high concentration of Si (above 12 at.%), the nanohardness decreases due to high volume fraction of amorphous phase and drastic reduction in the crystallite size (Sandu *et al.* 2006b). Cr– Si–N coatings show high hardness, low friction coefficient, and high wear resistance at Si concentration of 10.1 at.% (Lee *et al.* 2007). The films with silicon content lower than 3 at.% form fcc $Cr_{1-x}Si_xN$ compounds with a maximum hardness of 22 GPa, while the films containing more than 3 at.% of silicon shows the segregation of a SiN_x amorphous phase and highly columnar morphology (Martinez. *et al.* 2004b). The literature showing mainly mechanical and tribological properties of CrSiN hard coating deposited using sputtering and it allied processes are summarized in **Table 2.3.**

Table 2.3 Review of CrSiN coatings.

Research Group/s (year)	Hardness (GPa)	Modulus (GPa)	COF	Wear loss (mm^3/Nm)	Process and Variable Parameters	Remarks
Park J H *et al.* (2004)	22 (CrN), 34 (CrSiN	--	CrN – 0.5 CrSiN – 0.2	--	Hybrid system of Arc Ion Plating (AIP) and Sputtering techniques	Si (at.%) = 9.3
Martinez E *et al.* (2004, 2004a)	22 (Si<3%) 14 (Si>3%)	--	--	--	Reactive Magnetron Sputtering	Si<3%
Mercs D *et al.* (2005)	24.5 (CrSiN)	298	0.33	--	Balanced and Unbalanced Magnetron Cathode	various silicon content
Lee H Y *et al.* (2005)	32 (CrSiN)	--	--	--	Closed Field Unbalanced Magnetron Sputtering	various silicon content
Kim G S *et al.* (2005)	24 (CrSiN)	--	0.13 (With lubrication)	--	Closed Field Unbalanced Magnetron Sputtering	Si (at.%) = 9.8
Lee S Y *et al.* (2006)	18 (CrN), 24.2 (CrSiN)	--	0.04 (Lubricated condition)		Unbalanced Magnetron Sputtering	Si contents
Lee J W *et al.* (2007)	24.6 (CrSiN)	240	0.08	--	Bipolar Asymmetric Pulsed DC Reactive Magnetron Sputtering	Si (at.%) = 10.1%, Wear depth: 2.2 nm
Park I W *et al.* (2007)	23 (CrN), 35 (CrSiN),	---	0.5 (CrN), 0.3 (CrSiN)	--	Hybrid system of Arc Ion Plating (AIP) and Magnetron Sputtering	various Si / Al contents
Mercs D *et al.* (2007)	26-27 (CrN), 30 (CrSiN)	--	375	--	Reactive Magnetron Sputtering	Constant RF bias voltage -200V, various silicon content
Benkahoul M *et al.* (2008)	24 (CrSiN)	240	--	--	Pulsed Dc Reactive Dual Magnetron Sputtering	Si (at.%) = 2.3 at.% t

Bousser E *et al.* (2008)	26.6 (Cr–Si–N)	270	--	--	DC Reactive Dual Magnetron Sputtering	Si (at.%) = 6.7
Azzi M *et al.* (2009)	15 (CrSiN)	--	--	--	Dual Magnetron Sputtering,	Using a chromium interface layer (500 nm thick) on the top of plasma nitrided surface, No tendency to delaminate wear under 1.6GPa Hertzian stress
Zhang G *et al.* (2009)	25 (CrSiN)	--	0.4 --	--	Reactive magnetron sputtering	Various silicon contents
Benkahoul M *et al.* (2009)	25	254	0.4	2–4×10−7 mm3/N m	Duplex treatment consisting of surface nitriding and deposition of a Cr bond-coat	various silicon content
Shuyong T *et al.* (2010)	25 (CrSiN) at – 200 V 25 (CrSiN) at 773K	--	--	--	DC magnetron sputtering	Effect of bias and temperature keeping constant Si: 10 at.%

2.2.3 CrAlN Hard Coatings

Transition metal nitrides such as TiN, CrN and HfN, normally show the NaCl (B1) type lattice structure, possess excellent mechanical and chemical properties, which make them suitable for wear resistant, corrosion resistant, and diffusion barrier coatings. Studies on ternary nitride CrAlN coating have shown that it is best alternative to conventional CrN and TiN coatings due to low wear (Wuhrer *et. al* 2004, Uchida *et al.* 2004, Ding *et al.* 2005, Sánchez-López *et al.* 2005, Spain *et al.* 2005, Lin *et al.* 2006, Romero *et al.* 2006) and high oxidation resistance at elevated temperature (Ding *et al.* 2005, Lugscheider *et al.* 2000, Kawate *et al.* 2003, Banakh *et al.* 2003, Willmann *et al.* 2006, Barshilia *et al.* 2006). The effect of additions of Al, Si and Va on the mechanical and tribological properties of CrN coatings deposited using cathodic arc ion plating (Kawate *et al.* 2002, Uchida *et al.* 2004), Cathodic Arc Evaporation (Romero *et al.* 2006) and DC/RF magnetron sputtering (Ding et *al.* 2005, Barshilia *et al.* 2006, Pulugurtha *et al.* 2006, Li *et al.* 2007, Mayrhofer *et al.* 2008) has been reported in the literature. A significant increase in hardness, 30 GPa (Ding et *al.* 2005) to 35 GPa (Brizuela *et al.* 2005) or even higher values to 40 GPa (Ding *et al.* 2008a), has been achieved for the CrAlN coatings when compared to CrN coatings. It also exhibits higher thermal stability than pure CrN coatings.

Sun *et al.* (2004) deposited CrAlN on different substrate materials such as polished (100) silicon wafer, commercial aluminum alloy AA6061, and M42 high speed steel (HSS). They found that the substrate material influences phase evolution in reactively co-sputtered Cr-Al-N coatings with Al contents favorable for B1 phase formation. The **Figure 2.2** shows the possible transformation of a crystal structure in $Cr_{1-x}Al_xN$ against Al content. The crystal structure transforms from the NaCl into wurtzite type at x=0.6 to 0.7. The coatings deposited on (100) Si substrates show a single B1 phase (CrAl)N, which is in accordance with theoretical prediction. In the coatings deposited on the HSS substrates, clustering of Al cations at the B1 CrN {200} planes occur, which leads to the large contraction of interplanar spacing along the {200} planes. With increasing substrate bias voltage, the coatings became more compact and denser, and the microhardness and fracture toughness of the coatings increased correspondingly (Yu *et al.* 2009). $Cr_{1-x}Al_xN$ coatings deposited on Si and Stainless Steel substrates using RF magnetron sputtering with different atomic concentrations of aluminum ($0.51 < x < 0.69$) showed the evolution of (111), (200), and (102) crystallographic orientations associated to the $Cr_{1-x}Al_xN$ cubic and w-AlN phases, respectively (Sanchez *et al.* 2010).

Lin *et al.* (2007) investigated the dependence of structure and properties of CrAlN coatings deposited by pulsed closed field unbalanced magnetron sputtering (P-CFUBMS) on the substrate to chamber wall distance. It was found that increasing the substrate to chamber wall distance from 127 mm to 203 mm can significantly increase the ion flux in front of the substrate. The fully relaxed growth and the columnar structure can be attributed to limited ad-atom mobility on the initial $Al_xCr_{1-x}N(111)$ growth surface (Willmann *et al.* 2008). The CrNx films exhibit highly columnar growth mode when the substrate is oriented parallel to the flux of ionized species (Pulugurtha *et al.* 2006). The improvement of the ion flux in front of the substrate region facilitates ion bombardment on the substrate, increases the mobility of the ad-atoms on the substrate surface, thereby resulting in a denser film with reduced grain size. Varying the ion energy and ion flux in the plasma by pulsing reveals that increasing the pulsed ion energies and ion flux results in a transformation of CrAlN film texture from (200) to (111) (Lin *et al.* 2008).

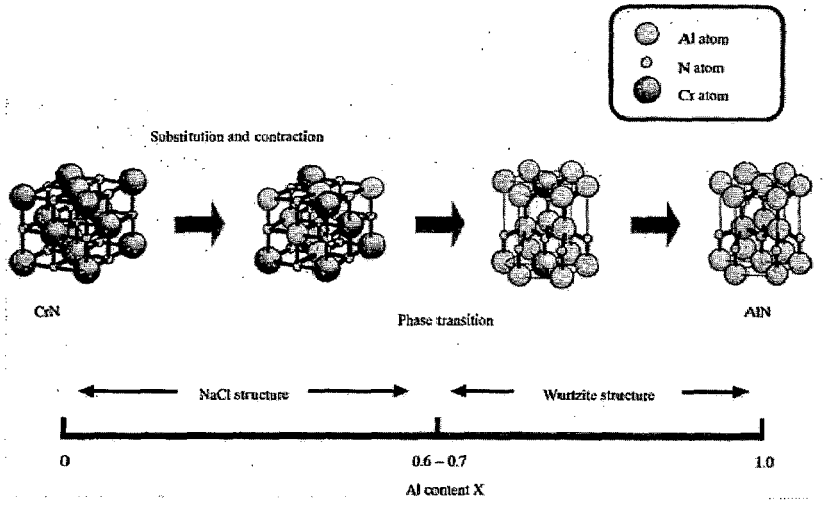

Figure 2.2: Transformation of a crystal structure in $Cr_{1-x}Al_xN$ against Al content showing crystal structure transforms from the NaCl into wurtzite type at x=0.6 to 0.7 (Kawate *et al.* 2002).

A comparative study of magnetron co-sputtered (Ti,Al)N and (Cr,Al)N coatings was made by Wuhrer *et al.* (2004). It was observed in their work that both coatings exhibit similar growth mechanism, the (Cr,Al)N coatings achieved much higher deposition rate and hardness with increasing nitrogen pressure, suggesting the coatings exploitable for many industrial applications. The wear resistance of the $Cr_{1-x}Al_xN$ was dependent on aluminum and nitrogen concentrations in the coatings (Pulugurtha *et al.* 2007). The nanostructured CrAlN coating exhibited less material transfer and thus better adhesive wear protection than the TiN coating under both laboratory pin-on-disc tribo tests and industrial trial conditions (Wang *et al.* 2008). Lin *et al.* (2008a) deposited CrN and CrAlN by pulsed closed field unbalanced magnetron sputtering. The dynamic oxidation behavior of the coatings has been characterized by thermal analysis using differential scanning calorimetry (DSC) and thermogravimetric analysis (TGA). It was found that the CrN_x films oxidized in air after 873K, while the addition of Al to CrN film can further improve the oxidation resistance, especially at the high temperature above 1073K. It was found that both the CrAlN and TiAlN coatings exhibited their best corrosion resistance, respectively, at a composition with Cr/Al or Ti/Al atomic ratio of around 1:1, while the CrAlN coatings showed an evidently better corrosion resistance than the TiAlN coatings (Ding *et al.* 2008) at 773K (Chim *et al.* 2009).

Similarly, Li *et al.* (2008) prepared a multilayer of $Cr_{0.58}Al_{0.42}N$ /$Cr_{0.84}Al_{0.16}N$ /$Cr_{0.51}Al_{0.49}N$ by a reactive magnetron sputtering method. It consists of a bonding layer, a Cr-rich intermediate layer, and an Al-rich outer layer. The multilayer structure provides the coating with good protection against different types of high temperature corrosion. The outer Al-rich layer gives the coating good oxidation resistance at 1273K and 1373K due to the formation of a continuous alumina scale. CrAlN coatings were deposited on silicon and AISI H13 steel substrates using a modified ion beam enhanced magnetron sputtering system (Yu *et al.* 2009a). The reduction in (111) peak intensity and the peaks broadening in the coatings occurs with increasing bias voltage at the same ratio of Al/Cr targets power, which is attributed to the variation in the grain size and microstrain. The wettability of PVD sputtered coated CrAlN surface can be optimized by means of adapting the adhesion energy, which in return leads to an optimized friction behavior as reported in the literature (Bobzin *et al.* 2009).

An incorporation of Al in to CrN coatings enhanced the tribological and mechanical properties as reported in the literature (Banakh *et al.* 2003, Ulrich *et al.* 2003, Baker *et al.* 2003 Uchida *et al.* 2004) due to the formation of complex aluminum and chromium oxides (the

individual element is reacting with atmospheric oxygen and formed oxides layers), which prevents oxygen diffusion to the bulk (Schulz *et al.* 1991, Knotek *et al.* 1991, Fleming et *al.* 1992, Su *et al.* 1997). The literature review on CrAlN hard coating, deposited by sputtering and its allied processes are summarized in **Table 2.4.**

2.3 Objective and Scope of the Present Work

Deposition and characterizations of Cr based coatings on different substrates using a magnetron sputtering deposition techniques have been reported in the literature. The thorough knowledge of microstructural and mechanical properties of Cr based nitride coatings is becoming increasingly important in tribological and diffusion barrier applications. It renders many advantages over other nitride compounds like Ti and W due to high hardness, modulus, good oxidation, corrosion resistance, wear properties, lower residual compressive stresses. The literature on correlation of structural and mechanical properties of CrN based coatings is not exhaustive. As there is a continuous demand on improving the performance of hard coatings for tribological applications, the present work has been envisaged to investigate the structural and mechanical properties of CrN, Cr-Si-N, and Cr-Al-N coatings. The main objectives of the present work are:

- Development of hard coatings especially CrN, CrSiN, CrAlN, on various substrates (SS, Si), by Reactive magnetron sputtering.
- To characterize the different phases of the deposited coatings by XRD and the microstructural features by FE-SEM, AFM and TEM.
- To measure the mechanical properties of the coatings such as hardness and Young's modulus by Microhardness and Nanoindentation techniques.
- To study the tribological properties (Dry sliding wear: mainly coefficient of friction and wear rate) of the coatings by using pin on disc (POD).

Table 2.4 Review of CrAlN coatings.

Research Group/s (year)	Hardness (GPa)	Modulus (GPa)	COF	Wear loss (mm^3/Nm)	Process and Variable Parameters	Remarks
Brizulea M *et al.* (2005)	35	316	0.45	--	DC Magnetron Sputtering	Effect of additions of Aluminium (<15 at.%)
Ding X Z *et al.* (2005)	30 (CrAlN)	270	0.4-0.6	--	Reactive Unbalanced Magnetron Sputtering	Addition of Aluminum
Barshilia H *et al.* (2006)	18 (CrN) 33 (CrAlN)	--	--	--	DC Magnetron Sputtering	Addition of Aluminum
Pulugurtha S R *et al.* (2007)	15 (CrN) 18 (CrAlN)		0.4-0.6	Wear rate is reduced	AC Magnetron Sputtering	Addition of aluminum , Different Ar/ N_2 flow rates
Basnyat P *et al.* (2007)	22 (CrAlN)	300	0.35	$3.36X10^{-6}$	Unbalanced Magnetron DC Sputtering	CrAlN-Ag nanocomposite films
Park I W *et al.* (2007)	23 (CrN), 25 (CrAlN)	---	0.5 (CrN), 0.84 (CrAlN)	--	Hybrid system of Arc Ion Plating (AIP) and Magnetron Sputtering	Various Si / Al contents
Lin J. *et al.* (2008a)	41 (CrAlN)		0.46	3.4×10^{-6}	Pulsed Closed Unbalanced Magnetron Sputtering (P-CFUBMS) with Electrostatic Quadrupole Plasma mass spectrometer (EQP)	Effect of pulsing to provide a wide range of ion energies and ion fluxes, Al: 36 to 43 at.%
Yu Chunyan *et al.* (2009 and 2009a)	28.6 (CrAlN) at -120V	-	--	--	Ion Beam Enhanced Magnetron Sputtering	Effect of substrate negative bias voltages
Sanchez J E *et al.* (2010)	30	303	0.45 to 0.70		RF Reactive Magnetron Co-Sputtering	Aluminum content

CHAPTER 3

EXPERIMENTAL DETAILS

3.1 Material Selection

Transition metal nitrides have been investigated in detail since the initial use of hard coatings to improve tool life and performance of mechanical components. These coatings show high hardness, chemical inertness, and excellent wear resistance due to their bond structure, comprising of one or mixture of bonding such as covalent, metallic and ionic bonding. The hardness of coatings is usually divided into two groups: (i) hard coatings with hardness $\leq$ 40 GPa, and (ii) super hard coatings with hardness > 40 GPa. There are only a few super hard materials, i.e. cubic boron nitride (c-BN), amorphous diamond-like carbon (DLC), amorphous carbon nitride (a-CNx), Ti-Si-N, and poly-crystalline diamond as compared to a large number of hard materials. However, these super hard materials are thermodynamically unstable, which strongly limits their use in tribological applications.

Diamond is an exceptional material with extreme hardness, good wear resistance, low friction coefficient and high thermal conductivity (Lin et *al.* 1998a). Therefore, it is extensively used as a protective coating for cutting tools. However, it does not last for longer time due to poor adhesion between the films and the substrate caused by high internal stress in the films (Lin *et al.* 1998). For instance, a high chemical affinity of carbon to iron limits the applicability of diamond coated cutting tools to machining of Al and their alloys and wood only. The similar problems can be expected when the c-BN coating is used in cutting of steels due to the chemical dissolution of boron in iron. To overcome these problems, nonoxide ceramics, the Si_3N_4/SiAlON ceramics are also used for diverse applications such as cutting tools, seal rings, valve seats, cylinder liners, and a variety of high-efficiency engines and other mechanical systems due to their superior combination of low density and high fracture toughness, hardness, strength, and thermal shock resistance (Kumar *et al.* 2009).

There is growing interests in developing protective hard coatings, which could withstand the above mentioned problems even at elevated temperature. The superhard materials of transition

metal nitrides based on superlattices and nanocomposites were developed to provide superior tribological properties along with their chemical stability (Veprek *et al.* 1999, Veprek *et al.* 2000, Mayrhofer 2006).

In the past decades, TiN-based films deposited by the physical vapour deposition (PVD) or chemical vapour deposition (CVD) method have found widespread applications in wear resistant situations such as cutting tools or machine parts because of their high hardness, good wear resistance, chemical inertness, and high temperature stability. Veprek (Veprek *et al.* 1996, Veprek *et al.* 1999, Veprek *et al.* 2000, Niederhofer *et al.* 2001, Ma *et al.* 2005) reported superhard TiSiN nanocomposite films with a hardness of 80–105 GPa, which is higher than that of diamond (70–90 GPa). They have proposed a two-phase structure model to interpret the mechanism contributing to superhardness in nanocomposite TiSiN films. It forms a structure of nanocrystalline (nc) TiN surrounded by amorphous Si_3N_4, known as nc-TiN/a-Si_3N_4. This concept is based on a strong, thermodynamically driven, and diffusion rate-controlled (spinodal) phase segregation that leads to the formation of a stable nanostructure by self-organization.

Recently, a lot of efforts have been focused on the development of other binary and ternary metal nitrides, grown by PVD processes, such as CrN, VN (Jung *et al.*, 2005, Ortmann *et al.* 2005), ZrN (Nose *et al.* 2002), WN (Veprek *et al.* 1996, Veprek *et al.* 1996a), CrSiN, and CrAlN. The reasons for due emphasis on particular CrN compound, is mainly due to its superior corrosion and wear properties (Jagielski *et al.* 2000), than the TiN films.

The descriptions of coating synthesis, structural and mechanical characterizations are discussed in the following sections.

3.2 Coating Synthesis

The choice of a deposition technique to deposit coating usually depends on the specific characteristics of films required for a study or application of interest. The basic requirement of good quality coatings are i) good uniformity of the films throughout exposed area, ii) the films with good physical and chemical properties such as low stress, good adhesion to the substrates, high density, low films defects (pinhole density), controlled grain size and its distribution, boundary property, and orientation, equipment initial cost, and running cost. There are wide

varieties of deposition techniques available, as shown in **Table 3.1**. Among the physical vapor deposition (PVD) and chemical Vapor Deposition (CVD) techniques, magnetron sputtering is found to be very effective for depositing thin films with good microstructural as well as mechanical characteristics. A comparative evaluation of thin film deposition techniques are summarized in **Table 3.2**.

In PVD, the synthesis of thin films is usually carried out from the same material and its purity depends on the starting materials, base vacuum, and purity of the ambient gas atmosphere (Xue *et al.* 2002, Chandra *et al.* 2006, Gohil *et al.* 2008). On the other hand, in chemical vapor deposition (CVD) technique, some un-reacted chemicals and products other than the desired one are often left behind after the deposition of coatings.

Table 3.1 Common thin film deposition techniques.

Physical Vapor Deposition (PVD)	Evaporation • Thermal evaporation • E-beam vaporation Sputtering • DC sputtering • DC Magnetron sputtering • RF sputtering Reactive PVD
Chemical Vapor Deposition (CVD)	Low-Pressure CVD (LPCVD) Plasma-Enhanced CVD (PECVD) Atmosphere-Pressure CVD (APCVD) Metal-Organic CVD (MOCVD)
Thermal Spray	Flame Spraying (FLSP) Plasma Spraying (PSP) Electric Arc Spraying (EASP) Detonation Gun (d-Gun) High-velocity Oxy/Fuel (HVOF)

In the evaporation methods, the source material to be deposited (evaporant) is loaded into the container or crucible, which is heated at high temperature. At sufficiently high temperature, the source material evaporates and it gets transported and impinges on the surface of the substrate. Subsequently, it condenses and absorbed by the surface. The main demerit of evaporation methods

is due to the decompsotion of compound materials prepared by this route at high temperature. Also, each component with different vapor pressure and different deposition rate, leads to formation of coating with different stoichiometry compared to the source or target.

Thermal spray processes deposit a continuous coating by melting the consumable material (target) into droplets and subsequently impinging these droplets on the substrate. Some common thermal spraying processes are flame Spraying (FLSP), plasma Arc spraying (PSP), electric Arc Spraying (EASP), detonation Gun (d-Gun), and high-velocity oxy/fuel (HVOF). Plasma spray is a preferred technique for spraying ceramics on metals due to very high temperature required for melting powders. The coatings are usually denser and show better adhesion than flame spray process. It is considered as the economical method for producing reproducible and durable thick zirconia coatings for thermal barrier applications used extensively in the aerospace industry (**Ravi *et al.* 2008**).

3.2.1 Sputtering

Sputtering belongs to one of the Physical Vapor Deposition (PVD) techniques. It includes any deposition technique that uses evaporation or collision impact, e.g. sputtering, to cause atoms from a molten or solid source to enter a condensable vapor phase in a reduced pressure environment and subsequent deposition on a substrate, forming the coating from this vapor phase (Behrisch *et al.* 1981, Sigmund *et al.* 1987). Examples of other PVD methods also include molecular beam epitaxy and ion beam deposition. Sputter deposition is a cost effective, time saving, and simple method for the deposition of metallic coatings on substrates in high vacuum and has an accelerating demand for productions in thin films and coating industries. Also, it is environmentally safe, as it involves transfer of vapor atoms instead of ions, which has no hexavalent chromium Cr^6 emission, as in electro-deposition techniques (Seok *et al.* 2001). This technique centers on the use of plasma to create ions, normally Ar+ ions, which strike a negatively charged target of a certain material. Neutral atoms are dislodged from the target due to momentum transfer and are subsequently deposited on a substrate that lies in typically the line

Table 3.2 Comparative evaluation of thin film deposition techniques.

Process	Material	Uniformity	Impurity	Grain Size	Film Density	Deposition Rate	Substrate temperature	Directional	Cost
Thermal Evaporation	Metal or low melting pint material	Poor	High	10-100nm	Poor	1-20 Å/s	50-100°C	Yes	Very low
E-beam Evaporation	Both metals and dielectrics	Poor	Low	10-100nm	Poor	10-100Å/s	50-100°C	Yes	High
Sputtering	Both metals and dielectrics	Very Good	Low	10 nm	Good	Metal: 100Å/s Dielectric: 10Å/s	200-300°C	Some Degree	High
PECVD	Mainly Dielectric	Good	Very low	10-100nm	Good	10-100Å/s	300-400°C	Some degree	Very high
LPCVD	Mainly Dielectric	Very Good	Very Low	1-10nm	Excellent	10-100Å/s	600-1200°C	isotropic	Very high

of site of the target. Plasma is generated when a large negative potential is applied between cathode and anode across the working gas, electrons will accelerate in between them. Those electrons traveling fast enough may collide with gas atoms and there is a possibility that an electron will be torn out of the atom. These electrons then generate more ions which result in plasma formation. Plasma is a gas consisting of a substantial and equal number of electrons and positive ions. In the present work, Cr based coatings were deposited by a DC magnetron sputtering system, the detailed description of this technique is given below.

This process is very complex in nature due to the basic physics of the process and interpretation of the results is further complicated by the properties of the sputtered films depending on several deposition parameters. The various deposition parameters can be listed as: (i) sputter gas, (ii) gas pressure, (iii) gas flow rate, (iv) target dimensions, (v) target to substrate spacing (vi) target voltage, (vii) discharge current, (viii) substrate material, (ix) substrate temperature, (x) target material composition, (xi) target density, and (xii) target temperature. It is generally believed that if all these parameters are kept constant from run to run, one should be able to obtain reproducible films. There are several difficulties, however, which arise in maintaining identical deposition conditions from run to run. Hence, reproducibility of the films becomes hard to achieve.

Sputtering is the process of ejection of atoms from the surface of a material by bombardment with energetic particles. This elementary event is an atomic collision cascade wherein the incident ion knocks atoms off their equilibrium sites in the targets, thus causing these atoms to move through the material, to undergo further collisions, and eventually to cause the ejection of atoms through the target surface. The ejected or sputtered atoms condense on a substrate and forms thin films. The general consensus is that sputtering is the most universal one, being active for ionic bombardment of all types of solids at appropriate ion energy. The sputtering phenomena have been known since 1852 (Grove 1952). The sputtering process is widely used in industries and research lab (Mahan 2000, Chopra 1969, Ohring 1992, Maissel *et al.* 1970, Wasa *et al.* 1992, Chapmann 1980, Vossen 1978).

The schematic diagram of the simplest form of a DC sputtering system is shown in **Figure 3.1**. It consists of a single vacuum chamber, one target, and a substrate holder. The target and substrate are placed inside a vacuum chamber. The target is a disc of material to be deposited is connected to the negative terminal of a DC power supply. The target is also known as cathode. The

substrate that faces the cathode may be grounded or electrically floating. The first step in the sputtering process is the pumping of the vacuum chamber to a typical base pressure of 10^{-6} Torr. Then an inert gas e.g. argon, is introduced, in which a glow discharge plasma is initiated and sustained. A very little current flows at first due to the small number of charge carriers in the system after the initial application of the voltage. Once sufficient number of charge carriers builds up, the free electrons will strike the Ar neutrals to create Ar+ ions and more free electrons. The newly created free electrons can now ionize additional Ar neutrals thus multiplying the number of Ar+ ions. In this visible glow maintained between the electrodes, the Ar+ ions in the plasma gets accelerated towards direction of the cathode and strike the target. The neutral target atoms are dislodged by the collision with the Ar+ ions through momentum transfer. Subsequently, these target atoms enter and pass through the discharge region and get deposited on all surfaces in the line of sight of the substrate.

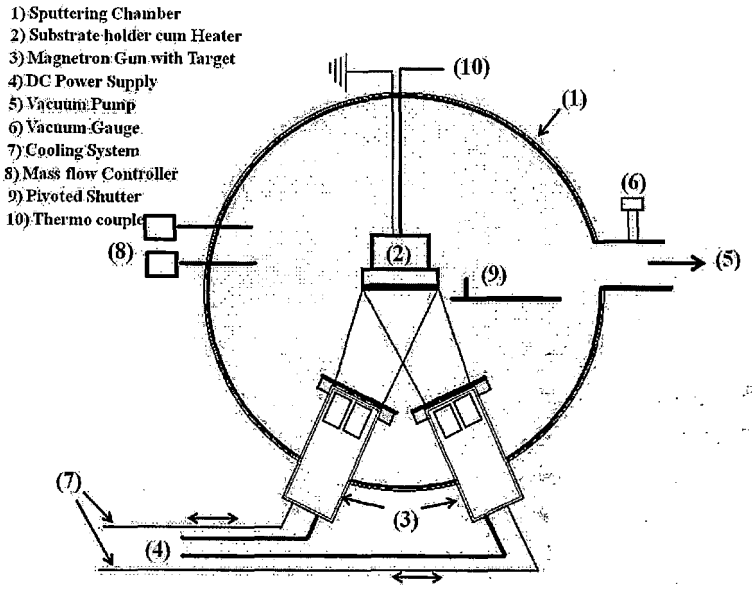

Figure 3.1 Schematic diagram of the simplest form of a DC sputtering system.

Sputtering is characterized by the sputter yield '*S*', which is the ratio of the ejected atoms to the number of incoming energetic particles, which are predominantly ions. Sputter yield depends

on the energy and direction of the incident (bombarding) ions, masses of the ions and target atoms, and the binding energy of atoms in the solid.

By Sigmund's theory (Sigmund 1969, Chawla 2008 PhD Thesis), the sputter yield is given as

$$S = \frac{3\alpha}{4\pi^2}\frac{4M_1M_2}{(M_1+M_2)^2}\frac{E}{E_b} \qquad \text{(For } E < 1 \text{ KeV)} \qquad (3.1)$$

where, E_b is the surface binding energy of the target atom being sputtered, E is the ion bombardment energy, α is a measure of the efficiency of momentum transfer in collisions, and M_1 and M_2 are the masses of the positive ion of the gas and target material, respectively.

When the ion bombardment energy is $E > 1$ KeV, the sputter yield is given by

$$S = 3.56\alpha\frac{Z_1Z_2}{Z_1^{2/3}+Z_2^{2/3}}\left(\frac{M_1}{M_1+M_2}\right)\frac{S_n(E)}{E_b} \qquad (3.2)$$

where, Z_1 and Z_2 are the atomic numbers of the incident ion and sputtered target atom respectively, and $S_n(E)$ is a measure of the energy loss per unit length due to nuclear collisions. It is a function of the energy as well as masses and atomic numbers of the atoms involved (Ohring 2002).

3.2.2 Magnetron Sputtering

There are various types of sputtering process, broadly divided into four categories: (a) Direct Current (DC) sputtering, (b) Radio Frequency (RF) sputtering, (c) Magnetron sputtering and (d) Reactive sputtering. Magnetron sputtering is a magnetically assisted discharge, which enables to increase the thin film deposition rates during sputter deposition. The deposition rate is increased by increasing mean free path of the electrons in the plasma. The longer the free electrons remain in the plasma, higher the collision probability and the number of Ar+ ions. This leads to a higher deposition rate. The mean free path of the electron in the plasma can be lengthened by placement of a permanent magnet on the back side of the target to create a magnetic field with a field direction parallel to the target surface as seen in **Figure 3.2.**

When the current density, which is proportional to ionization rate, increases to specific units i.e 100 times, then the required discharge pressure drops by same i.e 100 times to achieve the higher deposition rate as shown in **Figure 3.3.** In the magnetron sputtering, the magnetic field 'B' is superimposed on the electric field 'E' between target and substrate. The ions will experience dual field environment of Lorentz force that is given by

$$F = q\,[E + (v \times B)] \qquad (3.3)$$

where q, v are charge and velocity of ions, respectively. Recently, great attention has been devoted to the pulsed direct current (DC) reactive magnetron sputtering technique, due to its ability to reduce arcing and target poisoning, and its capability of producing insulating thin films (Lee *et al.* 2005).

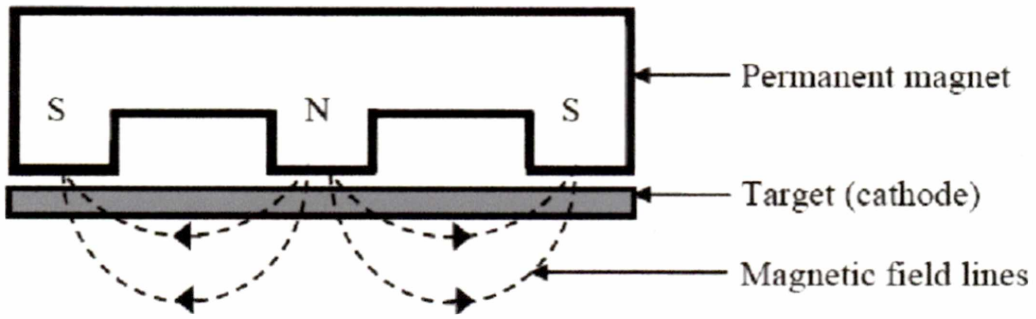

Figure 3.2 Position of permanent magnet and chromium target in the DC magnetron sputtering system.

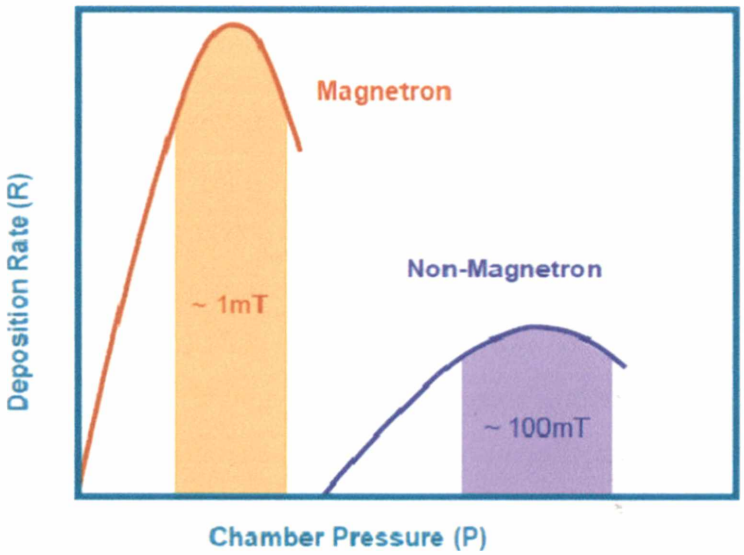

Figure 3.3 Effect of magnetron in the sputter deposition system.

3.2.3 Description of Sputter Deposition Technique

Figure 3.4 shows the actual magnetron sputtering system, assembled and installed in Nano Science laboratory for the synthesis of Cr based nitride thin films (CrN, CrSiN, CrAlN,

CrN/Si_3N_4). For DC sputtering, a Glassman LV DC power supply (0–600V, 0 –1.7A) or Aplab high voltage DC power supply (50-1000V, 0-1A) was used while for RF sputtering, a RF plasma products power supply (600W at 13.56 MHz) was used with a MWH- 5-01 impedance matching network. Metallic targets of Cr, Al and Si were used to prepare various Cr based hard coating of transition metal nitrides. For the preparation of Cr based hard coatings, the substrates such as silicon Si (100) wafer and Stainless steel SA304 substrates are fixed on a heater with the help of clips and silver paste. The temperature of the substrate is controlled via the temperature controller of heater. After mounting the substrates, the chamber is evacuated using a turbo molecular (Pfeiffer) pump, backed by rotary pump. A base pressure of $5x10^{-6}$ Torr could be achieved by pumping the chamber. After evacuation, a mixture of an inert gas such as argon (99.999% purity) and a reactive gas such as N_2 (99.999%) is supplied into the chamber via gas inlet valve. Simultaneously, the gate valve is brought into almost closed state (throttling) so as to match the gas influx and pumping-out rate. With proper throttling, the inert gas pressure and flow rate inside the chamber can be made very stable. DC sputtering is used for conducting targets; while in case of poorly conducting materials (non metals), RF-voltage is applied across the target and the substrate, the latter being kept at a common ground potential with the rest of the chamber.

3.3 Characterization Techniques

After deposition of coatings using magnetron sputtering techniques with altering different process conditions, the structural properties such as grain size, orientation, different phases formed, hardness, modulus, coefficient of friction, wear rate, film thickness etc. are investigated by characterization techniques such as XRD, AFM, SEM, TEM (Ambat *et al.* 2000). The hardness and Young's modulus of the coatings were measured by microhardness tester and nanoindentation techniques. The wear rate and coefficient of friction of the coatings were measured by Pin on Disc method. The brief description includes working principle, construction, and applications of each technique for the respective characterization as explained below.

Figure 3.4 Dual chamber magnetron sputtering technique.

3.3.1 Structural Characterization

3.3.1.1 X-ray Diffraction

X-ray diffraction is the most powerful non-destructive tool for determining the structure of solid matter and it finds wide range of applications in material characterization, especially for identification of unknown substances, trace analysis, determination of crystal structure, phase analysis, detection of crystal imperfection, layer thickness determination, determination of preferred orientation and crystallite size. The interaction of X-ray radiation with crystalline sample is governed by Bragg's law, which indicates a relationship among the diffraction angle (Bragg angle), X-ray wavelength, and inter-planar spacing. According to Bragg, the X-ray diffraction can be visualized as X-rays reflecting from a series of crystallographic planes as shown in **Figure 3.5**. The path differences introduced between a pair of waves traveled through the neighboring crystallographic planes are determined by the inter-planar spacing. If the total path difference is equal to $n\lambda$ (as n being an integer and λ being the wavelength), the constructive interference will occur and a group of diffraction peaks can be observed and give rise to x-ray patterns. The quantitative account of Bragg's law can be expressed as

$$2d_{hkl}\,Sin\theta = n\lambda \qquad (3.4)$$

where 'd' is the inter-planar spacing for a given set of *hkl*, 'θ' is the Bragg angle, and 'λ' is the wavelength shown in **Figure 3.5**. The intensity of powder diffraction peaks is in principal determined by the structural factor, F_{hkl} as expressed in equation 3.5, which depends on the crystal structures including relative positions of atoms in the unit cell, types of unit cells and other characteristics such as thermal motion and population parameters.

$$F_{hkl} = \sum_{i=1}^{n} g^i t^i(S) f^i(S) \exp\left[\, 2\pi i\,(hx^i + Ky^i + lz^i)\right] \qquad (3.5)$$

where f^i(s) is the atomic scattering factor, g^i is the population factor of i^{th} atom, t^i(s) is the temperature factor, *hkl* are the Miller indices, and xyz are the fractional coordinates of i^{th} atom in the unit cell.

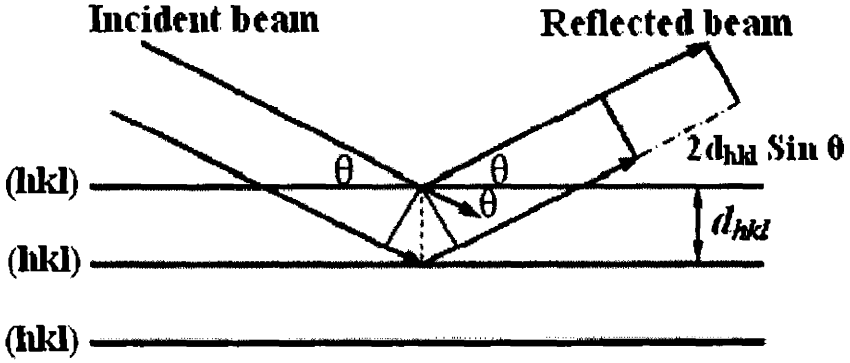

Figure 3.5 Crystal planes and Bragg's law.

One of the frequent applications of XRD analysis is to determine the crystalline size and lattice strain in nanocrystalline thin film materials. The peak broadening in XRD patterns for nanomaterials is the result of the finite size effect. For a finite size nanocrystal, the number of X-ray radiation reflected from successive lattice planes that add up to produce constructive or destructive interference becomes finite and therefore they cannot reinforce or cancel out completely. Additionally, some other factors such as inhomogeneous lattice strains, variation in the lattice constant from one crystallite to another and structural faults can also yield the broadening of the diffraction peaks. Scherrer formula (Eq. 3.6) offers a simple relationship between crystallite size and peak broadening.

$$D = \frac{0.9\,\lambda}{\beta\,Cos\,\theta} \qquad (3.6)$$

where D is the average crystalline dimension perpendicular to the reflecting phases, λ is the X-ray wavelength, θ is the Bragg angle, and β is the finite size broadening (FWHM). This formula is often used to estimate the average crystallite size.

For all X-ray diffraction experiments carried out in this work, a Philips X-ray diffractometer (8D Advance, brucker)) with Cu Kα (λ = 1.54187 Å) radiation was employed and operated at applied voltage of 40 kV and filament current of 30 mA. The phase identification for all samples reported here was performed by matching the peak positions and intensities in the experimental diffraction patterns to those patterns in the JCPDS (Joint Committee on Powder Diffraction Standards) database. The diffractometer used sodium iodide (NaI) scintillation counter as a detector. It could detect the diffracted radiations in the wavelength ranging from 0.5 to 3 Å. Monochromators were used to suppress the undesired portions of radiation. To restrict the irradiated specimen area, aperture diaphragm was arranged between the tube and the specimen as shown in **Figure 3.6**. The second aperture diaphragm shielded the strong scattered radiation of the first aperture diaphragm and the resolution depends upon the detector diaphragm. The scattered radiation diaphragm was used to suppress undesired scattered radiation.

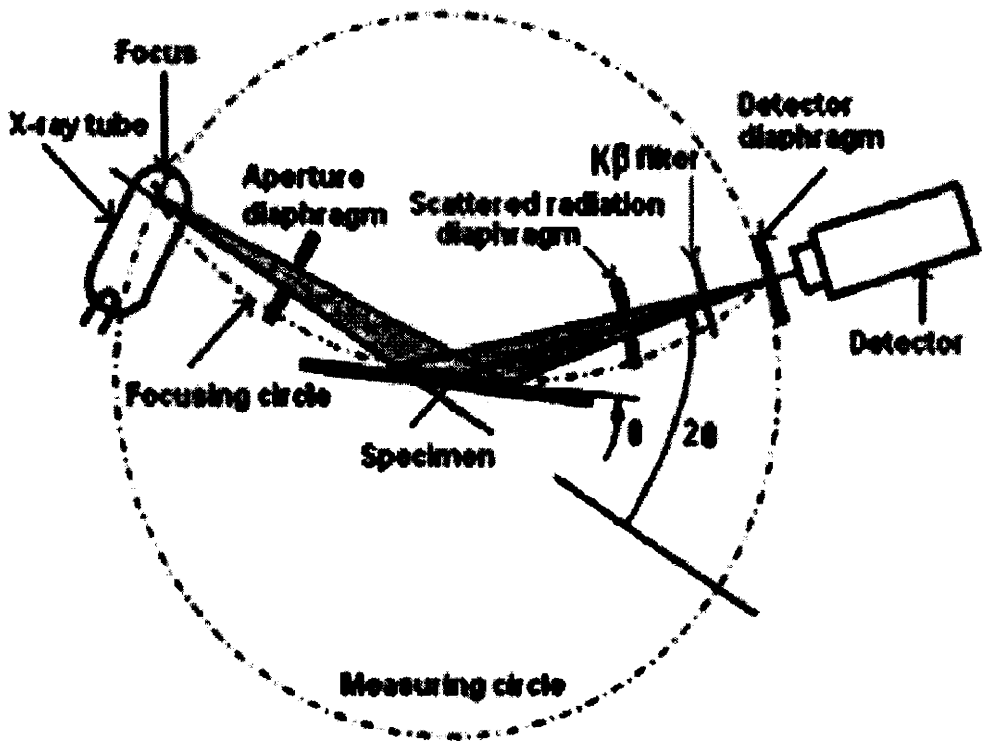

Figure 3.6 Schematic diagram of beam path.

The crystallographic information was obtained by evaluating the '*d*' values and indexing of reflections (Miller indices). The characteristic diffraction pattern of a given substance can always be obtained when the substance was present in pure state or as one of the constituents in a mixture of several substances. This fact is the basis of the diffraction method of chemical analysis. X-ray diffraction pattern is characterized by a set of line positions (2θ) and a set of relative intensities (I). The angular position of lines depends on the wavelength of the incident ray and spacing (d) of the lattice planes.

3.3.1.2 Scanning Electron Microscopy (SEM)

The scanning electron microscope (SEM) uses a focused beam of high-energy electrons to generate a variety of signals at the surface of solid specimens. The signals that derive from electron-sample interactions reveal information about the sample including external morphology (texture), chemical composition, and crystalline structure and orientation of materials constituting the sample. In most applications, data are collected over a selected area of the surface of the sample, and a 2-dimensional image is generated that displays spatial variations in these properties. The SEM has large depth of field, the amount of the sample that can be in sharp focus at one time, which can be up to 400 times higher than that of light microscope. Also, it has higher resolution and so the samples can be examined at a higher magnification than a light microscope. The wide range of magnification ranges from 10X to approximately 300,000X, spatial resolution of 5 to 10 nm. The SEM is also capable of performing analyses of selected point locations on the sample; this approach is especially useful in qualitatively or semi-quantitatively determining chemical compositions (using EDS), crystalline structure, and crystal orientations (using EBSD).

Accelerated electrons in an SEM carry significant amounts of kinetic energy, and this energy is dissipated as a variety of signals produced by electron-sample interactions when the incident electrons are decelerated in the solid sample. These signals include secondary electrons (that produce SEM images), backscattered electrons (BSE), diffracted backscattered electrons (EBSD used to determine crystal structures and orientations of minerals), photons (characteristic X-rays that are used for elemental analysis and continuum X-rays), visible light (cathodoluminescence-CL), and heat. Secondary electrons and backscattered electrons are commonly used for imaging samples, the former provides information pertaining to morphology and topography of the samples and the latter useful for illustrating contrasts in composition of

multiphase samples (i.e. for rapid phase discrimination). However, the secondary electron that reaches the Everhart-Thornley detector may originate from four different sources (**Figure 3.7**). X-ray generation is produced by inelastic collisions of the incident electrons with electrons in discrete orbital (shells) of atoms in the sample. As the excited electrons return to lower energy states, it generates X-rays with a fixed wavelength, which is related to the difference in energy levels of electrons in different shells for a given element. Thus, characteristic X-rays are produced for each element in a sample that is "excited" by the electron beam. SEM analysis is considered to be "non-destructive"; that is, X-rays generated by electron interactions do not lead to volume loss of the sample, so it is possible to analyze the same materials repeatedly.

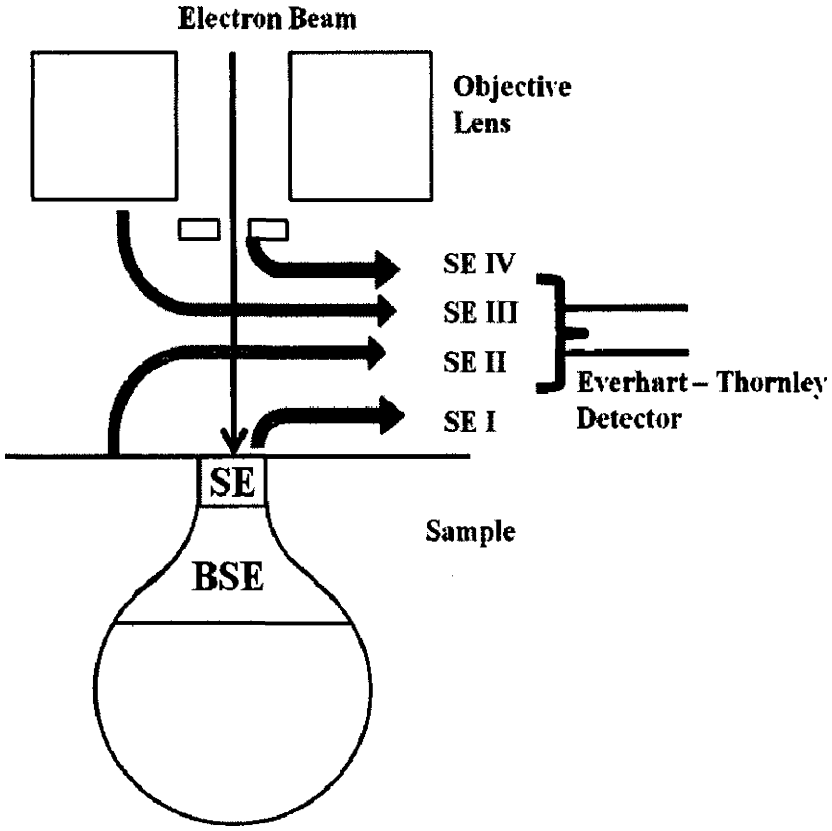

Figure 3.7 Origin of secondary electron in scanning electron microscopy.

The secondary electrons (SE) that reaches the Everhart –Thornley detector may originate from four different sources: SE from the area of sample beam interaction, SE from back scattered electrons as they exit the sample, SE produced by interaction between backscattered electrons derived from the samples and various parts of the samples chamber, SE produced by interaction between the electron beam and the final aperture as shown in **Figure 3.7.**

The basic diagram of SEM is shown in **Figure 3.8.** The electron gun produces a beam of electrons that is attracted through the anode and condensed by the condenser lens and then focused as a very fine point on the specimen by the objective lens. A set of small coils of wire, called the scan coils, is located within the objective lens. The coils are energized by a varying voltage produced by the scan generator and create a magnetic field that deflects the beam of electrons back and forth in a controlled pattern called raster. The raster is a very similar to the raster in a television receiver. The varying voltage from the scan generator is also applied to a set of deflection coils around the neck of a cathode ray tube (CRT). The magnetic field from this coil causes the deflection of a spot of light back and forth on the surface of the CRT. The pattern of deflection of the beam of electron on the sample is exactly the same as the pattern of deflection of the spot light on the CRT.

When the beam of electrons strikes the sample, a complex series of interactions occurs, resulting in the production of secondary electrons from the sample, which are collected by the detector, converted to a voltage, and amplified. The amplified voltage is then applied to the grid of the CRT and modulates or changes the intensity of the spot of light on the surface. For example, if at a given instance, the beam is projected on the surface, a large number of secondary electrons will be detected, causing a large voltage in the detector that result in a bright spot on the surface of CRT. If the beam of electrons moves to a depression on the sample, fewer electron will be detected and smaller voltage will be developed in the detector, resulting in a darker spot on the surface of the CRT. The SEM image, then, consists of thousands of spots of varying intensity in the face of CRT that correspond to the topography of the sample.

3.3.1.3 Energy Dispersive Spectroscopy (EDS)

Interaction of an electron beam with a sample target produces a variety of emissions, including X-rays. An energy-dispersive (EDS) detector is used to separate the characteristic X-rays of different elements into an energy spectrum. EDS system software is used to analyze the energy spectrum in order to determine the abundance of specific elements. EDS can be used to find the chemical composition of materials down to a spot size of a few microns, and to create elemental composition maps over a much broader raster area. These capabilities provide fundamental compositional information for a wide variety of materials. EDS systems are typically integrated into either an SEM or EPMA instrument. It include a sensitive X-ray detector, a liquid nitrogen dewar for cooling, and software to collect and analyze energy spectra. The detector is mounted in

the sample chamber of the main instrument at the end of a long arm, which is itself cooled by liquid nitrogen.

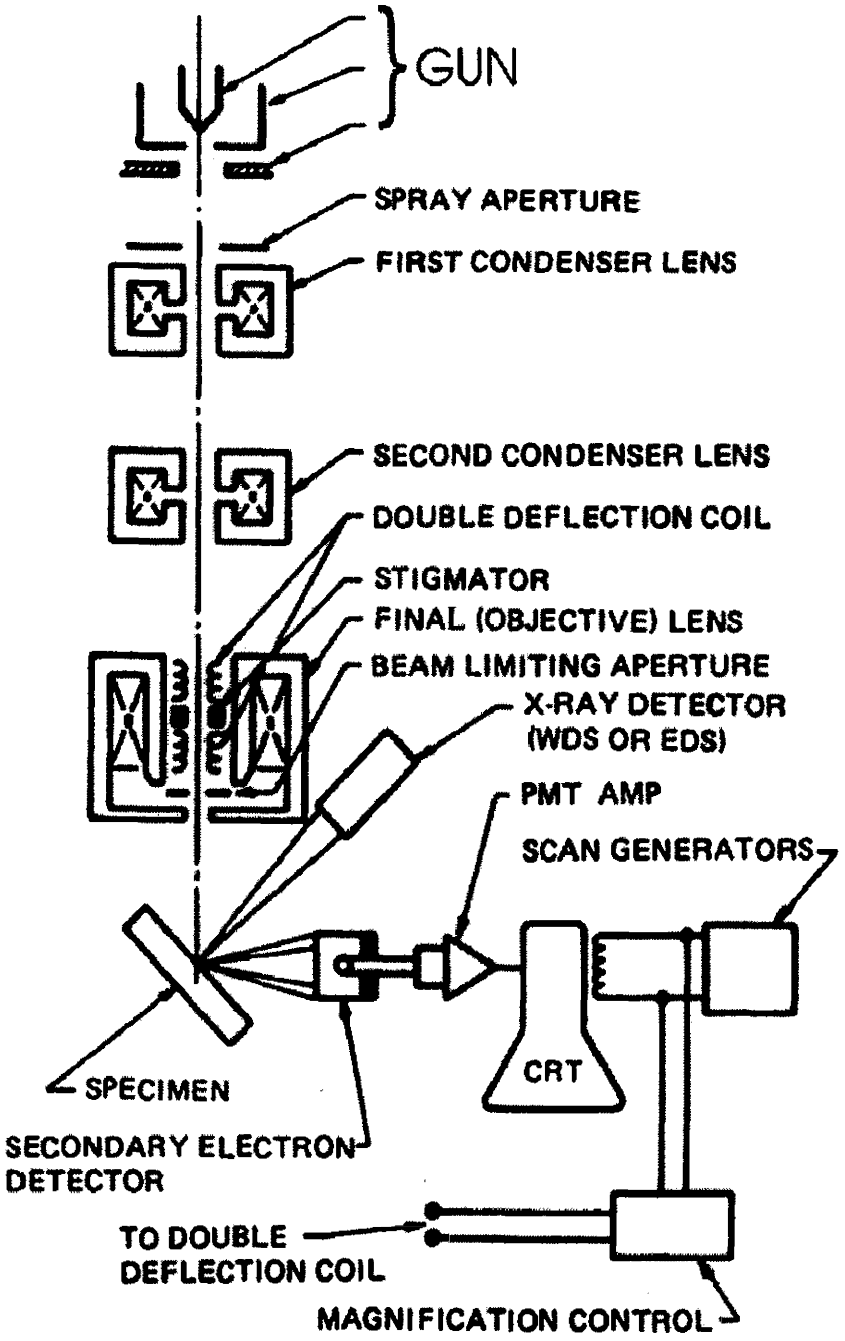

Figure 3.8 Line diagram of Scanning Electron Microscopy.

The most common detectors are made of Si(Li) crystals that operate at low voltages to improve sensitivity, but recent advances in detector technology make available so-called "silicon drift detectors" that operate at higher count rates without liquid nitrogen cooling. An EDS detector contains a crystal that absorbs the energy of incoming X-rays by ionization, yielding free electrons

in the crystal that become conductive and produce an electrical charge bias. The X-ray absorption thus converts the energy of individual X-rays into electrical voltages of proportional size; the electrical pulses correspond to the characteristic X-rays of the element.

3.3.1.4 Atomic Force Microscopy (AFM)

The AFM is one of the foremost tools for imaging, measuring, and manipulating matter at the nanoscale. STM was first developed in 1982 at IBM in Zurich by Binnig *et al.* (1982) for which Binnig and Rohrer was awarded the Nobel Prize in Physics in 1986. The STM has the ability to image and measure material surface morphology with atomic scale but the only good electrical conductors are candidates for this technique. This significantly limits the materials that can be studied using STM and led to the development, in 1986, of the atomic force microscope by Binnig, Quate, and Gerber (Binnig, G 1986). This enabled the detection of atomic scale features on a wide range of insulating surfaces that include ceramic materials, biological samples, and polymers. AFM provides a number of advantages over conventional available microscopy techniques. It probes the sample and make measurements in three dimensions, *x, y,* and *z* (normal to the sample surface), thus enabling the presentation of three-dimensional images of a sample surface. This provides a great advantage over any microscope available previously. With good samples (clean, with no excessively large surface features), resolution in the *x-y* plane ranges from 0.1 to 1.0 nm and in the *z* direction is 0.01 nm (atomic resolution). AFMs require neither a vacuum environment nor any special sample preparation, and they can be used in either an ambient or liquid environment. With these advantages AFM has significantly impacted the fields of materials science, chemistry, biology, physics, and the specialized field of semiconductors.

In AFM, the mechanical motion is created from electrical energy with an electromechanical transducer (piezoelectric ceramic). The piezoelectric material undertakes some changes in geometry when it is placed in an electric field. The amount and direction of motion depends on the type of piezoelectric material, shape of the material, and the field strength. **Figure 3.9** shows the motion of a piezoelectric disk when exposed to an electric potential. A typical piezoelectric material will expand by about 1 nm per applied volt. Thus, to get larger motions, it is common to make piezoelectric transducers with hundreds of layers of piezoelectric materials. By using one thousand layers of piezoelectric material, it is possible to get motions as large as 1000 nm per volt.

Thus, with 100V, it is possible to get 0.1 mm of motion with a multiple layer of piezoelectric transducer.

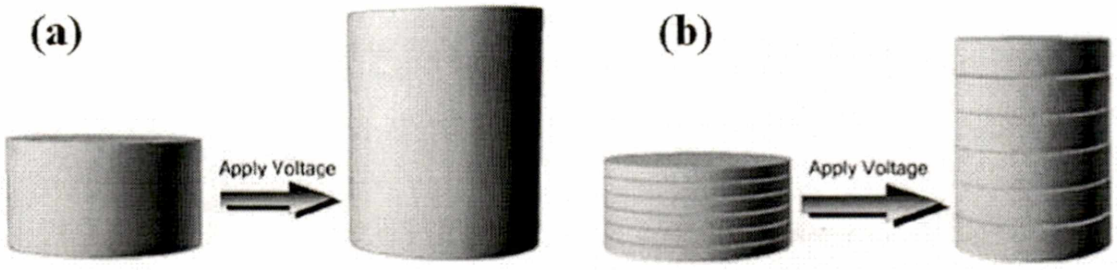

Figure 3.9 Movement of a piezoelectric disc when exposed to an electric potential a) single piezoelectric disc, b) a stake of piezoelectric disc.

The AFM system used in the present studies is the NTMDT, produced by NTEGRA Probe nanotechnology, Russia. The basic structure of the AFM system is sketched in **Figure 3.10**. Its working principle can be simply described as a measurement of the forces acting on the scanning tip via detecting the deflection of the moving cantilever. The interaction force between the scanning tip and sample surface is the essential parameter to determine the AFM scanning mode. In the force – distance diagram illustrated in **Figure 3.11**, the contact and non-contact regime are clearly indicated as the function of the distance between tip and sample surface. By decreasing the gap between the scanning tip and sample surface, the interaction forces can change from attractive to repulsive. As the atoms are gradually coming closer to each other, they first attract each other. This attraction increases until the atoms are so close together that they begin to repel each other. With further reducing the gap, the repulsive force can dramatically increase due to the Pauli Exclusion Principle and become the dominant interaction with progressive weakening of the attractive force. Further reduction in distance than this distance (zero force), the total van der Waals force becomes positive (repulsive). This distance will not change, therefore any more attempt to force the sample and tip closer will result in deformation or damage to the sample or the tip. With varying interaction force, the cantilever deflects in different ways. It can be bent upward, downward or twisted. There are two other forces that arise during the scan:

i) a capillary force that is caused by a build-up of water. In real conditions (in ambient air), practically always some humidity is present in air and a water layer is adsorbed on the sample and tip surfaces (Weblink 3).

ii) on the tip; the force is caused by the cantilever itself, which is like a force caused by a compressed spring .

For most applications, the AFM is operated in one of the following three modes:

a) Contact mode

b) Non-Contact mode

c) Semicontact mode / Intermittent mode / Tapping mode

Contact mode is the most common method of operation of the AFM and is useful for obtaining 3D topographical information on nanostructures and surfaces. As the name suggests, the tip and sample remain in close contact as the scanning proceeds. "Contact" represents the repulsive regime of the inter-molecular force curve, the part of the curve above the x-axis (**Figure 3.10**). Most cantilevers have spring constants < 1 Nm, which is less than effective spring constant holding atoms together. One of the drawbacks of the tip remaining in contact with the sample is that large lateral forces can be exerted on the sample as the tip is dragged over the specimen. These large forces can result in deformed images and damaged samples. Small lateral forces, however, can be used to provide information on the friction (drag resistance) between the tip and sample in a mode known as lateral force microscopy (LFM).

Tapping mode is another mode of operation for AFM. Unlike the operation of contact mode, where the tip is in constant contact with the surface, in tapping mode, the tip makes intermittent contact with the surface. As the tip is scanned over the surface, the cantilever is driven at its resonant frequency (hundreds of kHz). Because the contact time is a small fraction of its oscillation period, the lateral forces are reduced dramatically. Tapping mode is usually preferred to image samples with structures that are weakly bound to the surface or samples that are soft (polymers, thin films). There are also two other types of image contrast mechanisms in tapping mode:

Amplitude imaging. The feedback loop adjusts the *z*- axis movement so that the amplitude of the cantilever oscillation remains (nearly) constant. The voltages needed to keep the amplitude constant can be compiled into an (error signal) image, and this imaging can often provide high contrast between features on the surface.

Phase imaging The phase difference between the driven oscillations of the cantilever and the measured oscillations can be attributed to different material properties. For example, the relative amount of phase lag between the freely oscillating cantilever and the detected

signal can provide qualitative information about the differences in chemical composition, adhesion, and friction properties.

Non-contact mode is a method where the cantilever is oscillated above the surface of the sample at distance such that it is no longer in the repulsive regime but in the attractive regime of the inter-molecular force curve. The operation of non-contact imaging is quite difficult in ambient conditions because of the existing thin layer of water on the tip and the surface. As the tip is brought close to the surface, a small capillary bridge between the tip and the sample could cause frequently jump of the tip to-contact the surface. Every material exert (inherent propertiy) its own capillary force. If the tip is brought closer to the sample, there is an attractive force between tip material and sample surface. The intensity of attractive force is several times higher than the force generated by the tip material. Hence, the tip is forced to jump to contact the sample surface.

The choice of AFM mode depends on the surface characteristics of interest and on the hardness/stickiness of the sample. Contact mode is most useful for hard surfaces; a tip in contact with a surface, however, is subject to contamination from removable material on the surface. Excessive force in contact mode can also damage the surface or blunt the probe tip. Tapping mode is well-suited for imaging soft biological specimen and not for hard surface (DNA, carbon nanotubes, thin films). Non-contact mode is another useful mode for imaging soft surfaces, but its sensitivity to external vibrations and the inherent water layer on samples in ambient conditions often causes problems in the engagement and retraction of the tip. In the studies described in this thesis, intermittent contact mode (also named tapping mode) AFM is used to explore the surface morphology of coatings.

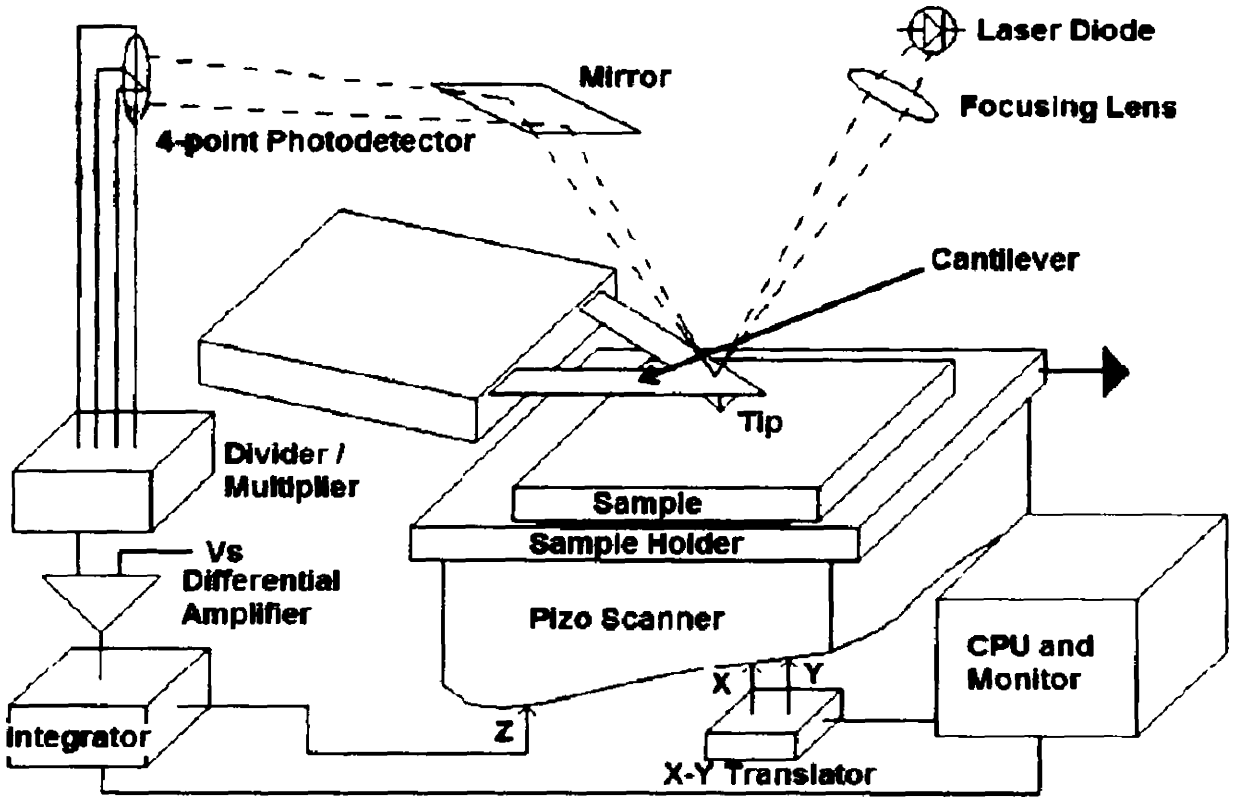

Figure 3.10 Skeleton diagram of set up for the atomic force microscopy.

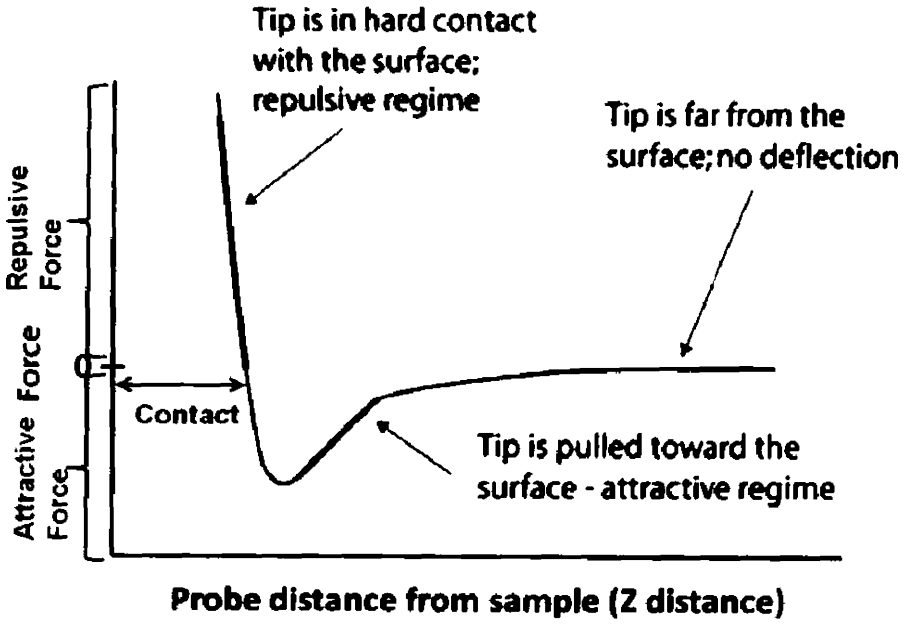

Figure 3.11 Interaction force between tip and the sample surface as function of distance.

3.3.1.5 Transmission Electron Microscopy (TEM)

Transmission Electron Microscopy is a unique tool for the characterization of structure and microstructure of materials simultaneously by diffraction and imaging techniques. The TEM is mainly used to characterize the microstructure of materials such as grain size, morphology, crystal structure and defects, crystal phases and composition, and in biological sciences, especially in the study of cells at the molecular level. The microstructure, e.g. the grain size and lattice defects are studied by use of the image mode, while the crystalline structure is studied by the diffraction mode. In addition, the chemical composition of small volumes, for example grain boundaries, can be obtained by detection of X-rays emitted from the films.

The fundamental principles of optics apply to the TEM imaging process in which the resolving power of a TEM is related to the wavelength of the energy source used to form the images. From De Broglie equation of wave nature of electrons:

$$\lambda = \frac{h}{mv} \qquad (3.7)$$

(where λ is the wavelength, h is Planck's constant, m is the mass of the particle and v is the velocity of the particle), the wavelength of a particle or beam of particles can be decreased by increasing the velocity of the particles.

The skeleton diagram of conventional TEM is shown in **Figure 3.12**. In a conventional transmission electron microscope, a thin specimen is irradiated with an electron beam of uniform current density. Electrons are emitted from the electron gun and illuminate the specimen through a two or three stage condenser lens system. The objective lens provides the formation of either an image or a diffraction pattern of the specimen. The electron intensity distribution behind the specimen is magnified with a three or four stage system and viewed on a fluorescent screen. The image can be recorded by direct exposure on a photographic emulsion or an image plate or digitally by a charge coupled device (CCD) camera. The acceleration voltage of TEM is 120 to 200 kV (200 kV electrons have a wavelength of 0.025 Å). Acceleration voltage determines the velocity, wavelength and hence the resolution (ability to distinguish the neighboring microstructural features) of the microscope.

To make optimum use of the TEM, it is important to understand how the individual components functions together to form a usable image. The source or electron gun of the electron beam, which is accelerated down the column. The theoretical resolution would increase with increasing accelerating voltage. The series of electromagnetic coils (shifts, tilts, stigmators etc.)

which ensure that the electron beam is symmetrical and centered as it passes down the optical column of the microscope; while the electromagnetic lenses (condenser, objective, intermediate, projector) act to illuminate the specimen and focus / magnify the specimen on the fluorescent screen/camera. The apertures, is a micron-scale holes through which the beam passes through and affect properties of that beam. The TEM specimen is fixed using specimen holder which positions the sample in the path of the electron beam. The area of beam/specimen interaction generates several types of signals that can be detected and processed to produce an image, diffraction pattern or spectra. There are controls for specimen position and orientation (x, y, z or height, tilt, rotation). The electron signal is converted through CCD camera and focused on fluorescent screen, which human eye can see properly. All the above parts are maintained at high vacuum levels.

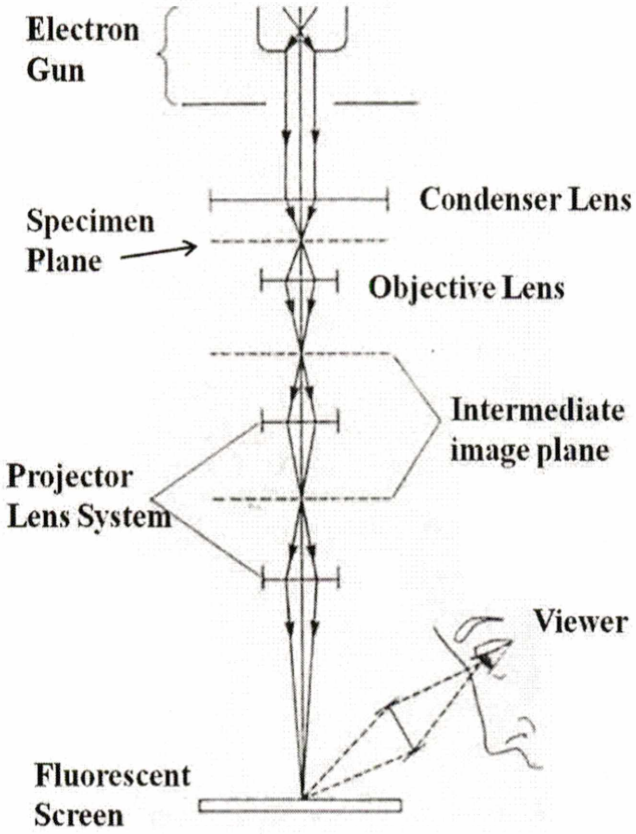

Figure 3.12 Skeleton diagram of Transmission Electron Microscope (TEM).

The **Figure 3.13** shows transmission electron microscope installed at Instrumentation center, IIT-R in the institute. The imaging in TEM can be of two types, viz., bright field imaging and dark field imaging. The electrons incident on the specimen can be directly transmitted, elastically scattered, or diffracted. In some cases, only those electrons, which are directly

transmitted without scattering, are used for image formation. The image produced in this way is called bright field image. It means that the formation of images only with the transmitted electron beam in bright field imaging. As the scattered or diffracted electrons are excluded from this image, only change in the intensity of the transmitted beam is only due to inhomogeneities in the sample with respect to density, thickness, and orientation which create an image contrast. The size of the objective aperture should be small enough to remove all diffracted electron beam caused by the specimen as shown in **Figure 3.14a**.

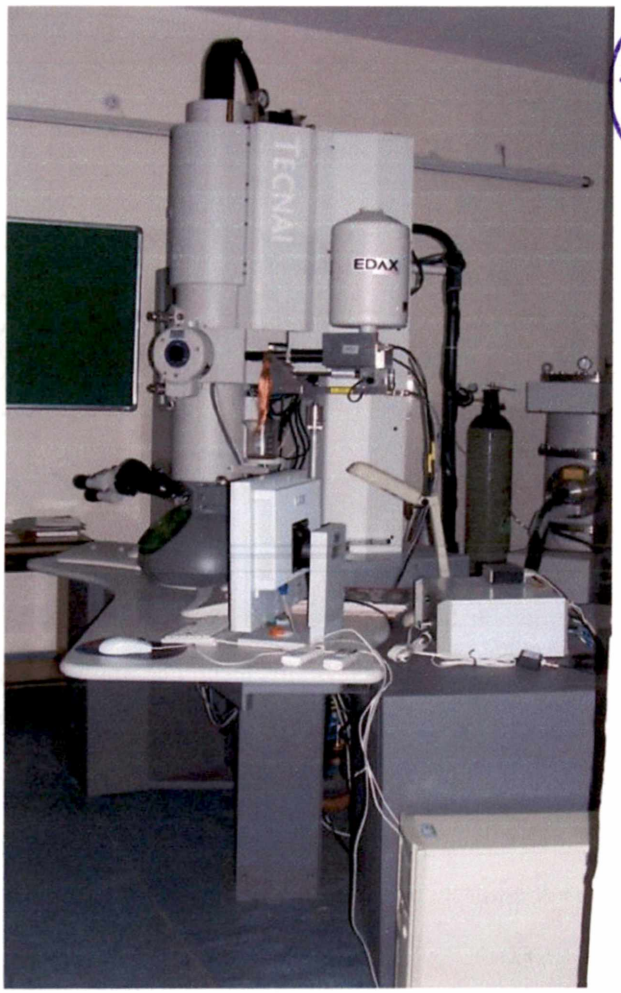

Figure 3.13 Transmission electron microscope setup.

Image can also be formed using specific diffraction beams, and such images are called dark field images. It means that the dark field images are formed if one or more diffracted electron is chosen by the objective aperture as shown in **Figure 3.14b**. In this case, the transmitted electron

beam should be blocked. In case of a dark field image of a polycrystalline sample, grains of a particular (hkl) orientation are illuminated in the image and hence differentiated from other grains. The advantage of dark field imaging method is its high diffraction contrast and it is mainly used for observing grain size distribution and dislocations.

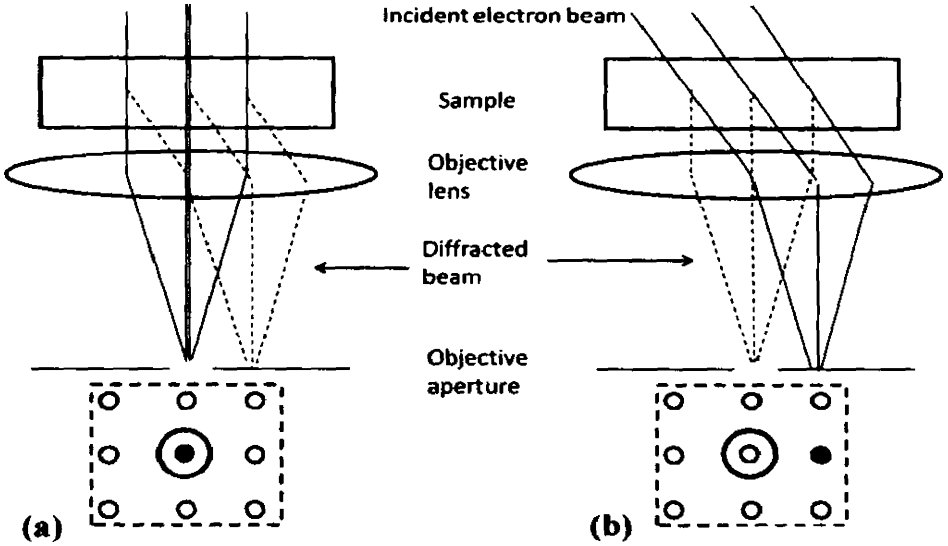

Figure 3.14 a) Bright field and b) dark field imaging.

Using a special aperture in the microscope column, it is possible to generate diffraction patterns from areas as small as 1μm in diameter. This technique known as selected area diffraction (SAD) and can be used to determine the identity and orientation of a crystallite in a sample, or to determine orientation relation between two crystallites. While electron diffraction pattern of a thin single crystal shows regular arrangement of spots, patterns from polycrystalline sample consist of a series of concentric rings. For amorphous materials, a diffuse halo around the bright central spot is observed.

For a single crystal, the diffraction spots from planes which are equivalent by symmetry are placed symmetrically around the central (Grundy et al. 1976). Interplanar distance, 'd' can be calculated from the expression

$$Rd = L\lambda \qquad (3.8)$$

where, 'λ' is the wavelength of the electron beam (0.025 A for 200 kV), 'R' is the distance of a particular spot form the central bright spot and 'L' is the distance between the specimen and the

diffraction plane, known as the lens constant. There are a number of drawbacks of the TEM. Many materials require extensive sample preparation to produce a sample thin enough to be electron transparent, which makes TEM analysis a relatively time consuming process with a low throughout of samples. The structure of the sample may also be changed during the preparation process. Also, the field of view is relatively small, raising the possibility that the region analyzed may not be characteristic of the whole sample. The sample may also be damaged by the electron beam in some cases.

3.3.2 Mechanical Characterization

The mechanical properties of materials on macro level are mostly determined using tensile tests, but such tests are very difficult to be conducted at nano-scale. Although nano-scale tensile test is possible in some circumstances, the cost involved would be very high due to inherent complexity of the instrument used. Furthermore, the preparation of film specimen for tensile test is also very difficult. Indentation tests on nano-scale or nanoindentation, are more convenient than tensile tests and can apply light loads in the range of micro-newtons or less (Dehong *et al.* 2007). Therefore, nanoindentation tests are most common in characterizing the mechanical properties of coatings. In nanoindentation tests, the elastic modulus and hardness are two easiest accessible mechanical properties. Furthermore, nanoindentation tests are also used to investigate other mechanical properties (Li *et al.* 2002, Chudoba *et al.* 2001, Li *et al.* 1999) such as time-dependent creep and relaxation, plastic flow, visco elasticity and fracture toughness.

3.3.2.1 Thickness Measurement using Stylus Profilometry

One of the most important parameters of a coating is its thickness, due to which a coating geometry reduces to two dimensions as compared to the bulk samples which are three dimensional. Most technological applications of coating require films of definite thickness as it affects properties of the coatings.

There are different ways of measuring the thickness of the deposited coatings: cross sectional SEM images of film and surface profilometry. We have used both techniques for more accurate measurement of film thickness. The stylus profilometry instrument used to measure the film thickness is shown in **Figure 3.15a**. This method consists of measuring the mechanical movement of a stylus as it is made to trace the topography of a film-substrate step. A metallic

needle stylus with tip radius of ~10 micron fastened to a lever arm serves as the electromagnetic pick up. The arm is delicately balanced so that the load on the stylus is very small. The stylus force is adjustable from 1 to 10 mg. A platinum stylus is moved vertically in contact with a film for specified distance and specified contact force. The vertical movement of the stylus is detected with a transducer, amplified 105 to 106 times, and then fed into a recorder. Then the film thickness is directly readout as the height of the resulting step contour trace as shown in **Figure 3.15b.** As an example, **Figure 3.15b** shows the thickness profile of a CrN single film. In this figure, vertical axis (y-axis) shows the thickness of the film and horizontal axis (x-axis) shows the horizontal displacement of the tip. Stylus instruments required a "step" in the film to measure thickness. It is often the preferred method when measuring opaque films, such as metals. The rquired steps in the films were obtained by masking some part of the substrates during deposition. We have measured these steps (i.e. thickness of the film) using a profilometer (Model: XP-2, Ambios Technology Inc. USA). This XP-2 stylus Profiler is a computerized, high sensitivity surface profiler, used to measure step height in a variety of applications. It features the ability to measure precision step heights from 10 Å to 100 microns.

3.3.2.2 Microhardness

The micro-hardness test, as distinct from the various familiar indentation methods for testing the hardness of materials, is applied to a specimen when it is important to measure the hardness at microscopically determined points on its surface. i.e checking of the hardness of a delicate watch gear might be typical problems with conventional hardness tester. The term microhardness test usually refers to static indentations made with very small loads (ranging from a few grams to 2 kgs). In the microhardness test, the indentation produced is exceedingly small. The indenter is either the Vickers diamond pyramid or the Knoop elongated diamond pyramid. The procedure for testing is very similar to that of the standard Vickers hardness test, except that it is done on a microscopic scale with high precision instruments.

a)

b)

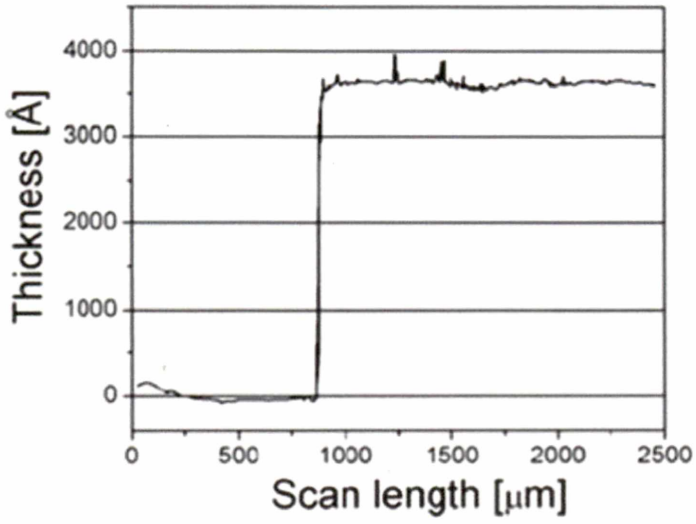

Figure 3.15 a) Stylus profilometer used for present work, and b) step contour trace of CrN films.

The Vickers indenter is shown in **Figure 3.16**. It has a square base diamond pyramid with included angle between opposite faces is 136°. The surface being tested generally requires a metallographic finish; the smaller the load used, the higher the surface finish required (**Weblink 4**). Optical microscopes are used to measure the indentations; these usually have a magnification of around X500 with an accuracy of ±0.5 μm. The Vickers Diamond Pyramid harness number (Vickers hardness number - VHN) is the applied load (kgf) divided by the surface area of the indentation (mm^2) given in Eq. 3.9.

$$Hv = 1{,}854\frac{F}{d^2} \qquad (3.9)$$

where F= Load in kgf, d = Arithmetic mean of the two diagonals, d_1 and d_2 in mm, Hv = Vickers hardness. The Vickers hardness test provides a continuous scale of hardness, for a given load, from

very soft metals to extremely hard materials. The microhardness tester installed at Welding Metallurgy laboratory is shown in **Figure 3.17**.

3.3.2.3 Nanoindentation

The CrN coatings are extremely thermally stable and reasonably hard, but they are fragile. The mechanical properties of coatings are well characterized by their hardness, H, effective Young's modulus, E^*, and elastic recovery W_e. For mechanical device stability, mainly four material properties of the device components are important: elastic modulus, yield strength, interfacial adhesion, and film fracture toughness. These quantities can be evaluated from the loading /unloading curves measured by a micro or nanohardness tester.

Nanoindentation has been recently rekindled because of a need for techniques to study the mechanical properties of coatings. For probing properties such as hardness and elastic modulus at the smallest possible scales, the Berkovich triangular pyramidal indenter is preferred over the four-sided Knoop or Vickers indenter. Because the conventional Knoop and Vickers microhardness tests require direct imaging of the indentations to obtain hardness, large errors may be introduced due to the measurement of the diagonal lengths, especially when the indentations are small, and also because a three-sided pyramid is more easily ground to a sharp point.

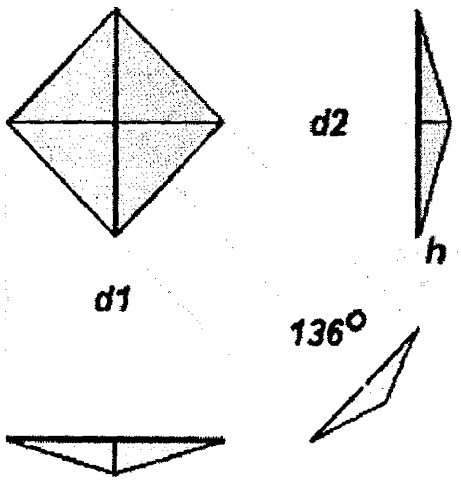

Figure 3.16 Vickers diamond indentations.

Figure 3.17 Microhardness tester.

The nanoindenter is depth-sensing equipment and offers the ability to obtain other material information such as elastic and time-dependent plastic properties. The depth resolution is on the scale of nanometers. Thus, it is possible to conduct indentation experiments on coatings. The triangular Berkovich-type diamond pyramid nanoindenter has an angle of 65.3° between the tip axis and the faces of the triangular pyramid, and with the same ratio of area (A) to the square of depth (h) as that of the traditional Vickers pyramid. Nanoindentation is similar to conventional hardness testing but performed on a much smaller scale. Nanohardness (H) is defined as the indentation load divided by the projected contact area, and it can be obtained using the relationship

$$H = \frac{P_{max}}{A} \tag{3.10}$$

where P_{max} is the maximum load applied during the indentation, and 'A' is the contact area between the indenter and specimen, projected into the plane of the surface. The area function of the diamond tip was given as

$$A(h) = 24.56\, h_2 + 225.9\, h_1 + 519.61\, h \tag{3.11}$$

where 'h' is the contact depth determined by the method of Oliver and Pharr, and $h=h_{max}- hs$, where 'h_{max}' is the total measured displacement and 'h_s' is the elastic surface displacement. The true hardness is slightly greater than the measured hardness because the elastic contributions to the displacement have been ignored.

Nanoindentation test involves indenting a specimen by a very small load using a high precision instrument, which records the load and displacement continuously. The mechanical properties of thin films coatings and substrates can be derived from the measured load-displacement (loading / unloading curve) through appropriate data analysis. In nanoindentation, a prescribed load is applied to a pyramidal or spherical indenter or other shapes in contact with the specimen surface. As load is applied to the indenter, the depth of penetration into the specimen is measured. A nanoindentation, shown in **Figure 3.18**, instrument provides experimental results in the form of a load-displacement curve for the loading and the unloading parts of the indentation process as shown in **Figure 3.19**. where h_f is the final unloading depth, h_{max} the maximum loading depth during indentation tests, and P_{max} the maximum load. S^* is the slope of the tangent line to the unloading curve at the maximum loading point (h_{max}, P_{max}) and is termed the system contact stiffness. h_c is the intercept value of the above mentioned tangent line down to P=0 and is termed the contact depth. The mechanical properties were calculated by directly measuring physical dimensions of the indention using the empirical equations.

Figure 3.18 Nanoindentation set up used for the present work.

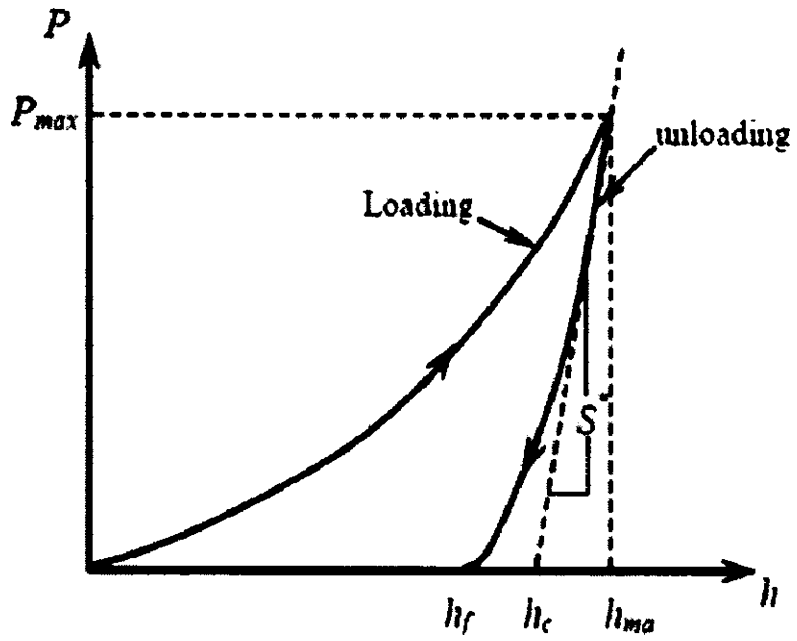

Figure 3.19 Load – Displacement curve generated during nanoindentation test.

There are main three basic relations, $H=f(E^*)$, $H^3/E^{*2}=f(H)$, and $We=f(H)$, between mechanical properties of coating. It is necessary to obtain materials that possess high hardness but lower elastic modulus values for enhancing the resistance to plastic deformation, This behavior could be expressed by the H^3/E^{*2} ratio, where H and E^* are the hardness and effective modulus of the coating (Chang *et al.* 2005). The area between the loading/unloading curve and the value of h_{max} decreases with increasing (i) hardness (H) (ii) reduced modulus of effective Young's modulus $E^*=E/(1-\nu^2)$ and (iii) universal hardness H_U, where E and ν are the Young's modulus and the Poisson ratio, respectively; and there is no simple relation between the mechanical response of the coating and H or E^* alone; however, this response is strongly dependent on the ratio H/E^*. Measured values of H and E^* permit to calculate the ratio H^3/E^{*2} which is proportional to a resistance of the material to plastic deformation. The plastic deformation is reduced in materials with high hardness and low modulus E^*. In general, a low modulus is desirable as it allows the given load to be distributed over a wider area. The higher H^3/E^{*2} gives a possibility of tailoring the mechanical properties of a coating for a given application, e.g. to prepare coatings with high hardness H, high resistance to plastic deformation ($\approx H^3/E^{*2}$), high elastic recovery W_e, but with low E^* and high d_{max}.

Among the methods for analyzing load-penetration depth data (Pethica *et al.* 1983, Doerner *et al.* 1986, Fischer-Cripps 2002), the most popular analysis technique is that of Oliver and Pharr

(Oliver *et al.* 1992), which is based on the elastic solution of Sneddon (Sneddon *et al.* 1965) for indentation by an axisymmetric body. The relation between penetration depth 'h' and load 'P' for some given indenter geometry can be represented as

$$P = K(h - h_f)^m \qquad (3.12)$$

where 'K' is a fitting parameter which contains geometric constants, elastic modulus and Poisson's ratio of the specimen and the indenter, m is a exponent depends on the geometry of the indenter. For a flat-ended cylindrical indenter, m =1; for a paraboloid of revolution, m =1.5; and for a cone indenter m =2. The specimen contact stiffness is given by $S = 2aE_r$ where S is the experimentally measured stiffness of unloading data, 'a' is the contact radius and 'E_r' is a reduced modulus, accounting for the deformation of both indenter and specimen, can be calculated by

$$\frac{1}{E_r} = \frac{(1-\nu^2)}{E} + \frac{(1-\nu_i^2)}{E_i} \qquad (3.13)$$

where 'E' and 'ν' are the elastic modulus and Poisson's radio of specimen respectively, while 'E_i' and 'ν_i are the elastic modulus and Poisson's ratio of the indenter material, respectively.

3.3.3 Tribological Characterization

3.3.3.1 Dry Sliding Wear Test using Pin on Disk (POD) method

It is a surface phenomenon and occurs mostly at outer surfaces and therefore it is more appropriate and economical to use surface modification techqnique to improve the wear resistance of the metals and alloys instead of using high-cost wear resistant alloys/metals (Singh *et al.* 2008). In the relative motion of two bodies in contact, a force acts in the direction as shown in **Figure 3.20**. The region beneath the contact point is highly stressed. The force is called friction and the material removal process by microfracture occurring near the surface is called wear. In general, wear depends on a number of factors including environment, temperature and materials as well as sliding velocity and applied load. In the frictional surface, true contact area is extremely smaller than nominal contact area due to the microscopic roughness or asperity, which is inevitably present on the surface. It results in a highly stressed field forming around the contact point. Under a localized high pressure during the sliding motion, the metallurgical bonding may occur. In general, for the most practical applications, sliding surfaces are lubricated in some way and that wear is called lubricated sliding wear. While in some cases, mainly in laboratory investigation, surfaces slide in air without lubrication and the resulting wear is called dry sliding wear. The wear associated with the presence of hard particles, either as a separate component or fragment between

sliding surfaces or as an element of the structure of one or both surfaces, it is called abrasive wear. There is no rigid boundary between difference types of wear i.e under some conditions; sliding wear can generate debris which then causes further wear by abrasion. It may be mentioned that wear rate and friction are often critically dependent on the sliding conditions; apparently minor changes in conditions can divert the dominant mechanism. A continuous record of friction forces not only provides numerical values of μ but also provides the changes in sliding behavior i.e a rise or fall in μ or change from a smooth trace to an irregular one. These changes often indicate changes in surface nature, topography or wear mechanism.

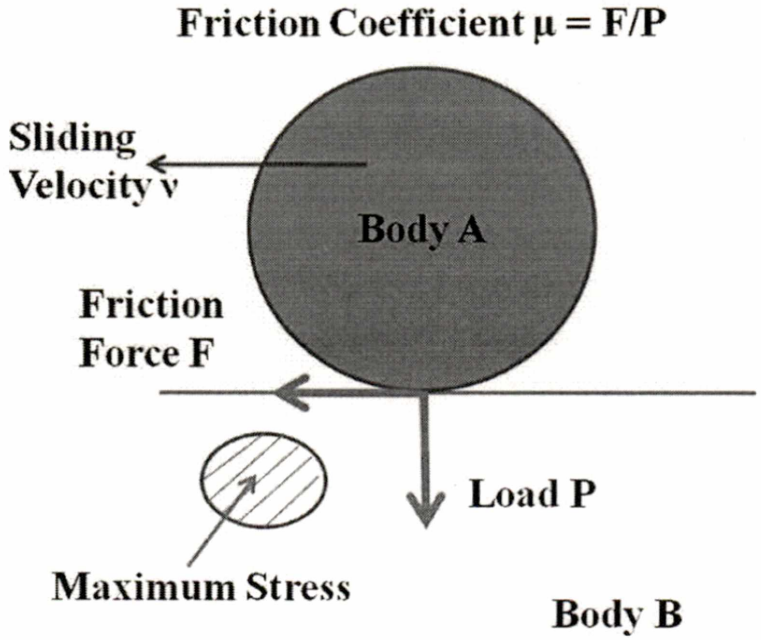

Figure 3.20 Stress field around the surface of body B, when body A slides on body B under a load *P* at a sliding speed v (Hosokawa et al. 2007).

Adhesive wear often observed in friction of metal contact, occurs by micro fracture around the metallurgical bonding, generating fragments called debris. When a hard material slides on a relatively soft material the material removal rate from the hard material surface occurs by cutting or ploughing by fragment of hard material embedded on the soft material surface. The ASTM standards for this test (ASTM G99-05) specify the use of rounded pin, does not specify specific values for the parameters, but allows those to be selected by the user to provide simulation of an application. The parameters that can vary (Bayer 2004) include size and shape of the pin, normal

load, speed, and material pairs. The test can also be done in a controlled atmosphere and with or without lubrication.

Wear under sliding conditions depends on the sliding distance, but also to some extent on both sliding velocity and the duration of the test. The sliding velocity affects the rate of frictional energy dissipation and abrupt transitions in wear mechanism with wear rate may occur as the sliding speed is changed.

The tribological properties also depends on the nominal contact pressure between two sliding surfaces as transitions are commonly induced by changes in contact pressure and sliding speed. However, the COF is independent of the sliding speed for the test conducted in LN_2 environment (Basu *et al.* 2009). Usually, the COF decreases with higher hardness and lower ductility (Jain *et al.* 2010) and is calculated using Eq. 3.14 (Kaur *et al.* 2010).

$$\mu = \frac{Friction\ Force}{Applied\ Normal\ Load} \tag{3.14}$$

The linear dimensions of the specimen are also important, independently of the contact pressure, since wear debris formed near the leading edge of a long specimen will have more influence during its passage through the contact zone than the shorter specimen (Hutchings 1992). **Figure 3.21** shows the combined influence of load and sliding speed on dry sliding wear process in metal. Apart from the major variables of normal load, contact area, sliding speed and sliding time, several other factors must also be considered and monitored in wear testing. The surrounding temperature at the time of testing may influence the mechanical properties and thermal activated chemical process of the materials, though these may often be dominated by frictionally generated temperature rise at the time of sliding of two materials. The wear is usually measured either by removing the specimen at intervals and weighing or measuring it or continuously measuring its position with an electrical or mechanical transducer and deducing the wear from its change in dimensions.

As sliding proceeds, the load originally borne by the asperity is progressively transferred to other asperity junctions. Continuous sliding leads to the regular formation and destruction of individual asperity contacts. The average volume of materials δV worn away per unit sliding diatance due to sliding of the asperities is given by

$$V = \frac{KN}{H} \tag{3.15}$$

where K is the dimentionless wear coefficient always less than unity, N is the normal load and H is the hardness of the softer surface, often called Archard equation. Here in this model, the H term is considered to be nearly equal to P, the yield pressure required for plastically deforming asperity.

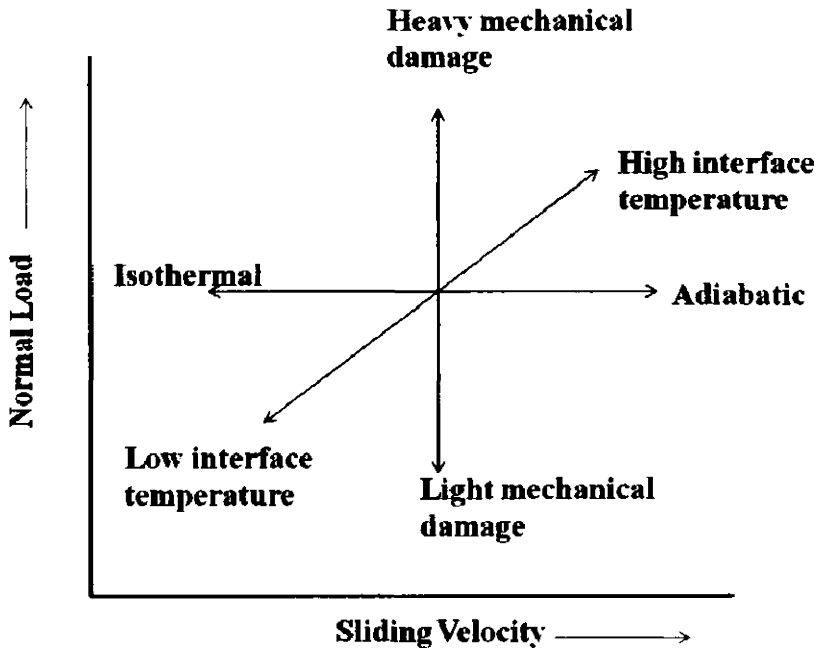

Figure 3.21 Influence of load and sliding speed in dry sliding wear.

The wear volume of the coated surface after testing, the 2D profile of worn surface was measured at different locations using a stylus profilometer and the average cross-sectional areas (A) of the worn tracks were determined. The wear rates (W) were obtained by following relationship (Feng et al. 2010)

$$W = \frac{\pi dA}{LN} \tag{3.16}$$

where d is diameter of wear track, L is total sliding distance, and N is load applied.

The sliding velocity (v), corresponding to the rotational speed (rpm), is calculated using Eq. 3.16 (Basu *et al.* 2009).

$$v = 2\pi r\, X\, \frac{N}{60} \tag{3.17}$$

where r= track radius (m) and N = rotational speed (rpm)

The present test is limited to laboratory investigation and select dry sliding wear test due to the lubricant, liquid and solid both, is comparatively expensive and poses an environmental

concern for disposal (Kim and Cha, 2004). A Pin on Disc tribo tester (**Figure 3.22)** (Make: Magnum, Bangalore) is used to measure wear. The unit consists of a gimbaled arm to which the pin is attached, a fixture which accommodates disc, an electronic force and temperature sensor for measuring the friction force and surrounding temperature respectively.

Figure 3.22 Pin on Disc apparatus used for the present work.

The wear is measured by removing the specimen at regular 15 min intervals and measuring its weight after each interval. The specifications of tribo-tester are: Velocity: Up to 12m/s, Pin size: 3 to 12mm diameter or diagonal, Disc size: Ø 50 to 170mm, Normal load: Up to 200N and friction force: 200N. The 160 mm pitch circle diameter (PCD) and 8 mm thick disc made from EN32 (65HRC) with below 100nm surface roughness were used for the wear test. Wear is quantified by measuring the wear groove with a profilometer followed by measuring the amount of material removed.

CHAPTER 4

CHROMIUM NITRIDE (CrN) COATINGS

4.0 Synthesis and Characterization of CrN Coatings on Si(100) and Stainless Steel Substrates by DC Reactive Magnetron Sputtering

The synthesis and characterizations of CrN coatings deposited on Si(100) and Stainless steel (SA 304) substrates are described in this chapter. The influence of processes parameters such as substrate temperature, working pressure, target power, different sputtering and reactive gas environment, gas proportion, and gas flow rate on microstructural and mechanical properties of the CrN coatings are discussed.

4.1 Effect of Working pressure, Temperature and Target Power on DC Magnetron Sputtered CrN Coatings Deposited on Si(100) and Stainless Steel (SA304) Substrate

4.1.1 Introduction

Nitrides based coatings such as TiN, CrN, and WN are used extensively in microelectronics and coating industries due to their superior chemical stability, excellent strength, wear, and corrosion resistance. Also, transition metal nitrides (i.e TiN and CrN) are used in coating industries due to its excellent strength, wear and erosion resistance. CrN has been found to be ideal candidate for the aforementioned applications owing its ease of fabrication, excellent strength, hardness, wear and corrosion resistance, and chemical stability. Among the various techniques available for the deposition of CrN coatings, reactive magnetron sputtering could be used effectively to tailor the microstructural features of the coatings as a function of sputtering variables such as substrate temperature, gas pressure, and power. One of the main advantages is the control of stoichiometry and composition possible in DC-reactive magnetron sputtering as compared to RF system. The CrN coatings deposited by reactive magnetron sputtering, exhibit good mechanical properties such as high micro hardness and low thermal conductivity, good wear and corrosion resistance as reported in the literature (Safi *et al.* 2000, Tillmann *et al.* 2007). Fabis *et al.* (1990) investigated the CrN films and using statistical technique ANOVA, they reported that the

sputtering pressure, substrate bias, and target power are vital parameters for tailoring the microstructure of the coatings with the desired properties. Fabis *et al.* (1992) have investigated the 100 nm thick CrN films deposited on vitreous carbon and soda-lime glass substrate by DC planar magnetron sputtering and observed the formation of single phase polycrystalline films of CrN with strong (111) fiber texture from the XRD analysis. It was reported in their work that the surface and cross sectional morphologies of CrN coatings showed a smooth free surface and random spherical growth. Fornies *et al.* (2006) have investigated the growth of CrNx coatings deposited on single crystal Si(100) wafer by DC planar magnetron sputtering under constant nitrogen and argon gas flow condition. At low N_2 ($\leq$ 2%) concentration, pure Cr was detected in CrN coatings, while with N_2 concentration up to 40%, [Cr+N], [Cr+CrNx], and [Cr+CrN] phase sequences were found in their work. The coatings exhibited columnar growth under positive and negative bias voltages (+20V, 0V, -50V) but it transformed into granular structure at -100V and -150V. The Cr_2N with (111) orientation was found at the applied bias +20V, 0V, -150V but it transformed into (110) orientation at -100 V as reported in their work.

Nam *et al.* (2000) have investigated the influence of high deposition rate, in magnetron sputtering, to control the microstructures of CrN coatings deposited on AISI 304 stainless steel. They found that deposition rate of CrN compound has increased up to 90% than pure Cr coatings due to increase in ionization efficiency affected by negative pulsed DC bias. With N_2 flow rate of 20 sccm, mixed phases consisting of Cr(110), CrN(200), and Cr_2N (111) were observed but with increasing the flow rate, CrN coatings has transformed from hexagonal phase, Cr_2N phase, in to a cubic CrN phase. The film density of CrN coatings has increased with increasing N_2 flow rate. The thermal stability of CrN nanometric coatings (110-120 nm thick) deposited on stainless steel, by DC reactive magnetron sputtering, was investigated by Paternoster *et al.* (2008). They observed that the annealing of CrN coatings in vacuum resulted in the phase transformation of CrN into Cr_2N, but upon annealing in air, only Cr_2O_3 phase was found. The application of bias has no effect on the phase formation but it influences the preferred crystal orientation and the residual tensions in DC magnetron sputtered CrN coatings (Forniés *et al.* 2006). The thermal stability of CrN and CrAlN coatings deposited by DC reactive magnetron sputtering on mild steel and silicon substrate has been investigated and observed that oxidation of CrN films occurs at around 873K, while in CrAlN, no detectable oxides were formed even at 1073K (Barshilia *et al.* 2006). Seok *et al.* (2001) have investigated the sputter deposited (pulsed DC-Magnetron sputtering) nanocrystalline Cr and CrN coatings on steel. Using X-ray diffraction analysis, with increasing nitrogen content (3 - 7%),

the formation of CrN phase with (220) orientation was observed in their work. The adhesion property of the coatings also increases with increasing nitrogen content. The properties of CrN coatings deposited on Si(100) substrate by pulsed DC reactive magnetron sputtering was investigated (Lee *et al.* 2006) and found that the preferred orientation of the CrN coatings changed from (111) to (200) with increasing substrate temperature and negative bias. Carlo Paternoster *et al.* (2008) found that the annealing of CrN coatings in vacuum has induced phase transformation of CrN into Cr_2N, while after annealing in air, only Cr_2O_3 phase was observed.

The CrN has been identified as a better substitute for TiN coatings for tribological applications due to its superior wear resistance and corrosion resistance as reported in the literature (Safi *et al.* 2000). The micro hardness of CrN coatings was found to be insensitive to variation in the deposition parameters due to shallower transitions in different phases (Hones *et al.* 1997). The mechanical and tribological properties of CrN coatings deposited under different ratio of sputtering gas and reactive gases are reported in the literature (Meunier *et al.* 1998, Fornies *et al.* 2006, Essen *et al.* 2006). Cunha *et al.* (1999) studied the CrN coatings produced by DC and RF reactive magnetron sputtering on SA316 substrate and found that the average density of the coatings varies between 55 and 85% of the bulk density and it affects the mechanical properties of the coatings. The sputter deposited coatings with high residual stresses affects the film-substrate interface adhesion and film thickness, while it improves the erosion resistance of the brittle materials (Bielawski *et al.* 2005). The residual stresses in coatings are due to deposition temperature, working gas entrapment, and interfacial tension at the film/substrate interface (Ohring *et al.* 2002). Barshilia *et al.* (2006) investigated the unbalanced magnetron pulsed DC sputtered CrN hard coatings and reported that the film hardness is affect by the several factors such as packing factor, residual stress, stoichiometry, preferred orientation, and grain size. They have also investigated the effect of high temperature on CrN and CrAlN coatings deposited by DC magnetron sputtering on mild steel and silicon substrate and reported that the oxidation of CrN coatings has occurred around 873K but no detectable oxides were formed on CrAlN coatings even at 1073K. Also, sputter deposited CrN coatings with high residual stresses affects the film-substrate interface adhesion; while it improves the erosion resistance of the brittle materials. The residual stresses in coatings are due to low deposition temperature, working gas entrapment, and surface tension forces at the film / substrate interface (Ohring *et al.* 2002). Safi *et al.* (2000) investigated the influence of the DC reactive sputtering conditions such as hysteresis effect in the gas flow and instability in the gas pressure, differential poisoning of target during deposition of coatings. The

sputtering process was controlled effectively by higher pumping speed, increasing target to substrate distance, obstructing the reactive gas flow to the target, pulsed reactive gas flow, plasma emission monitoring, and voltage control.

A detailed investigation on the influence of process variables, in DC reactive magnetron sputtering, on microstructural characteristics of high quality CrN coatings is lacking in the literature. Also, the CrN coatings with higher thickness (>3 μm) and the effect of working pressure ranging from 1.33, 1.99 and 2.66 Pa on the coatings during deposition by DC-magnetron sputtering is scarce in the literature. It is very essential to substantiate the role of sputtering conditions to achieve the desired microstructural characteristics such as higher density, fine grains, and smooth surface in the CrN coatings with the enhanced mechanical and tribological properties. Therefore, the present work has been focused to study the microstructural features of the CrN coatings, deposited by DC-reactive magnetron sputtering, as a function of sputtering conditions such as substrate temperature, gas pressure, and power. XRD, AFM, and FESEM were used to elucidate the effects of process parameters on the microstructural characteristics of the CrN coatings such as phase formation, grain morphology, textures, and surface roughness. Microhardness tester was used to measure the hardness of CrN coatings deposited on stainless steel substrate and the deformation characteristics of the coatings are explained using its microstructural features.

In a reactive DC magnetron sputtering system, the elemental metal target is sputtered in the presence of reactive gases, which react with sputtered materials and deposit films on the substrate. It provides the capability of producing thin compound with controlled stoichiometry and composition, high deposition rate, simple and comparatively cheaper than RF sputtering system. DC reactive sputtering technique has been chosen in the present work due to aforementioned unique advantages as compared to other PVD techniques.

4.1.2 Experimental Details

4.1.2.1 Deposition Parameters of CrN Coatings

The CrN coatings were deposited on silicon Si(100) and stainless steel (SA304) substrates by DC-reactive magnetron sputtering (Model: DCSS – 12, Excel Industries, Mumbai equipped with Baratron Capacitance Manometer and Vacuum Gauge). The Si (100) substrate with dimension of (10 mm X 5 mm), while stainless steel substrate SA304 with dimension of (10 mm X 10 mm X 0.9 mm) were prepared for the deposition of CrN coatings. The details of sputter

deposition process are explained in Section 3.2.3. During the deposition, gas ratio, base pressure, substrate to target distance, and deposition time were held constant while sputtering pressure, temperature, and power were set to different values. The deposition conditions are summarized in **Table 4.1**. The equal proportions of N_2 and Ar with two different flow rates of 4 sccm and 16 sccm, were used during the experiments. The deposition pressure was controlled by mass flow controller. A Cr (99.99% purity) target of 50 mm in diameter was used during the sputter deposition.

Table 4.1 Sputtering conditions of CrN coatings deposited on Si(100) and SA304 substrates.

Sr. No	Process parameters and their corresponding values	
1	Base Pressure	$< 5 \times 10^{-4}$ Pa
2	Working Pressure	1.33 / 1.99 / 2.66 Pa
3	Target to Substrate distance	50 mm
4	Power	75 W / 100 W
5	Substrate Temperature	473 K / 573 K /673 K
6	Deposition Time	60 minute
7	Gas Mixture	$Ar+N_2$
8	Gas Mixture ratio	50:50

4.1.2.2 Characterization

The phases and its preferred orientation of CrN coatings were characterized by X-Ray Diffraction (Bruker AXS, D8 Advance). The basic structural properties of coatings in the as deposited condition were determined by $\theta/2\theta$ scans with CuKα radiation (λ = 0.15418 nm) in the range of 30° to 100° to find out the possible changes in the texture orientation. The scan rate was 1°/min with an increment of 0.05°. The excitation voltage and current were set to a 40 kV and 30 mA respectively, in the diffractometer. For each (hkl) plane, full width half maximum (FWHM) was determined and from this value, the grain size of coatings was calculated using the Scherrer equation **(Eq. 3.6)** (Cullity 2001). The grain size is inversely related to the FWHM of the diffraction peak. The large grain size exhibits a narrow peak, which is due to the periodicity of the individual grain domains, which are in phase, reinforcing the X-ray beam.

The morphologies of CrN coatings in the as deposited conditions were characterized by FE-SEM (FEI, Quanta 200F) and Atomic Force Microscopy (AFM, NT-MDT) and its chemical composition were measured using Energy Dispersive Spectroscopy (EDS). The micro hardness of

CrN/SS was measured by using microhardness tester (Kim and Cha 2004). The details of instruments used for characterization are discussed in Chapter 3.

4.1.3 Results and Discussion

4.1.3.1 Analysis of CrN Coatings Deposited on Si (100)

The CrN coatings were prepared under deposition conditions such as changing temperature, power, and working pressure using DC-Magnetron sputtering. The observed variations in relative intensity of the peaks as shown in **Figure 4.1** is due to the intrinsic differences in the microstructure and stress state of the CrN coatings. In the Cr–N system, three solid phases exist such as the terminal solid interstitial solution, body centered cubic Cr(N), hexagonal Cr_2N, and face centered cubic CrN (Wei *et al.* 2001). The formation of both CrN and Cr_2N phases have been identified in the reactively sputtered CrN coatings depending on the Ar to N_2 flow ratio as reported in the literature (Zhao *et al.* 2005). Initially, in the present work, a dominant CrN (111) and a weak CrN (200) peaks were identified in the XRD pattern at low deposition pressure and temperature (1.33 Pa and 473 K) and the (111) peak remained dominant even at comparatively high pressure and temperature (2.66 Pa and 673 K). It is because of the equal proportion of argon and nitrogen content in the chamber with N_2/Ar flow rate of 4 sccm maintained throughout the experiments. The preferred orientations of CrN (111) and (200) observed in the present work are in tandem with the textures reported for CrN film deposited on Si (100) substrate (Seok *et al.* 2001, Lee *et al.* 2006, Wei *et al.* 2001).

The peaks of CrN (220) and CrN (311) are not observed as seen in the **Figure 4.1** and **Figure 4.2**, at 50% N_2 content in the sputtering chamber with high temperature (673K). At low temperature (473 K), with increasing deposition pressure, the intensity of the peak (222) decreases, but another peak (200) appears. It is due to the reduction in deposition rate favors preferential growth of the coatings along (200) orientation, which exhibits lower surface free energy. At higher temperatures (573 K and 673 K), the peak (222) increases with increasing deposition pressure and the peak (200) does not appear any more. The formation of (222) orientation of grains is due to the enhanced mobility of adatoms in the film surface at higher deposition temperature. At low working pressure, 1.33 Pa, the CrN (311) phase is observed, while at 1.99 Pa and 2.66 Pa pressure, intensity of CrN (311) peak is reduced due to simultaneous influence of pressure and temperature on sputtered atoms and high nitrogen content inside the chamber during deposition.

At high deposition pressure and low deposition temperature, sputtered atoms undergo more collision and lose their energy, which is not able to diffuse/grow uniformly on the surface of the substrate. The intensity of CrN (311) is increased with temperature and also with slight increase in power as shown in **Figure 4.1**. It is evident that the combined effect of temperature and pressure, and high amount of N_2 contribute to the formation of CrN phase with different orientation.

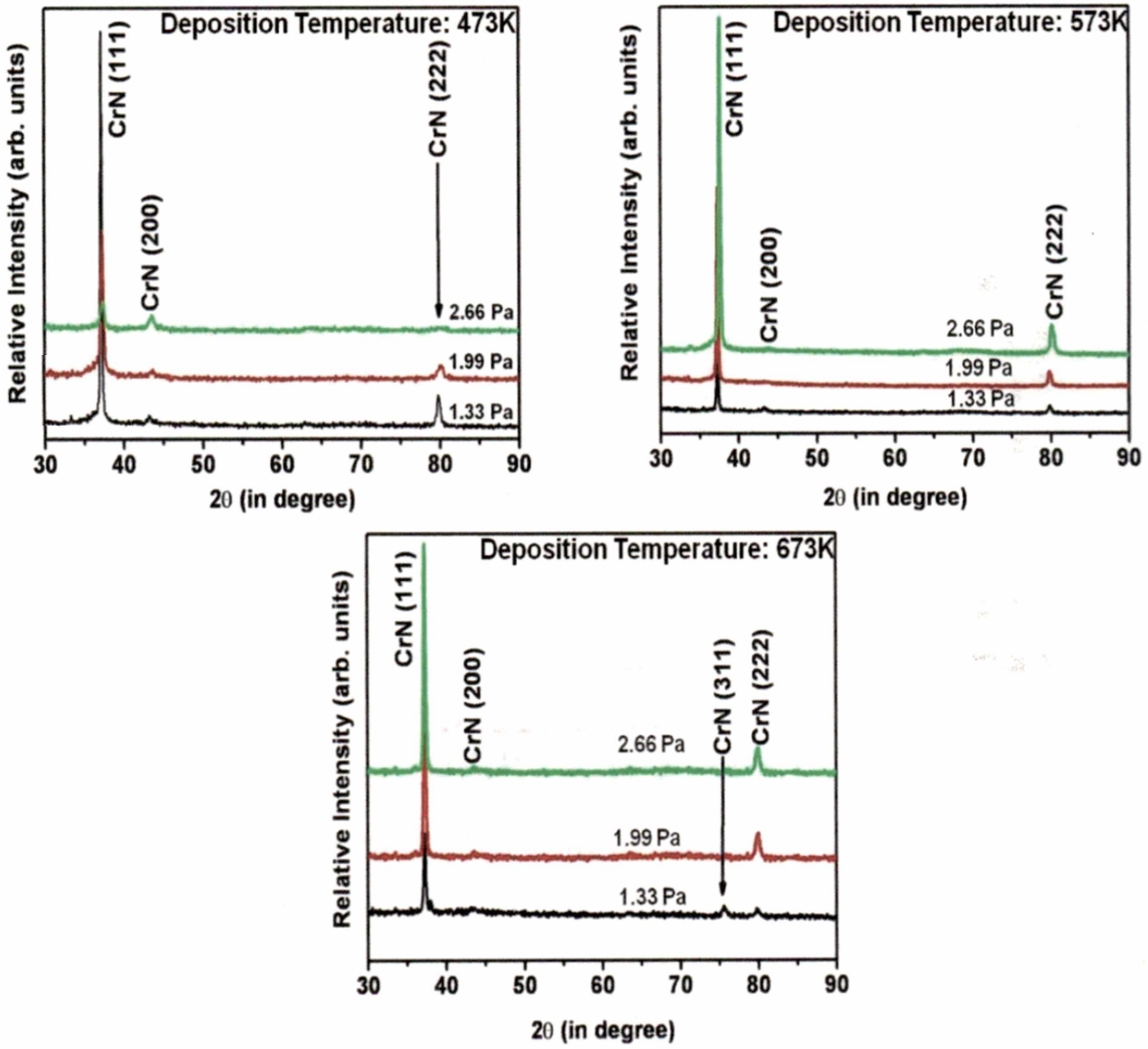

Figure 4.1 XRD spectrum of CrN coatings deposited on Si (100) substrate as a function of working pressure and temperature with power 75W.

The formation of Cr_2N phase is not observed due to the high percentage of N_2 (50%) used during deposition in the present work. The grain size was calculated using Scherrer equation (**Eq. 3.6).** The calculated grain size from XRD peaks is shown in **Table 4.2**. **Figure 4.3(i)** and **4.3(ii)**

show the dependence of crystallite size on working pressure of CrN coatings deposited at different temperatures.

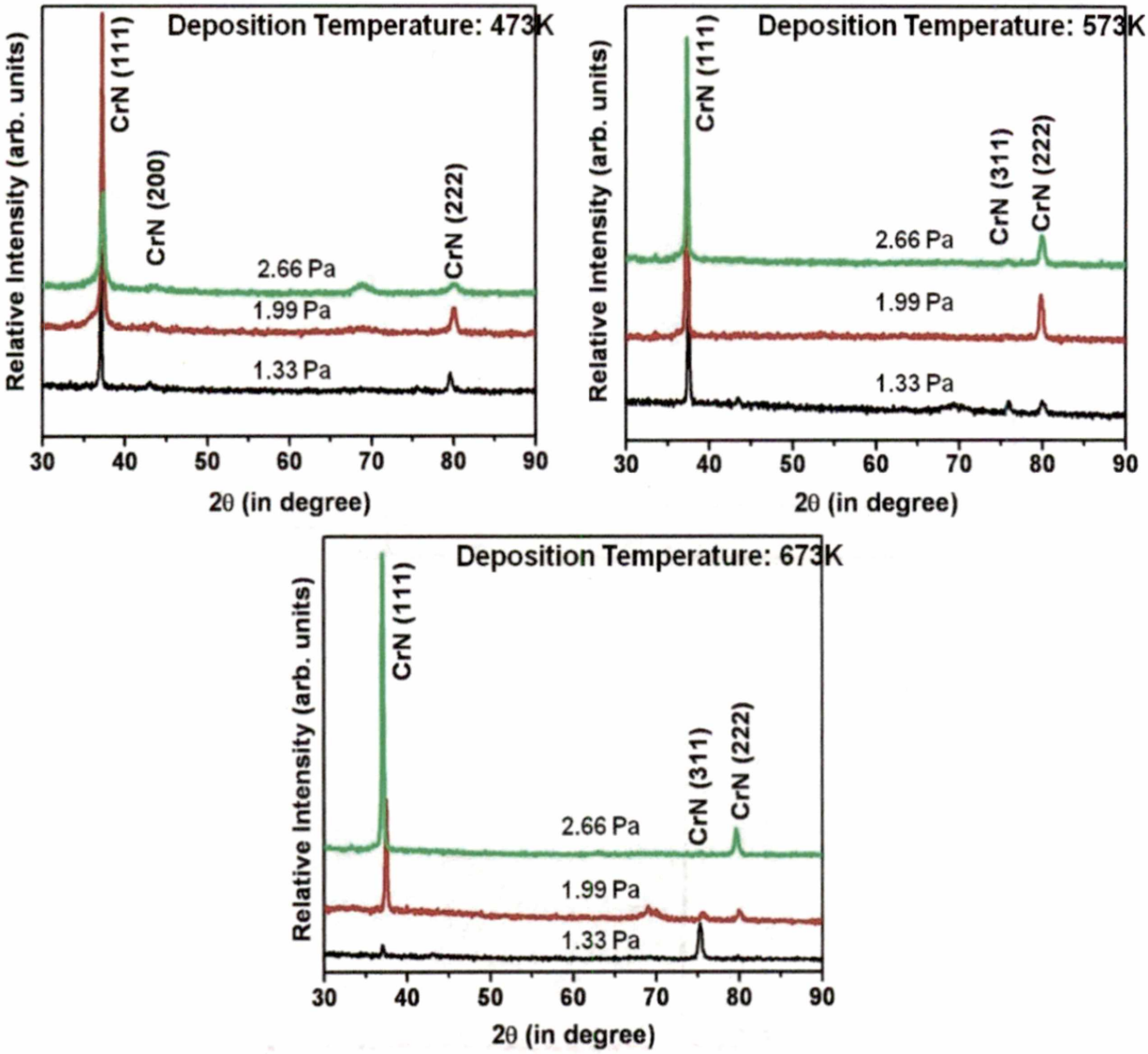

Figure 4.2 XRD spectrum of CrN coatings deposited on Si (100) substrate as a function of working pressure and temperature with power 100 W.

It is evident from the figure that the grain size is decreasing with increasing working pressure at lower deposition temperature, 473K. At high working pressure (1.99 Pa and 2.66 Pa) and low deposition temperature (473K), the frequent collision of sputtered atoms may result in losing its energy and get deposited on the substrate with a smaller grain size. It does not grow due to lower surface diffusivity of the atoms. The reduction of grain size in the coatings, at the deposition temperature of 473K, is also due to the N_2 content (Chandra *et al.* 2005). However, the

grain size increases at high deposition temperature and higher working pressure due to the higher adatom mobility, which facilitates atomic migration to the grain boundaries followed by grain growth. Here, the effect of temperature is more pronounced than the working pressure.

Table 4.2 Grain size, Roughness and Microstrain of CrN coatings deposited on Si (100) Substrate.

Sample (CrN) No.	Temp. (in K)	Power (in W)	Working Pressure (in Pa)	Particle Size (in nm) measured with XRD	Roughness (in nm)		Micro Strain
					Average	RMS	
1	473	75	1.33	38	5	6	1.2487
2			1.99	22	5	6	0.8438
3			2.66	14	3	4	0.7057
4		100	1.33	33	9	13	1.4086
5			1.99	30	9	14	0.9860
6			2.66	17	11	14	0.8522
10	573	75	1.33	33	4	5	0.8689
11			1.99	30	6	9	0.9317
12			2.66	30	7	9	0.2539
13		100	1.33	39	12	15	0.2246
14			1.99	33	12	15	0.8647
15			2.66	33	67	85	0.6597
19	673	75	1.33	25	41	43	0.8187
20			1.99	30	9	12	0.8647
21			2.66	33	16	21	1.3751
22		100	1.33	30	12	15	1.5048
23			1.99	33	13	16	0.4003
24			2.66	38	14	18	1.5467

The texture coefficient (T) of the CrN coatings as a function of working pressure and temperature is calculated using the **Eq. 4.1** (Chawla *et al.* 2008a).

$$T = \frac{I_{hkl}}{I_{111}+I_{200}+I_{222}} \qquad (4.1)$$

where *hkl* represents the (111), (200) or (222) orientations of the coatings. The texture coefficient is affected by the working pressure and temperature during deposition. At low temperature (473 K), the (111) orientation transforms in to (200) orientation at higher value of working pressure. It is due to decrease of deposition rate, which favors preferential growth of the coatings along (200) orientation. At high temperature with varying working pressure, the intensity of (111) orientation increases mainly due to influence of temperature.

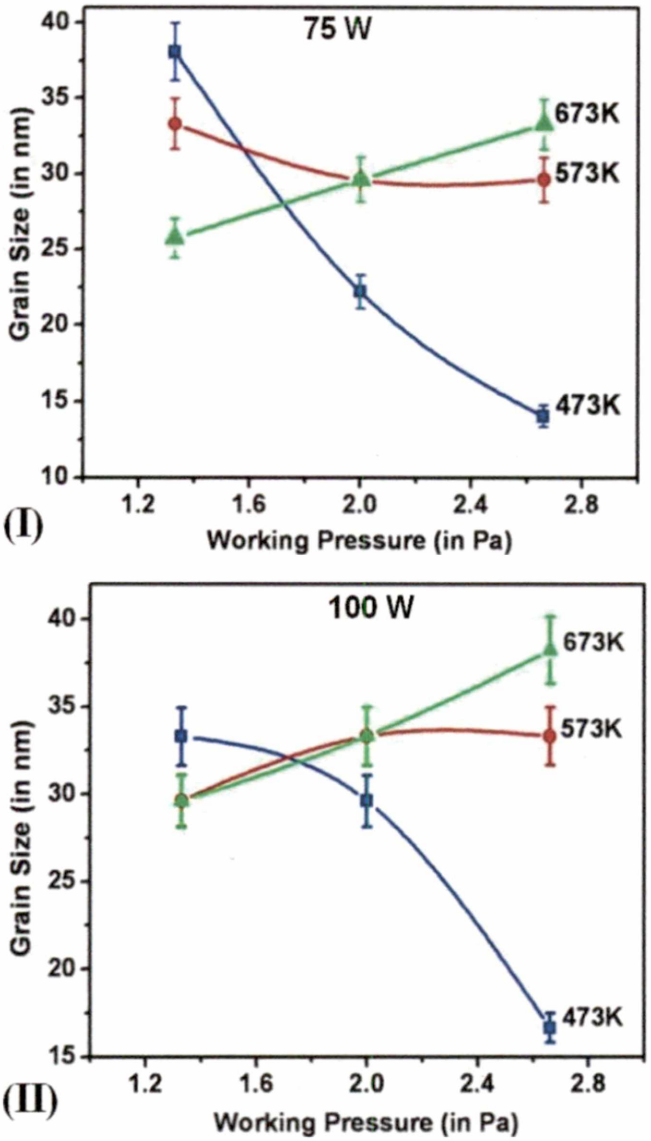

Figure 4.3 Crystallite Size of CrN coatings as a function of working pressure at different temperature (i) coatings deposited at 75 W and (ii) coatings deposited at 100 W on Si(100) substrate.

Figure 4.4 shows that at high temperature, the intensity of preferred orientation (111) is increased with increase in working pressure due to its low strain energy. However, the reduction in intensity of (200) and (222) orientation occurs with increasing working pressure. The combined effect of working pressure and power has shown that the pressure affects the stress induced in the coatings deposited at low power than the coatings deposited at higher power. An intrinsic stress in the coatings decreases with increase in deposition temperature.

substrate with average grain size of 35 nm long with few 110 nm particles. Seok *et al.* (2001) have reported the formation of similar columnar structure in the CrN coatings deposited on steels. It is observed that overall grain size calculated from FE-SEM is higher compared to that of it calculated from XRD spectrum; it is because of the average mean crystallite size and agglomeration of small particles due to higher surface free energy, calculated from XRD and FESEM, respectively (Singh *et al.* 2007). The cross-sectional image of CrN coatings shows the formation of less dense coatings with pores as a function of working pressure, which is due to the reduction in deposition rate. The poisoning effect of the target and the reduction of mean free path affect the deposition rate.

Figure 4.6 shows atomic force microscope (AFM) images of the CrN coatings deposited under different working pressure (1.33 Pa, 1.99 Pa and 2.66 Pa). A small decrease in the average particle size was observed at the 1.33 Pa to 2.66 Pa working pressure and deposition temperature of 473K and then it increases with further increase in temperature, 573K and 673K, within same working pressure (**Table 4.2**). The uniform grain size distribution is observed from the surface morphology. The surface roughness, both average and root mean square (RMS) changes with grain size. The average surface roughness values are 5, 5 and 3 nm for the working pressure of 1.33 Pa, 1.99 Pa and 2.66 Pa, respectively, at 473 K, 75W power. However, the different values of average surface roughness are observed such as 4 nm, 6 nm and 7 nm for the similar working pressure of 1.33 Pa, 1.99 Pa and 2.66 Pa, respectively, at 573K, 75W power. The surface roughness increases with increasing working pressure as evident from the **Table 4.2.**

The measured thickness of CrN coatings (**Figure 4.5-iv, v and vi**) was 3.63, 3.31, and 3.08 μm at 1.33 Pa, 1.99 Pa and 2.66 Pa working pressure, respectively. The thickness of the coatings decreases with increasing working pressure and higher concentration of N_2 due to the reduced mean free path of Cr atoms as explained below.

The mean free path (MFP) of a sputtered atom is given by the following equation (Maissel *et al.* 1970).

$$\lambda = 2.330X10^{-3}\frac{T}{p_m\delta_m^2} \qquad (4.4)$$

where T (in K) is the temperature, P_m (in Torr) is the pressure and δ_m (in cm) is the molecular diameter. The mean free path of the sputtered Cr atoms is 35.6 mm and 11.6 mm, in pure Ar and pure N_2, respectively, at P = 1.33 Pa.

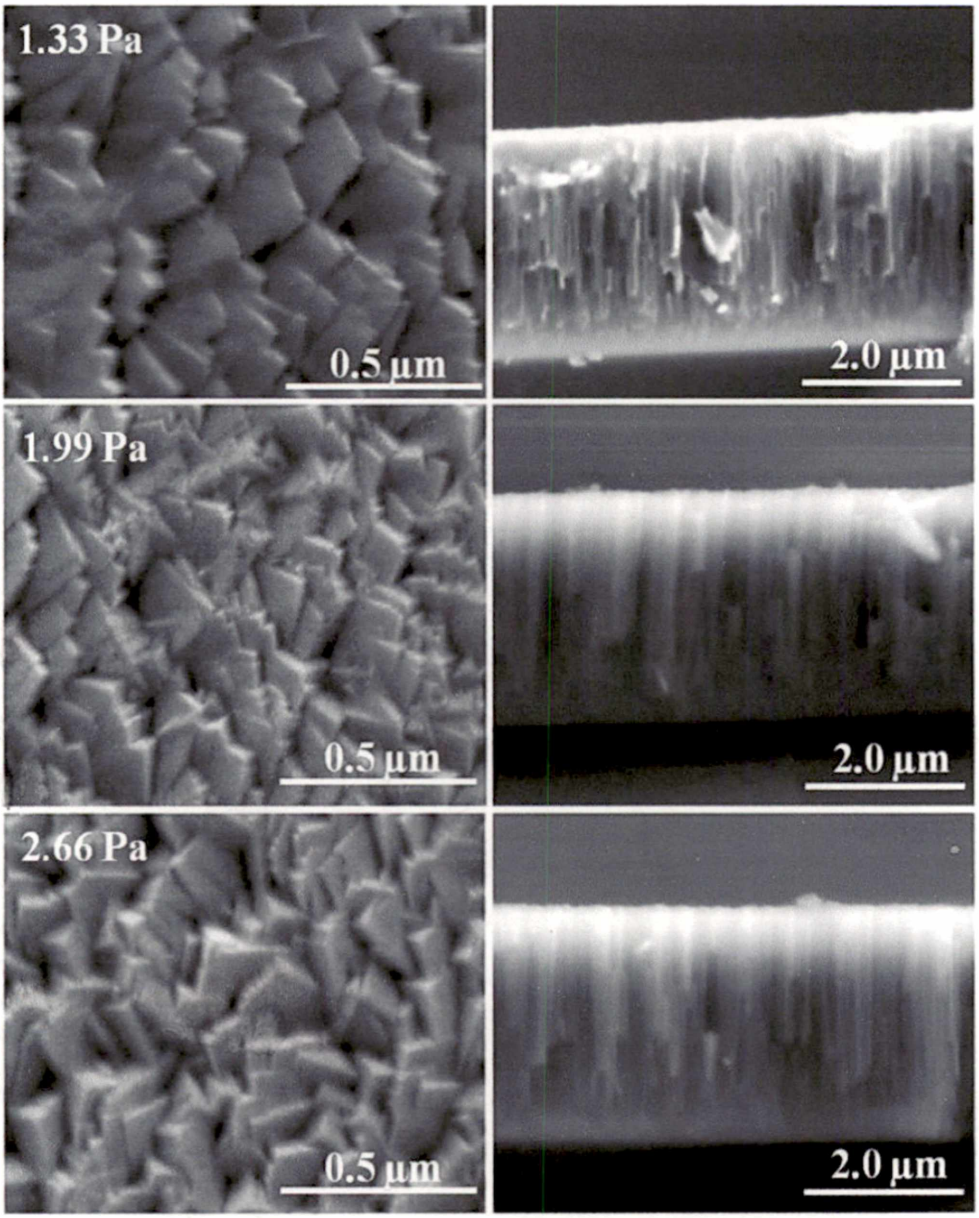

Figure 4.5 FESEM plane and cross sectional view of CrN coatings deposited on Si (100) substrate as a function of working pressure.

It may be inferred that the lower nitrogen concentrations increases the MFP of Cr atoms sputtered from the target, for a given pressure, which results in atoms hitting the substrate with higher energy. It may cause the compressive residual stress in the coatings due to atomic peening mechanism (Kusaka *et al.* 2002). A reduction in deposition rate at higher working pressure as well as the formation of CrN phase at higher N_2 concentration may contribute to the decrease in coating thickness. The higher lattice parameter value of CrN deposited at higher N_2 (1:1) indicates the presence of compressive residual stress in the coatings.

The microstrain from (111) peak of CrN coatings on Silicon substrate is calculated by the **Eq. 4.2** (Chawla *et al.* 2009, Ong *et al.* 2002, Singh *et al.* 2008).

$$\varepsilon = \frac{(c-c_0)}{c_0} X\ 100 \qquad (4.2)$$

where 'c' is a lattice parameter of the deposited coatings calculated from XRD data (in strained condition), while 'c_0' is a standard lattice parameter (in unstrained condition). The film exhibits fcc structure and the parameters 'a' and 'c' are equal. The lattice parameter 'a' can be related with d-spacing using the **Eq. 4.3** (Cullity *et al.* 2001).

$$\frac{1}{d^2} = \frac{(h^2+k^2+l^2)}{a^2} \qquad (4.3)$$

where, 'd' is the interplanar distance obtained from the position of the (111) peak using the Bragg condition.

The microstrain values calculated for the CrN coatings are given in **Table 4.2**. It has been observed that with constant power of 75W and working pressure of 1.33 Pa, the microstrain decreases in the CrN coatings with increasing deposition temperature from 473K to 673K. The higher deposition temperature relaxes the induced strain in the coatings. However, it does not change for the working pressure of 1.99 Pa with increase in deposition temperature but it again increases for the working pressure of 2.66 Pa. At higher working pressure, the lower deposition rate may affect the induced microstrain in the coatings. Similarly, for the constant power 75W and temperature, 473K, the microstrain in the coatings decreases with increasing working pressure (1.33 Pa to 2.66 Pa).

The microstrain values for the coatings stabilize and then increases, with increase in working pressure, for the constant deposition temperature of 573K and 673K, respectively. It may be mentioned that the induced strain in the coatings depends on the energy of the sputtered atoms, which is affected by deposition rate influenced by sputtering pressure and temperature used in the present work. The observed changes in the textures of the CrN coatings were due to the competition between strain energy and surface free energy during deposition of coatings under various process conditions such as substrate temperature, working pressure, and power.

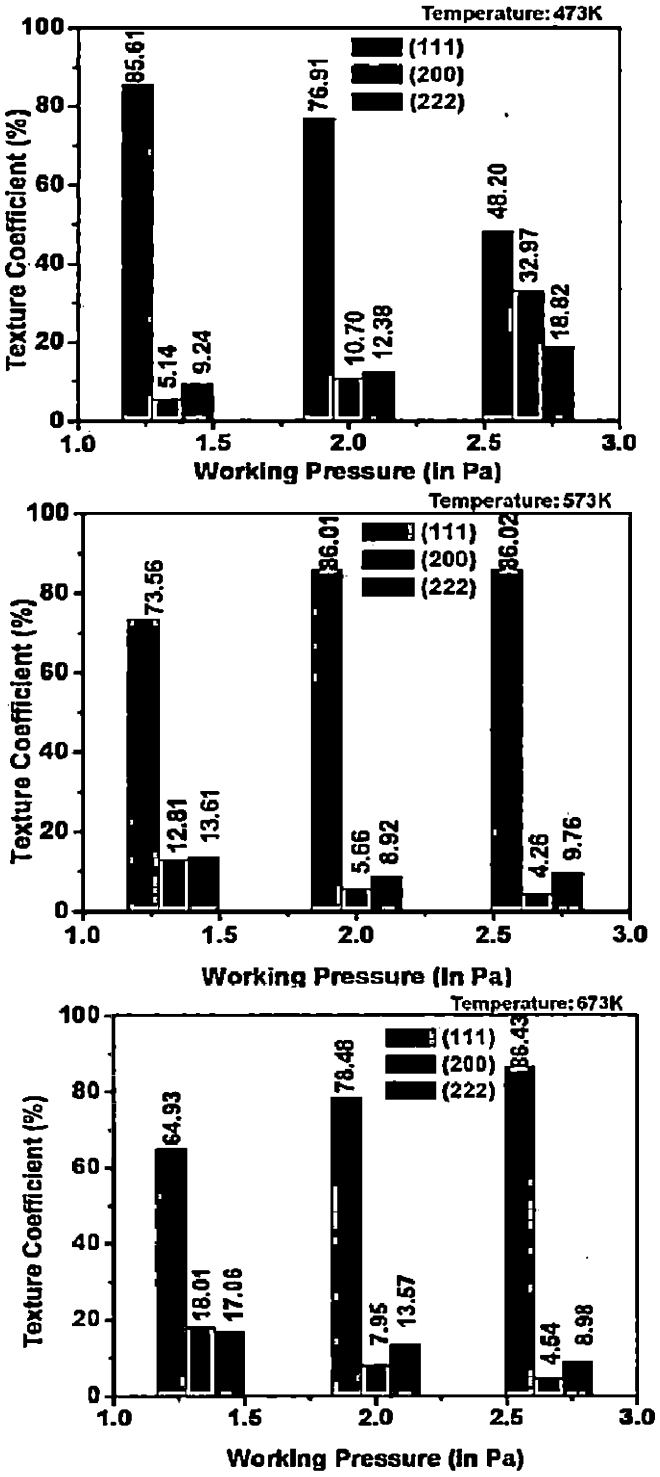

Figure 4.4 Texture coefficients of CrN coatings deposited at 75 W with different working pressure 1.33, 1.99, 2.66 Pa and temperature 473, 573 and 673K.

The FE-SEM micrographs of surface morphologies and cross-sections of the CrN coatings at 1.33 Pa, 1.99 Pa and 2.66 Pa working pressure are shown in **Figure 4.5**. The coatings deposited on Si (100) substrate exhibits columnar grain morphology, which has grown perpendicular to the

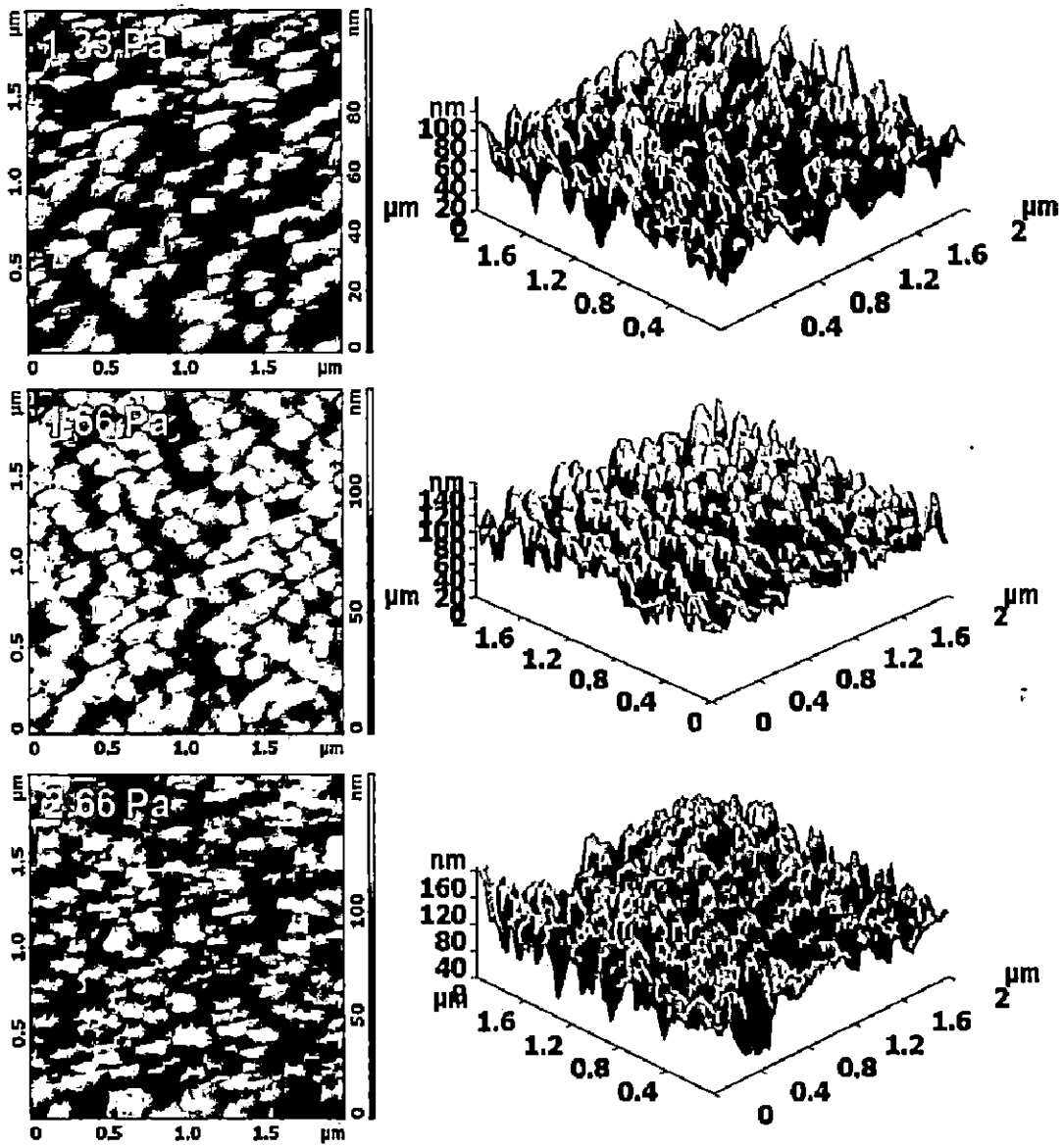

Figure 4.6 AFM plane and 3D views of CrN coatings deposited on Si (100) substrate are a function of working pressure.

4.1.3.2 Analysis of CrN Coatings Deposited on SA304

The effect of working pressure and temperature on XRD peak intensity of CrN coatings deposited on the stainless steel SA-304 substrate in Ar+N_2 chamber, while keeping remaining parameters constant is shown in **Figure 4.7a** and **4.7c**. The coatings exhibit (111) preferred orientation and it changes with working pressure and temperature. It is found that the dominant (111) orientation becomes a preferred orientation even with increase in working pressure. It is due to narrow lower range selection of working pressure in the present study. However, during the initial time of lower working pressure, a mixture of (111), (200) and (222) orientations (compared

to the values d_0 reported in JCPDS 76-2494 card) with 72.53%, 11.63% and 15.85%, respectively, were observed. However, at the higher working pressure, (200) and (222) preferred orientations have increased among the (111), (200) and (222) orientations; while (111) intensity is reduced. Also, at low working pressure, (101) and (201) orientations of Cr_2N phase were observed and (101) phase of Cr_2N transforms in to (111) phase of CrN phase at higher working pressure and temperature. The formation of (101) and (201) orientations could be due to high surface free energies of substrate material and high N_2 content in the sputtering chamber. The texture coefficient (Chawla *et al.* 2008a) of the CrN coatings as a function of working pressure and temperature are calculated using the **Eq. 4.1** and the results are shown in **Figure 4.7b** and **4.7d**, respectively. The texture coefficient is affected by the working pressure and temperature during deposition. The (111) orientation transforms in to (200) orientation at higher value of working pressure.

Intrinsic stress in the coatings increases (from compressive to tensile) linearly and it remains constant even after deposition, called low mobility Volmer-Weber growth, which increases at higher temperature (Ohring *et al.* 2002) . The changes in the preferred orientation of CrN coatings are due to the following reasons. The deposition rate decreases with increase in sputtering pressure owing to the reduction of mean free path (MFP). With the increase in working pressure, more collision of sputtered particles occurs when the particles move from target to substrate and due to the frequent collisions, some of the sputtered particles are back scattered and therefore, it reduces the deposition rate. Hence, the reduction in deposition rate with increasing working pressure influences the crystallinity, texture, and the porosity of as deposited coatings. It is evident that the peak intensity of (111) orientation is decreasing with increasing the value of working pressure and temperature.

The interplanar spacing, d-value of the coatings, is calculated using Bragg's relation from the position of the (111) peak. After 1.99 Pa value of working pressure, the increase in d-value is due to tensile stresses in the deposited coatings. The grain size of CrN coatings is calculated based on Scherrer formula and plotted in **Figure 4.8.** It observed that the grain size of (111) peak decreases with increase in working pressure. The grain size reduces due to reduction in the improvement in the degree of crystallinity of the coatings and high compressive residual stresses induced in the coating during deposition.

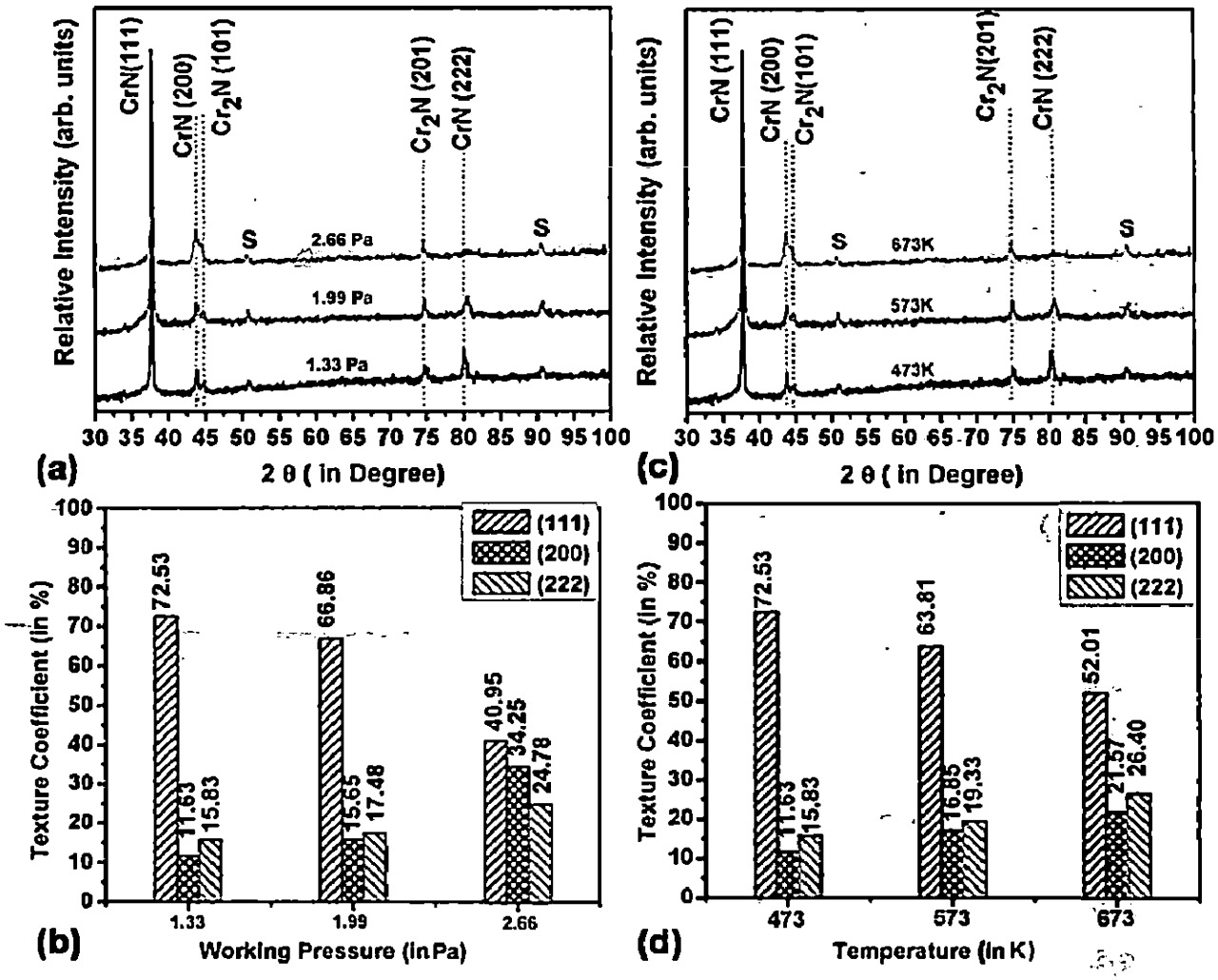

Figure 4.7 XRD peaks and texture coefficient of CrN film deposited on SS-304 substrate (a) and (b) as a function of working pressure at 473K, while (c) and (d) as a function of temperature at 1.33 Pa.

A pyramid shaped topographical growth and columnar morphology of the coatings are observed at different working pressures as shown in cross sectional SEM images of CrN (**Figure 4.9**). The rate of deposition was restricted with increasing working pressure. The thickness of CrN coatings deposited at different working pressures is shown in **Table 4.3**. A limiting crystallite size of the coatings has been identified in the grain refinement process.

The crystallite size of the coatings deposited at 1.33, 1.99 and 2.66 Pa working pressure and with power of 75 W, is found to be 35, 26 and 19 nm, respectively. The rate of reduction of crystallite size is found to be slower due to highly textured grains in the coatings and the narrow range of working pressure. The highly textured grains indicate that the strain energy is higher in

the coatings and the grains are heavily dense. The surface morphologies of the as deposited CrN coatings were studied by using AFM. The 3D surface morphologies of CrN coatings are shown in **Figure 4.10**. The root mean square (RMS) roughness values of the as-deposited CrN coatings were calculated and its value at 473K temperature were 8 nm, 8 nm, and 3 nm for 1.33, 1.99 and 2.66 Pa pressure, respectively. However, with the increasing temperature (473K, 573K, and 673K) at the same working pressure (1.33 Pa), the RMS values were 8, 14 and 21 nm.

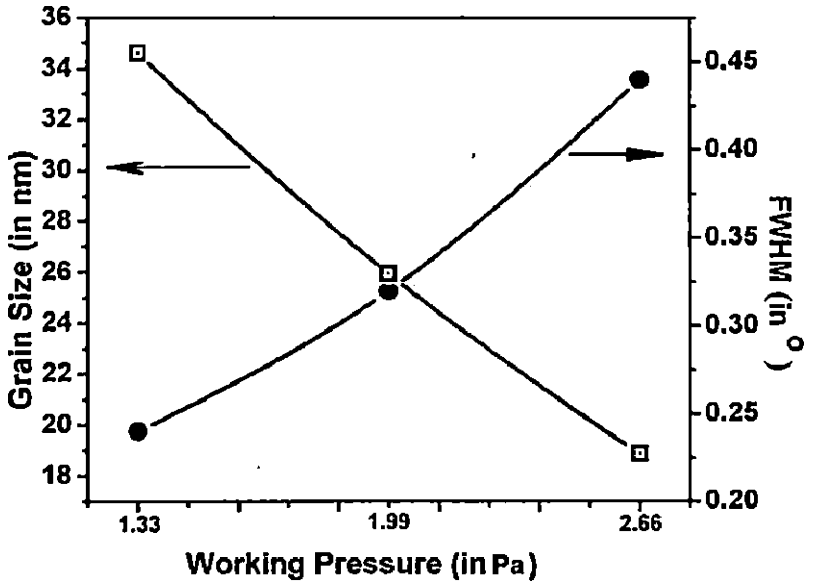

Figure 4.8 Dependence of the grain size and FWHM on the working pressure of CrN coatings deposited at 473K and power 75W.

The increasing deposition temperature affects the grain size as evident from the results of AFM and XRD. The higher grain size of the CrN coatings at higher temperature may due to increased diffusivity of atoms facilitating the grain growth. The mobility of grain boundaries leads to variations in the surface topography and morphology of the CrN coatings as observed from its AFM images.

The coatings developed by physical vapor deposition techniques normally contain internal or residual stress within it. The magnitude of residual stress present in coatings affects its properties, particularly adhesion and mechanical properties. The residual stress induced in the coatings is controlled by the various process parameters at the time of deposition. The biaxial stress (σ_{xy}) in the CrN coatings is calculated using **Eq. 4.5**.

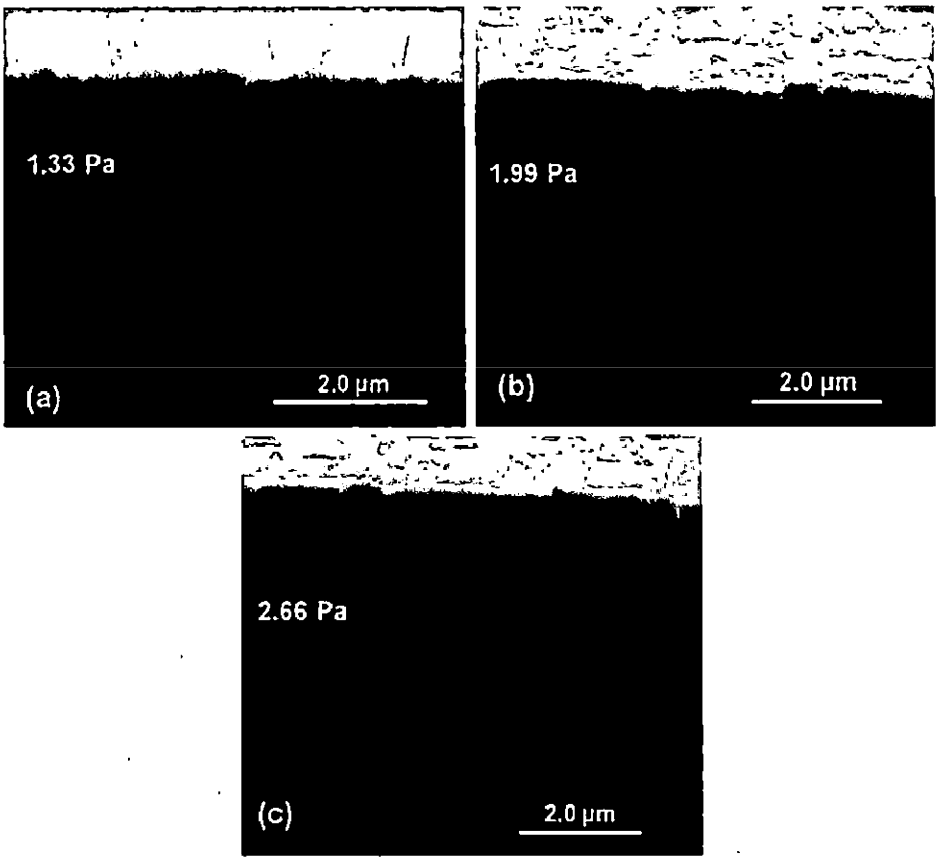

Figure 4.9 Scanning Electron Micrograph of fracture cross section of the coatings at different working pressure.

$$\sigma_{xy} = -\frac{1}{\vartheta}(E\varepsilon_z - \sigma_z) \tag{4.5}$$

where ε_z along the direction z perpendicular to the X-Y plane given by **Eq. 4.6.**

$$\varepsilon_z = \frac{(d_{hkl} - d_0)}{d_0} \tag{4.6}$$

and E is Young's modulus of coating (245 GPa), v is Poisson ratio of film (0.23) (Lamastra *et al.* 2006), d_{hkl} is spacing between two planes in stressed condition (during deposition), d_0 is standard interplanar spacing in unstressed condition of CrN coatings, and σ_z is stress in z direction (perpendicular to substrate) is zero assuming a biaxial stress condition. It is evident from the stress analysis of CrN coatings that the stresses are reduced with the increase in working pressure and temperature as shown in **Table 4.3**. It has been reported in the literature (Fabis *et al.* 1990) that the average stress in deposited CrN coatings is affected mainly by three parameters: sputtered flux, incidence angle, sputtering pressure, and film thickness. In DC reactive sputtering deposition technique, increasing the working pressure ($Ar+N_2$) reduces the intrinsic stress generated in the coatings, as shown in **Figure 4.11**, because of mainly two reasons; the reduction in energies of

plasma particles due to inelastic scattering of gas and a decrease in discharge voltage at fixed current with increasing working pressure. Similarly, power density also affects the intrinsic stress of the CrN coatings by influencing the effect of other deposition parameters.

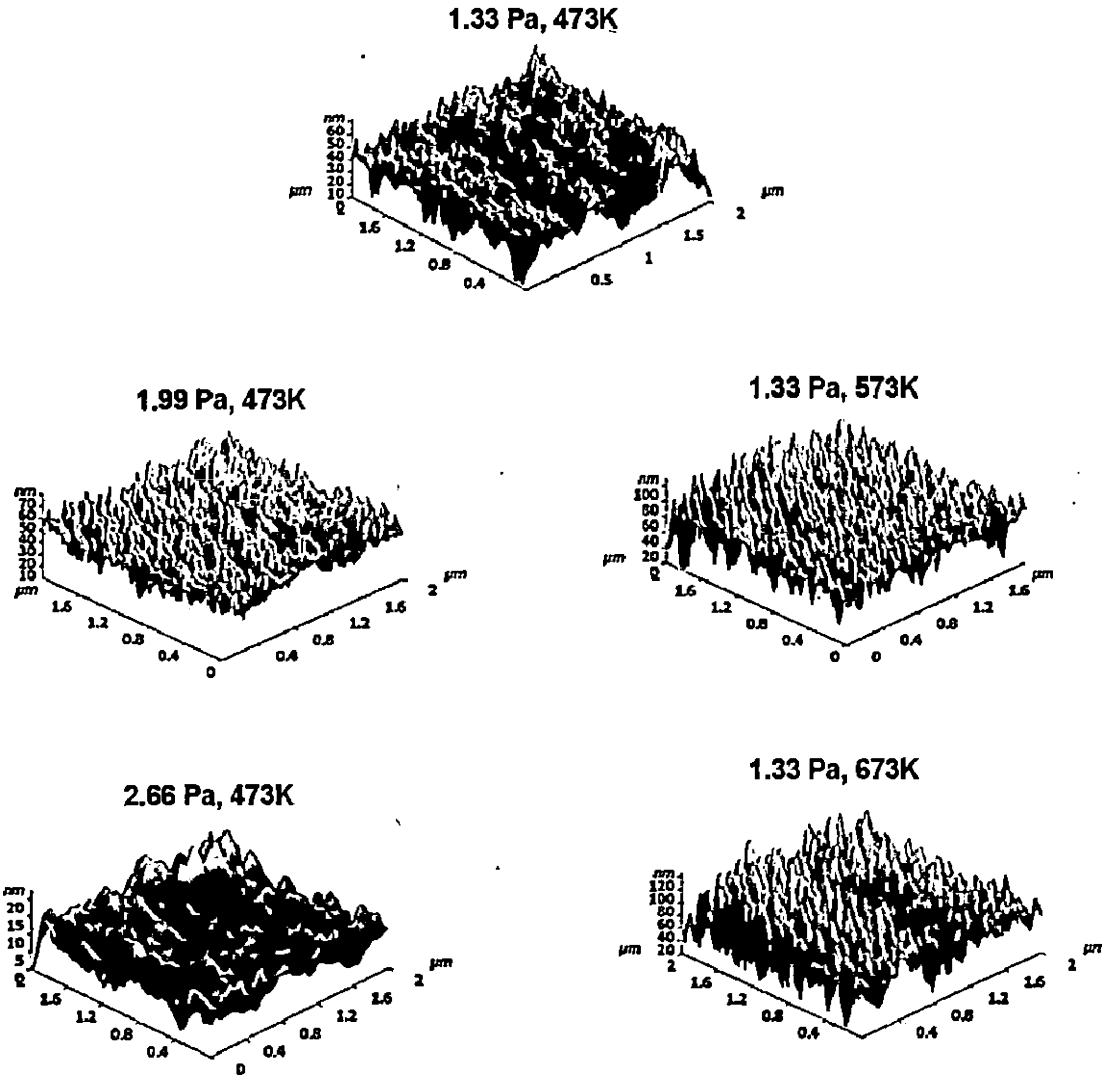

Figure 4.10 AFM surface morphologies of CrN coatings: as a function of working pressure deposited at 473K and as a function of temperature deposited at 1.33 Pa pressure.

Table 4.3 Average crystallite size using XRD peaks and AFM, Thickness, Deposition Rate and stresses developed at different working pressure and temperature on CrN coatings deposited on SA304 substrate.

CrN Sample No	Temperature (K) and Power (W)	Working Pressure (Pa)	Crystallite Size (nm)		Average film Thickness (μm)	Deposition Rate (nm/min)	Stresses (GPa)
			XRD	AFM			
1	473K, 75W	1.33	35	32	2.22	37.00	0.68
2		1.99	26	35	2.04	34.00	1.49
3		2.66	19	24	1.94	32.33	-0.10
4	473K, 100 W	1.33	28	102	3.63	60.50	-1.77
5		1.99	38	90	3.31	55.16	-0.81
6		2.66	32	116	3.08	51.33	1.02
10	573K, 75W	1.33	35	54	2.08	34.66	-0.55
11		1.99	38	33	2.37	39.50	0.36
12		2.66	45	124	2.65	44.16	-1.64
13	573K, 100W	1.33	30	48	3.51	58.50	-1.80
14		1.99	38	74	3.56	59.33	-1.82
15		2.66	35	*412	3.24	54.00	-1.62
19	673K, 75W	1.33	32	65	1.96	32.66	-0.81
20		1.99	32	96	2.56	42.66	-1.81
21		2.66	26	91	3.44	57.33	-0.68
22	673K, 100W	1.33	38	81	2.96	49.33	-0.41
23		1.99	30	61	3.31	55.16	-1.46
24		2.66	32	71	3.56	59.33	-1.50

The hardness of CrN coatings was measured by an optical micro hardness tester (Model: Miniload-II, Mfg: Leitz, Germany) with Vickers indentation tip. The indenter tip is made up of diamond with pyramid shape, its square sides with opposite faces, edges, and face angles are at an angle of 136°, 148°, and 68°, respectively. VDH (Vicker's diamond hardness) is calculated using **(Eq. 3.9)** with the input of the indenter load and the actual surface area of the impression. The applied load value was 15 grams with 28 sec loading time. The indentation was made on five different points in each CrN/SS sample to obtain its average hardness value. The calculated hardness is given in **Table 4.4a** and **4.4b**. It is observed that the CrN coatings deposited at 473K (with 75W power), exhibits a reduction in hardness from 10.30 to 8.56 GPa with increasing working pressure from 1.33, 1.99 and 2.66 Pa. It is because of the presence of crystal imperfection during film growth at increased working pressure and low temperature. However, the hardness of coatings increases slightly from 10.30 to 12.26 GPa with increase in deposition temperature to

673K for same working pressure. The increase in the hardness may be due to lower surface roughness (**Figure 4.10**) and comparatively higher deposition rate (Mayrhofer *et al.* 2001). On the other hand, the effect of power showed that the CrN coatings deposited at 100 W, showed an increase in hardness value from 13.71 GPa to maximum of 18.31 GPa for the temperature and working pressure of 673K and 1.33, 1.99 and 2.66 Pa, respectively. The micro hardness of the coatings increases with increase in substrate temperature T_s as reported in the literature (Gautier *et al.* 1996). With increasing T_s, the mobility of atoms is increased leading to a more perfect structure. The hardness values of CrN coatings measured in the present work are in tandem with that of the reported hardness value of 18 GPa, which is higher than of its bulk CrN (11 GPa) (Hones *et al.* 1997).

Table 4.4a Hardness values of CrN coatings deposited at 75 W.

CrN Sample No.	Temperature (K) and Working Pressure (Pa)	Hardness in (GPa)
1	473, 1.33	10.30
2	1.99	8.91
3	2.66	8.56
10	573, 1.33	9.90
11	1.99	12.26
12	2.66	13.93
19	673, 1.33	12.26
20	1.99	11.74
21	2.66	11.58

Table 4.4b Hardness values of CrN coatings deposited at 100 W.

CrN Sample No.	Temperature (in K) and Working Pressure (Pa)	Hardness in (GPa)
4	473, 1.33	14.83
5	1.99	9.52
6	2.66	7.57
13	573, 1.33	13.71
14	1.99	14.26
15	2.66	16.79
22	673, 1.33	13.71
23	1.99	14.83
24	2.66	18.31

The hardness of conventional metallic material can be well described by Marsh relations (Marsh *et al.* 1964). Normally, the maximum theoretical strength of a solid is a function of the strength of inter atomic bonds between atoms and it is given by *E/10* (Kelly *et al.* 1986), which comes to around 32 GPa for CrN coatings (E = 245 GPa and υ = 0.23), However, in actual practice, it is never observed due to the presence of crystal imperfections and defects in the form of cracks present in the coatings. The strength and hardness of bulk material can be increased by increasing its dislocation density during plastic deformation. The hardness increases with higher density of immobile dislocation, which increases due to the reduction in grain size leading to higher volume fraction of grain boundaries. The minimum stresses required to activate dislocation sources will increase with reduction in particle size to nano phase (Mayrhofer *et al.* 2006). The similar mechanisms may be applicable to strengthening of coatings in addition to the role of residual stress and substrate effect.

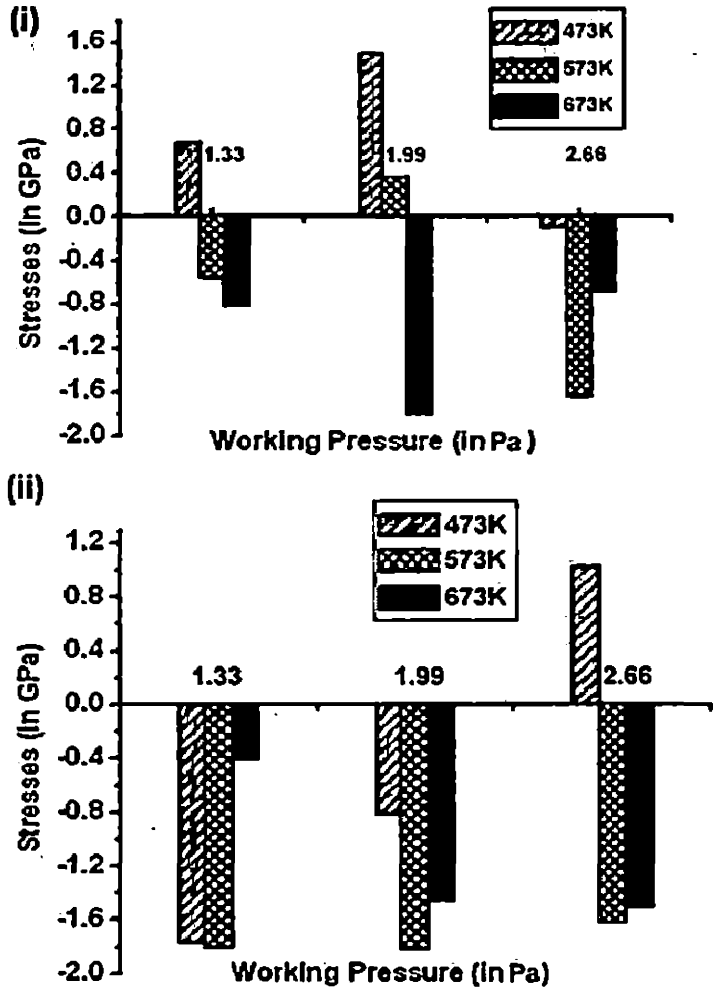

Figure 4.11 Intrinsic stresses produced in CrN coatings deposited at (i) 75 W and (ii) 100 W.

4.1.4 Conclusion

The CrN coatings deposited on Si (100) substrate by reactive magnetron sputtering process has been investigated in the present work. The effect of working pressure, temperature, and power on the microstructural characteristics such as texture, grain morphology, and surface roughness of CrN coatings has been analyzed. The experimental results have shown that CrN coatings exhibits (111) preferred orientation and it transforms into (200) orientation with the increasing working pressure. The coatings deposited at lower working pressure showed a large grain size with higher crystallinity, but it has reduced with increase in working pressure. The preferred orientations of the CrN coatings depend on sputtering conditions, thickness of the coatings, and the induced microstrain in the coatings as observed in the present work. Also, the texture coefficient is affected by the working pressure and temperature during deposition. The microstrain in the CrN coatings is decreasing with increasing working pressure for the low deposition temperature of 473K as evident from the present work. The columnar grain morphology is observed for the coatings for the chosen deposition conditions.

The CrN coatings deposited on stainless steel substrates by reactive magnetron sputtering process has also been investigated in the present work. The effect of working pressure, temperature and power on the microstructural characteristics such as texture, grain morphology, and surface roughness of CrN coatings has been analyzed. The experimental results have shown that CrN coatings exhibits (111) preferred orientation and it transform into (200) orientation with increasing working pressure. The film exhibits a high crystallinity with the large grain size at lower working pressure (1.33 Pa). The preferred orientations of the CrN coatings depend on sputtering conditions, thickness of the coatings, and the induced residual stress in the coatings as observed in the present work. The microhardness of CrN coatings showed an increasing trend due to the combined effect of temperature, working pressure, and power density. The high hardness of the coatings is due to the grain size effect, highly textured grains, and compressive residual stress in the coatings.

4.2 Influence of Sputtering Parameters and Reactive Gases on Microstructure and Mechanical Properties of Chromium Nitride Coatings Deposited on SA-304 Substrates by DC Magnetron Sputtering

4.2.1 Introduction

Zhao *et al.* (2005) synthesized chromium nitride coatings, by reactive DC magnetron sputtering, onto multiple moving substrates and observed the distinct phase structure, stress state and growth morphology in the coatings, depending on nitrogen flows. The coatings deposited at very low nitrogen flows (2.8 sccm) exhibit a significantly refined microstructures, which occurs continuously accompanied by decrease in surface roughness with increase in nitrogen flow.

Nam *et al.* (2000) studied the influence of high deposition rate, in magnetron sputtering, to control the microstructures of CrN coatings. They found that deposition of CrN compound has increased up to 90% than pure Cr coatings due to increase in ionization efficiency caused by applying negative pulsed DC bias. The effect of N_2 gas on microstructure and mechanical (includes tribological and wear) properties of CrN coatings developed by DC reactive magnetron sputtering is well studied in the literature (Tu *et al.* 2005, Van *et al.* 2006, Wu *et al.* 2000, Zhao *et al.* 2005, Olaya *et al.* 2005, Levy *et al.* 1999, Hones *et al.* 1997, Fornies *et al.* 2006). However, a detailed investigation pertaining to the formation of different phases, orientation and growth mechanism of grains, which are affected by reactive as well as sputtering gases in addition to other parameters, is very much essential to synthesis CrN coatings with superior mechanical and tribological properties. Therefore, the present work has been focused to investigat the relationship between microstructural and micro hardness of the CrN coatings, deposited by DC-reactive magnetron sputtering, as a function of sputtering conditions such as sputtering gas, different concentrations of reactive gas and substrate temperature. X-ray diffraction (XRD), atomic force microscopy (AFM), and field emission scanning electron microscopy (FE-SEM) were used to reveal the effects of process parameters on the microstructural characteristics of the CrN coatings such as phase formation, grain morphology, textures, and surface roughness. The hardness of the CrN coatings prepared under different processing conditions was measured by microhardness tester using diamond indenter tip and related with the observed microstructural morphology. The smallest applied load was set to 15 grams during hardness test.

4.2.2 Experimental Details

4.2.2.1 Deposition

CrN coatings were deposited on stainless Steel (SA-304) substrate by using reactive magnetron sputtering (Model: DCSS – 12, Manufactured by Excel Industries, Mumbai) equipped with Baratron Capacitance Manometer and Vacuum Gauge using DC power source. The substrate used were austenitic stainless steels (SS) normally used for structural materials i.e for fast reactors, because of their excellent mechanical properties at high temperatures and good corrosion resistance in general (**Kamachi *et al.* 1998**). The chemical compositions of the substrate are given in **Table 4.5**. The SA-304 substrate with dimension of (15mm X 15mm X 0.9 mm) was prepared and mechanically polished to a surface roughness (Ra) less than 0.1 μm using Fe_2O_3 powder in water. The similar procedures as used for the deposition of CrN coatings on Si were followed during deposition of the coatings on stainless steel. The proportion of sputtering gas (Ar) and reactive gas (N_2) was varied during deposition. The gas flow was controlled by mass flow controller. During all experiments, the deposition temperature used was 573K except the coatings deposited in pure N_2 environment in which the temperature was 473K, 573K and 673K. The main deposition parameters are summarized in **Table 4.6**.

Table 4.5 Compositional analysis of SA304 Stainless Steel substrate (As per ASME Section II- Ferrous materials).

Element	C	Mn	Si	Cr	Ni	P	S
Weight %	0.08	2.0	1.0	18.0-20.0	8.0 –10.5	0.045	0.03

Table 4.6 Sputter deposition conditions of CrN coatings deposited on SA304 substrates.

Process parameters and their corresponding values	
Target	Pure Cr (99.995%)
Substrate	Stainless Steel (SA 304)
Base pressure	$< 5.3 \times 10^{-4}$ Pa
Working Pressure	1.33 Pa
Target power / density	75 W (3.82 W/cm^2)
Distance between target and substrate	50 mm
Temperature	573 K
Substrate biasing	No
Deposition Time	60 min

4.2.2.2 Characterization

In the present study, a reactive magnetron sputtering was used to produce chromium nitride coatings, with a controlled microstructure, on stainless steel substrate. The deposition conditions for tailoring the microstructure was achieved with change in different gaseous environment and proportion of sputtering gas (Ar) and reactive gases (N_2) in the chamber. The microstructure and phases in the coatings were analyzed by Field Emission Scanning Electron Microscopy (Model: 200F, FEI-Quanta) and Atomic Force microscopy (NT-MDT), and X-ray diffraction (Model: D8 Advance, Brucker), respectively. The FESEM was operated at 20 kV to capture images of the coatings at different magnification. The surface roughness of the coatings was measured by using analysis software attached with AFM, adopting root mean square and average roughness statistics. The chemical analysis of CrN coatings was performed using EDS which is attached with FE-SEM, while mechanical characterization was done by micro hardness tester using diamond indenter tip with pyramid shape (Leitz, Germany). The smallest applied load value was 15 grams during hardness test. The phases and preferred orientation of CrN coatings in the as deposited condition were characterized by X-Ray Diffraction with CuKα radiation (λ=1.54 Å) and Ni filter. The excitation voltage and current were set to a 40 kV and 30 mA respectively, in the diffractometer. The scans range used was 30° to 90° to find out the possible changes in the texture of coatings. The scan rate used was 1°/min with step size 0.05°. The grain size of coatings was calculated by two different approaches: i) by using the Scherrer formula (Cullity *et al.* 2001); and ii) using the basis of the surface morphology characterized by AFM attached with software for the calculation of grain size.

The mechanical properties of the CrN coatings were characterized by Microhardness (miniload – II, Mfg: Leitz, Germany), Nanoindentation (CSM NHT, Switzerland), and Pin on Disc (Magnum, Bangalore) to reveal hardness, modulus and wear properties like coefficient of friction and wear rate. Nano hardness testing has been performed on the coatings, using a fixed load mode, fixed depth mode or varying loading – unloading rate with fixed load, depending upon its thickness. The fixed mode with 15 mN maximum load of testing was continued for complete set of CrN coatings samples deposited with varying Ar+N_2 environment. On the other hand, the CrN coatings deposited in pure N_2 environment with different temperature was characterized by using fixed depth mode (125 nm). During test, the parameters like time, applied indent load (P_{max}) and corresponding penetration depth (h_{max}) were recorded with a personal computer. The load was

increased and decreased with predetermined rate, depending upon selection of load mode, with hold time of 5 seconds at maximum load. Load versus displacement curve was generated during the indentation tests.

The wear testing was performed using a pin on disc tribometer. The pin was coated by 2.0 to 4.37 μm thick CrN coatings on stainless steel (SA304) and prepared with square configuration (7 mm to 7 mm, **Figure 4.21**), while EN 32 material is used as a counter material. The EN32 material is common case-hardening steel used mainly for wear-resistance applications such as camshafts, tappets, gears, gudgeon pins, etc. The normal load was kept constant, 10 N, with the relative sliding speed of 0.5 m/s. The test was carried out in room atmosphere under dry condition. The friction force between the deposited coatings and the counter material was measured, and divided by the normal load to calculate the friction coefficient. The wear track was characterized by using a field emission scanning electron microscope (FESEM).

4.2 3 Results and Discussion

4.2.3.1 Influence of Nitrogen

It requires the higher amount of nitrogen (above 50%) to form the CrN and other stoichiometric phases, but the deposition rate is decreasing during deposition as observed in the present work. Normally, the sputtering yield is higher, in Ar environment, during sputtering of any material (Olaya *et al.* 2005). The effect of different proportion of reactive gas (N_2) and the sputtering gas (Ar) on the formation of CrN coatings is shown in **Figure 4.12.** It clearly shows that the films orientation is changing from (200) to (111) with increase in nitrogen content in the sputtering chamber. The coatings deposited using the lower content of N_2 (up to 30%) gas exhibit a dual structure, a mixture of CrN and Cr_2N, in which the most dominating peak orientation is (200) with a relatively weak (111) peak orientation, indicating a textured films. Also, the peak with (200) orientation is broad and its intensity is reduced with increasing nitrogen content from 30% to 40%. On the other hand, the peak intensity of (111) is increasing with increase in nitrogen content in the chamber. The preferred orientation of (111) plane is due to its lowest strain energy as compared to (200) plane. The result of preferred orientation is in tandem with Forniés et al. (2006) work on CrN coatings in which the preferred (200) orientation was observed up to 30% N_2 content. The dependence of nitrogen content on deposition rate and its influence on the coatings thickness and grain size of CrN coatings is plotted in **Figure 4.13.**

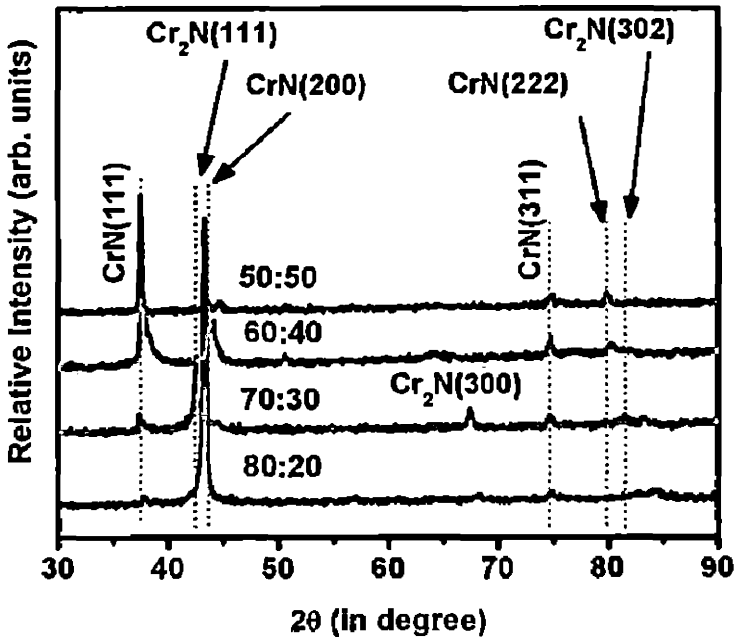

Figure 4.12 XRD spectrum of CrN coatings deposited at 573 K with different Ar : N_2 gas mixture ratio.

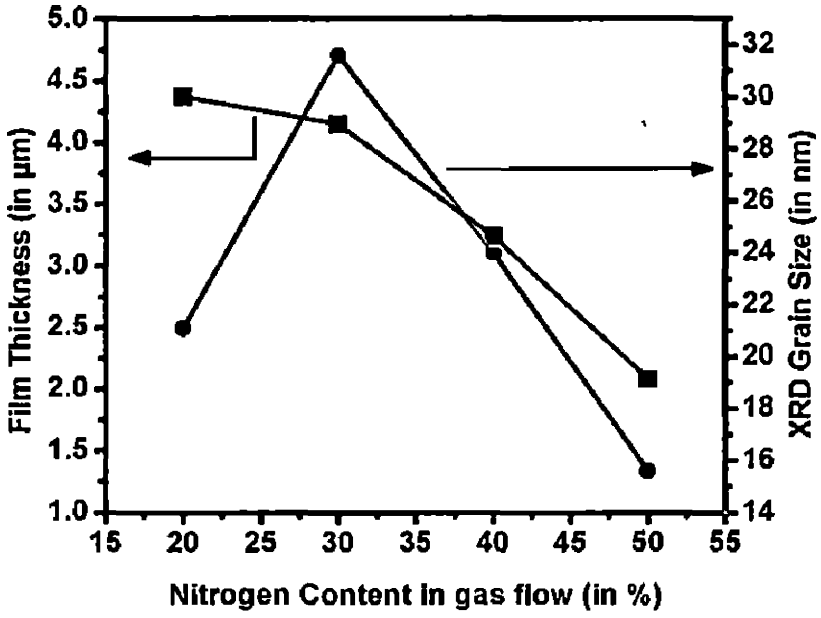

Figure 4.13 Dependence of nitrogen content on coating thickness and grain size in CrN coatings.

The deposition rate is decreasing with increase in nitrogen content in the chamber and is in agreement with the reported data in literature (Fornies *et al.* 2006, Van *et al.* 2006, Zhang *et al.* 2007). As soon as pressurized N_2 is introduced in the chamber, the deposition rate decreases rapidly with increased pressure. It is because of the reactive gas, N_2, reacts with Cr target and form a nitride layer at the outer surface of the target, this nitride compound exhibits a lower sputtering

rate than metals leading to a low sputtering yield. Hence, a film thickness is reduced from 4.37 μm to 2.08 μm with increasing N_2 content in the sputtering chamber (**Table 4.7**), which can be observed from cross sectional FESEM. images shown in **Figure 4.14**. However, the coatings density is increasing with N_2 content as observed in this figure. Also, initially, the grain size is increased with increasing nitrogen content (between 20% to 30%) as shown in **Figure 4.13**. It is due to the higher ad-atom mobility, which facilitates the atomic migration to the grain boundaries followed by grain growth. For the deposition conditions of substrate temperature, 573K, and increasing nitrogen content up to 30%, the adatom mobility is influenced predominantly by substrate temperature than the latter during deposition of the coatings. However, the effect of nitrogen is more pronounced when it is above 30% for the same deposition temperature. However, above 30% nitrogen content, the grain size is reduced due to the higher nitrogen gas content in the chamber. It is because of the lower atomic diameter of nitrogen compared to argon, results in higher MFP, causing less number of collisions with gas particles in the chamber. The sputtered Cr atoms would also undergo less collisions leading to a low probability of agglomeration and growth even before arriving at the substrate (Chandra *et al.* 2006). In such a case, a reduction in the particle size occurs with lower atomic mass of the sputtering gas. The detailed XRD analysis shows that the deposited coatings undergo phase changes from a mixture of Cr_2N+CrN phases to single-phase CrN with increasing nitrogen content (above 40%). The variation of nitrogen content is responsible for the formation of different phases such as Cr, Cr_2N and CrN.

4.2.3.2 Effect of Different Sputtering Gases

The chromium nitride coatings were deposited on stainless steel with different proportions of gases such as 80% Ar + 20% N_2, 100% N_2, and 80% He + 20% N_2 referred to as Ar+N_2, pure N_2,.and He+N_2 respectively. In the sputtering deposition system, mainly two types of deposition modes were observed during deposition of nitride compound: metallic mode and nitride mode (Sumi *et al.* 1997). In the nitride mode, for a N_2/Ar ratio of more than 50%, the deposition rate is small. When N_2/Ar ratio is less than 50%, the deposition rate is high and called metallic mode. So, in the presence of Ar + N_2 mixture, more or less a metallic mode of sputtering occurs due to very low content of N_2 gas in the chamber and its less reaction with target. However, in the case of 100% N_2 as a sputtering gas, a nitride mode of sputtering occurs with a much lower sputtering rate (Chandra *et al.* 2005).

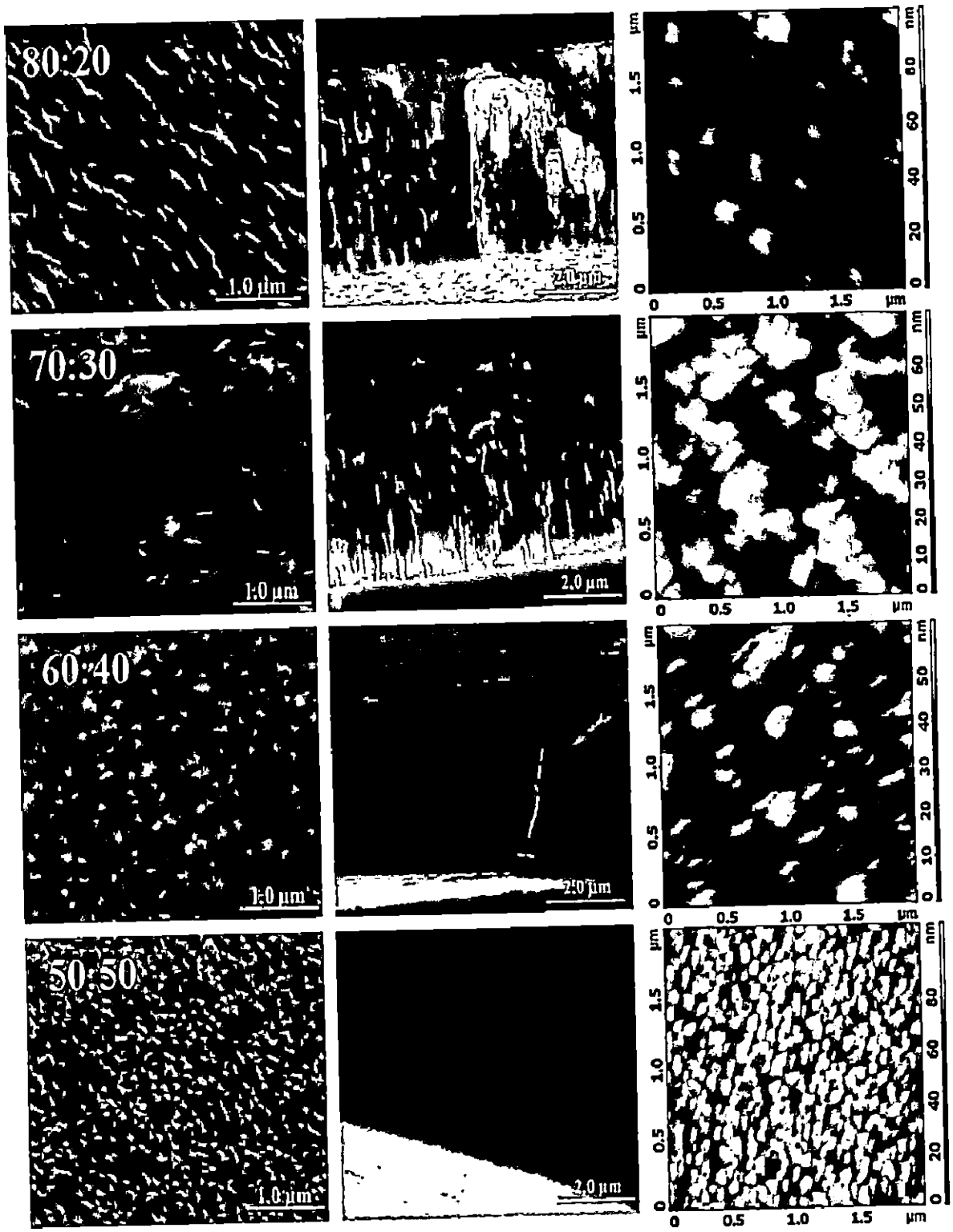

Figure 4.14 Surface topography and morphology of CrN coatings at different Ar: N_2 content at 573 K temperature.

Figure 4.15 and **Figure 4.16** show the XRD patterns and topographical images of chromium nitride with different gas mixtures, respectively, in which the deposited coatings showed denser morphology in pure N_2 and He+N_2 environments compared to coatings deposited in Ar+N_2 environment. Also, different coating thickness is observed as 4.37 μm, 1.73 μm and 1.30 μm for Ar+N_2, pure N_2 and He+N_2, respectively. The differences in grain size under different sputtering conditions can be explained by the relationship of the mean free path, λ (cm), with the molecular diameter of the sputtering gas as given by **Eq. 4.4** (Maissel et al. 1970).

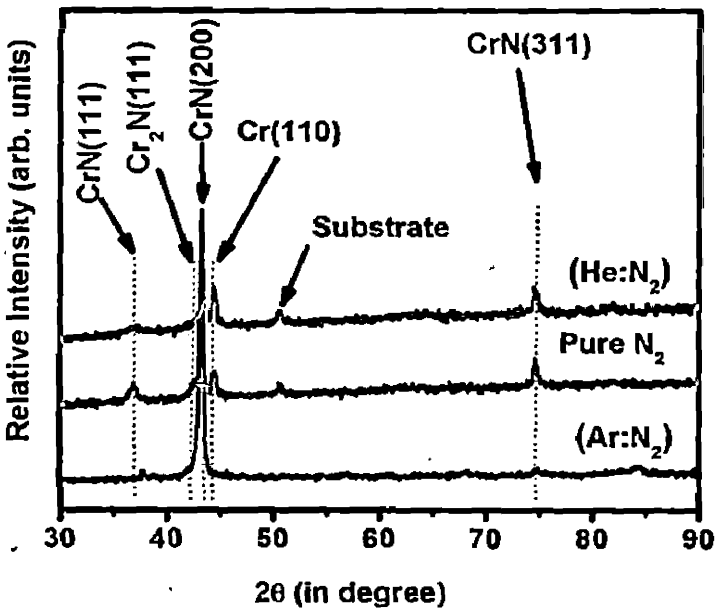

Figure 4.15 XRD spectrum of CrN coatings deposited in the different gaseous environment.

It is evident from **Eq. 4.4** that the grain size becomes larger in the case of the Ar+N_2 gas due to larger atomic diameter of Ar as compared to other two N_2 and He gases. The grain size were calculated by XRD, found to be 21, 16 and 17 nm for Ar:N_2, Pure N_2 and He:N_2 respectively and the similar results were observed from AFM analysis. The higher atomic diameter leads to lower MFP, which causes higher collision with gas particles in the chamber. Hence, the collision frequency increases with increasing size of sputtering gas atoms due to which sputtered Cr atoms would also undergo multiple collisions leading to a higher probability of agglomeration and growth even before arriving at the substrate. Therefore, the grain size is increasing with increasing atomic mass of the sputtering gas. During sputtering in the mixture of He and N_2 atmosphere, the ionized He atoms bombarding the target may get backscattered and implanted into the coatings. In the sputter deposition system, the deposition rate is limited by sputtering gas ionization and its

sputtering yield, sputtered atom diffusion from the target to the substrate. The sputtering yield of Cr element in He is 0.17 at 500eV and in Ar gas environment, it is 1.18 (Vossen *et al.* 1978). However, the use of helium gas as the sputtering gas may be advantageous for ionization of elements as it eliminates some of the common polyatomic interferences associated with conventional argon plasmas.

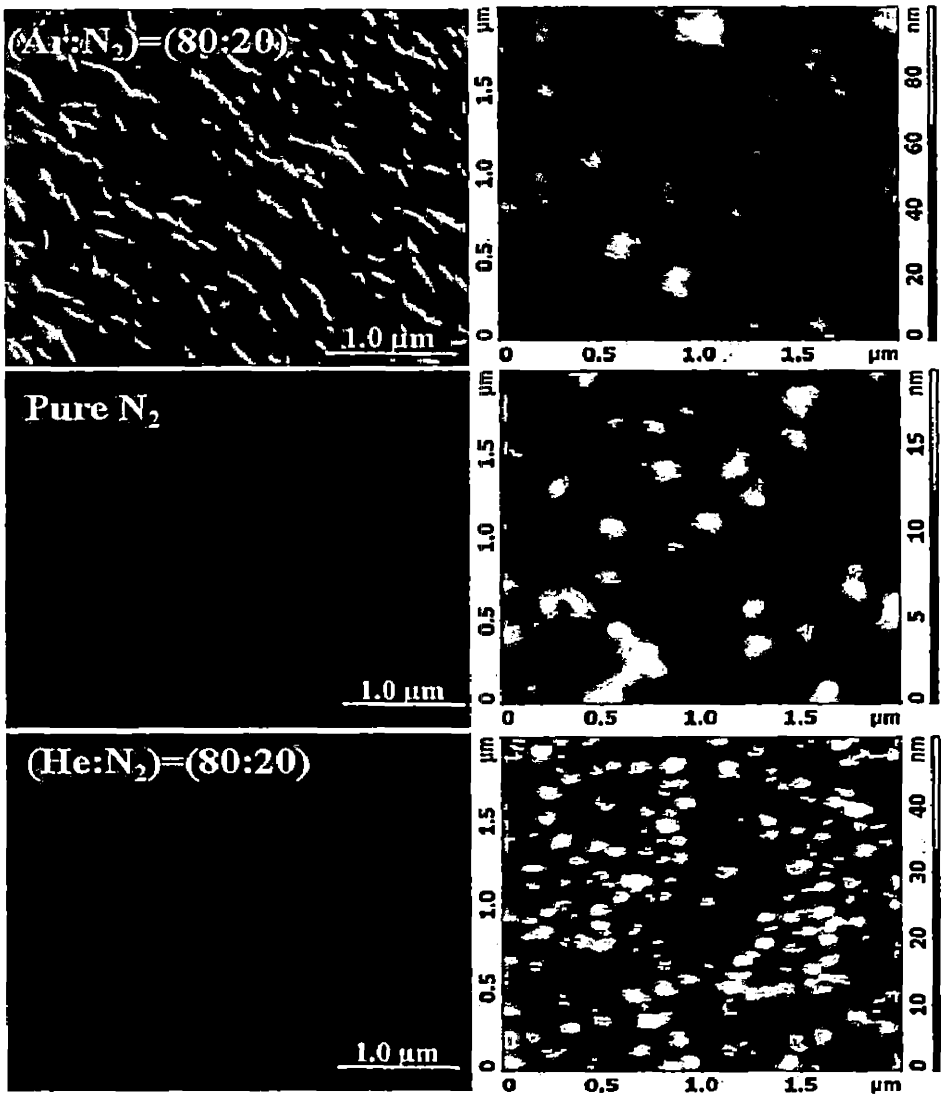

Figure 4.16 Surface topography and morphology of CrN coatings deposited in different gaseous environment.

4.2.3.3 Effect of Substrate Temperature

The CrN coatings deposited in pure N_2 environment at different temperature were analyzed and the influence of substrate temperature on microstructure of the coatings is discussed using structure zone diagram as follows. The columnar structure is observed in CrN coatings when ratio of substrate temperature T_s and its melting temperature Tm, $Ts/Tm \leq 0.3$, with voids in the grain boundaries due to very low mobility of ad-atoms on the surface. The structure has changed when $T_s/T_m \geq 0.3$ due to the changes in plasma state between the target and substrate occurs with the increasing substrate temperature.

At higher substrate temperature, the temperature of the target surface also increases due to thermal radiation. It causes the changes in plasma volume which influence the ion density and electron density. The film thickness has decreased to 1.81 μm, 1.73 μm and 1.55 μm for the substrate temperature 473K, 573K and 673K respectively, during deposition of CrN coatings as shown in **Figure 4.17** and **Figure 4.18**. Also, the coatings density increases with increasing temperature. As explained above, the deposition in pure nitrogen environment leads to low deposition rate owing to nitride mode. The observed lower deposition rate at higher substrate temperature, despite the higher adatom mobility during the nitride mode of deposition, is probably due to more collision between sputtered particle and gas atom, causing less number of atoms to arrive on the substrate.

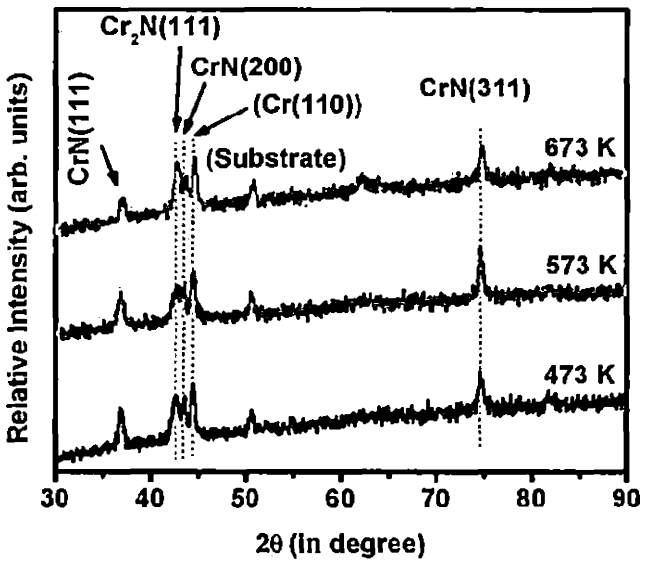

Figure 4.17 XRD spectrum of CrN coatings deposited at different temperature in pure N_2 environment.

4.2.3.4 Mechanical Properties of CrN Coatings

4.2.3.4.1 Microhardness

The hardness of CrN coatings was measured by an optical micro hardness tester (Model: Miniload-II, Mfg: Leitz, Germany). The diamond indenter tip with pyramid shape, its square sides with opposite faces, edges, and face angles are at an angle of 136°, 148°, and 68°, respectively, is used for indenting the samples. VDH (Vicker's diamond hardness) is calculated by using standard equation with the input of indenter load and the actual surface area of the impression. The smallest applied load value was 15 grams with 28 sec loading time. An average of hardness measured on five different points in each CrN/SS sample is shown in **Table 4.7.** The microhardness of magnetron sputtered CrN coatings is dependent on nitrogen content used in the deposition chamber (Han *et al.* 2003). At a low N_2 content up to 30%, dual structure CrN+Cr_2N coatings has formed, which possess a high hardness of 16.95 GPa, which is due to the presence of hexagonal crystal structure and strong covalent bonding in the Cr_2N phase present in the coatings. The lower hardness of CrN coatings as compared to Cr_2N coatings may be due to its higher degree of ionicity of the bonding (Hones *et al.* 1997).

Table 4.7 Effect of N_2 + Ar gas environment on CrN coatings grain size, film thickness and hardness.

% N_2 in the chamber	Grain Size (μm) XRD			Surface Roughness (nm)	Coating Thickness (μm)	Micro-Hardness in GPa
	D_{111}	D_{200}	D_{Ave}			
20 %	14	28	21	13	4.37	9.12
30 %	28	35	32	11	4.15	16.95
40 %	34	14	24	9	3.24	10.5
50 %	17	14	16	14	2.08	9.9

It is found that microhardness of CrN coatings depends on composition, morphology, crystal structure, and its orientation. The growing coating is bombarded by lower density ions and therefore, the ratio of the number of ions to the number of neutral chromium atoms is lower for magnetron sputtering. The formation of ions and release of Cr atoms from the target depends on the current density and deposition rate, respectively, which in turn affect the morphology of the

deposited coatings. Also, during film deposition with varying temperature in the magnetron sputtering under pure N_2 environment, the grain growth becomes inevitable with increasing T_s as it leads to the formation of columnar morphology of the grains in the coatings. The microhardness of CrN coatings decreases due to the grain growth facilitating the formation of columnar grains as observed in the present work. The columnar growth of the coatings is suppressed by using comparatively higher nitrogen content in the chamber, which facilitates re-nucleation kinetics for the formation of fine grains.

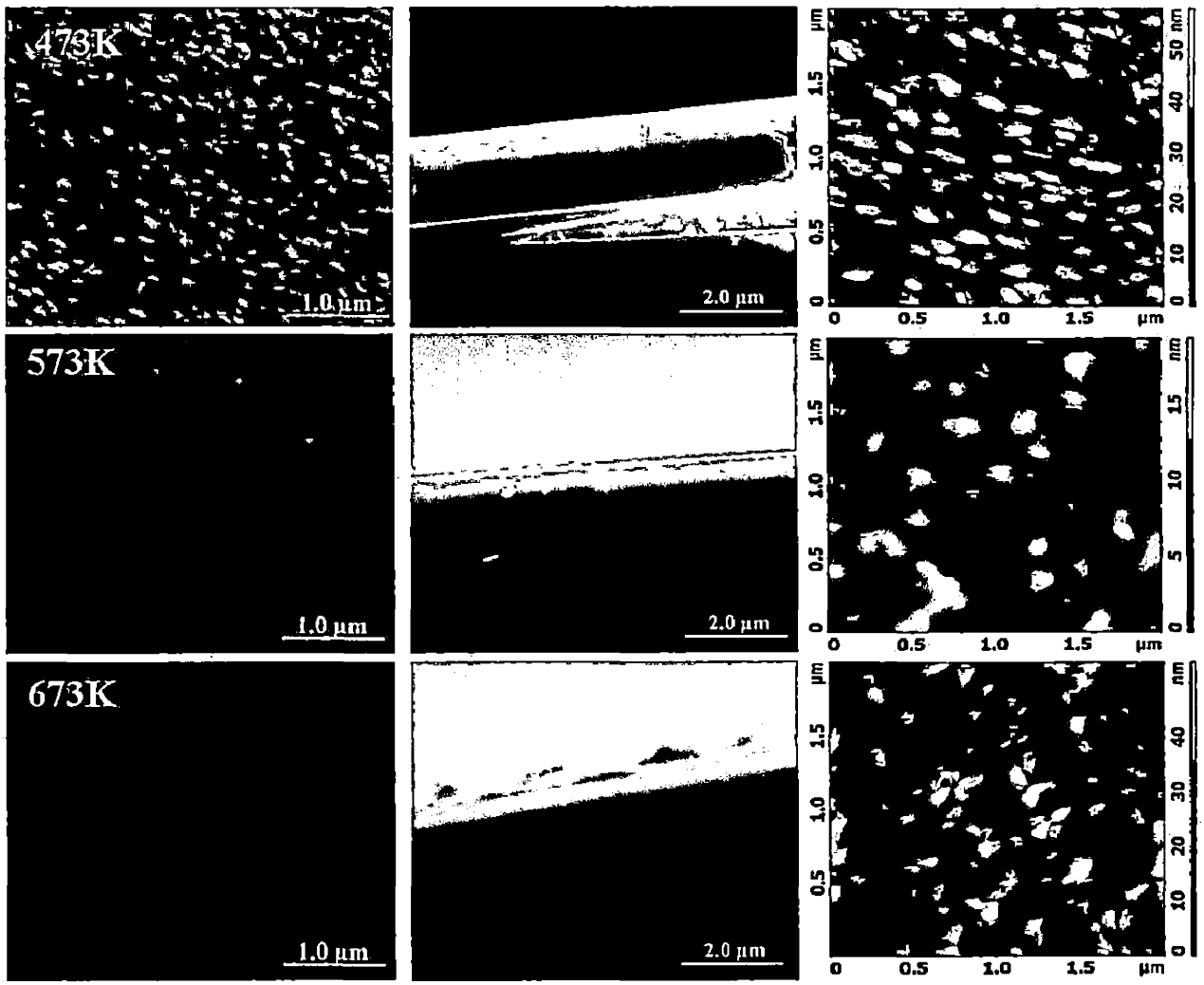

Figure 4.18 Surface topography and morphology of CrN coatings deposited in pure N_2 environment at different temperature.

4.2.3.4.2 Nanoindentation of CrN Coatings Deposited Under Varying Ar+N_2 Atmosphere

The indentations were made on the CrN coated (Grade SA304) substrate samples using a Berkovich diamond indenter. The load was increased and decreased with predetermined rate (30 mN/min) with hold time of 5 seconds at the maximum load applied. The load versus displacement curve was generated for each loading and unloading cycle of the samples. The indentation tests were carried out on load mode with maximum load set to 15mN. For each coatings, a matrix of 4 indentations was performed with a penetration depth lower than $1/10^{th}$ of coatings thickness. The maximum indentation depth found was 225nm, which is 10 times lower than the coatings thickness and varies between approximately 5.0% to 8.1% of the film thickness in the case of coatings deposited under different proportions of Ar:N_2. As mentioned in section 3.3.2.3, the plastic deformation curve is the area between the loading and unloading curves. It is observed from the **Figure 4.19** that the curve 70:30, 60:40 and 50:50 are more "elastic" than sample 80:20, since the ratio of plastic work, sometimes called irreversible work, the total work is smaller for 70:30, 60:40 and 50:50 than for 80:20. Hence, the ratio of hardness over elastic modulus is proportional to the ratio of plastic or irreversible work to total work. The hardness and modulus of CrN coatings are calculated using the load-displacement curve obtained during indentation. The hardness value of bulk CrN is reported to be 11 GPa (Holleck 1986).

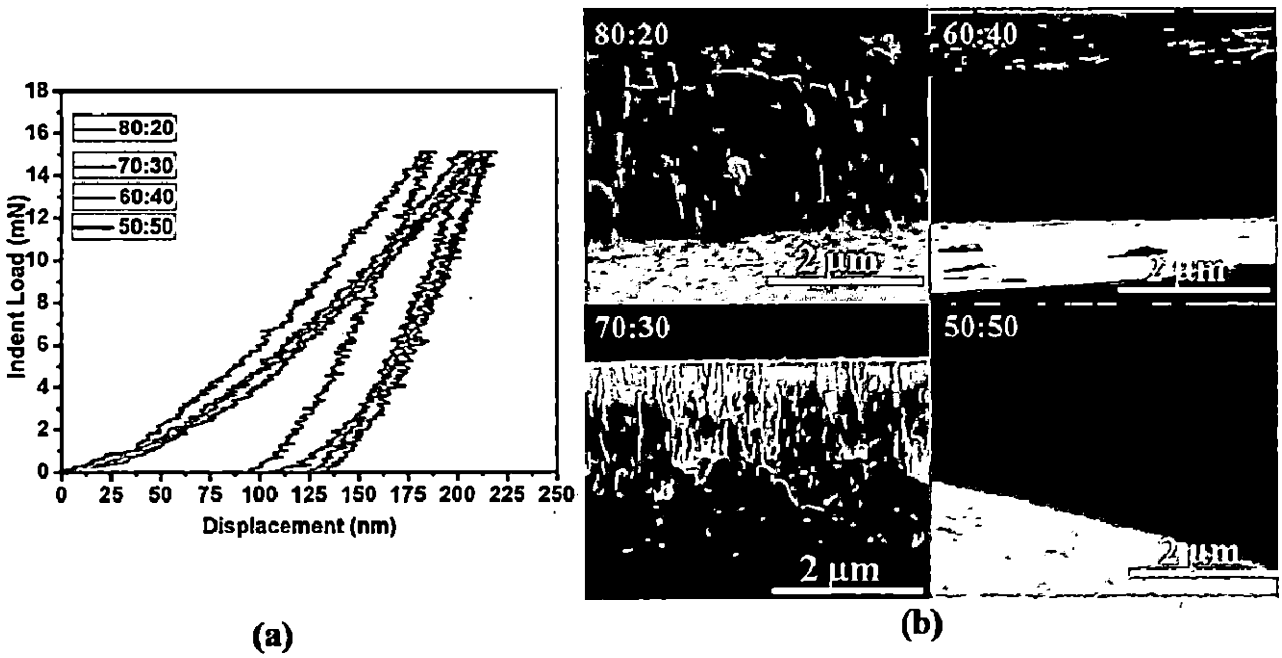

Figure 4.19 a) Load versus displacement curve; b) Cross-sectional SEM images of CrN coatings deposited on SA 304 substrate under different under Ar:N_2 environment.

The maximum and minimum hardness of the CrN coatings was found to be 21 and 15 GPa respectively, while its modulus was found to be maximum of 276 and minimum of 247 GPa. Similar hardness trends (but different values, dependent on the characterisation technique) were reported in our earlier work and by other researchers (Mercs *et al.* 2005, Mercs *et al.* 2007, Hones *et al.* 2003, He *et al.* 2000, Rebholz *et al.* 1999, Shah *et al.* 2010) with increasing nitrogen flows rates for coatings deposited at substrate temperatures around 573K. The high hardness of CrN coatings, 21 GPa, is due to the following reasons. At 60:40 Ar:N_2 content, the mixture of CrN and Cr_2N phase has formed, with the latter showing the hexagonal crystal structure and strong covalent bonding compared to CrN. The hexagonal Cr_2N exhibits a dense crystal arrangement (Hones *et al.* 2003) and hence higher hardness as shown in **Figure 4.19**. It may be also due to relative reduction in surface roughness (RMS) and low coatings defects (porosity), which increase the density of the coatings, as observed in the present work. On the other hand, reduction in grain size leads to increase in hardness value, following the Hall-Petch relation as shown in **Table 4.8**. With further increase in nitrogen, 50:50 argon: nitrogen, the hardness of the coatings has decreased to 15 GPa from 21 GPa due to single phase CrN with its higher degree of ionicity of the bonding as compared to Cr_2N (Hones *et al.* 1997, Hones *et al.* 1998). With the further increase in nitrogen content, 50:50 (Ar:N_2), reduction in hardness occurs despite the reduction in grain size to 15 nm. In addition to the grain size, the surface roughness also affects hardness. However, the hardness decreases to 15 GPa with further increase in nitrogen content from (Ar:N_2) 60:40 to 50:50. It is mainly attributed to the formation of single phase columnar CrN structure.

4.2.3.4.3 Nanoindentation of CrN Coatings Deposited in Pure N_2 with Different Temperature

The CrN coatings deposited on SA304 substrate in pure nitrogen environment with different temperature such as 473K, 573K and 673K. These temperature ranges were chosen for obtaining coatings with zone T microstructures with the improved mechanical properties as reported in the literature (Thornton 1977). The indentation test was carried out in fixed depth mode value set to 125 nm for the CrN samples deposited in pure N_2 with different temperature as shown in **Figure 4.20**.

Table 4.8 Typical Grain size, Thickness and roughness of CrN coatings and influence on hardness and modulus.

Variable	Grain Size (nm)	RMS Roughness (nm)	Coating Thickness (μm)	Nano Hardness (GPa)	Modulus (in GPa)
CrN coatings with varying Ar+N_2 ratio					
80:20	21	13	4.36	14	247
70:30	30	11	4.14	16	273
60:40	24	9	3.23	21	276
50:50	15	8	2.08	15	235
CrN coatings with varying temperature in pure N_2 environment					
473K	15	6	1.81	24	221
573K	16	4	1.73	25	253
673K	16	7	1.54	27	241

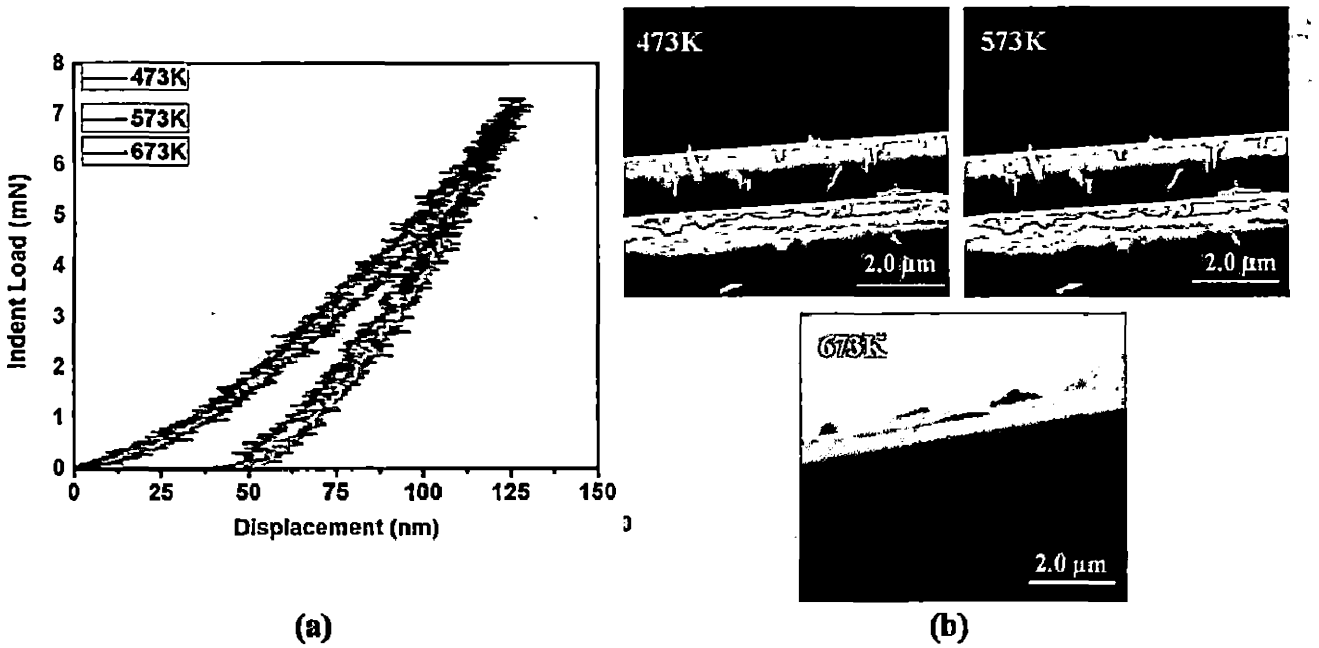

Figure 4.20 a) Load versus displacement curve; b) Cross sectional SEM images for CrN coatings deposited on SA304 substrate in pure N_2 environment with different temperatures.

Hardness of the samples was found to be 24 GPa (minimum) and 27 GPa (maximum), while its modulus values were 221 GPa (minimum) and 241 GPa (maximum). It showed higher hardness and modulus when compared to the CrN coatings deposited under varying $Ar:N_2$ proportions. With increasing nitrogen partial pressure, nitrogen in the solid solution of CrN has increased. Hence, the high microhardness of the coatings can be explained in terms of solid-solution strengthening of the chromium coatings by nitrogen atoms (Rebholz *et al.* 1999). However, the grain size as well as mechanical properties has not changed as function of temperature (**Table 4.8**). The grain size, in this case, is in the lower range (15 nm) as compared to grain size of the coatings observed under different argon:nitrogen ratio (15 nm), which remains constant within a temperature range from 473K to 673K. The factors apart from the grain size such as morphology, coatings density, and surface roughness affect the hardness of coatings as reported in the earlier literature (Sandu *et al.* 2006, Mercs *et al.* 2007, Vaz *et al.* 1998, Vaz *et al.* 2002).

4.2.3.5 Tribological Properties of CrN Coatings

Tribological evaluation of all the CrN coated samples was performed on Pin on Disc (POD) configuration. Tests were conducted in laboratory atmosphere: a temperature of 28±2°C and a relative humidity of 32±5% Rh. Nitride coated pin of 6 X 6 mm^2 were subjected to slide against EN32 counterpart. All the deposited samples were tested at load and velocity of 10 N load and 0.5 m/s, respectively, at room temperature. The total sliding distance was kept constant (2000 m) for the entire test, however the number of laps were different according to distance between pin and disc center, called wear scar radius. The total duration was approximately 66 min for each wear test. Wear test parameters are given in **Table 4.9**. The friction force and weight loss were recorded over regular time interval of 15 minutes during each 2000 m test. Finally, wear rate was calculated from wear scar radius and recorded data. The major chemical compositions and typical mechanical properties of counter material are given in **Table 4.10**. There were no special cleaning methods adopted prior to each test of the sample except cleaning by acetone. The physical shape and dimensions of coated pin is shown in **Figure 4.21**.

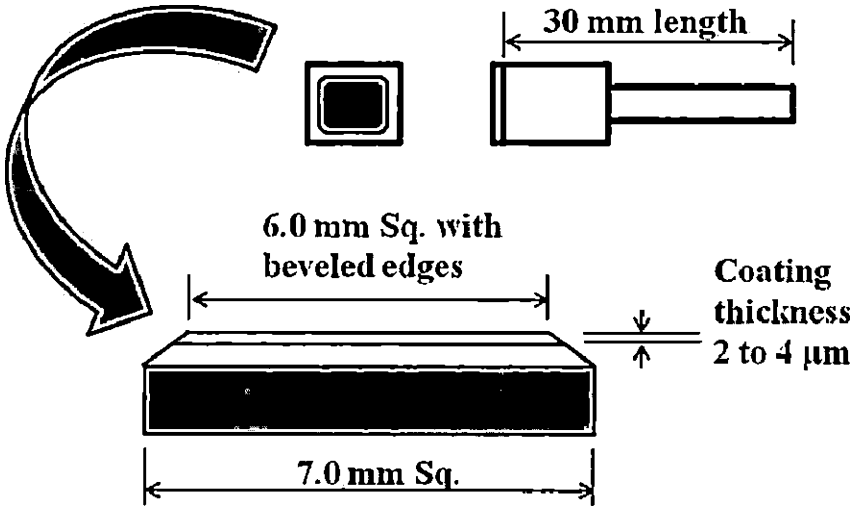

Figure 4.21 Physical shape and dimensions of coated pin prepared for pin on disc test.

When coated pin slides against its counter material with surface roughness of below 100nm. (EN32, 65HRC), the behavior of the material is highly influenced by the differences in hardness between the coated material and its counter material. As can be seen in **Figure 4.22**, the counter material was severely worn by coatings with comparatively high hardness, i.e. the CrN / CrSiN / CrAlN coated stainless steel pin.

Table 4.9 Wear test parameters.

Coatings	CrN, CrSiN and CrAlN coatings
Substrate / Pin material	Stainless steel SA304
Counter Material (Disc)	EN32 (65 HRC)
Normal load applied	10N
Sliding Speed	0.5 m/s
Environment: Room Temperature	28±2°C
Humidity:	32±5% Rh

Table 4.10 Chemical compositions and typical mechanical properties of counter material (EN32).

C%	**Si%**	**Mn%**	**S%**	**P%**
0.36 / 0.44	0.10 / 0.40	0.60 / 1.0	0.050 max.	0.050 max.
Tensile Strength	**Yield Stress**			
600 N/mm^2	340 N/mm^2			

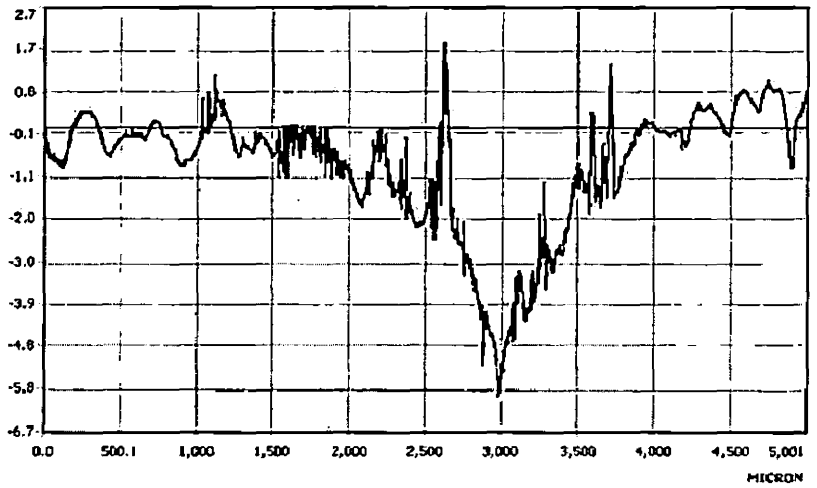

Figure 4.22 The severely worn surface of countermaterial due to the differences in hardness between the coated material and its countermaterial.

4.2.3.5.1 Analysis of CrN Coated Pin Deposited with Different Argon : Nitrogen Content in Fed Gas

The structural analysis of CrN coatings deposited on SA304 substrates are already discussed in Section 4.3.3.1 and the results are summarized in **Table 4.9**. In the present work, the maximum hardness reported was 21 GPa at 60:40 argon : nitrogen proportion. The same coating was characterized by pin on disc tribometer to check influence of nitrogen content in the fed gas on its tribological properties mainly coefficient of friction and wear rate.

During the POD test of CrN coatings, deposited with different argon:nitrogen content in the fed gas (**Figure 4.23**) , initially the friction force was found to be around 4 to 5 N up to 5 minutes, which is purely attributed to the lower surface roughness of coatings as well as a countermaterial, below 10 nm and 100 nm, respectively. Also, it may be due to the perfect surface asperity contact of sample pin with the rotating disc. After 2 to 3 minutes of initial test run, friction force has increased suddenly to a range of 5 - 8 N in the next 5 to 7 minutes following the generation, breaking, and agglomeration of wear particles between pin and disc. Finally, it comes close to a steady-state range around 4.5 to 7.0 N when the friction was governed by the viscous shearing of the coating (Luo, 2010).

The coefficient of friction (COF), μ, has been calculated for the coating materials using **Eq. 3.14. Figure 4.23** shows the friction forces produced during CrN coated pin, deposited with different nitrogen gas flow, tested with the parameters given in **Table 4.9**. The CrN coated pin

with 80:20 argon nitrogen proportions shows the average coefficient of friction of 0.64, while with 70:30 and 60:40, it is found to be 0.68 and 0.63, respectively. The CrN coatings deposited in pure N_2 shows the mean coefficient of friction of 0.64. The SEM analysis of coated pins revealed that an adhesive wear mechanism was promoted in the contact area during the test. In addition to the optical photographs, the EDS carried out on the worn coated pin does not reveal transfer of any coating material. However, few Cr elements were observed in EDS results but the overall percentage is low and it lies between 2 to 4 %, though it is depends on selected area. The sudden increase of the friction coefficient curve after a sliding time indicates a substrate contact with its counter material, which increases the friction force during wear test. The substrate contact is established during test mainly due to: i) the fragmented hard material is entrapped between pin and disc, which enables to increase contact between two sliding part and ii) there may be a possibility of delamination of coatings from the substrate. The friction coefficient was observed to be in the range of 0.634-0.683, which is lower than that of it reported in the literature (Zhang et. al 2007). The coefficient of friction and wear loss of respective samples are summarized in **Table 4.11**.

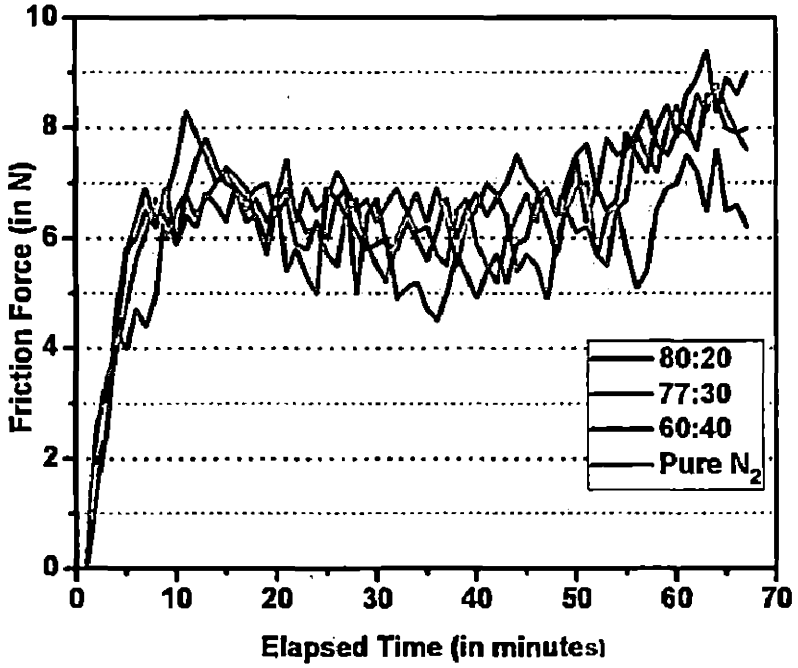

Figure 4.23 Friction force produced during CrN coated pin slides against its counter material disc of steel (with 10N normal force).

Table 4.11 Influence of Nitrogen content on coefficient of friction and wear loss of CrN coatings studied using POD method (Test parameters: 10N, 0.5m/s, 28°C).

Sample	Nitrogen gas flow (%) in fed gas	COF (With counter material used EN32)	Wear loss of coating $K*10^{-4}$ (mm^3/ Nm)
SS28	20%	0.64	8.95
SS29	30%	0.68	5.65
SS30	40%	0.63	2.45
SS31	100%	0.64	1.40

The wear volume calculated using 2D surface profiles of the worn surface was measured using a stylus profilometer. The measured wear rate is 8.95 X 10^{-4} mm^3/Nm at 20% nitrogen gas flow in fed gas, which is reduce to 1.40 X 10^{-4} mm^3/Nm with increase in nitrogen gas flow in the fed gas as shown in Table 4.11. It is apparent that SS30 (60:40 Ar:N_2) and SS31 (100% N_2) are the most wear resistant of the CrN coatings in this study **(Table 4.11)**.

Wear debris; in general, are composed of the particles spalling from the pin, a stationary part considered as a upper part, and the disc, a dynamically active part having specific sliding velocity considered as a lower specimen during the wear process. In order to understand the correlation between wear debris and wear rate of the specimens, the constituents of the debris were determined. The mean particle size is naturally related to operating conditions. In the present study, the load applied to wear tests was kept constant at 10 N. The micrographs of wear debris reveal that the mean particle size produced at different chemical composition cannot be used as the standard of evaluating specimen's wear rate due to the similar behavior observed in CrN and subsequent CrSiN and CrAlN coatings (discussed in Chapter 5 and 6, respectively). The constituents of the wear debris generated at the sliding speed of 0.5 m/s are mostly composed of iron and ironic oxides as well as a small amount of hard coatings i.e CrN or Cr particles, as shown in **Figure 4.24**.

During wear test, the transferred materials from the counter material get compacted and mechanically mixed with the coating material. Subsequently the mixture of debris has formed a layer and stick to the coated surface as shown in **Figure 4.24**, which contribute to the reduction in wear (Yang et. al 2008). Due to the localized high temperature caused by friction during dry sliding, the surface layer also reacted with oxygen in the ambient room atmosphere and formed oxides. This tribo-oxidation plays an important role in controlling friction between the sliding pin

and disc surface, therefore affecting the wear behavior of the coatings. Usually, a relatively rough surface causes a higher contact pressure (as number of contact asperities are low) resulting larger tangential stress, and leading to more wear loss by grain pullouts and fragmentations. Formation of rather softer phase increases the contact area which in-turn reduces the frictional contact stress. This reduces the tendency of fracture wear and hence low wear loss **(Dey and Biswas, 2009).**

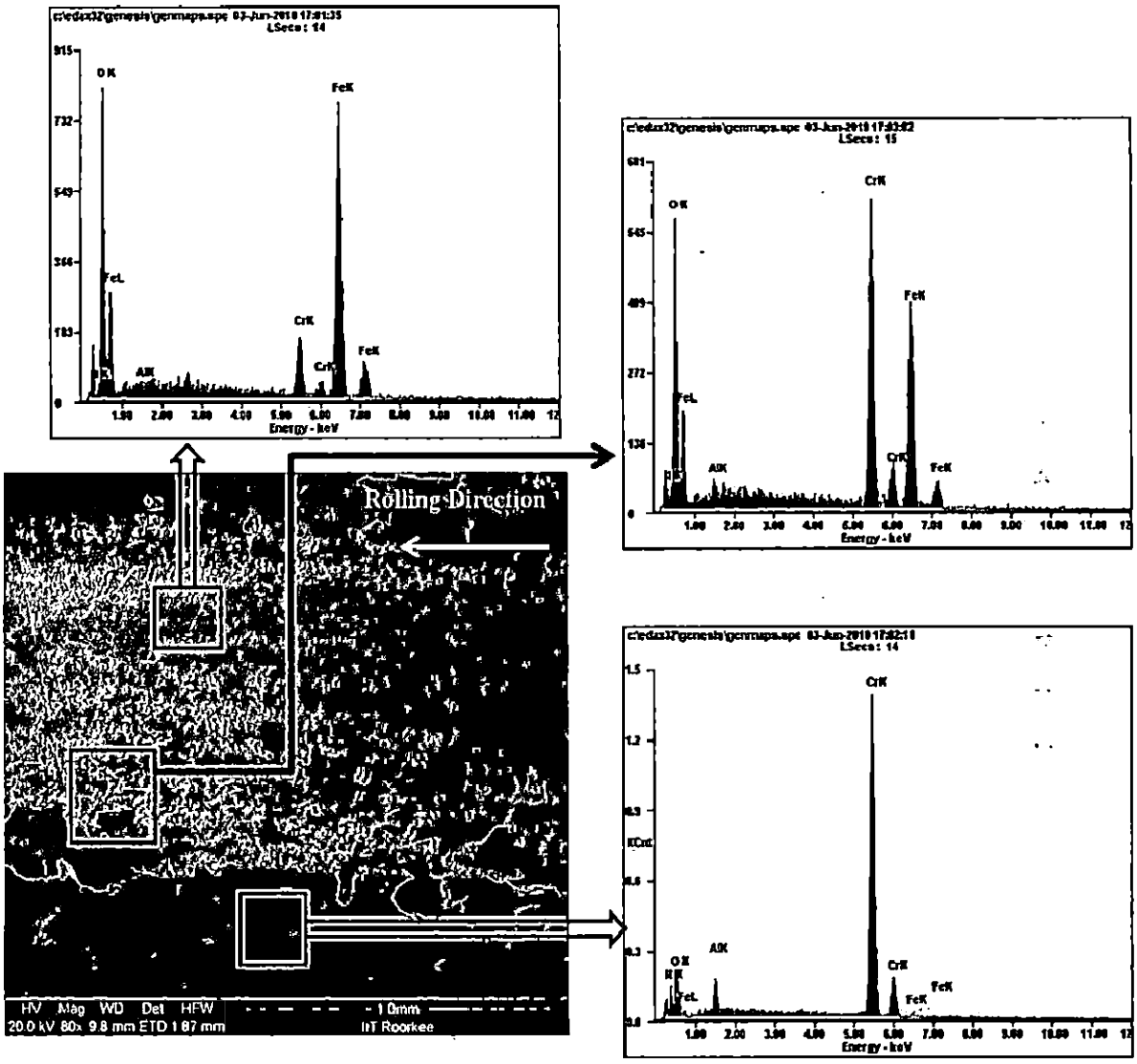

Figure 4.24 SEM morphologies of wear track and composition analysis (EDS) of wear debris after POD test of CrN ($Ar:N_2 = 80:20$) coatings.

4.3.4 Conclusion

The CrN coatings have been deposited on SA304 substrates by using reactive magnetron sputtering in the present work. The influence of substrate temperature and varying contents of N_2 and Ar gases on the morphological and microhardness of the CrN coatings were investigated by using XRD, SEM, AFM and microhardness tester, respectively. The grain size of CrN coatings is decreasing with increase in nitrogen content in the sputtering chamber. The coatings become denser at higher nitrogen percentage in the gas mixture. The surface roughness of CrN coatings decreases with increasing nitrogen content and substrate temperature. The coatings deposited in ($He+N_2$) atmosphere lead to lower coatings thickness and grain size as compared to coatings deposited in $Ar+N_2$ atmosphere. It may be due to lower sputtering yield of helium ions than argon ions. A mixture of different gases affects the surface morphology, grain size and microhardness of CrN coatings as observed in the present work. A mixture of CrN + Cr_2N phase has formed up to 30% nitrogen content in the chamber while at very high N_2 content, there is a phase change and single phase CrN coatings is observed. The hardness value of CrN +Cr_2N (at 30% N_2 content in the chamber) phase is higher than the CrN (above 40% N_2 content) phase. The hardness and modulus of the coatings were influenced by the factors such as grain size, grain morphology, film defects, density, and surface roughness of the coatings. The CrN coatings deposited, at 60:40 $Ar:N_2$ content, showed the high hardness value of 21 GPa, which is attributed mainly to the mixture of Cr_2N and CrN phase present in the coatings in which Cr_2N phase is more pronounced having hexagonal structure. The enhancement in hardness may also be due to reduction in surface roughness (RMS) and low film defects (porosity), which increase density of the coatings. The CrN coatings deposited in pure N_2 exhibits a high hardness (27 GPa) and modulus (253 GPa) as compared to that of the coatings deposited in $Ar:N_2$ environment, mainly due to fine grain size (≈15nm) and low roughness.

The tribological properties, coefficient of friction, and wear rate of CrN coatings were tested using POD tribometer and COF was found to be in the range of 0.63 -0.68. The coatings deposited in pure N_2 environment show comparatively lower COF (0.64) than CrN coatings deposited under different $Ar:N_2$ proportions (0.68). The wear rate of CrN coatings deposited in pure N_2 atmosphere was found to be $1.40x10^{-4}$ mm^3/Nm, which is comparatively lower than the coatings deposited in different argon : nitrogen proportion. The SEM analysis of coated pins revealed that an adhesive wear mechanism was promoted in the contact area during the test. During wear test, the transferred materials from the counter material get compacted and

mechanically mixed with the coating material. Subsequently, the mixture of debris has formed layers, which stick to the coated surface contributing to the reduction in wear.

4.3.5 Comparison of Present work with the Existing Literature

From Section 2.2.1 and **Table 2.2** in Chapter 2, it is clear that the mechanical and tribological properties are influenced by the microstructure and orientation of the grains, which depends on the process parameters used during deposition of coatings by sputtering techniques. For CrN coating, the hardness is found to be varying from 13 GPa to 25 GPa (irrespective of above cited factors), very few research groups have reported hardness values above 23 GPa i.e 31 GPa (He *et al.* 2000), 38.4 GPa (Mayrhofer *et al.* 2001), 30 GPa (Essen *et al.* 2006), 26-27 GPa (Mercs *et al.* 2007), 26 GPa (Lin *et al.* 2010) for the coatings deposited by using magnetron sputtering. In the present work, the CrN coatings were deposited using simple DC magnetron sputtering with different argon:nitrogen gas proportions and in pure nitrogen environment without using biasing, during deposition, and keeping all parameter under precise controls. The hardness of CrN coating deposited with different argon:nitrogen environment was 21 GPa while the CrN coatings deposited in pure nitrogen environment was 27 GPa. The achieved hardness is in good agreement with the literature and moderately at the higher level. The higher hardness leads to improvement in tribological properties, which can be exploited for industrial applications.

CHAPTER 5

CHROMIUM SILICON NITRIDE (CrSiN) COATINGS

5.0 Synthesis and Characterization of CrSiN Coatings on Si(100) and Stainless Steel Substrates by Reactive Magnetron Sputtering

Deposition of CrSiN coatings on Si(100) and Stainless steel (SA 304) substrates by reactive magnetron sputtering, their microstructural characteristics, and mechanical properties are discussed in this Chapter. The effect of Si content on structural, mechanical, and tribological properties of CrN coatings is discussed in Section 5.1. The influence of process parameters such as power density, substrate temperature, working pressure, deposition time, and gas proportion on microstructural and mechanical properties of CrSiN coatings has been investigated and discussed in section 5.2

5.1 Influence of Silicon Content on the Microstructure, Mechanical, and Tribological Properties of CrN coatings Deposited by Reactive Magnetron Sputtering

5.1.1 Introduction

Hard protective coatings for tribological applications include CrN, TiN, TiAlN, CrSiN, TiC, carbonitrides, and borides synthesized by a variety of techniques such as high-temperature chemical vapor deposition (CVD), low-temperature reactive sputtering (PVD), activated reactive evaporation, and plasma CVD (Holleck *et al.* 1986, Mtlnz *et al.* 1986). In the recent years, various efforts have been made to improve the mechanical, tribological, and oxidation resistance of transition metal nitrides for their industrial applications such as machining, wear resistance, forming, and casting (Lee *et al.* 2006). Nitrides based coatings such as TiN, CrN, and WN are used extensively in microelectronics and coating industries due to their superior chemical stability, excellent strength, wear, and corrosion resistance. The CrN coatings deposited by reactive magnetron sputtering, exhibit good mechanical properties such as high micro hardness and low thermal conductivity, good wear and corrosion resistance as reported in the literature (Safi *et al.* 2000, Tillmann *et al.* 2007). The preferred orientations of the CrN coatings depend on sputtering

conditions, thickness of the coatings, and the induced microstrain in the coatings (Shah *et al.* 2009).

An addition of third element such as Si and/or Al into the CrN binary compound has shown promising nanocomposite properties such as ultrahigh hardness and high temperature oxidation resistance. Hardness of these nanocomposite coatings are improved due to presence of an amorphous phase (Si_3N_4) at the grain boundary. M. Benkahoul (2008) deposited CrSiN coatings by pulsed DC reactive dual magnetron sputtering and reported that the increasing Si content does not affect the grain size, but it leads to solid solution hardening. Lee *et al.* (2007) studied the microstructures and mechanical properties of CrSiN coatings deposited by pulsed DC reactive magnetron sputtering and observed that the surface roughness, hardness, and friction coefficient of CrSiN coatings decrease with increasing Si contents. Mercs *et al.* (2005) deposited CrN and CrSiN coatings with different nitrogen flow rates, 6 and 10 sccm, for a constant argon flow rate of 20 sccm and found that increase of silicon content up to 2.5 at.% into the coating leads to a maximum hardness (*H*) (24.5 GPa) and a low Young's modulus (*E*) (298 GPa). A further increase of the Si content leads to the decrease of H and E in both cases. It was reported in their further work (Mercs *et al.* 2007) that when the CrN and CrSiN film produced with at.% Si $\leq$ 0.92, in Ar/N_2 mixture atmosphere, the formation of amorphous silicon nitride phase has occurred at the grain boundaries of CrN. Martinez *et al.* (2004) investigated the electrical, optical and mechanical properties of reactive magnetron sputtered CrN and CrSiN coatings as a function of N and Si contents and observed that the hardness of CrN coatings is influenced by the film morphology. The nanohardness values of (111) and (200) CrN are typically between 12–18 GPa. An addition of small amounts of Si increases the hardness values up to 22 GPa for CrSiN as reported in their work. A detailed investigation on the influence of process parameters, in the reactive magnetron sputtering technique, on the microstructural characteristics and mechanical properties of CrSiN coatings is limited in the literature. Therefore, the microstructural characteristics and hardness of CrN and CrSiN coatings deposited, under different process conditions, by using DC- reactive magnetron sputtering were investigated in the present work. The techniques such as XRD, FE-SEM/EDS, and AFM were used to characterize CrN and CrSiN coatings. Microhardness and tribological properties of the coatings were measured by using optical microhardness tester and pin on disc, respectively.

5.1.2 Experimental Details

5.1.2.1 Deposition of Coatings

CrN and CrSiN coatings were deposited on Stainless Steel (Grade: SA304) and Silicon (100) substrates using spherical sputtering chamber equipped with Baratron capacitance manometer and vacuum gauge, mounted horizontally on the table. The coatings were deposited under Ar/N_2 gas atmosphere in the deposition chamber. Prior to deposition, all the SA304 steel substrates were manually polished using Fe_2O_3, ultrasonically cleaned in acetone for 10 min while Si wafers were HF treated, cleaned in acetone and both placed in the chamber until a minimum pressure of $5X10^{-3}$ Pa was reached. The two targets of pure Cr and Si (50 mm diameter) fixed at 25° apart were mounted in deposition chamber. The substrates were fixed on substrate holder which moves in such a way that it covers an entire region of plasma created from both the targets. The depositions were carried out with varying Si contents and working pressure. The Si content in the coatings were controlled by input RF power between 50 to 125 W, while maintaining Cr target with constant DC power (175W). The other parameters were kept constant and summarized in **Table 5.1**. The working pressure was varied between 1.33 to 3.99 Pa. The ratio of Ar/N_2 gas mixture was 1:1 during deposition and corresponding flow rate of Ar and N_2 (set equal in both the gas) was 6, 12, 15 and 18 sccm for 1.33, 2.66, 3.33 and 3.99 Pa working pressure, respectively. Before co-sputtering of CrSiN, a layer of Cr (for 5 min. in Ar atmosphere) was deposited on the substrates to improve adhesion properties of the coatings.

Table 5.1 Typical deposition conditions of CrSiN coatings deposited on Si(100) and SA304 Substrates.

Sr. No	Process parameters and their corresponding values	
1	Base Pressure	$\leq 5 \times 10^{-6}$ Torr ($\leq 5 \times 10^{-4}$ Pa)
2	Working Pressure	10 mTorr (1.33 Pa)
3	Target to Substrate distance	50 mm
4	Power	175 W DC/ 50-125 W RF
5	Substrate Temperature	573 K
6	Deposition Time	60 min
7	Gas Mixture	$Ar+N_2$
8	Gas Mixture ratio	50:50

5.1.2.2 Characterization of Coatings

The structure of CrN and CrSiN coatings was determined by a D8 X-ray diffractometer with Bragg–Brentano geometry using CuKα (λ = 0.15418 nm) radiation. The basic structural properties of coatings in the as deposited condition were determined in the range of 30° to 90° to find out possible changes in the texture orientation. The average grain size is calculated according to the Scherrer's formula (Cullity *et al.* 1978). Atomic Force Microscope (AFM) was used to measure the surface topography and roughness of the coatings. The microstructures of CrN and CrSiN coatings were characterized by Field Emission Scanning Electron Microscopy (FE-SEM, FEI Quanta 200F). Energy dispersive X-ray (EDX) analyses have also been performed with the SEM to acquire composition of deposited coatings.

The mechanical properties of CrSiN coatings are influenced by their structural, morphological, and chemical changes as evident from XRD, FE-SEM, and AFM results. The mechanical characterization was carried out by microhardness tester using Vickers diamond tip and nanoindentation technique using Berkovich diamond indenter tip (CSM+ NHT, Switzerland). For microhardness testing of CrSiN coatings, the applied load value was 15 grams with 27 sec loading time. The indentation was made on five different points in each CrSiN/SA304 sample to obtain its average hardness value. Also, in the present work, coatings were characterized by using a computer-controlled nanoindentation test with calibrated indenter. Nano hardness testing has been performed on the coatings, using a load of 25 mN, with loading – unloading rate set to 10 mn/min and 5 seconds hold time to substantiate the influence of Si concentration on hardness of the coatings. During test, the parameters like time, applied indent load (P_{max}), and corresponding penetration depth (h_{max}) were recorded with a personal computer. The load was increased and decreased with predetermined rate, depending upon selection of load mode, with hold time of 5 seconds at maximum load. Load versus displacement curve was generated during the indentation tests. The wear properties of CrSiN coatings were evaluated using pin on disc tribo-tester.

5.1.3 Results and Discussion

5.1.3.1 Microstructural Analysis of CrSiN Coatings Deposited on Si(100) and SA 304 Substrates

XRD peaks of CrN and CrSiN coatings deposited on the SS-304 and Si (100) substrate in Ar+N_2 atmospheres at 573 K are shown in **Figure 5.1**. The chromium nitride coatings deposited

without silicon content is highly crystalline and showed a higher grain size as compared to that of the coatings with Si addition. The peak has deflected towards higher angle, due to preferred orientation, than the standard diffraction angle as shown in **Figure 5.1**.

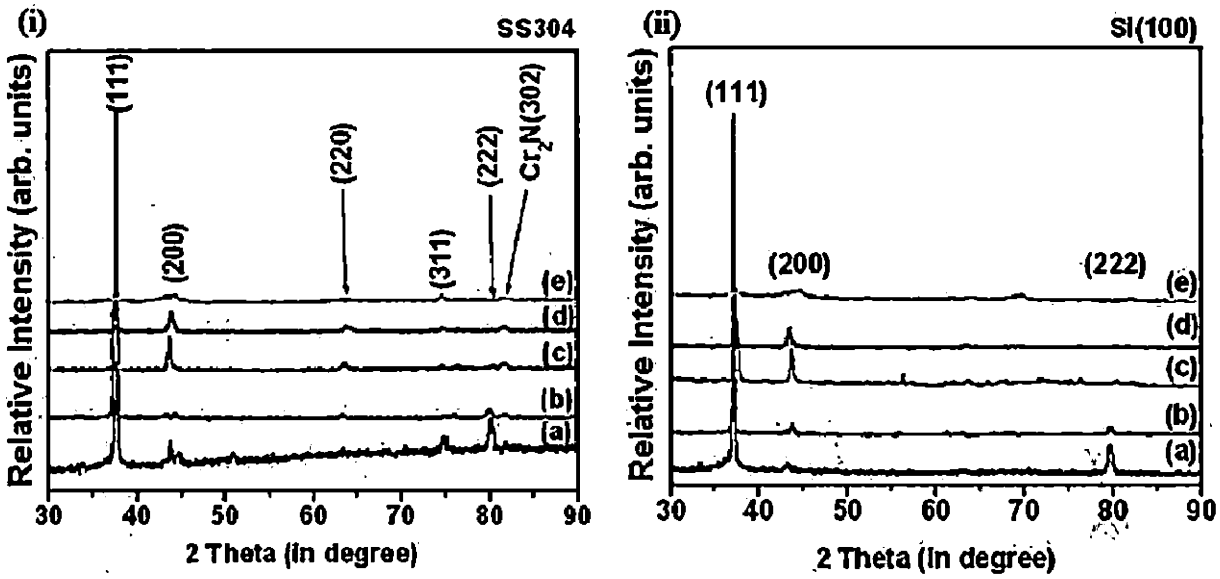

Figure 5.1 XRD pattern of CrN and CrSiN coatings on i) SS304 and ii) Si(100) substrates, as a function of Si content: a) without Si b) with Si: 2.67 at.%, c) 6.33 at.%, d) 14.88 at.%, and e) 18.65 at %.

A small amount of silicon addition (2.67 at.%) leads to a strong reduction in grain size of the coatings as shown in **Table 5.2.** Also, the reduction of grain size indicates amorphization of the coatings associated with an increase of the CrN lattice parameter to 4.1682 Å. With further increase in Si content, a reduction in lattice parameters occurs due to the migration of N from CrN, at the grain boundaries to form an amorphous silicon nitride (SiN_x) compound (Mercs *et al.* 2007, Mercs *et al.* 2005). It is evident from the **Figure 5.1** that the intensity of a dominating peak (111) is decreasing, from (a) to (e), with increase in Si content but (200) intensity is increasing up to 6.33 at.% Si, during deposition on both SS 304 and Si(100) substrates. In addition, a peak broadening occurs, indicating a reduction in particle size. A further increase in Si (up to 14.88 at.% Si) content reduces the peak intensity of (200) orientation with broadening. Finally, all the peaks are suppressed at very high Si content (at 18.65 at.% Si), crystallinity is almost negligible, indicating an amorphous structure due to formation of SiN phase. There is no evidence of crystalline peaks of $Si_{1-x}N_x$ (silicides) in the XRD patterns of SS304 as well as Si(100) substrates, as reported in the

literature (Mercs *et al.* 2005, Martinez *et al.* 2004, Kim *et al.* 2006, Park *et al.* 2004, Thobor-Keck *et al.* 2005). It may be due to the nitrogen atom reacting with Si and form an amorphous SiN, which moves to grain boundaries (Castaldi et *al.* 2007). The segregation of silicon nitride at grain boundaries is due to sufficient substrate temperature T_s, which is reducing the atom to atom bonding strength (Veprek *et al.* 1996). The precise analysis of XRD spectrum shows that the (220) and (311) orientation is almost negligible in the coatings deposited on Si(100) substrate, while in the case of SS304 substrates, the (220) and (311) orientation is increasing and decreasing respectively, with increase in Si content.

The values of full width at half maximum (FWHM) of the most dominating XRD peaks (111) and (200) were used to calculate the grain size (D_{111} and D_{200}). The average values of the grain size (D) and thickness of coatings deposited on stainless steel and Si are summarized in **Table 5.2.** It is observed that the reduction in crystallite size occurs due to grain refinement with increase in Si content in the coatings. XRD analysis of the CrSiN coatings indicated that preferred (111) orientation decreases with increasing Si content. Parallely, a peak broadening occurs with an increase in the Si content, leading to the reduction in grain size. The grain size of the CrSiN coatings was 38 nm (Si: 2.67 at.%), which has decreased to 18 nm for the coatings with 18.65 at.% Si. The reduction of the average grain size (D_{ave}) with the Si content, shown in **Figure 5.2**, is due to the segregation of the Si_3N_4 phase, at regular time interval, at the CrN grain boundaries.

Table 5.2 Influence of R.F power on grain size, thickness and hardness of CrSiN coatings deposited on SA304 substrate.

Si target Power (in W)	*Si* Content (in at.%)	*d* Spacing	*D* Average (nm)	CrSiN Thickness (μm)	Hardness (GPa)
0	Nil	2.0804	41	--	18.39
50	2.67	2.0841	38	3.71	23.92
75	6.33	2.0716	31	3.31	25.70
100	14.88	2.0611	20	4.13	18.96
125	18.65	2.0782	18	3.59	16.95

The surface morphology of coatings was obtained using an atomic force microscopy operated under tapping mode. The root mean square (RMS) roughness and average roughness of the coatings were derived from images of 1024 X 768 pixels. All images were taken from 2 μm^2 regions with scanning frequency of 1.5 Hz. **Table 5.3** shows the influence of R.F power on surface roughness of CrSiN coatings. The surface roughness is decreasing regularly in the deposited coatings (on both the SS304 and Si(100) substrates) with increasing RF power to the Si target. The thickness of the deposited coatings was measured by means of cross sectional SEM, and found that it varied between 3.31 and 4.13μm. It has been reported in the literature (Martinez et *al.* 2004) that during reactive magnetron deposition of CrSiN coatings, silicon atoms substitute chromium atoms in the CrN lattice and form (Cr,Si)N coatings with a corresponding decrease in its lattice parameter.

The surface morphology of CrSiN coatings deposited at different RF power applied to Si target was studied by field emission scanning electron microscopy and atomic force microscopy. All the coatings were deposited at equal proportion of Ar and N_2 gas with varying flow rate. The FESEM and AFM images of the coatings are shown in **Figure 5.2.** Cross-sectional FESEM of CrN and CrSiN coatings without Si content (**Figure 5.2 I**) and with Si content of 2.67, 6.33, 14.88 and 18.65 at % (**Figure 5.2 II, III, IV & V**), showed a highly columnar morphology and become denser and smooth microstructure with increasing Si content. The surface morphology of the CrN and CrSiN coatings with varying Si contents, obtained using AFM is shown in **Figure 5.2 (I-c to V-c).** It is evident that the coatings become smooth and denser with increasing Si contents as observed in FEM images. It may be mentioned that the addition of relatively higher contents of silicon (14.88 at.%) in the coatings, during sputtering, modifies the triangular needle-shaped columnar morphology into a finer columnar one. It may be attributed to the segregation of the higher fraction of amorphous SiN_x phase at the grain boundaries during the film growth. The influence of Si content on the particle size and surface roughness of the coatings is given in **Table 5.3.**

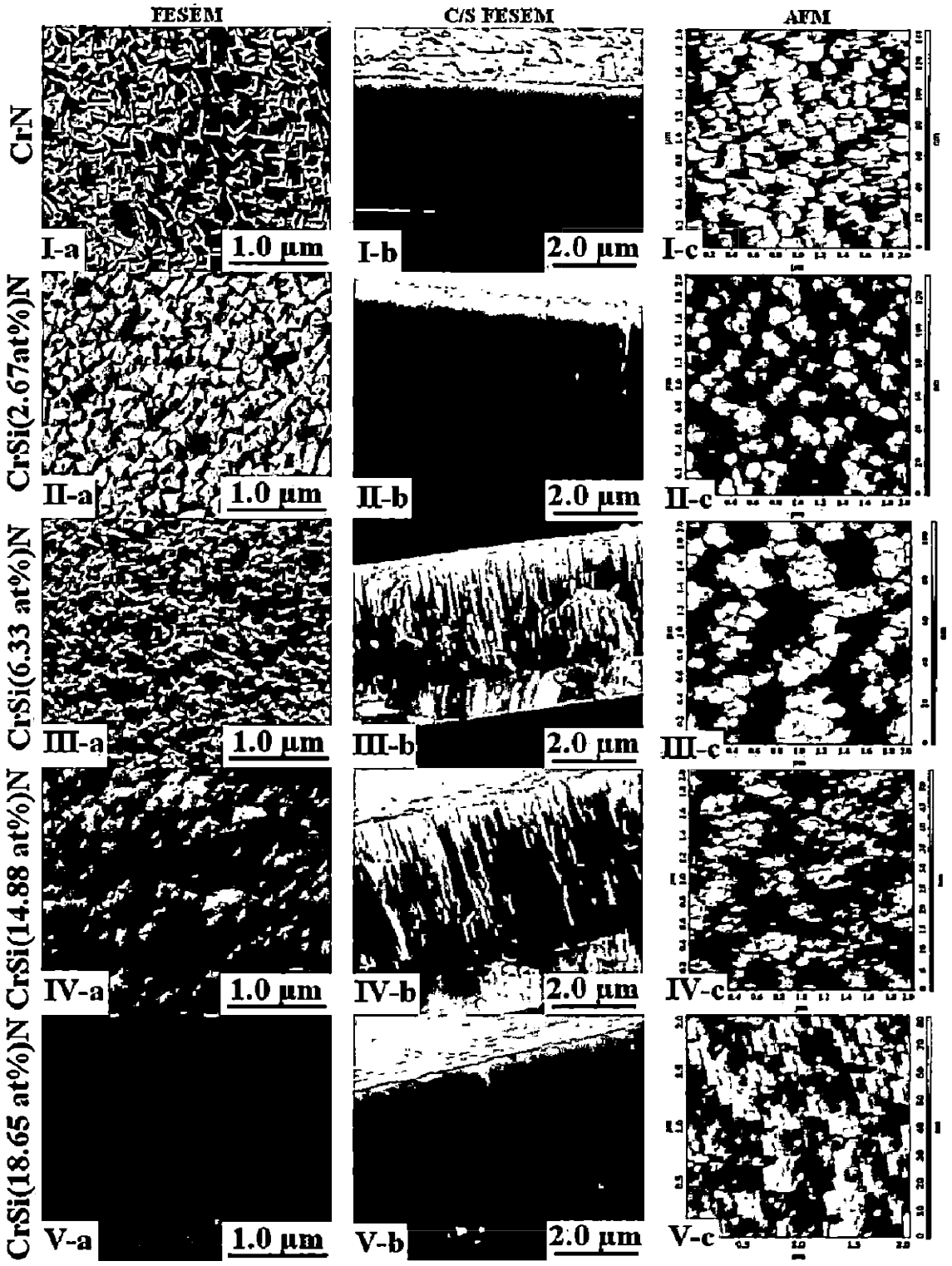

Figure 5.2 a) FESEM, b) Cross Section FESEM and c) AFM images of CrN and CrSiN coatings on SA304 deposited at 10mTorr: i) CrN coating without Si content, ii) CrSiN coating with Cr interlayer and Si content (Si: 2.67 at.%), iii) CrSiN coating with Cr interlayer and higher Si content (Si: 6.33 at.%), iv) CrSiN coating with Cr interlayer and higher Si content (Si: 14.88 at.%), v) CrSiN coating with Cr interlayer and higher Si content (Si: 18.65 at.%).

Table 5.3 Influence of R.F power on surface roughness of CrSiN Coatings on SA304 substrate.

Si Power (W)	*Si* Content (at.%)	*D* Average (nm)	Surface Roughness (nm)	
			Average	RMS
0	Nil	41	16	20
50	2.67	38	24	30
75	6.33	31	15	19
100	14.88	20	14	17
125	18.65	18	7	6

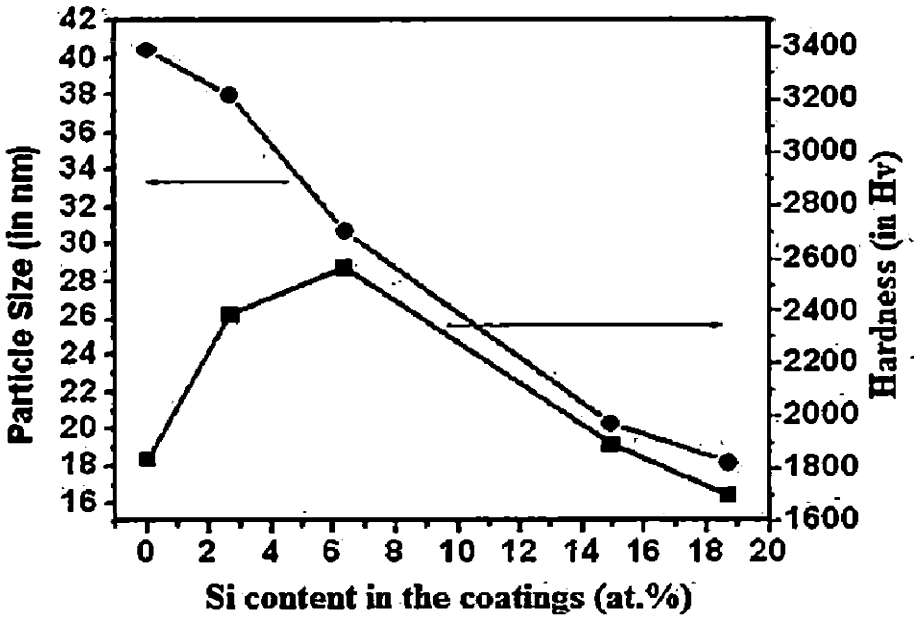

Figure 5.3 Influence of Si content on particle size and microhardness of CrSiN coatings.

5.1.3.2 Mechanical Properties of CrSiN Coatings Deposited on SA304 Substrate

The Vickers indentation tip was used to measure hardness of CrSiN coatings using an optical micro hardness tester. The indenter tip is made up of diamond with pyramid shape. VDH (Vicker's diamond hardness) is calculated using Eq. 3.9 with an input of the indenter load and the actual surface area of the impression.

The microhardness of CrSiN coatings as a function of Si content is shown in **Figure 5.3**. It is observed from this figure that the hardness value increases from 18.39 GPa, for CrN coatings, to

23.92 GPa for the deposited CrSiN coatings with 2.67 at.% silicon. The hardness value increases further to 25.70 GPa for CrSiN with 6.33 at.% silicon and then decreases to 18.96 GPa for the coatings with 14.88 at.% silicon. The Si content up to 6.33 at.% in the CrSiN coatings leads to a significant grain refinement and results in substantial improvement in hardness of the coatings. The increase in hardness of CrSiN coatings is due to very fine composite microstructure consisting of fine grained CrN phase and amorphous SiN phase. The reduction in hardness with further increase of Si content (from 6.33 at.% to 14.88 at.%), may be due to the high volume fraction of amorphous Si_3N_4 phase as reported in the literature (Veprek *et al.* 1995).

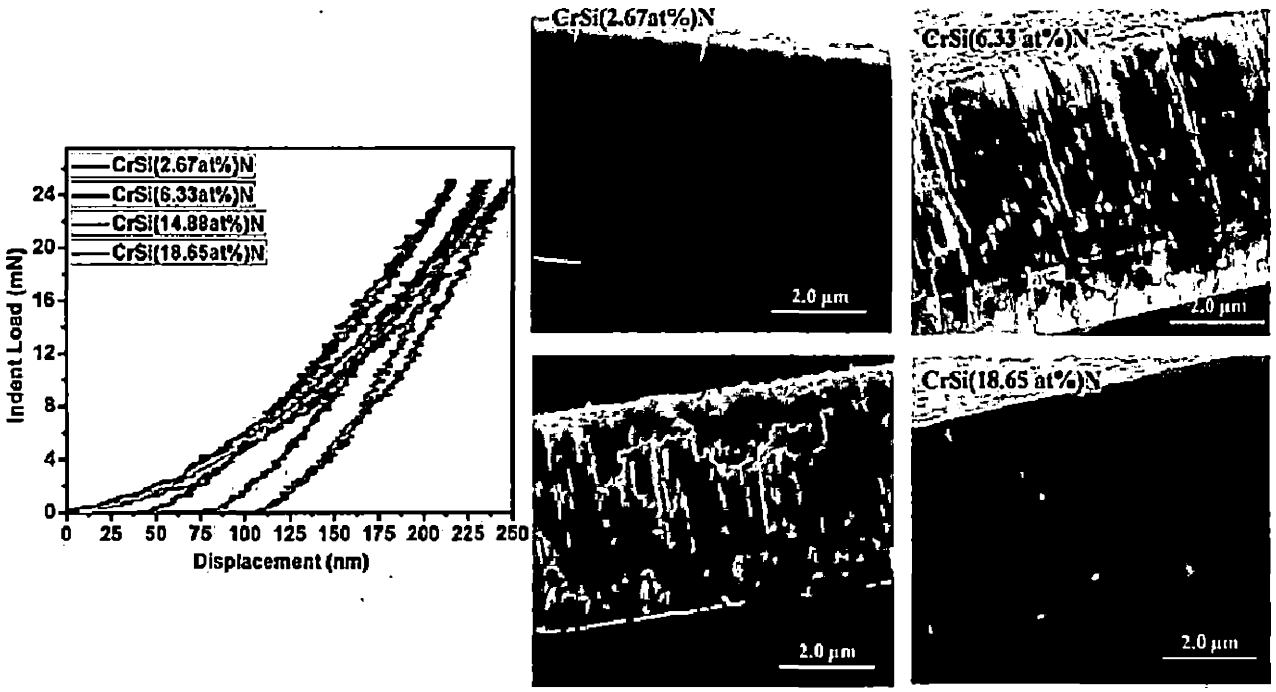

Figure 5.4 a) Load versus displacement curve b) Cross sectional SEM images of CrSiN coatings deposited on SA304 substrate in $Ar+N_2$ environment with different Si concentration.

The indentations were made on the coated SA304 samples, using a Berkovich diamond indenter, to a maximum indentation depth of 250 nm, which is less than $1/10^{th}$ of coatings thickness to avoid substrate effect. The minimum thickness of coatings was 4.61 µm in all the samples as shown in **Table 5.4**. The maximum and minimum hardness of the coatings was found to be 28 and 21 GPa, respectively. The coatings showed a modulus value of 278 GPa (max) and 230 GPa (min). In particular, the grain size of Si containing coatings is found to lie between 18 to 38 nm with a subsequent reduction in surface roughness. The coatings exhibit a columnar structure

SEM, EDS (**Figure 5.6**), and XRD analyses have shown that the wear track indicates the transfer of materials is mainly an iron oxide, which could be Fe_2O_3 according to its brown color. There may be iron-based oxides of FeO-type and Fe_2O_3-type which might have generated on worn surfaces. The low friction coefficients (**Figure 5.5**) of coatings observed could be attributed to the formation of a lubricating iron oxide (Ouyang and Sasaki 2004, Mercs *et al.* 2005). Also, no silicon oxide has been detected in XRD. **Figure 5.6a** shows the worn surface of CrSi(2.67at.%)N and corresponding compositional analysis after POD test. The **Figure 5.6b-c** indicates that the transferred materials (in form of debris) get compacted and mechanically mixed with the coating materials and stick to the coated surface. It reduces the COF as softer phase increases the contact area which in-turn reduces the frictional contact stresses. This reduces the tendency of fracture contributing low wear loss (Dey and Biswas 2009).

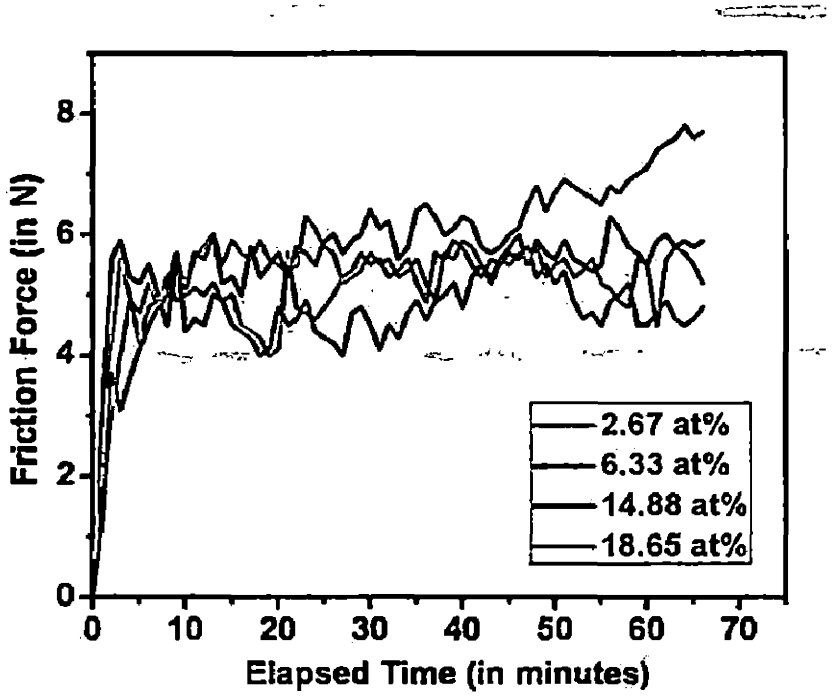

Figure 5.5 Coefficient of Friction of CrSiN coatings with different Si content against a EN32 countermaterial.

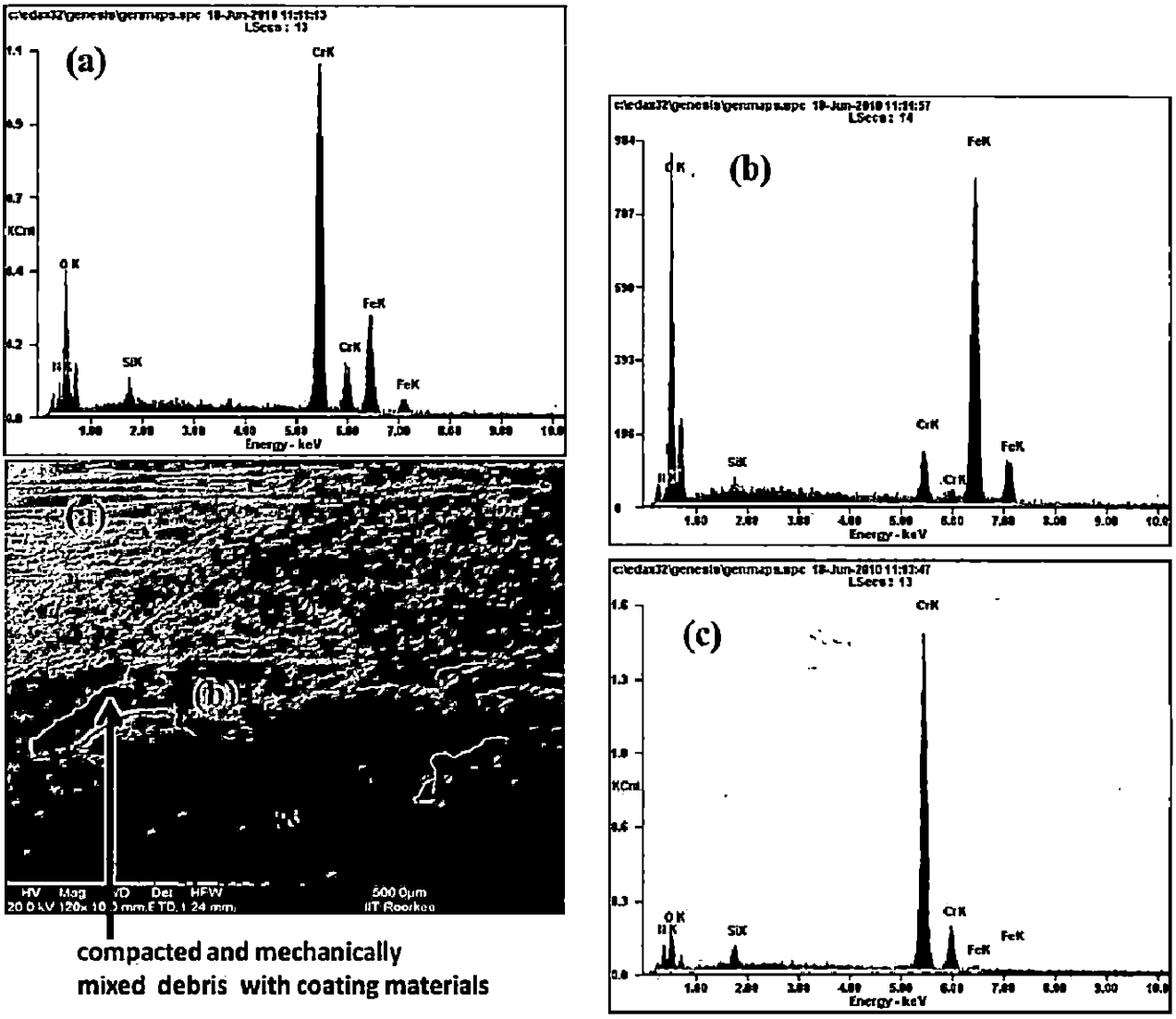

Figure 5.6 SEM morphologies of wear track and composition analysis (EDS) of wear debris after POD test of CrSi(2.67 at.%)N: a) covers whole surface area, b) a layer of debris formed on a coated surface and c) EDS of coated surface.

The wear test of coatings performed against EN32 countermaterial has shown that a significant wear of countermaterial has occurred as it is softer than the coating and wear of the coatings has been observed in the range of 10^{-6} mm^3/Nm. The wear rate of CrSiN coatings compared to CrN coating found to be very low due to its superior hardness (28 GPa). It is observed that a large amount of the softer material is transferred to the coating surface as shown on the wear track profile due to hard material slides on relatively softer materials, which results in adhesive wear behavior (Wilson and Alpas 1996, Hutchings 1992).

as shown in **Figure 5.4b**, the enhancement of hardness (**Figure 5.4a**) is mainly due to grain size effect following a typical Hall–Petch relationship. The coatings exhibit a high hardness (28 GPa) at 6.33 at.% Si, which is also due to very fine composite microstructure consisting of fine grained CrN phase surrounded by amorphous SiN phase. With further increase in Si content (14.66 at.%), the hardness and Young's modulus have reduced despite the reduction in the grain size, because of the high volume fraction of a-Si_3N_4 (Vepřek *et al.* 1995, Park *et al.* 2004, Vepřek *et al.* 2007). The similar trend in hardness variations with respect to Si content in the Cr–Si–N coatings have been reported in the literature (Shah *et al.* 2010, Park *et al.* 2004, Park *et al.* 2007, Sandhu *et al.* 2006) However, the hardness of CrSiN coatings, 28 GPa, observed in the present work is higher than the reported value in the literature (Benkahoul *et al.* 2008, Lee *et al.* 2007, Mercs *et al.* 2005, Martinez *et al.* 2004, Benkahoul *et al.* 2009). On the other hand, it is lower than the reported value of 30 GPa (Mercs *et al.* 2007), due to different process parameters used in the deposition techniques. The elastic modulus of CrSiN coatings exhibits increasing trend with increasing Si content but a sharp reduction in modulus to 243 GPa from 278GPa was observed when at.% silicon is 14.88.

Table 5.4 Typical grain size, thickness, surface roughness and hardness of CrSiN coatings and their influence on hardness and modulus.

Variable	Grain Size (nm)	RMS Roughness (nm)	Coatings Thickness (μm)	Nano Hardness (GPa)	Modulus (GPa)
CrSiN coatings with varying Si content					
CrSi(2.67 at.%)N	38	30	5.43	22	230
CrSi(6.33 at.%)N	31	19	5.01	28	246
CrSi(14.88 at.%)N	20	17	4.61	25	278
CrSi(18.65 at.%)N	18	7	4.89	21	243

5.1.3.3 Tribological Properties of CrSiN Coatings Deposited on SA304 Substrate

CrSiN coatings on stainless steel (SA304) substrates were deposited by DC/RF magnetron sputtering. The effect of additions of silicon content on the microstructural, mechanical and tribological properties of CrSiN coatings has been investigated. Silicon has been incorporated into CrN by co-sputtering of chromium target (99.999% purity) and silicon (99.995% purity) in a

mixture of argon and nitrogen. Microstructural and mechanical properties have been evaluated by XRD, FESEM, and AFM, and microhardness and nanoindentation, while tribological tests have been carried out using pin-on-disc apparatus. Pin-on- disc tests (POD) under a normal load of 10 N were performed to investigate the coefficient of friction and wear resistance of the CrSiN coatings. The Cr–Si–N coatings showed low friction coefficients and no measurable wear after 2000 m of sliding at 0.5 m s^{-1}. The countermaterial used was steel (EN32) with 65HRC. The POD tests of CrSiN coated materials were performed with same parameters used for CrN coated samples. The parameters are described in **Table 4.11** in **Chapter 4**.

There is an improvement in tribological properties of CrSiN coatings, with addition of Si content in the coatings as compared to CrN coatings deposited with same parameters. The COF (μ) has been calculated for the coating materials using **Eq. 3.14.** The overall friction coefficient of CrSiN coatings with different Si contents was found to vary between 0.49–0.61. **Figure 5.5** shows the coefficient of friction of CrSiN coatings deposited with different Si content, against EN32. The average coefficient of friction is reduced with the incorporation of Si element in to CrN binary compound and is found to vary between 0.49 - 0.61. The CrSiN coatings with 6.33 at.% and 14.88 at.% Si contents exhibit comparatively lower coefficient of friction, 0.49 and 0.50 respectively, than the coatings with 2.67 at.% Si content (0.61). At 18.65 at.% silicon content, the coefficient of friction is found to be 0.54. The COF and wear rate of CrSiN coating as a function of Si content in the coating are summarized in **Table 5.5.** The low value of friction coefficient of the CrSiN coatings than CrN coatings is due to smoother surface created by two factors such as amorphous phase, which reduce the surface roughness with increase in Si content as reported in our previous work (Shah *et al.* 2010) (as discussed in Section 5.1.3.1 and table 5.3), and tribo-chemical reaction (Takadoum *et al.* 1998, Xu and Kato 2000, Park 2004, Park *et al.* 2007). The tribo-chemical reaction often takes place between Si_3N_4 and atmospheric water vapor (H_2O), if there is higher humidity in the atmosphere. Alternately, when POD test is carried out with water lubricants, it canes produce SiO_2 or $Si(OH)_2$ tribolayer. This tribolayer act as a self lubrication layer (Takadoum *et al.* 1998) and is responsible for lower coefficient of friction. The tribo-chemical reactions of Si_3N_4 ceramics with atmospheric H_2O is given below:

$$Si_3N_4 + 6H_2O = 3SiO_2 + 4NH_3$$

$$SiO_2 + H_2O = Si(OH)_2$$

Table 5.5 Typical hardness and modulus of CrSiN coatings with their corresponding tribological properties.

Variable	Nano Hardness *H* (GPa)	Modulus *E* (GPa)	Coefficient of Friction COF	Wear rate of Coating $K*10^{-6}$ (mm^3/N.m)
CrSiN coatings with varying Si content				
CrSi(2.67at.%)N	22	230	0.61	8.95
CrSi(6.33at.%)N	28	246	0.49	1.93
CrSi(14.88at.%)N	25	278	0.50	4.13
CrSi(18.65at.%)N	21	243	0.54	9.93

5.1.4 Conclusions

CrN and CrSiN coatings on stainless steel and Si substrates were deposited by DC/RF reactive magnetron sputtering. The surface roughness and grain size of CrSiN coatings decrease with increasing Si content as observed in the present work. The coatings exhibit a triangular needle-shaped columnar morphology, which transforms into a finer columnar morphology at higher Si contents of 14.88 at.%. The hardness of CrSiN coatings increases from 23.92 GPa to 25.70 GPa with increase in Si content from 2.67at % to 6.33at %, which is due to size effect caused by grain refinement. The Si contents higher than 6.33 at % in the coatings reduces the microhardness due to higher volume fraction of amorphous Si_3N_4 phase. The nanoindentation result of CrSiN coatings showed the enhancement of the hardness and modulus, 28 GPa and 246 GPa, respectively, up to 6.33 at.% Si content in the coatings. It is attributed to the fine composite microstructure consisting of fine grained CrN phase surrounded by amorphous SiN. However, the modulus increases with further incorporation of Si content in the CrSiN coatings. The mechanical properties of the coatings (H = 21 GPa and E=243 GPa) have decreased with the high volume fraction of a-Si_3N_4. However, the high hardness of the CrSiN coatings (28 GPa) has been obtained with the composition of Si content varying between 6.33 at.% to 14.88 at.% in the coatings. The friction coefficient of CrSiN coatings is lower than that of CrN coatings, due to the formation of amorphous phase (with increase in Si content in the CrSiN coatings) and the iron oxide. The enhanced values of COF and wear rate were found to be 0.49 and 1.93 X 10^{-6} mm^3/Nm, respectively.

5.1.5 Comparison of Present Work with the Existing Literature

From **Section 2.2.2** and **Table 2.3** in Chapter 2, the hardness of CrSiN coatings with small amount of silicon during deposition is found to be varying between 23 to 35 GPa as reported in the literature. Like CrN coatings, the CrSiN coatings were also deposited using DC magnetron sputtering under normal condition (without biasing or any special treatment) in the present work. The hardness of 28 GPa was achieved with 6.33 at. % Si content in the CrSiN coatings. The reduced modulus (270 GPa) and the resistance to plastic deformation (H^3/E^{*2}) (0.30) achieved are quite comparable the values to reported in the literature (**Table 2.3**). The COF and wear rate are also improved with addition of small amount of Si content (6.33 at.%) in the coatings.

5.2 Synthesis and Microstructural Characterization of CrSiN Coatings Deposited on Si (100) and SA304 Substrate

The effect of deposition time, sputtering pressure, substrate temperature, and argon:nitrogen concentration on the microstructural morphologies and phase compositions of sputter deposited CrSiN coatings has been investigated by FE-SEM/EDS, AFM, and XRD in the present work.

5.2.1 Introduction

Chiba *et al.* (1993) have reported that CrN coatings deposited by PVD exhibit better wear resistance than TiN coatings under dry condition due to its intrinsic properties such as lower friction coefficient and higher toughness, which prevent the crack initiation and propagation, despite the similar hardness with TiN coatings (Chiba *et al.* 1993). The main advantage associated with the deposition of CrN film is the low deposition temperature, which makes it suitable for fabricating coating onto temperature-sensitive materials and low melting point metals (Münz *et al.* 1987). The addition of third element such as Si and/or Al into the CrN binary compound has shown improved properties such as high hardness, wear resistance, and high temperature oxidation resistance. A maximum hardness up to 55 GPa was reported for W-Si-N and Ti-Si-N coatings (Vepreak *et al.* 1996, Diserens *et al.* 1999, Cavalerio *et al.* 2002, Mannling *et al.* 2001). Hardness of these coatings is improved due to presence of an amorphous phase, which moves to grain boundary and forms strong bonds. Sandu *et al.* (2006) reported that in all M–X–N systems, the segregation of X (X = Si, Ge) to the grain boundaries limits the crystallite growth and involves the formation of a new phase. For example, in the case of M–Si–N systems, the addition of Si leads to the formation of two-phases containing MN_x nanocrystallites, where M is (Cr, Ti, W) surrounded by the SiN_x amorphous phase as reported in the literature (Holleck *et al.* 1986, Bertrand *et al.* 2000, Vepreak *et al.* 1996, Diserens *et al.* 1999, Cavalerio *et al.* 2002). The microstructural transformations of coatings due to the Si addition into CrN results in improved corrosion resistance and oxidation resistance (Kim et *al.* 2002, Choi *et al.* 2004, Veprek *et al.* 1996).

Lee (2007) studied the microstructures and mechanical properties of CrSiN coatings deposited by pulsed DC reactive magnetron sputtering and observed that the surface roughness, grain size, hardness, and friction coefficient of CrSiN coatings decrease with increasing Si contents. The coatings with silicon content up to 3 at.% form fcc $Cr_{1-x}Si_xN$ phases and for above 3

at.% Si, it segregates at the grain boundaries and form a-SiN*x* phase. Shah *et al.* (2010) investigated Cr and CrSiN coatings deposited on SA304 and Si(100) substrates by DC/RF reactive magnetron sputtering and found that surface roughness and grain size decreases with increasing Si content from 2.67 at.% to 6.33 at.%. Benkahoul (2008) deposited CrSiN coatings by pulsed DC reactive dual magnetron sputtering and reported that the increasing Si content does not affect the grain size, but it leads to solid solution hardening. The film hardening is due to the formation of solid solution and nc-CrN/a-Si_3N_4 in the coatings. The nanohardness values of (111) and (200) CrN are typically between 12–18 GPa. Wang and Kim (2009) studied the microstructural evolution of CrSiN coatings deposited by hybrid arc ion plating and magnetron sputtering process and concluded that the morphology of coatings changes from long and coarse crystallite to shorter and finer ones, with the increase in Si content. Subsequently, the nanoclusters disperse in an amorphous matrix as reported in their work.

In this present study, the effect of the deposition time, working pressure, substrate temperature and argon: nitrogen content on the microstructural properties of CrSiN coatings deposited on Si (100) and SA304 substrates, by Magnetron sputtering, has been investigated. XRD, FE-SEM/EDS, AFM and TEM were used to characterize the CrSiN coatings to substantiate the influence of deposition conditions on their microstructural features.

5.2.2 Experimental Details

5.2.2.1 Deposition of CrSiN Coatings

CrSiN coatings were deposited on Si (100) and SA304 substrates by DC magnetron sputtering. The sputtering targets of 99.995% pure Cr and Si disc of 2-inch diameter and 5 mm thick were used for the deposition of coatings. The similar procedures as given in Section 5.1.2.1 are followed for the preparation of substrates prior to deposition of the coatings. The base pressure was less than 2×10^{-6} Torr in all the deposition. The sputtering environment and target-to-substrate distance were Ar + N_2 atmospheres and 50 mm, respectively. The sputtering power mainly DC for Cr target and RF for Si target were used during the study of influence of deposition time on film structural morphology. The deposition parameters are given in **Table 5.6**. The two targets of pure Cr and Si fixed at 25° apart were mounted in deposition chamber for co-sputtering. The substrates were fixed on substrate holder, which moves with constant speeds (RPM) (with delay time, 1 second) in such a way that it covers an entire region of plasma created from both the targets.

Table 5.6 Deposition parameters of CrSiN coatings deposited on Si(100) and SA304 substrate.

Process parameters and their corresponding values	
Constant process parameters for all the experiments	
Gas Environment in the chamber	$(Ar+N_2)= (50+50)$
Temperature	573K
Power :- Cr Target	175 W (DC)
Si Target	50 W (RF)
Working Pressure	1.33 Pa
Base Pressure	$< 6.5 \times 10^{-4}$ Pa
Substrate to Target distance	≈ 50 mm
Varying process parameters during sputtering	
Deposition Time	15, 30,45, 60, 75 and 90 min
Substrate temperature	373, 473, 573, 673 and 773 K
Working Pressure	1.33, 2.66, 3.32 and 3.99 Pa
Argon : Nitrogen gas flow proportion	4 sccm to 20 sccm of different combination

5.2.2.2 Characterizations

The CrSiN coatings were characterized by a XRD (D8 diffractometer with Bragg–Brentano geometry) using CuKα (λ = 0.15418 nm) radiation. The basic structural properties of coatings in the as deposited condition were determined in the range of 30° to 100° to characterize the texture orientation. The average grain size was calculated according to the Scherrer's formula.

The surface morphology and surface roughness of each CrSiN coatings were measured by atomic force microscopy (AFM - NT-MDT, NTEGRA) operated in semi contact (tapping) mode and using the root-mean-square (RMS) statistics. The cross-sectional morphologies of CrSiN coatings were examined by using a field emission scanning electron microscopy (FESEM - FEI Quanta, 200F) operated at an acceleration voltage of 20 kV. The chemical compositions of coatings were investigated by energy dispersive spectroscopy (EDS) attached with FESEM. The details of these characterization techniques are explained in the **Chapter 3**.

5.2.3 Results and Discussion

5.2.3.1 Analysis of CrSiN Coatings Deposited on Si(100) with Different Deposition Time and Sputtering Pressure

The XRD spectrum of CrSiN coatings deposited on Si (100) substrates with different deposition time (15 to 60 minutes) shows that the texture coefficient of the (111) orientation is very high compared to other orientations in the CrSiN coatings deposited in the $Ar+N_2$. It is mainly due to high concentration of reactive nitrogen gas in the chamber along with argon gas. At very high deposition time (above 75 min), a reduction in (111) orientation but increase in (222) and (200) peak intensity was observed. The observed changes in textures are influenced by the deposition temperature, time, and the competition between surface energy and strain energy during film growth. At particular film thickness called critical thickness, a transition point occurs at which texture of the coatings changes. In addition, the substrate roughness may also affect the film texture. From the XRD peaks, the crystallite size of the CrSiN coatings was found to be in range of 34 to 73 nm, after 75 min of deposition time, under equal proportion of $Ar+N_2$ atmospheres but it decreases to 61 nm after the deposition time of 90 min. It is observed that the increase in grain size with the deposition time is not high due to the formation of highly textured grains in the CrSiN coatings. XRD peaks of CrSiN coatings deposited on the Si (100) substrate under equal proportion of $Ar+N_2$ atmospheres at 300°C with varying sputtering pressure in the chamber are shown in **Figure 5.7.**

The grain size and surface roughness of the coatings are affected with change in the sputtering pressure. The grain size was found to be 42 nm (max.) and reduces to minimum of 28 nm with increasing sputtering pressure as shown in **Table 5.6.** Similarly, the thickness of the coatings has decreased with increasing working pressure and higher concentration of N_2 due to the reduced mean free path of Cr and Si atoms. However, the deposition rate is very low with increasing sputtering pressure. A reduction in deposition rate at higher working pressure as well as the formation of CrN phase at higher N_2 concentration may contribute to the decrease in coating thickness. The peak-broadening effect of CrSiN coatings was caused by the small grain size and the lattice strain given in **Table 5.7.**

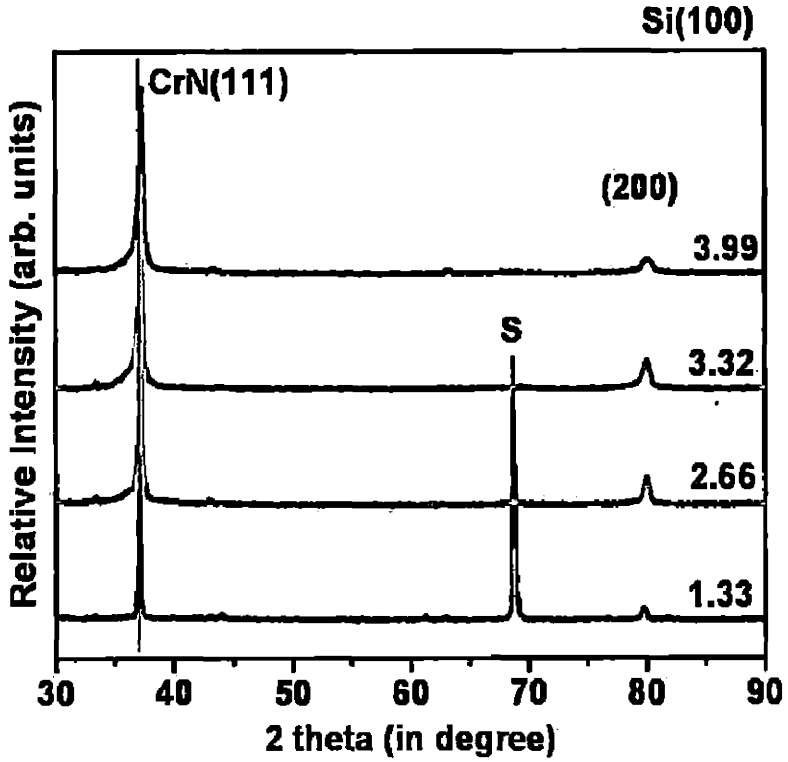

Figure 5.7 XRD pattern of CrSiN coatings deposited on Si (100) substrates at Ar: N_2 is 50:50 and at 573K temperature with varying values of sputtering pressure.

Table 5.7 Influence of deposition parameters on crystallite size, surface roughness, and microstrain of CrSiN coatings deposited on Si(100) substrate.

Sample Name	Variable parameter	*d* Spacing (Å)	Grain Size *D* (XRD) nm	Grain Size (AFM) (nm)	Surface Roughness (RMS) (nm)	Microstrain
Variation in Sputtering Pressure (Peak (111))						
Si01	1.33 Pa	2.4258	42	75	21	1.4879
Si05	2.66 Pa	2.4192	38	135*	38	1.2101
Si06	3.30 Pa	2.4181	31	62	17	1.1642
Si07	3.99 Pa	2.4116	28	107*	33	0.8937
Variation in Time (Peak (111))						
Si08	15 min	2.4126	34	60	14	0.0347
Si09	30 min	2.3975	40	79	18	0.3019
Si10	45 min	2.4102	37	23	6	0.8333
Si11	60 min	2.3974	44	26	7	0.2995
Si12	75 min	2.4040	73	34	7	0.5748
Si13	90 min	2.4057	61	28	8	0.6473

*indicates grain size with one or two few hundred nm size.

The CrSiN coatings show a triangular morphology and the grain size is reduced with increasing working pressure as observed from SEM images shown in Figure5.8. It is observed from SEM images shown in **Figure 5.9** that the particles in the coatings exhibit triangular needle type morphology and it grows with deposition time. The (111) preferred orientation observed, in the present work, for the coatings deposited under $Ar+N_2$ atmosphere, is different from the (200) orientation reported for the coatings as reported in the literature (Park *et al.* 2004, Benkahoul *et al.* 2008, Thobor-Keck *et al.* 2005). It is due to the difference in deposition temperature, substrate orientation, and proportion of $Ar+N_2$ mixture used in these cases. Up to deposition time 30 minutes, the proper growth and crystallinity of the coatings was lacking, but the coating has grown with triangular needle shape at 45 min, 60 min, 75 min and 90 min of deposition time as clearly seen from the FESEM images shown in **Figure 5.9**. The layer of coatings deposited on the substrate at less than 45 minutes of deposition time is insufficient to facilitate the formation of crystallite CrN, resulting in low or absence of peaks in the XRD spectra, which is further confirmed by chemical analysis. The coatings deposited on Si (100) substrate exhibit columnar grain morphology, which has grown perpendicular to the substrate with particle size varying between 34 nm to 72 nm. It is observed that the grain size of the coatings calculated from FE-SEM and AFM is higher compared to that of it calculated from XRD spectrum; it is because of the average mean crystallite size and agglomeration of small particles due to higher surface free energy, calculated from AFM and FESEM, respectively (Singh *et al.* 2007).

The chemical compositions of CrSiN coatings with different deposition time, obtained from EDS analysis, are shown in **Figure 5.10**. A maximum Si content of 31.24 at.% is observed in the coatings deposited at minimum time duration (15 min), whereas a very low Si content, 2.46 at.%, is observed for the coatings deposited at 75 min of deposition time. The reduction in Si content in the coatings, with deposition time, is due to the reaction between Si and N_2 forming $Si_{x-1}N_x$ compound, which moves finally to grain boundary. The Si content is reduced with increase in deposition time while Cr content is increased. During initial time of 15 min to 45 min, the Si content has drastically reduced from 31.24 at.% to the 3.80 at %. Also, the Cr at.% followed the trend in a reverse manner, and settled at 45 min deposition time. The nitrogen concentration remains constant or exhibits a slight variation with increasing deposition time. Hence, Si concentration of the coatings decreases due to the higher reactivity of Si with N. It is in tandem with the similar results reported for the same compound of CrSiN coatings in the literature (Martinez *et al.* 2004, Sandhu *et al.* 2006).

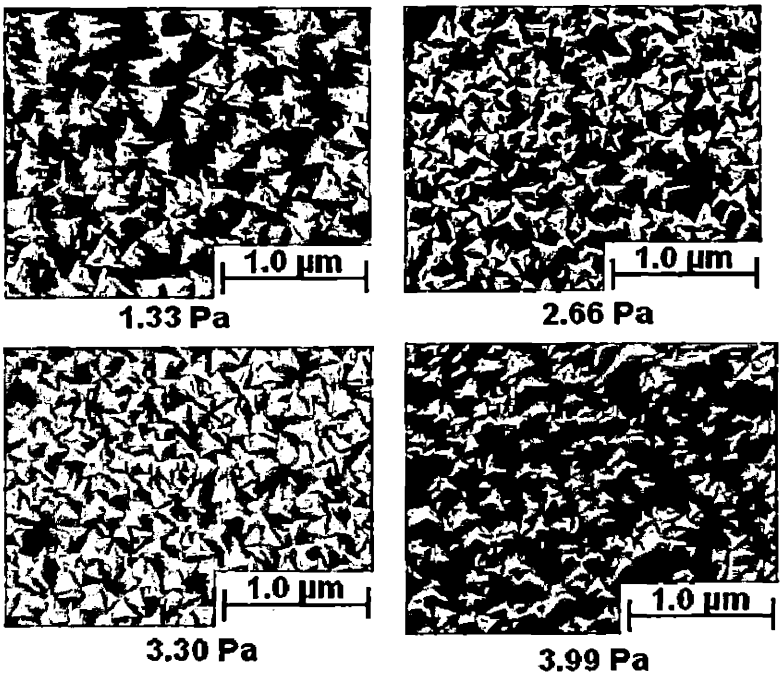

Figure 5.8 FE-SEM images of CrSiN coatings deposited on Si (100) substrates at 573K with varying values of working pressure.

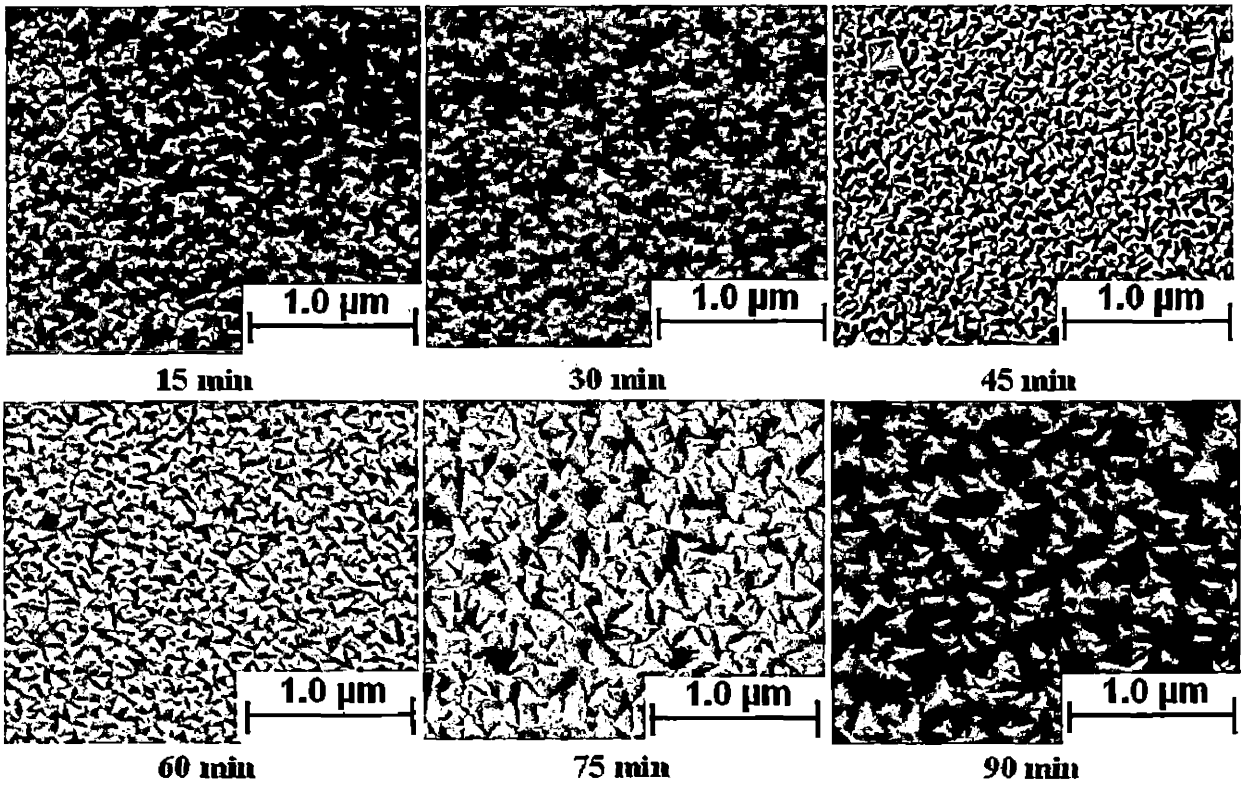

Figure 5.9 FE-SEM images of CrSiN coating deposited on Si(100) substrates at 573K with different deposition time.

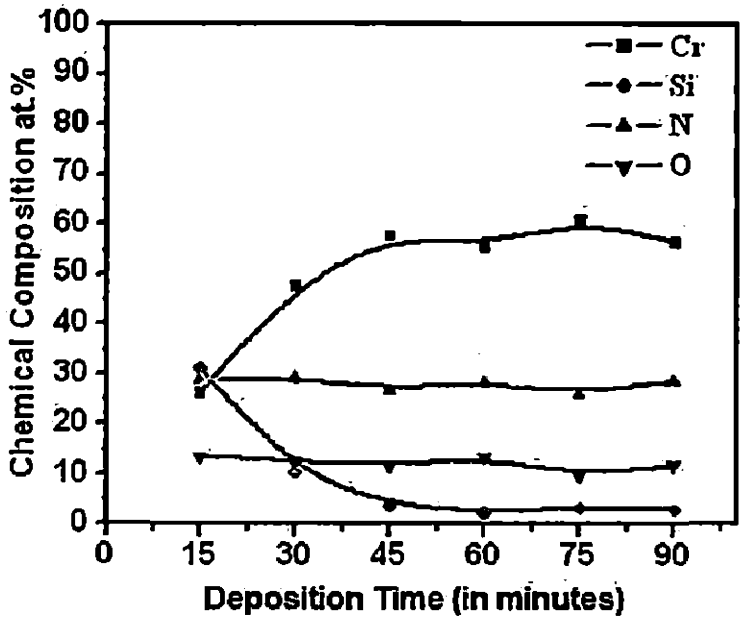

Figure 5.10 Elemental compositions of CrSiN coatings as a function of deposition time during magnetron sputtering.

The microstrain (ε) and interplanar spacing (d) from (111) peak of CrSiN coatings on silicon Si (100) substrate is calculated by the **Eq. 4.2** and **4.3.**

At temperature 573K with varying working pressure of 1.33, 2.66, 3.32 and 3.99 Pa, the intensity of preferred orientation (111) has increased up to 2.66 Pa working pressure and then it is reduced due to its higher strain energy and lower surface energy. However, the reduction in intensity of (200) and (222) orientation occurs with increasing working pressure up to 2.66 Pa. Similarly, at same temperature, 573K, with varying deposition time, the intensity of preferred orientation (111) is increasing with time. With increasing deposition time, stress relaxation may occur leading to the reduction in strain energy. At initial and intermediate deposition times (15, 30, 45 and 60 min), the strain fluctuates broadly while at the later deposition time (75 and 90 min), microstrain is stabilized at the value of **0.64**. The rate of reduction in strain energy is sensitive to the time and is much higher than the rate of increase in surface energy during the initial deposition time.

5.2.3.2 Analysis of CrSiN Coatings Deposited on SA 304 and Si(100) Substrates with Different Ar:N_2 Gas Proportion

Figure 5.11a shows the XRD pattern of CrSiN coatings deposited, on SA 304 substrate, with various sputtering and reactive gas proportions. It is observed that CrN (111) orientation is dominating throughout the range of gas proportions. A small amount of silicon content (3.67at.% Si) plays an important role in addition to the increase in nitrogen content as it is responsible for: a) formation of substitutional solid solution, b) Reaction between extra Cr and nitrogen, c) grain size reduction, and d) decrease of surface roughness due to reduction in crystallites and increase in density of the coatings. In the present work, a single CrN phase is observed in the coatings deposited with Si (3.67 at.%) content, as reported in the literature (Lee *et al.* 2007). Initially, at argon : nitrogen mixture (80:20) proportions, the high intensity peak at $2\theta = 37.42$ corresponds to cubic CrN (111) and the peak with lower intensity at $2\theta = 42.71$ belongs to cubic CrN (200). The intensity of a strong (111) peak is decreasing when the argon: nitrogen proportions were varied from (80:20) to (60:40). With the further increase of nitrogen content, from (60:40), in the sputtering gas mixture to (40:60) argon-nitrogen, sudden increase in (111) peak intensity occurs and above (40:60), the peak reduction rate is very slow than the previous one. On the other hand, the (200) peak intensity is slowly decreasing initially with increasing nitrogen contents and then increasing with further increase in nitrogen content. However, the (111) and (200) peak intensity variations are very limited due to higher nitrogen present in the CrSiN coatings.

It is evident from **Figure 5.11a** that there is a very limited shifting in the 2θ value (very narrow variation towards higher angle) corresponding to the (111) and (200) orientations, which can be attributed to a decrease in lattice parameters of CrSiN due to substitution of some Cr atoms by Si atoms in the CrN lattice. With increasing nitrogen content from 50:50 to pure N_2 deposition, the lattice parameter is reduced to standard d- spacing value. The measured lattice parameter of CrSiN (80:20) coatings was 4.1589 Å, which is higher than the stoichiometric CrN value of 4.140 Å as given in the International Centre for Diffraction Data (JCPDS, 1999), Joint Committee on Powder Diffraction Standards database No. 11-0065. This positive deviation of the lattice parameter with respect to the standard value indicates the presence of residual compressive stress in the coatings, which is observed until 50:50 argon: nitrogen mixture. For the nitrogen content of above 50%, the lattice parameter decreases and reaches close to the standard values. However,

estimations of the residual stress by profilometry and the Stoney's equation lead to errors in the calculated stress (Cunha *et al.* 1999), probably because of the much lower coating thickness and the non-uniformities in the coating/substrate stress distribution. Comparatively, the residual stress in magnetron sputtered Cr based coating is lower than the coatings deposited by other PVD as it enables deposition of thick coatings without spalling or substrate distortion (Navinsek *et al.* 1997). The texture coefficient (Chawla *et al.* 2008) of the CrSiN coatings as a function of working pressure and temperature are calculated using the **Eq. 4.1** and the results are shown in **Figure 5.11b**. The peak intensity corresponding to CrN (111) and CrN (200) as a function of the argon: nitrogen content during co-sputtering of CrSiN coating with fixed amount of silicon content (3.67 at.% Si). The insertion of silicon atoms into the CrN lattice leads to an amorphization of the structure with an associated decrease of the CrN (200) diffraction peak intensity (Mercs *et al.* 2007). The peak intensity of CrN (200) is below 20% as shown in **Figure 5.11b**. The small variation in the peak intensity, with a fixed amount of Si content, may be due to variation in argon: nitrogen content in the chamber.

The transmission electron microscopy micrographs of CrSiN coatings deposited, on Si substrate, at 773 K with 3.67 at.% Si, with (50:50) argon: nitrogen mixture is shown in **Figure 5.12**. The absence of peak in XRD and diffused ring for SiN shown in TEM confirm the amorphous nature of SiN. The CrN matrix surrounded by amorphous SiN is observed in this figure. The Si atoms tend to diffuse into the matrix and segregate around dislocations so as to reduce the overall strain energy as reported in the literature (Benkahoul *et al.* 2008). Also, the silicon segregates at the grain boundaries to form an a-SiN_x phase for the coatings containing above 3% Si content (Martinez *et al.* 2004, Martinez *et al.* 2004a). Hence, there is no effect of higher nitrogen content on crystallinity of the coatings despite falling under nitride mode of deposition.

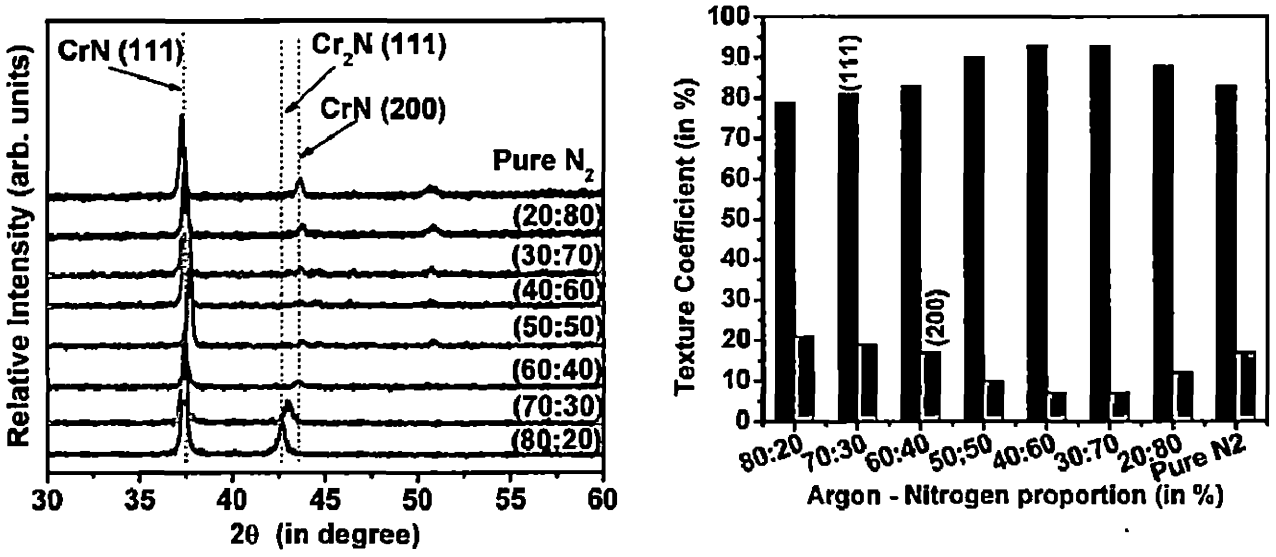

Figure 5.11 a) XRD pattern and b) Texture coefficient of CrSiN coatings deposited on SA304 substrate in varying argon nitrogen gas mixture with fixed amount of Si content (3.67 at % Si).

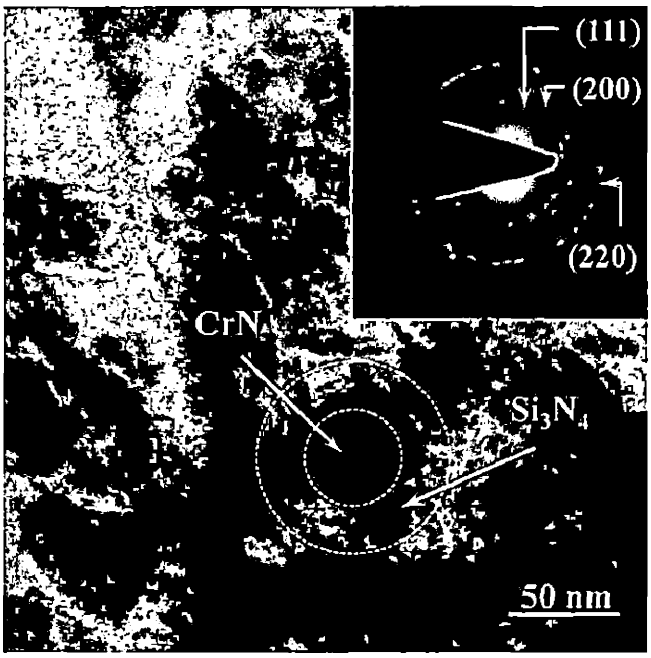

Figure 5.12 TEM bright field image and diffraction patterns of CrSiN coatings deposited on Si substrate with 3.67 at.% Si content under 50:50 Ar:N_2 atmosphere at 773K.

The FESEM and AFM images of CrSiN coatings deposited on both the substrates with argon: nitrogen ratio (80:20) and (20:80) are shown in **Figure 5.13** and **Figure 5.14,** respectively. The coatings morphology change from columnar-triangular shape to columnar-needle shape and exhibits a cone growth with a surface roughness of few nanometers at the deposition condition, argon: nitrogen ratio of (20:80) in the sputtering chamber. A smooth surface with good adherence to the substrate and the cone structure showing a narrow size distribution are observed in the AFM micrographs. The average agglomerate size for each sample was calculated from the AFM images. In general, the grain size calculated from the AFM image is slightly larger than that of it calculated from XRD line broadening. Unlike XRD results, a systematic decrease in grain size with increase in nitrogen content is observed from the AFM images of the coatings. The cone growth is observed for the argon: nitrogen ratio of above (50:50), but its growth rate is restricted due to higher nitrogen content. At argon: nitrogen ratio of 20:80, the grain size and surface roughness of the coatings have reduced compared to that of the coatings deposited at argon: nitrogen gas ratio of 80:20 due to nitride mode of deposition. However, there is no specific trend observed for grain size of the coatings with increasing nitrogen contents for both the substrate. Thickness of the coatings ranges from 5.07 nm to 2.31 nm due to variation in the argon – nitrogen gas content, increasing nitrogen in the gas mixture leads to nitride mode of deposition, during sputtering (**Table 5.8**). The higher deposition rate of 1.40 nm/s is observed at argon: nitrogen ratio of (80:20) and it is reduced to 0.64 nm/s for the CrSiN coatings deposited with increasing nitrogen content. However, the coating thickness is decreasing rapidly from 5.07 nm to 2.57 nm up to proportion of 40% argon and 60% nitrogen contents, in the sputtering chamber, shown in **Table 5.8**. There was no appreciable reduction in the deposition rate with further increase in nitrogen flow content from 60% up to pure nitrogen environment.

Figure 5.15 shows the cross-sectional SEM of CrSiN coatings on silicon substrates. The columnar film morphology is observed for the coatings deposited at 80:20 $Ar:N_2$ ratio and it becomes a finer column with increasing nitrogen content during deposition. The roughness of coatings observed at argon: nitrogen ratio of (80:20) was 34 and 17 nm for stainless steel and silicon substrate, respectively, while at (20:80) argon: nitrogen mixture, it was found to be 9.0 and 9.5 nm, respectively.

Table 5.8 Properties of CrSiN coatings deposited, on SA 304 substrate, at various argon nitrogen gas values at 773K.

Sample	Argon-Nitrogen Proportion (in %)	Grain Size "D" (in nm)		RMS Roughness (nm)	Thickness (μm)
		XRD	AFM		
SS01	80:20	41	97	34	5.07
SS02	70:30	40	54	13	4.37
SS03	60:40	34	46	13	3.89
SS04	50:50	31	47	15	3.42
SS05	40:60	40	41	13	2.57
SS06	30:70	42	33	8	2.69
SS07	20:80	41	31	9	2.48
SS08	100% N_2	36	18	5	2.31

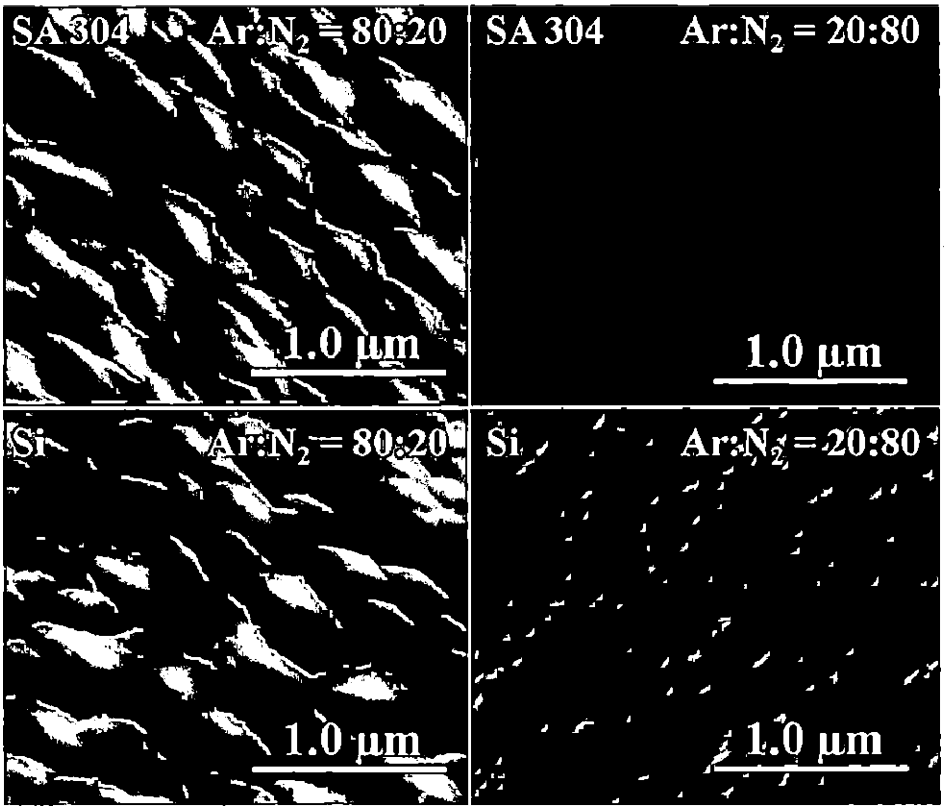

Figure 5.13 SEM images of CrSiN coatings with 80:20 and 20:80 argon- nitrogen gas mixtures in the sputtering chamber, deposited on SA304 and Si substrates.

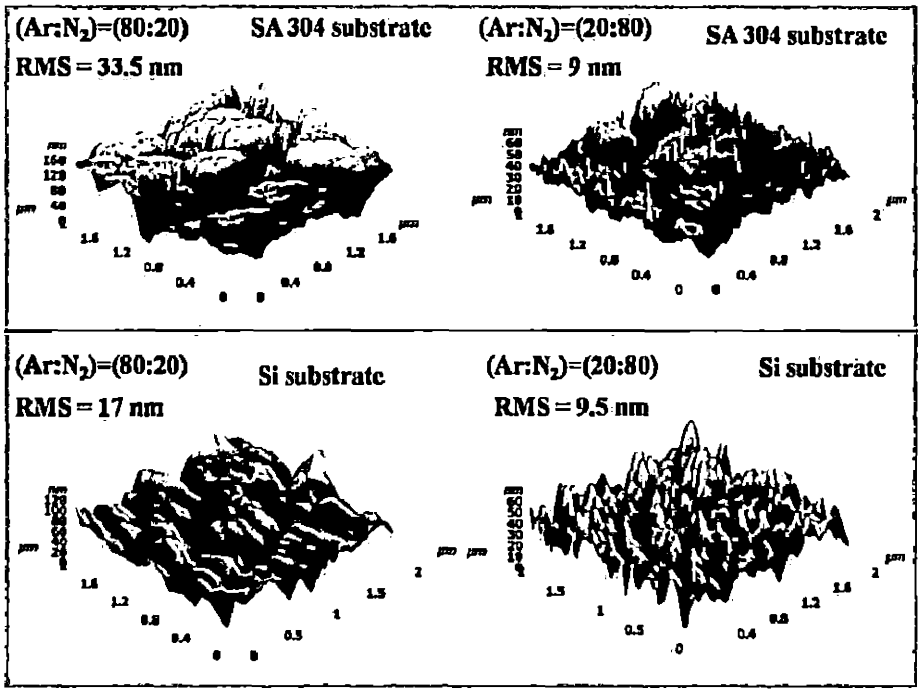

Figure 5.14 AFM images of CrSiN coatings deposited on SA 304 and Si substrates, at 80:20 and 20:80 argon- nitrogen gas mixtures.

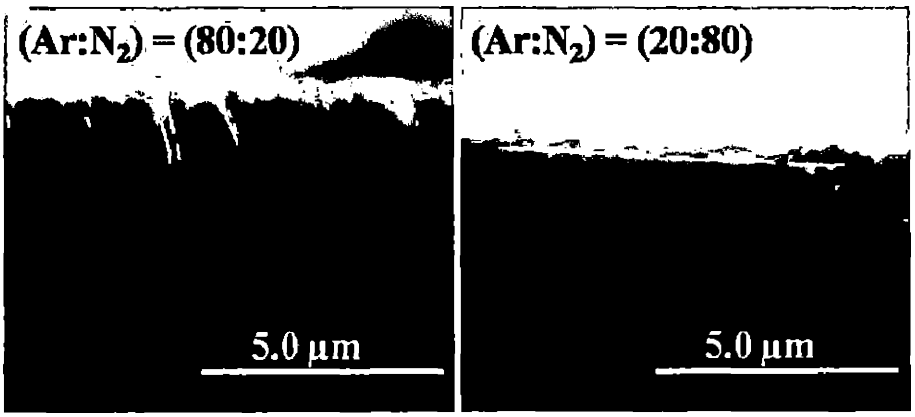

Figure 5.15 Cross sectional FESEM of CrSiN coatings deposited on silicon substrates in varying argon: nitrogen gas mixture with fixed amount of Si content in the coatings (3.67 at % Si).

5.2.3.3 Analysis of CrSiN Coatings Deposited on SA304 and Si(100) with Different Deposition Temperature

Figure 5.16 shows XRD patterns of the CrSiN coatings, deposited on SA304 substrate, at different substrate temperature. It exhibits a FCC crystalline structure as evident from the XRD results. The (111) orientation is observed in the coatings deposited at high concentration of N_2 in the sputtering chamber. The main phases in all the coatings were identified as cubic CrN, with

diffraction peaks of (111) and (222). The (200) peak is observed in the XRD pattern at 673K as shown in **Figure 5.16**. No other phases such as Cr_3Si, $CrSi_2$ or Si_3N_4 peaks were identified. The reduction in (111) peak intensity with peak broadening occurs with increasing temperature from 373K to 773K. The full width at half maximum (FWHM) of the coatings with most intense XRD peaks, corresponding to the (111) and (200) planes, were considered for the average grain size calculation. The intrinsic stress in the coatings increases (from compressive to tensile) linearly and it remains constant even after deposition, called low mobility Volmer-Weber growth, which increases at higher temperature (Ohring 2002).

Table 5.9 shows different properties of CrSiN coatings (grain size, surface roughness and coating thickness) deposited on SA304 and Si substrates with varying substrate temperature, measured by X-ray diffraction and atomic force microscopy (AFM), and scanning electron microscopy (SEM). The average grain size, calculated from XRD results, increases from 31 to 45 nm and 41 to 51 nm for the coatings deposited on SA304 and Si(100), respectively, with increase in temperature from 373K to 773K (**Figure 5.17a**). The increase in grain size in the coatings deposited on SA 304 substrates is due to high adatom mobility at high temperature. The similar trend is observed for the coatings deposited on Si(100) substrate. However, the grain size of CrSiN coatings deposited on Si(100) substrate falls initially to 37 from 41 nm up to 573K, although it is not appreciable reduction. With further increase in temperature to 773K, grain size increases to 51nm. The reduction in grain size initially, between deposition temperature of 373K and 573K, may be due to the instability in the temperature on substrate and rapid decrease of surface energy (with increase in temperature) with crystalline growth (Subramanian *et al.* 2008, Sinha *et al.* 2007). The deposition rate and surface morphology at various substrate temperatures can be explained as follows: The substrate temperature controls the mobility of the ad-atoms on the surface. The deposition at low substrate temperature of the environment exhibits low ad-atom mobility and tends to form preferred crystal structure, which leads to increase in surface roughness. So, the adsorbed atoms are stacked on the energetic crystalline plane rather than random stacking which leads to a rougher surface. With increasing temperature from 373K to 773K, the adatom gains extra thermal energies and forced to move to another preferred sites, which occurs in a random manner due to free atomic motion. Also, the adatom has higher probability to desorb from the surface at high substrate temperature because of thermal energy. The surface roughness decreases **(Figure 5.17b)** at higher temperature and creates a dense structure. The estimated grain size was found to be increasing up to 773K and it could be estimated from FWHM of the XRD patterns.

The values evaluated from the (111) diffraction peaks were found to be between 31-45 and 37- 51 nm for the coatings deposited on SA304 and Si(100), respectively as shown in **Table 5.9**.

Table 5.9 Different properties of CrSiN coatings deposited on SA304 and Si substrates with varying substrate temperature.

Temperature (K)	Coatings deposited on SA304 substrate			Coatings Deposited on Si(100) substrate			Coatings Thickness (nm)
	XRD Grain Size (nm)	AFM Grain Size (nm)	RMS Surface roughness (nm)	XRD Grain Size (nm)	AFM Grain Size (nm)	RMS Surface roughness (nm)	
373	31	229	69	41	86	25	4749
473	32	156	47	44	82	20	4741
573	34	100	31	37	64	19	4511
673	40	86	28	39	118*	22	4360
773	45	93	32	51	38	11	3897

* Few grains having bigger size.

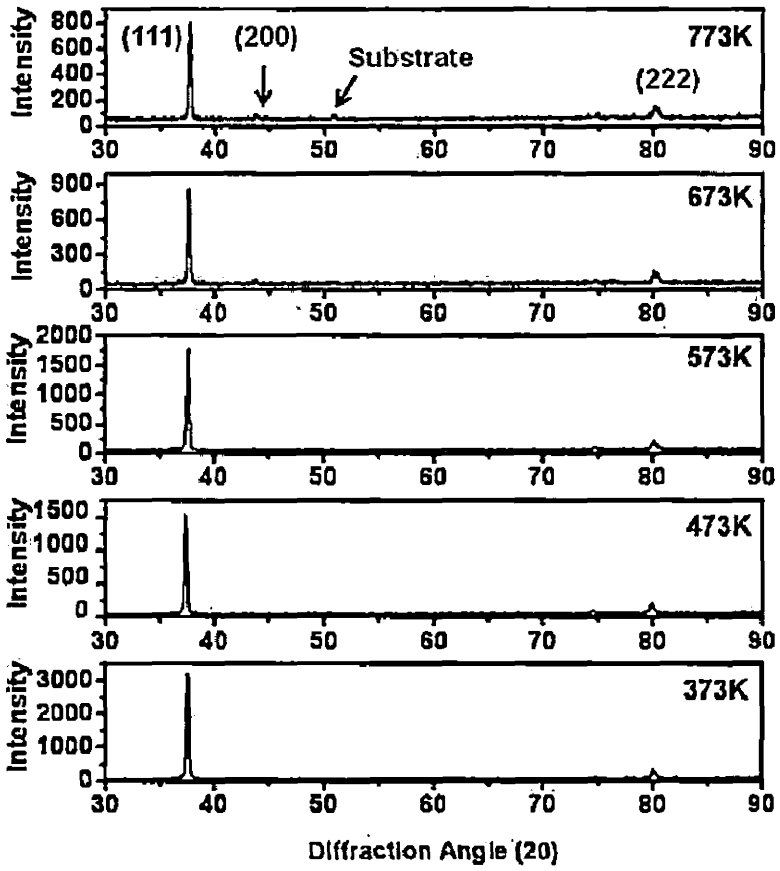

Figure 5.16 X-ray diffraction patterns of the CrSiN coatings deposited on SA 304 substrate at different substrate temperature.

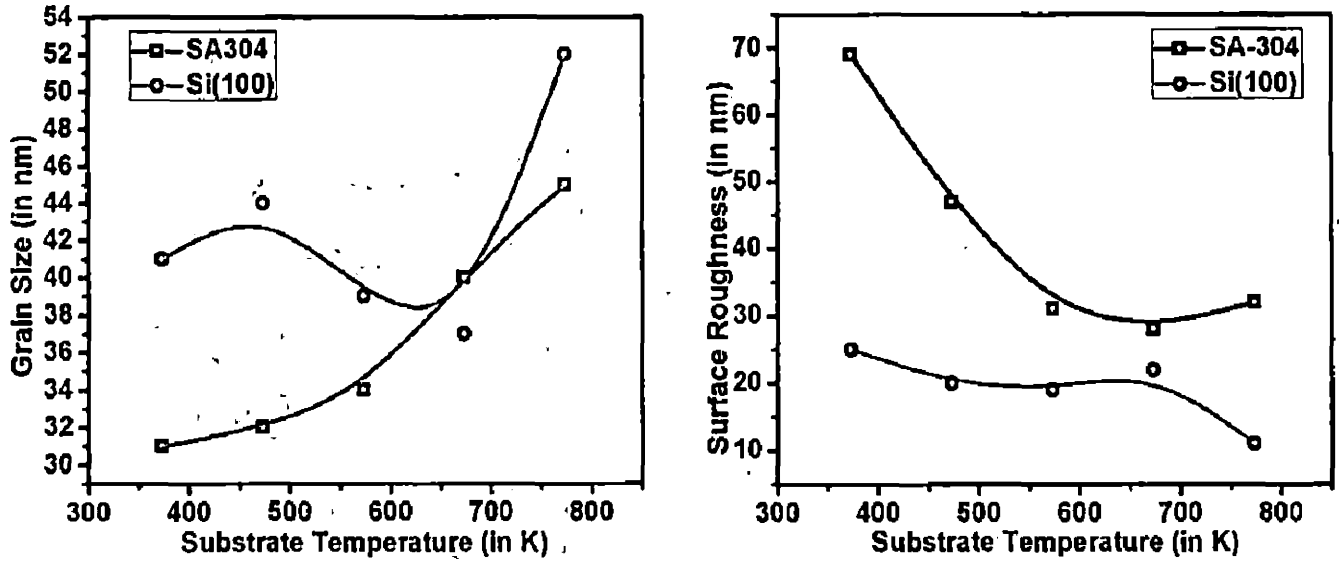

(a) (b)

Figure 5.17 a) Grain size and b) Surface roughness of CrSiN coatings deposited on SA304 and Si(100) substrates as a function of temperature.

The surface morphologies of the CrSiN coatings, deposited on SA304 and Si(100) substrates, were studied using AFM and FE-SEM and shown in **Figure 5.18** and **Figure 5.19**. The root mean square (RMS) roughness values of the as-deposited CrSiN coatings were calculated at different temperature and found to be decreasing with temperature. However, with increasing temperature from 373K to 673K, keeping the remaining parameters constant, the RMS values were found to be decreasing from 69 and 25 nm to 28 and 22 nm, for SA304 and Si(100) substrate, respectively. With further increase in temperature, 773K, the RMS values were stable in the case of coatings deposited on SA304, while it decreases further from 22 to 11 nm for the coatings deposited on Si(100) substrate. It is observed from FESEM micrograph (**Figure 5.19**) that the grain size of CrSiN coating deposited on Si(100) substrate is increasing with increase in temperature from 573K to 773 K. However, there is no appreciable change in the grain size with initial increase in temperature from 373 to 673 K. On the other hand, the coatings deposited on SA304 substrate showed an increase in grain size with increase in temperature from 373 K to 773K. Hence, the deposition temperature affects the grain size as evident from the results of AFM, FESEM and XRD.

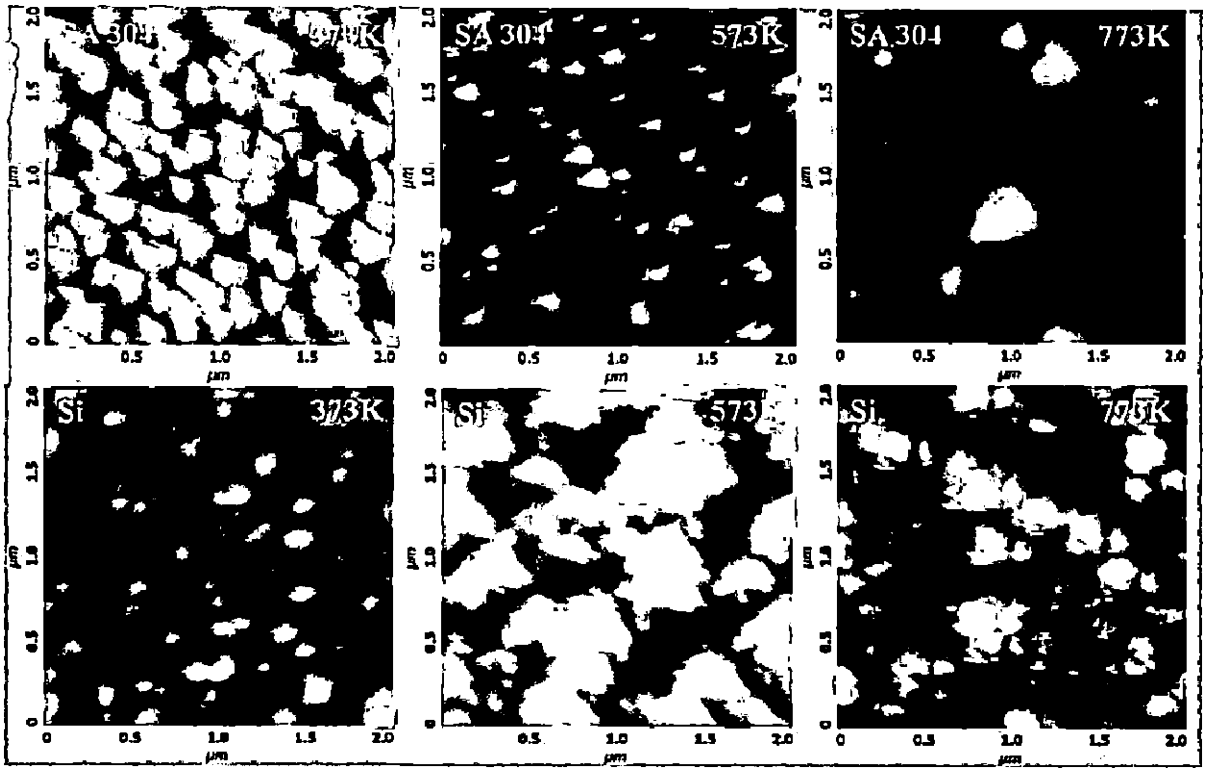

Figure 5.18 AFM images of CrSiN coatings deposited under various temperatures.

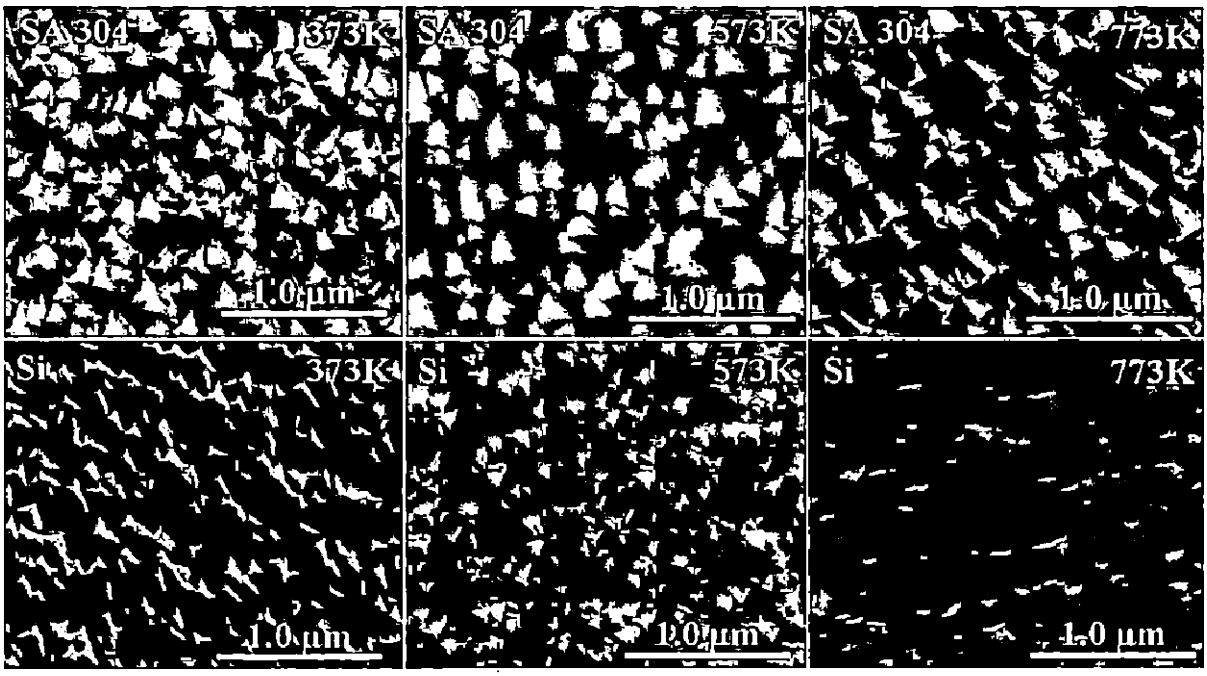

Figure 5.19 FE-SEM images of CrSiN coatings deposited under various temperatures.

5.2.4 Conclusions

The CrSiN coatings have been deposited on Si (100) and SA304 substrates by using reactive magnetron sputtering in the present work. The influence of working pressure, deposition time, substrate temperature and argon: nitrogen gas flow proportion on the morphological and structural properties of the CrSiN coatings were investigated by using XRD, FE-SEM and AFM. The grain size in the CrSiN coatings has increased to 73 nm up to 75 min deposition time in equal proportion of $Ar+N_2$ atmospheres but a reduction in grain size to 61 nm occurs with further increase in the deposition time, at 90 minutes. The elemental compositional analysis of the coatings, by EDS, has shown that Si at % content is reduced while the Cr at.% content is increased with increase in deposition time. However, the nitrogen concentration remains almost constant with increasing deposition time. The reduction in Si content with time is due to reactivity between Si and N leading to the formation of SiN phase at the grain boundary in the coatings. The strain in the coatings has reduced with increasing sputtering pressure during deposition. At temperature 300°C with increasing working pressure, the intensity of preferred orientation (111) has increased due to its lower strain energy.

A small amount of silicon content (3.67 at.% Si) and the increase in nitrogen content contribute for the formation of CrSiN coatings. A shift in the 2θ value to the higher angle corresponding to the CrN(111) and CrN(200) is observed. The CrSiN coatings consist of nanocrystalline CrN grains, show a columnar growth and become dense, with varying crystallite sizes for the increasing nitrogen content with small amount of Si content (3.67 at.%). The films morphology changes from columnar-triangular shape to columnar-needle shape and exhibits a cone growth with a surface roughness of few nanometers at higher nitrogen content (80%). The surface roughness of coatings is decreasing with increasing N_2 content during sputtering. The grain size calculated using XRD, increases from 31 to 45 nm and 41 to 51 nm for the coatings deposited on SA304 and Si(100), respectively, with increase in temperature from 373K to 773K. The RMS values are found to be decreasing from 69 nm and 25 to 28 nm and 11 nm for SA304 and Si(100) substrates, respectively, with increasing substrate temperature from 373 to 773K.

CHAPTER 6

CHROMIUM ALUMNIUM NITRIDE (CrAlN) COATINGS

6.0 Synthesis and Characterization of CrAlN Coatings on SA 304 and Si (100) substrates by Reactive Magnetron Sputtering

The CrAlN coatings on stainless steel (SA 304) and Si (100) substrates were deposited by reactive magnetron sputtering. The influence of addition of Al content on microstructural, mechanical, and tribological properties of CrAlN coatings is discussed in this Chapter.

6.1 Influence of Aluminum Contents on CrAlN Coatings Deposited on SA304 and Si(100) Substrates

6.1.1 Introduction

Transition metal nitrides such as TiN, CrN and HfN, with the NaCl (B1) type lattice structure possess excellent tribological and chemical properties, which enable their use as wear resistant, corrosion resistant, and diffusion barrier coatings. The effect of additions of Al, Si, and, Va on the mechanical and tribological properties of CrN coatings using cathodic arc ion plating (Kawate *et al.* 2003, Uchida 2004), cathodic arc evaporation (Romero *et al.* 2006), and DC/RF magnetron sputtering (Ding *et al.* 2005, Barshilia *et al.* 2006a, Pulugurtha *et al.* 2006, Li *et al.* 2007, Mayrhofer *et al.* 2008) has been reported in the literature. A significant increase in hardness value of 30 GPa (Ding *et al.* 2005), 35 GPa (Brizuela *et al.* 2005), and maximum value of 40 GPa (Ding *et al.* 2008), has been achieved for the CrAlN coatings when compared to CrN coatings. The coatings also exhibited higher thermal stability than pure CrN coatings.

Sun et al. (2004) investigated CrAlN coatings deposited on different substrate materials such as Si (100), commercial aluminum alloy (AA6061), and M42 high speed steel (HSS). They found that the substrate material influences phase evolution in a reactively co-sputtered CrAlN films with Al contents favorable for B1 phase formation. The films deposited on Si (100) substrate showed the formation of single B1 phase (CrAl)N, which correlated well with theoretical predictions. A clustering of Al atoms in the B1 CrN (200) planes seems to occur, which leads to the large contraction of interplanar spacing for the films deposited on the HSS substrate. The coatings became more compact and denser, and the microhardness and fracture toughness of the

coatings increased correspondingly with increasing substrate bias voltage (Chunyan *et al.* 2009). $Cr_{1-x}Al_xN$ coatings deposited on Si and Stainless Steel substrates using RF magnetron sputtering with different atomic concentrations of aluminum ($0.51 < x < 0.69$) showed the evolution of (111), (200), and (102) crystallographic orientations associated to the cubic $Cr_{1-x}Al_xN$ and w-AlN phases, respectively (Sanche'z *et al.* 2010). The insertion of Al or AlN in the B1 type nitride coatings beyond solubility limits leads to phase transition from B1 to B4. Also, the solubility limit of AlN in B1 CrN has been calculated theoretically and found to be 77% as reported in the literature (Makino *et al.* 1998). The B4 Wurtzite phase showed low hardness and poor ductility, which are not desirable for many industrial applications (Sun *et al.* 2004).

An incorporation of Al in to CrN coatings enhanced the tribological, oxidation and mechanical properties as reported in the literature (Banakh *et al.* 2003, Ulrich *et al.* 2003, Baker *et al.* 2003, Uchida 2004) due to the formation of complex aluminum and chromium oxides, which prevents oxygen diffusion to the bulk (Brizuela *et al.* 2005, Su *et al.* 1997, Knotek *et al.* 1991, Schulz et al. 1991, Fleming *et al.* 1992). It has been reported that PVD CrN coatings deposited on turning and milling tools for machining titanium and it alloys, where TiN coating is not suitable due to its strong adhesion (Banakh *et al.* 2003, Ulrich *et al.* 2003, Baker *et al.* 2003, Uchida 2004). With sufficient aluminium content, ($Cr_{1-x}Al_xN$, $x > 0.2$) coating was found to be more oxidation resistant than CrN films (Banakh *et al.* 2003). Wuhrer *et al.* (2004) have made a comparative study of magnetron co-sputtered (Ti,Al)N and (Cr,Al)N coatings and reported that both coatings followed similar development pattern (growth mechanism). The (Cr,Al)N coatings showed high deposition rate and hardness with increasing nitrogen pressure, suggesting its potential for many industrial applications in their work. The wear resistance of the $Cr_{1-x}Al_xN$ was dependent on Al and N concentrations in the coatings (Pulugurtha *et al.* 2007). The nanostructured CrAlN coatings exhibited less material transfer and thus better adhesive wear protection than the TiN coatings under both laboratory pin-on-disc tribo tests and industrial trial conditions (Wang *et al.* 2008). CrAlN coatings deposited on silicon and AISI H13 steel substrates using a modified ion beam enhanced magnetron sputtering system were investigated by Chunyan *et al.* (2009). It was reported in their work that the (111) diffraction peak intensity of the coatings has decreased and the peaks broadened as the bias voltage increased at the same ratio of Al/Cr targets power, which is attributed to the variation in the grain size and microstrain.

A detailed investigation on the influence of microstructural characteristics of reactive magnetron sputtered CrAlN coatings on their mechanical properties, mainly hardness and modulus

The surface roughness of the coatings is decreasing with increasing Al content. The reduction in surface roughness and high density of the coatings may be due to increasing applied voltage to Al target, which increase mobility of the atoms and results in higher nucleation density (Cunha *et al.* 1999) during the formation of denser coating. The high mobility of the adatoms can move in to inter granular voids and diffuse in to the coatings. High nucleation density helps to produce denser coatings and atoms with high mobility diffuse in to the inter granular voids (Lin *et al.* 2008, Cheikh Larbi *et al.* 2006).

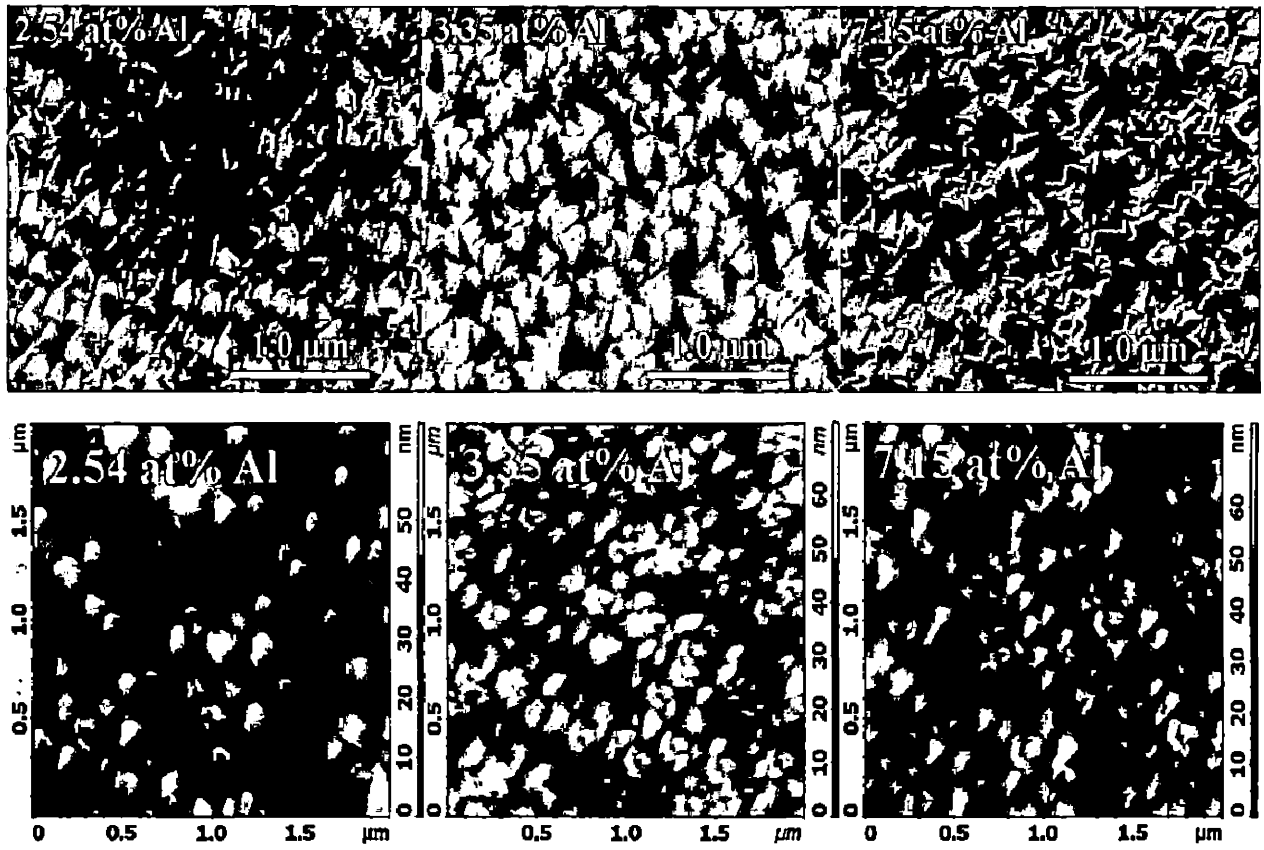

Figure: 6.5 FESEM and AFM images of CrAl(<10%)N coatings deposited on SA304 as a function of Al content.

6.1.2.2.2 Mechanical Properties of CrAlN Coatings Deposited on SA304 Substrate

The Vickers indentation (optical micro hardness tester) was used to measure hardness of CrAlN coatings. The indenter tip is made up of diamond with pyramid shape. The minimum applied load was 5 grams and an average of 5 indents was made to calculate hardness value of CrAlN coated SA304 samples. VDH (Vicker's diamond hardness) is calculated using **Eq. 4.7** with the input of the indenter load and the actual surface area of the impression.

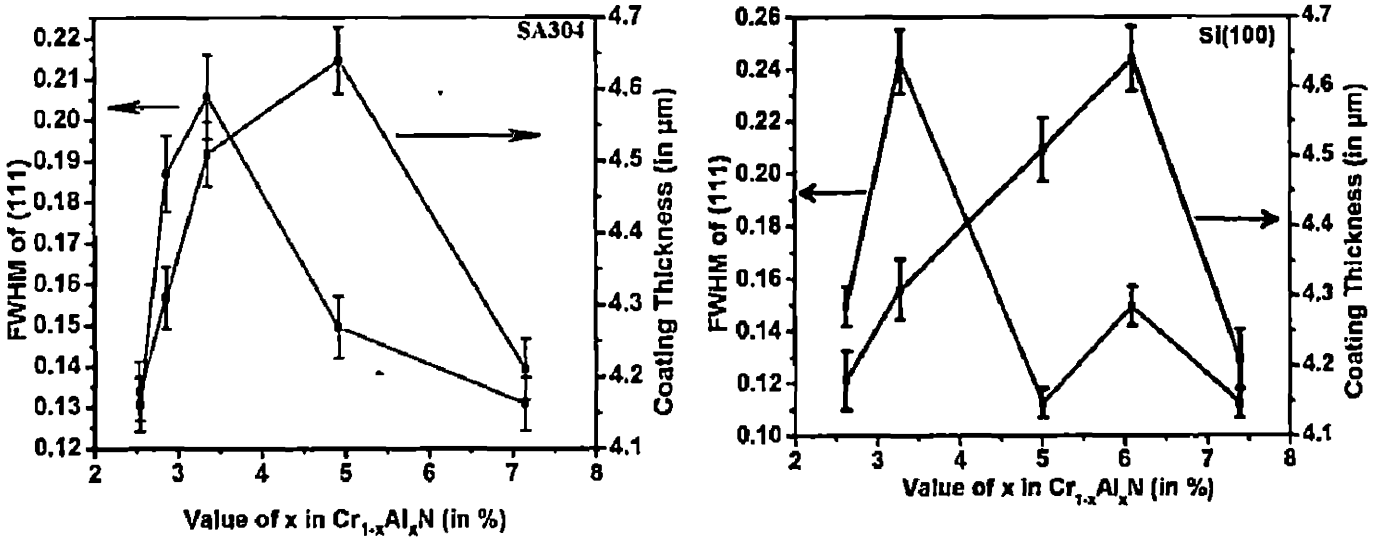

Figure 6.4 FWHM and coating thickness as a function of Al content in CrAl(<10%)N coatings deposited on a) SA304 and b) Si(100) substrate.

Table 6.3 Grain size and surface roughness of CrAlN coatings at different Al content deposited on SA304 and Si(100) substrate.

Substrate	Sample	Grain Size (nm)		Roughness (nm)		Deposition Rate (nm/min)
		XRD	AFM	RMS	Av	
SA304	CrAl(2.53 at.%)N	63	38	10	8	70
	CrAl(2.86 at.%)N	44	36	9.5	7.5	72
	CrAl(3.35 at.%)N	40	37	10	8	75
	CrAl(4.92 at.%)N	56	29	8	7	78
	CrAl(7.15 at.%)N	63	33	9	7	70
Si(100)	CrAl(2.62 at.%)N	56	119	32	26	70
	CrAl(3.28 at.%)N	55	99	27	21	72
	CrAl(5.01 at.%)N	46	91	26	21	75
	CrAl(6.09 at.%)N	33	98	29	28	78
	CrAl(7.39 at.%)N	44	112	35	23	70

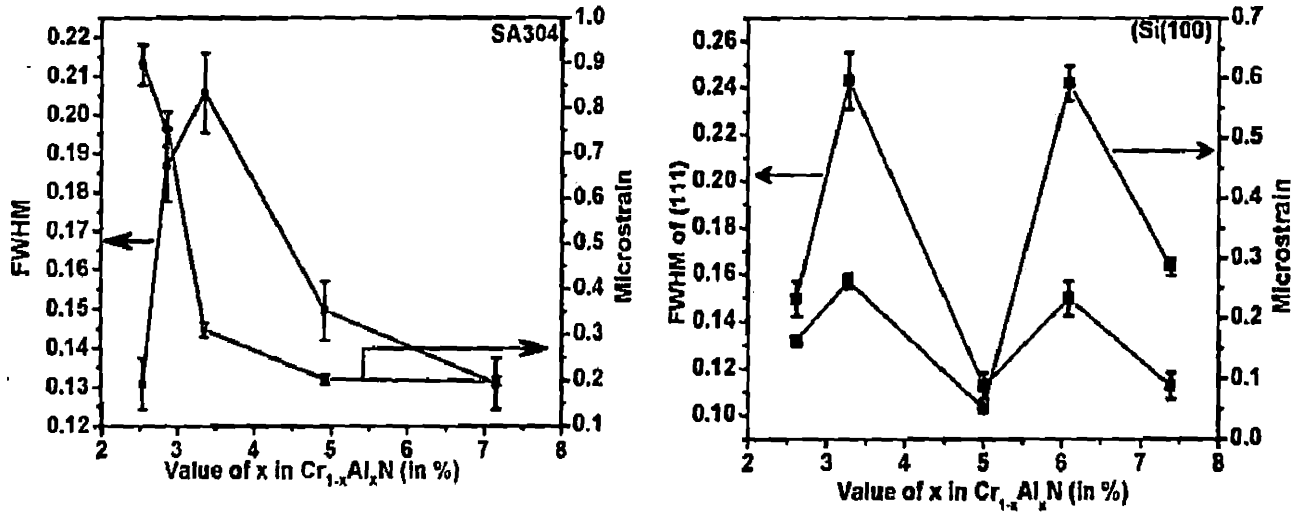

(a) (b)

Figure 6.3 FWHM and Microstrain as a function of Al content in CrAl(<10%)N coatings on a) SA304 and b) Si(100) substrate.

It is evident from the **Figure 6.3a** and **6.3b** that the microstrain of CrAlN is reducing with coating thickness. The lattice microstrain is reducing despite of its higher deposition rate (**Figure 4a and 4b**), which may due to the formation of c-AlN (Li *et al.* 2007). The high residual stresses are responsible for phase separation i.e c-AlN from CrAlN matrix. During the phase separation mechanism, there is a relaxation of the lattice microstrain. However, the phase separation i.e c-AlN from CrAlN, is not reflected in XRD patterns, in both cases, due to the lower intensity of residual stresses. The separation of phase with lower elemental content of Al in the coatings is not possible in the XRD. However, it is reported that c-AlN is a high pressure phase (Pandey *et al.* 1993, Ueno *et al.* 1992, Christensen and Gorczce 1993, Li *et al.* 2007).

Two dimensional surface topography of CrAlN coatings deposited at different Al content, hence different Al target power, was characterised by atomic force microscopy (AFM) and the morphology of same samples were obtained by field emission scanning electron microscopy (**Figure 6.6**). The images show that the coatings become more compact and denser. The overall roughness of the coatings deposited on SA304 substrate was summarized in **Table 6.3**.

coatings on Si(100) substrate (**Figure 6.2b**) shows that the FWHM is reducing with increase in aluminum content, which indicates that the AlN is completely dissolved in CrN phase.

Table 6.2 Calculated FWHM, d-spacing, lattice constant, and lattice microstrain as a function of Al content of CrAlN coatings deposited on SA304 and Si(100) substrates.(Lattice constant: a_0=4.140).

Substrate	Sample	FWHM	D-Spacing	Lattice Constant 'a' for (111) orientation	Micro strain $\varepsilon = (a-a_0)/a_0$
SA304	CrAl(2.53 at.%)N	0.1308	2.4117	4.1771	0.8961
	CrAl(2.86 at.%)N	0.1869	2.4083	4.1712	0.7536
	CrAl(3.35 at.%)N	0.2056	2.3977	4.1529	0.3115
	CrAl(4.92 at.%)N	0.1495	2.3951	4.1484	0.2028
	CrAl(7.15 at.%)N	0.1308	2.3950	4.1482	0.1980
Si(100)	CrAl(2.62 at.%)N	0.1495	2.3965	4.1648	0.1618
	CrAl(3.28 at.%)N	0.2430	2.3916	4.1508	0.2608
	CrAl(5.01 at.%)N	0.1121	2.3941	4.1423	0.0555
	CrAl(6.09 at.%)N	0.1495	2.4046	4.1467	0.5990
	CrAl(7.39 at.%)N	0.1121	2.3971	4.1518	0.2850

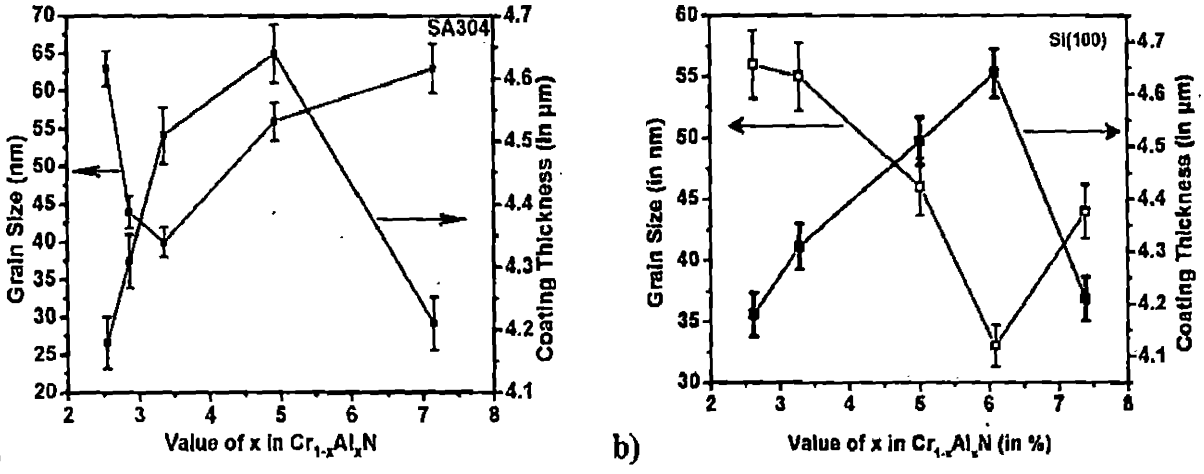

Figure 6.2 Grain size and coating thickness as a function of Al content in CrAl(<10%)N coating on a) SA304 and b) Si(100) substrate.

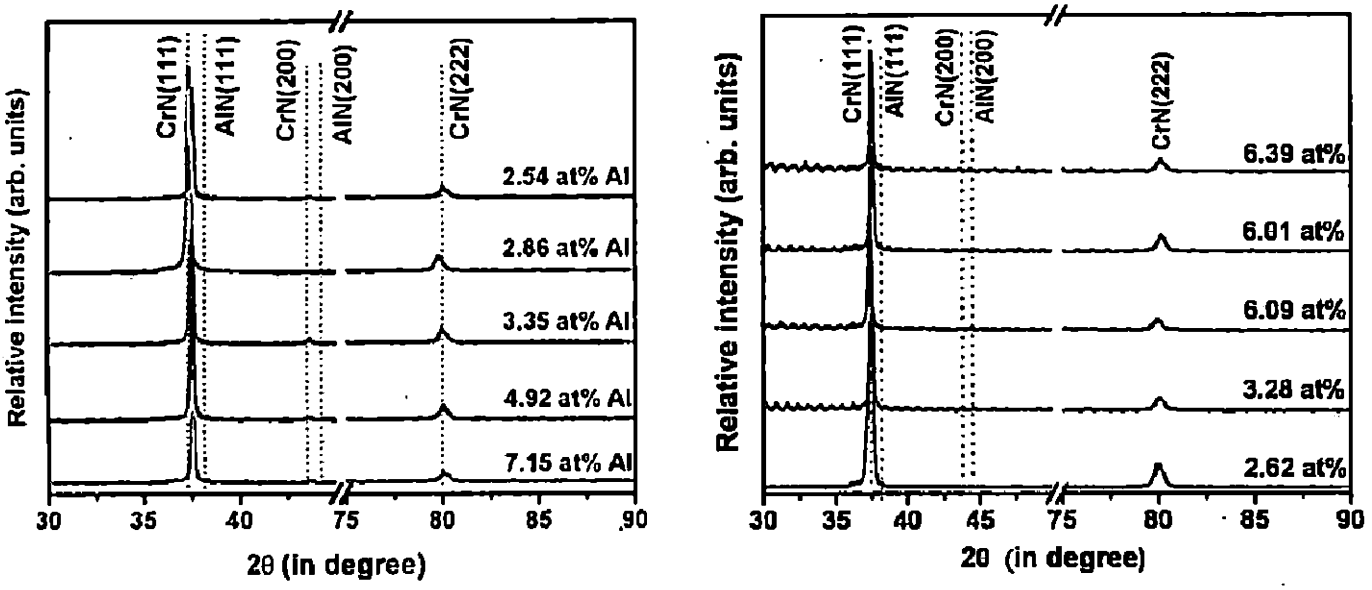

a) b)

Figure 6.1 X-ray diffraction profiles of the as deposited CrAl(<10%)N coatings prepared with different Al content by magnetron sputtering on a) SA304 and b) Si(100) substrates.

It may be because of the high nitrogen content during deposition and high thickness of coating, which favors (111) plane due to the influence of strain energy (Ong *et al.* 2002, Singh *et al.* 2008a, Chawla *et al.* 2009). The lattice constant is calculated from CrN(111) peaks for coating deposited on SA304 and Si(100) substrates. The lattice constant 'a' and lattice microstrain 'ε' were calculated by using equation (4.3) and (4.4) (Gautier *et al.* 1997, Pelleg *et al.* 1991, Schell *et al.* 2003).

The CrAlN coatings were deposited at the same temperature (573K), and therefore, thermal stresses of all the coatings were presumed to be the same in the present work. The grain size and deposition rate of CrAlN coating as a function of Al content is shown in **Figure 6.2.** It was found that with the incorporation of Al atoms in to the CrN coatings, the full width at half maximum (FWHM) of the CrN (111) diffraction peak is increased, and hence there is a reduction in grain size in the CrAlN coatings. The FWHM and microstrain as a function of Al content in CrAlN coatings on SA304 and Si(100) substrates are shown in **Figure 6.3.** CrAl(3.35 at.%)N coatings **(Figure 6.2a)** show a minimum grain size due to its comparatively higher deposition rate (75nm/min). The FWHM of CrAl(3.35 at.%)N coatings, is higher due to its lower grain size. The lattice microstrain of the CrAlN coatings is reducing with Al content and at CrAl(3.35 at.%)N, a lower microstrain value is observed despite its comparatively higher deposition rate. CrAlN

6.1.2.2 Results and Discussion

6.1.2.2.1 Microstructural Analysis of CrAlN Coatings (< 10% Al content) Deposited on SA304 and Si(100) Substrate

All the coatings exhibit NaCl - B1 structure with AlN dissolved in CrN if the composition is within a solubility limit (77%) as discussed in the previous

6.1.1 and it is in accordance with the reported literature. The XRD patterns of the $Cr_{1-x}Al_xN$ coatings deposited on SA304 and Si(100) substrates with various values of Al content is shown in **Figure 6.1a** and **6.1b**, respectively. It is shown that coatings are highly textured with dominant peak of CrN(111) with position being shifted to higher 2θ angle with increasing Al content in the coatings deposited on SA304. Initially, the peak is slightly shifted to lower angle and then shift to higher angle. The peak shift in $Cr_{1-x}Al_xN$ coatings may be due to substitution of Cr atoms by smaller Al atoms in CrN lattice (Sánchez-López *et al.* 2005, Barshilia *et al.* 2006a) as observed in the coatings deposited on SA304 and Si(100) substrates. The peak shifting to higher diffraction angle means that there should be a reduction in'd' spacing and lattice constant and vice versa, as shown in **Table 6.2**. The peak shifting to higher angle indicates that the amount of AlN dissolved in the c-CrN leads to decrease of lattice constant (Sun *et al.* 2004) as shown in **Table 6.2.** It is also noted that the lattice constant of the CrN phase on SA304 and Si substrate decreases with Al content in the coatings. Ding *et. al.* (2008) reported that the reduction in lattice constant indicates the possibility of formation of hexagonal, h-AlN (004) reflection.

The actual solubility limit of Al in the coatings depends on the deposition conditions and the solubility of AlN in cubic CrN is as high as 77 mol%. The saturated CrAlN phase is thermodynamically metastable (Tlili *et al.* 2010, PalDey *et al.* 2002, Mayrhofer *et al.* 2006). The one diffraction peak corresponding to B1 CrAlN was detected from coated SA 304 and Si(100) substrates. There is no appreciable peak separation found within the range of applied power to the Al target as reported by the Li *et al.* (2007). Also, there is no peak between 45° to 75° diffraction angle in both the cases. Only one highly textured peak corresponding to CrN(111) position with very weak CrN(200) orientation is observed from the XRD results instead of two high intensity peak corresponding to CrN(111) and CrN(220) orientations reported in the literature (Sun *et al.* 2004).

is limited in the literature. The transformation from B1 to B4 phase (Wurtzite structure) occurs in CrAlN coating, when the Al content is within the 51% to 69% (Sanche'z *et al.* 2010) and it show comparatively lower hardness and modulus (Sun *et al.* 2004, Zhou *et al.* 1999) than the B1 structure. The Al rich coatings are with B4 phase has good oxidation resistance at high temperature (Li *et al.* 2008). Owing to these facts, the whole experiments on deposition of CrAlN coatings were carried out in two stages in the present work. In first stage, the Al content in CrAlN coatings has been fixed below 10 at.% and its influence on microstructural, mechanical and tribological properties of the coatings has been investigated. In the second stage of experiment, the Al at.% is kept between 10 % to 35 % during deposition of the coatings. The CrAlN coatings were characterized by using the techniques such as XRD, FE-SEM/EDS, and AFM. The hardness was evaluating by using microhardness tester with Vickers diamond indenter. Wear rate and coefficient of friction of the coatings were measured by using Pin-on-Disc tribo tester in the present work.

6.1.2 Microstructural, Mechanical, and Tribological analysis of CrAlN Coatings (< 10% Al content) Deposited on SA304 and Si(100) Substrate

6.1.2.1 Experimental Procedure

CrAlN coatings were deposited on SA304 steel (92 HRb) (15 mm x 15 mm and 0.9 mm thick with a surface finish of 0.01 μm Ra) and silicon wafer, Si(100) (15 x 15 mm) substrates by using DC/RF magnetron sputtering (Model: DCSS – 12, Manufactured by Excel Industries, Mumbai). Chromium target (cathode power fixed at 200 W) and aluminum targets (cathode power varied from 50 W to 110 W) in a mixed Ar/N_2 atmosphere were used for the deposition of coatings. The Ar/N_2 flow ratio was maintained constant at 1:1, while the argon and nitrogen flows set to value of 10 sccm, separately. The thickness of as the deposited coatings varied from 4.0 to 4.5 μm. The SA304 samples were ground and polished to an average surface roughness less than 0.01μm and then cleaned with acetone in an ultrasonic container for 15 min. Similarly, the Si(100) substrates were cleaned by HF treatment followed by rinsing in acetone. The samples were mounted on the rotational substrate holder cum heater and rotated in forward and reverse manner. The rotation angle were set to (25°) in such a way that it covers maximum plasma region. Prior to deposition, the targets were sputter cleaned in Ar gas (1.33 Pa) for 10 min. The deposition parameters are summarized in **Table.6.1**.

The coating thickness was measured by using its cross sectional scanning electron micrographs and stylus profilometer (XP-200 Ambios Technology Inc., USA). The microstructural and topographical analyses were made by field emission scanning electron microscopy (FESEM, Model: 200F, FEI Quanta) and atomic force microscopy (AFM, NTMDT). The coatings composition was determined by using the energy-dispersive X-ray (EDS) technique. The coatings were also analyzed by X-ray diffraction (XRD, Model: D8 Advance, Brucker), to determine the phase composition and orientation using a Ni-filtered CuKα X-ray source. The wear testing of coatings was performed with a pin on disc tribometer (Make: Magnum, Bangalore). The mechanical characterization was carried out by microhardness tester using Vickers diamond tip (Miniload II, Leitz, Germany). For microhardness testing of CrAlN coatings, the applied load value was 5 grams with 27 sec loading time. The indentation was made on five different points in each CrSiN/SA304 sample to obtain its average hardness value. The wear properties were obtained with the help of worn-out surface of pin and disc, wear debris, and friction force produced during tribo test. The stainless steel (SA 304) pin was coated with CrAlN coatings and prepared with square configuration (6 mm x 6 mm), while EN 32 (65 HRC) material used as a counter material. The normal load was kept constant, 10 N, with the relative sliding speed of 0.5 m/s during the test, which was carried out at room atmosphere in dry condition. The friction force between the deposited coatings and the counter material was measured, and divided by the normal load to calculate the friction coefficient. The observation of worn surface of coated pin was performed by a field emission scanning electron microscope (FESEM) and optical microscope (Model: Stemi 2000-C, Zeiss) with high resolution Camera (SONY – Cybershot 4.1 mega pixels Model: DSC – 585).

Table 6.1 Deposition condition for CrAl(<10%)N coatings.

Process parameters and their corresponding values		
Size of Cr and Al target		2" (50.8 mm)
Substrate		SA 304 and Si(100)
Substrate Temperature		573 K
Gas environment and Gas Flow		$Ar+N_2$, 10 sccm
Working Pressure		1.33 Pa
Base Pressure		$5.33x10^{-4}$ Pa
Power:	Cr target	200 W Fixed
	Al target	50, 65, 80, 95, 110 W
Target to Substrate distance		50 mm

The microhardness of CrAlN coatings as a function of Al content is shown in **Figure 6.6**. It is observed from this figure that the hardness value increases from 13.93 GPa, for CrN coatings deposited with similar parameters, to 15.28 GPa for the deposited CrAlN coatings with 2.53 at % Al content. The linear relationship is found between microhardness and Al content (at.%) in the CrAlN coatings. The minimum and maximum hardness of the coatings was found to be 15.28 GPa and 18.81 GPa, respectively. The hardness of coatings measured as a function of Al contents is summarized in **Table 6.4**. The increasing trend of microhardness is quite similar to the result reported by Ding *et al.* (2008). The surface roughness is considerably lower in all the samples; however it is higher than hardness value of CrN. Subsequently, the reduction in grain size (up to 3.35 at.% Al) as well as higher nitrogen content during deposition (50:50) contributes to increase in hardness. Al having smaller atomic size than Cr, also contributes to enhanced hardness of the coatings due to solution hardening. The decrease in the lattice parameter of CrAlN (approximately 0.7%) due to the substitution of some of the Cr atoms by Al atoms in the CrN lattice was observed.

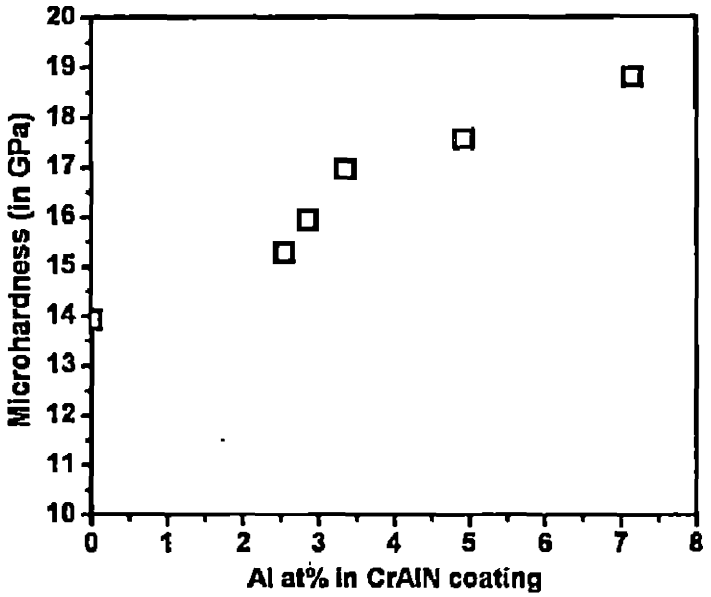

Figure 6.6 Microhardness of CrAlN coatings as a function of Al content.

The increase in hardness is mainly due to reduced lattice constant, covalent nature, solution hardening of CrAlN coatings. The increase in hardness of coatings has also been reported in the literature (Sanche'z *et al.* 2010), if the Al at % increase is within a solubility limit (< 51%).

Table 6.4 Effect of Al content on structural and mechanical properties of CrAlN coatings deposited on SA304 substrate.

Sample	Grain Size (in nm)XRD	Roughness (in nm)		Deposition Rate nm/min	Hardness (GPa)
		RMS	Av		
CrN	70	21	18	67	13.93
CrAl(2.53 at.%)N	63	10	8	70	15.28
CrAl(2.86 at.%)N	44	9.5	7.5	72	15.94
CrAl(3.35 at.%)N	40	10	8	75	16.95
CrAl(4.92 at.%)N	56	8	7	78	17.56
CrAl(7.15 at.%)N	63	9	7	70	18.81

6.1.2.2.3 Tribological Properties of CrAlN Coatings Deposited on SA304 Substrate

When coated pin slides against steel disc (with surface roughness below 100nm), behavior of the material is highly influenced by the differences in hardness between the coated pin and the disc. As can be seen in **Figure 6.7**, the steel disc is severely worn by pin coatings with high hardness, i.e. the CrN and CrAlN coated stainless steel pin. The wear test parameters are given in **Table 6.5**. **Figure 6.8** shows the friction forces produced during slding wear testing of CrAlN coated pin, deposited with different Al at.% concentration. During the pin-on-disc test of CrN coatings, initially, the friction force is found to be around 3 to 5 N up to 5 minutes. Similarly, during the pin-on-disc test of CrAlN coatings, the friction force is found to be around 2.0 to 3.0 N, and then it has increased with sliding distance. It is purely attributed to the lower surface roughness of pin as well as disc, a counterpart, with their values below 10 nm and 100 nm, respectively. Also, it may be due to the perfect surface asperity contact of sample. After the initial time of around 2 to 3 min, friction force is increased suddenly to a range of 5 -8 N (for CrN) and 4–7 N (for CrAlN) in the next 5 to 7 minutes following the generation, breaking, and agglomeration of wear particles between a kinetic pair of pin and disc. Finally, a steady-state range of around 4.5 to 7.0 and 4 to 6.5 N for CrN and CrAlN, respectively, is observed when the friction is governed by the viscous shearing of the coating (Luo 2010).

The CrAlN coatings with lower % of Al content (2.53 at%), within around 2.5 to 3 minutes, the friction force is increased to 5.5 N and it is slowly increased to 7.9 N friction force at 66 minutes of sliding distance as shown in **Figure 6.8.** Similarly, the CrAlN coating with 2.86 at% Al content, the friction force versus sliding distance curve follows the same trend as in the case of coatings with Al content of 2.53 at%. At 58 minutes, the friction force is drastically increased from 4.8N and touches the value of 7.0N. The sudden increase of friction force may indicate the delamination of coatings from the stainless steel substrate and at the same instance, the substrate is touching the disc causing higher friction force. It can be concluded from these results that the wear rate is decreasing with increase in Al content in the coatings and the enhanced tribological properties is due to reduction of mean coefficient of friction to 0.48 N. With further increment of Al at% to 4.92 and 7.15, the COF is found to be 0.57 and 0.51, respectively, with more consistency in the case of highest Al at% (7.15 at%), throughout the testing time. In the case of CrAlN-coatings, the average friction coefficient is found to vary from 0.48 to 0.59.

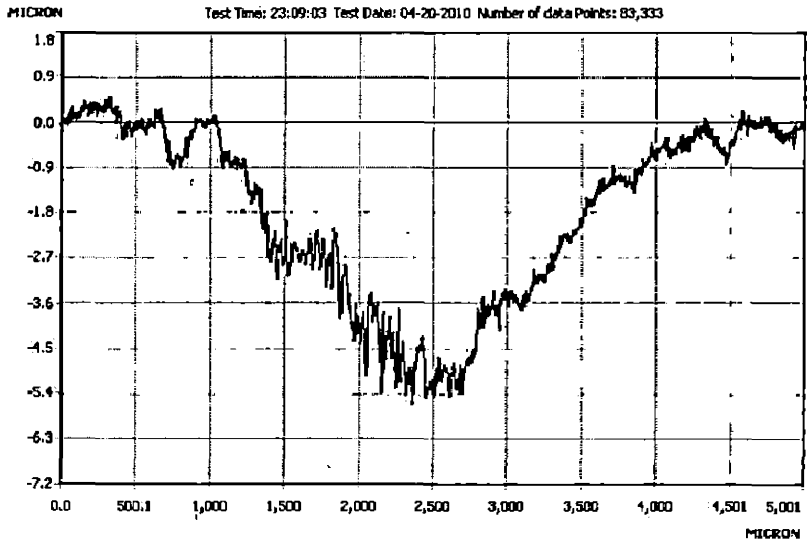

Figure 6.7 Wear track produced on counter disc material (EN32) during sliding of CrAlN coated pin over specific time period. (Test condition: 10N, 0.5m/s, 2000 m sliding distance, 30°C, 32% Rh).

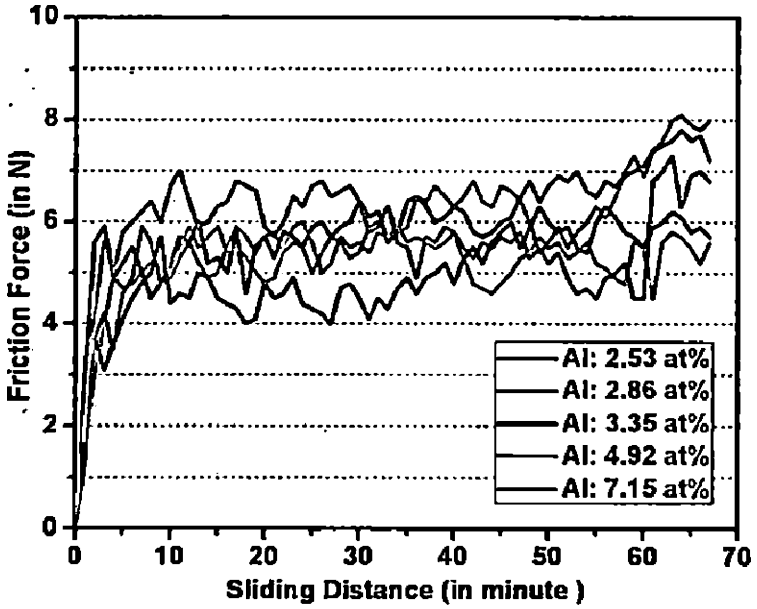

Figure 6.8: Friction force produced during CrAlN coated pin sliding against its counterpart disc of steel (with 10N normal force).

The SEM analysis of the worn out CrAlN coated pin did not show any transfer of Cr or Al element on the counter material, disc, which indicates better adhesion of coating with the substrate. The results are quite similar to Wang *et al.* (2004). In addition to the optical photograph, the EDS carried out on the worn coated pin, reveals the transfer of material from the counter material, which shows lower hardness than coatings.

Table 6.5 Pin on Disc wear test parameters for CrAl(<10%)N.

Coating	CrN and CrAlN Coatings
Substrate / Pin material	Stainless steel (SA304)
Counter Material (Disk)	EN32 (65 HRC)
Normal load applied	10 N
Sliding Speed	0.5 m/s
Environment: Room Temperature	28±1°C
Humidity:	32±5%Rh

The countermaterial (EN32) has worn out strongly than CrN and CrAlN coated pin. The worn particles from countermaterial, mainly Fe element, are oxidized during the tests, which is found as wear debris, get transferred and stick on the surface of the coated pin as shown in **Figure**

6.9. However, the coating material, mainly CrN and CrAlN are not found on counter material, as evident from EDS results. The effects of different Al at% on tribological properties of the coatings (in terms of COF and wear loss) are summarized in **Table 6.6.**

Table 6.6 Influence of Al content on coefficient of friction and wear loss of CrAl(< 10 %)N coatings studied using Pin on Disc method.

Sample	Al at % in the coating	COF (With counter material used Steel)	Wear loss of coating $K'*10^{-5}$ (mm^3/ Nm)
CrN	0%	0.63	6.45
CrAlN	2.53 at%	0.59	4.80
CrAlN	2.86 at%	0.57	5.50
CrAlN	3.35 at%	0.48	2.25
CrAlN	4.92 at%	0.57	3.35
CrAlN	7.15 at%	0.51	3.10

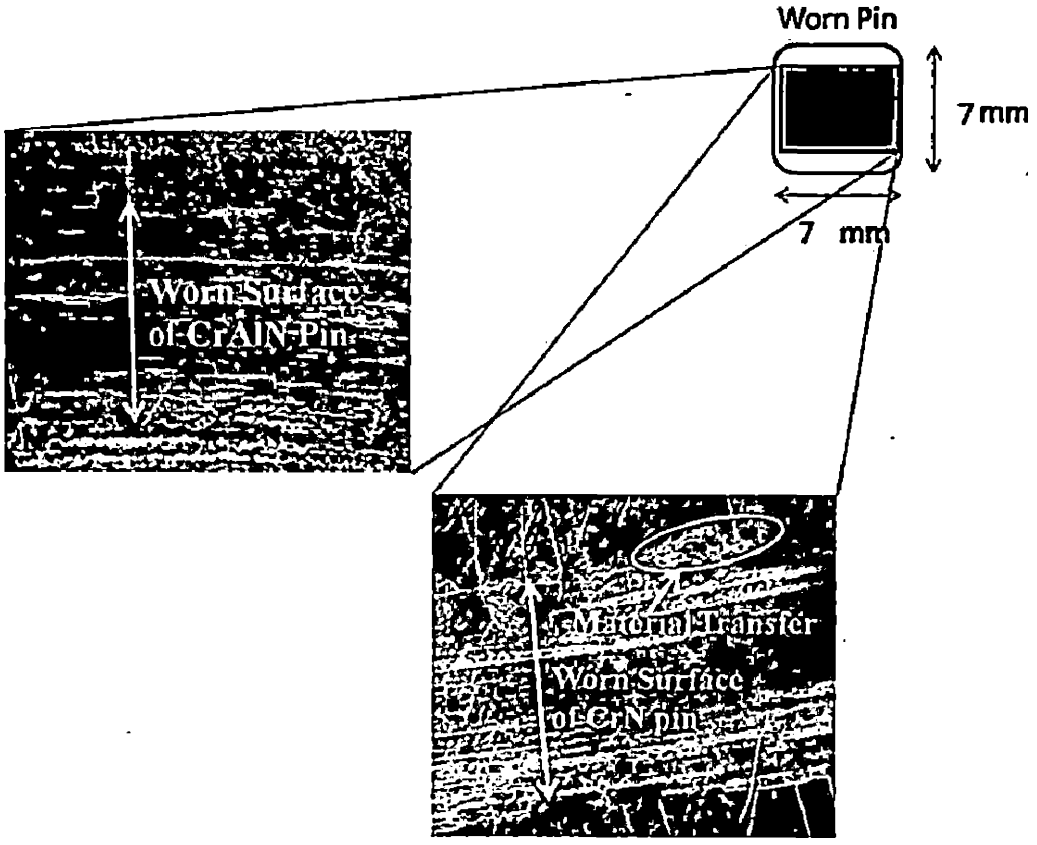

Figure 6.9 Worn out surface of CrN and CrAl(<10%)N pin after pin on disc test.

6.1.3 Microstructural, Mechanical and Tribological analysis of CrAlN Coatings (10% ≤ Al ≤ 35 %) Deposited on SA304 and Si(100) Substrate

6.1.3.1 Experimental Procedure

The CrAlN coatings were deposited on SA304 with the similar procedures as given in Section 6.1.2.1 with slight changes in the process parameters to obtain the desired microstructure and hence, the improved mechanical and tribological properties. The chromium target power was fixed at 60 W while it was varied from 60 W to 110 W for aluminum target in a mixed Ar/N_2 atmosphere during the deposition of coatings. The Ar/N_2 flow ratio was maintained constant at 1:1, while the argon and nitrogen flows were set to value 5 sccm. The deposition parameters are summarized in **Table.6.7**.

The CrAlN coatings were characterized by using XRD, AFM, SEM and EDS, while mechanical and tribological characterization were carried out by using Vicker's microhardness and pin on disc tribotester, respectively. The description of characterization parameters and techniques is given in Section 6.1.2.1 and in Chapter 3 respectively.

Table 6.7 Deposition condition for CrAl(10%≤Al≤35%)N coatings.

Process parameters and their corresponding values	
Target and size	Cr and Al (2" dia.)
Substrate and size	Stainless steel SA304
Base pressure	1×10^{-4} Pa
Temperature	573K
Deposition Time	60 minute
Sputtering pressure	0.66 Pa
Gas environment	$Ar+N_2$ (50:50)
Gas flow	5 sccm
Target to Substrate distance	≈ 50 mm
Power density Cr Target	3.1 W/cm^2
Al Target	3.1 – 5.8 W/cm^2

6.1.3.2 Result and Discussion

6.1.3.2.1 Chemical Analysis

For the analysis of elemental compositions of the CrAlN coatings, EDS is performed and is shown in **Figure 6.10**. It shows the Al/Cr atomic ratio of the as deposited coatings as a function of the ratio of sputtering currents applied onto the Al targets and Cr targets (I_{Al}/I_{Cr}). The result

shows that the Al/Cr atomic ratio in the coatings has increased monotonously with the increase of sputtering current applied to the Al targets. The sputtering current ratio, I_{Al}/I_{Cr}, is much higher than the Al/Cr atomic ratio for each sample, indicating the much lower sputtering yield of aluminium target as compared to that of chromium target. This fact could be ascribed to the formation of an insulating AlN layer on the Al target surface during the reactive sputtering process, which is responsible for reduction in sputtering yield of Al.

6.1.3.2.2 Microstructural Analysis of CrAlN Coatings Deposited on SA304 Substrate

With the addition of aluminum, the CrN coatings gradually crystallize in rocksalt-type cubic structure with CrAlN(111) as a preferential orientation along with lower intensity CrAlN(200) peak as shown in **Figure 6.11**. The lower intensity of CrAlN(200) is mainly due to higher nitrogen content in the chamber during deposition, which favors (111) preferential growth facilitated by comparatively lower strain energy. The Wurtzite-type (B4) structure phase is not observed as the AlN content in the coatings, which is below the critical composition for the phase transition from B1 to B4.

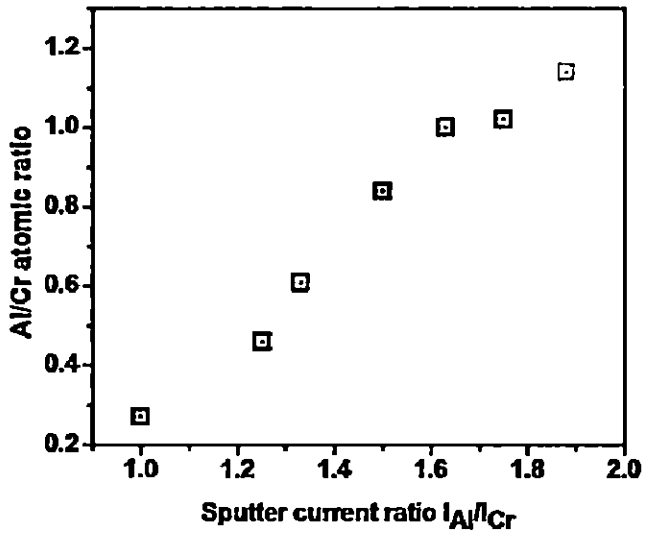

Figure 6.10: Al/Cr atomic ratio in the as-deposited CrAlN coatings as a function of the sputtering current ratio I_{Al}/I_{Cr}.

It is reported that the solubility of AlN in cubic CrN could go as high as 70 mol% (Brizuela *et al.* 2005, Mayrhofer *et al.* 2008), but the supersaturated CrAlN phase is thermodynamically metastable and hence the actual solubility limit finally depends on deposition conditions (Ding *et al.* 2008). The XRD results of the coatings show mainly two diffraction peaks

(111) and (200). The intensity of both the peaks has increased to maximum and then it is slightly reduced to lower intensity value, which shows that initially with the incorporation of Al content, the crystallinity is increased but it gets reduced with the further increase in Al content due to competition between surface and strain energy produced during deposition. The peak position of CrAlN(111) is shifted to higher angle side, indicating a gradual decrease in lattice constant with increase in the aluminum content as shown in **Table 6.8.** This shifting indicates the formation of the CrAlN and the fact could be attributed to lattice distortion caused by smaller aluminium atom incorporation, which substitutes chromium atoms in the coatings. With the incorporation of Al in to the CrN coatings, the full width at half maxima (FWHM) of the (111) diffraction peak has increased to a maximum and then it decreases with the increasing AlN content. The higher deposition rate results in fine grain size with higher microstress as reported in the literature (Barshilia *et al.* 2006, Pulugurtha *et al.* 2006, Li *et al.* 2007). The deposition rate is increased and reaches a maximum at (44 nm/min) for the CrAl(30.06 at%)N coatings deposited with Al/Cr atomic ratio of 0.86. The microstress is increased with deposition rate and the higher kinetic energy of the incident ions distort the crystal lattice, which may result in high FWHM (Figure 6.13). The lattice constant '*a*' is calculated from CrAlN(111) peaks for the coatings deposited on SA304 substrate and lattice microstrain 'ε' was calculated by using equation (4.3) and (4.2) respectively (Gautier *et al.* 1997, Pelleg *et al.* 1991, Schell *et al.* 2003). The lattice constant was found to be decreasing with increasing Al content as shown in **Table 6.8.**

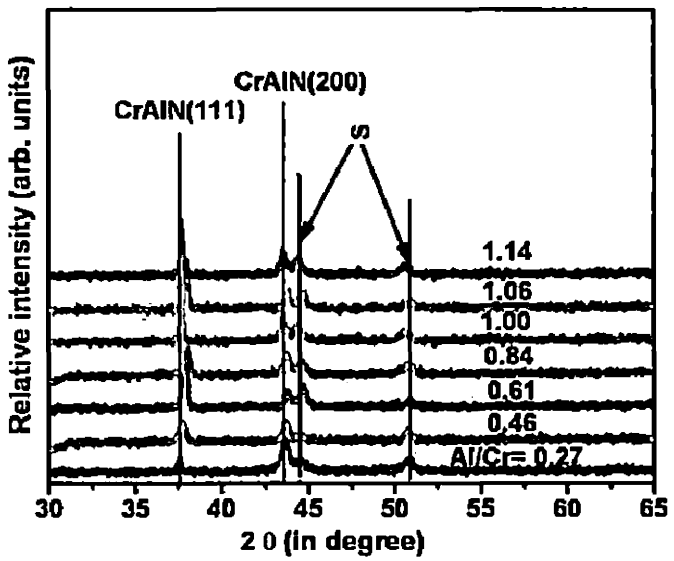

Figure 6.11 X-ray diffraction profiles of the as deposited CrAlN with different Al/Cr atomic ratio. The diffraction peaks marked with S comes from the stainless steel SA304 substrate.

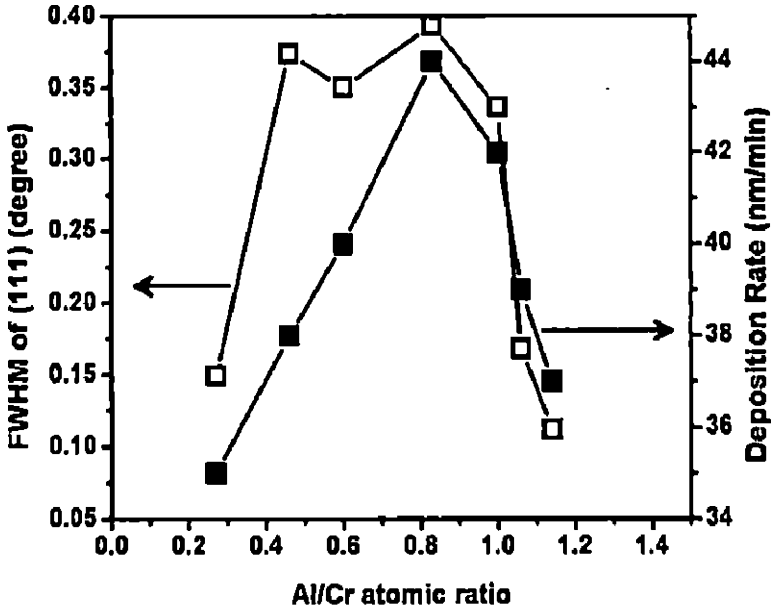

Figure 6.12: FWHM and deposition rate of CrAlN coatings deposited on SA304 substrate as a function of Al/Cr atomic ratio.

Table 6.8 Grain size and hardness of CrAlN coatings as a function of Al/Cr atomic ratio

Al/Cr atomic ratio	Al at% in CrAlN film	FWHM of (111) (degree)	Lattice constant 'a'	Grain Size (nm)	Deposition rate (nm/min)	Surface roughness (nm) RMS	Hardness (GPa)
0.27	14.40	0.1495	4.1473	55	35	7.42	18.28
0.46	20.77	0.3739	4.1299	22	38	8.68	20.16
0.60	25.47	0.3504	4.1335	24	40	8.81	24.8
0.83	30.06	0.3934	4.1094	21	44	3.64	26.2
1.0	31.86	0.3365	4.0916	25	42	8.02	25.3
1.06	33.98	0.1682	4.1035	49	39	6.71	27.2
1.14	34.72	0.1121	4.1127	74	37	9.34	27.9

It has been reported in the literature (Lugscheider *et al.* 2002) that the microstress increases with the deposition rate and hence coating thickness, because of the distortion of crystal lattice of the coating due to the comparatively high kinetic energy of the incident ions. The CrAlN coatings were deposited at the same temperature (573K), and therefore thermal stresses of all the coatings

were presumed to be the same in the present work. The grain size and deposition rate of CrAlN coatings as a function of Al content is shown in **Figure 6.13.** The grain size calculation of all the CrAlN coatings has shown that it is decreasing initially and subsequently reach a minimum for CrAl(30.06at%)N coatings. The minimum grain size at 0.86 Al/Cr atomic ratio is due to higher deposition rate as shown in **Figure 6.13.** Also, the microstrain is observed to be highest among all the coatings due to the high deposition rate. AFM has been used to characterize two and three dimensional surface topography of CrAlN coatings deposited at different Al content and shown in **Figure 6.14.** The morphology of the coatings was characterized by using FE-SEM. The coating becomes more compact and denser as seen in these micrographs. The overall roughness of the coatings deposited on SA304 substrate is summarized in **Table 6.3.** The surface roughness is initially reducing up to 30.04 at% Al and then increasing with increasing Al content. Initially, the reduction in surface roughness and high density of the coating may be due to increasing applied voltage to Al target, which increases mobility of the atoms and results in higher nucleation density (Cunha *et al.* 1999), which leads to the formation of denser coating. The high mobility of adatoms can move in to intergranular voids and diffuse in to the coatings. Higher nucleation density helps to produce denser coatings and atoms with high mobility diffuse in to inter granular voids (Lin *et al.* 2008, Cheikh Larbi *et al.* 2006).

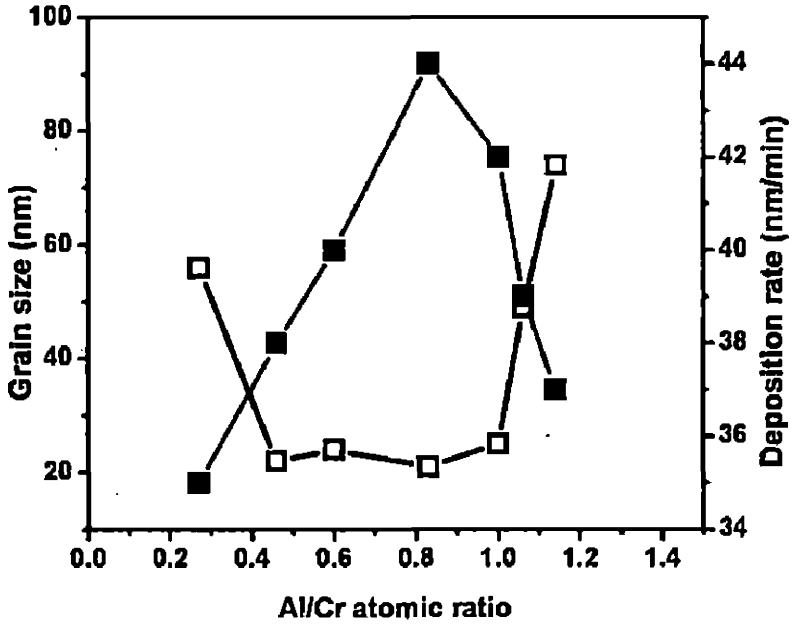

Figure 6.13: Grain size and deposition rate of CrAlN coatings as a function of Al/Cr atomic ratio.

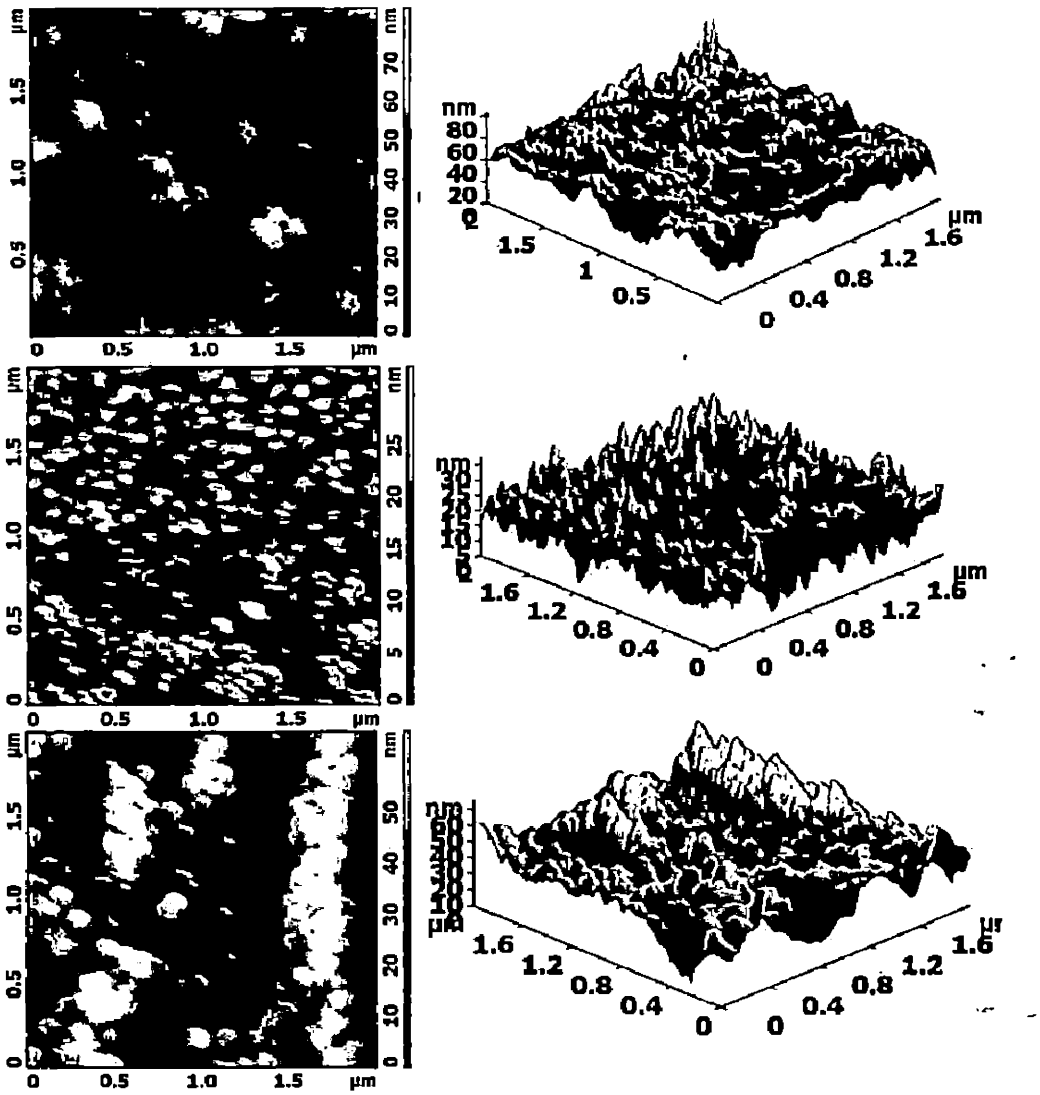

Figure 6.14: 2D and 3D AFM surface morphologies of CrAlN coatings deposited with different Al/Cr atomic ratio.

6.1.3.2.3 Mechanical Properties of CrAlN Coatings Deposited on SA304 Substrate

The microhardness of CrAlN coated SA 304 samples was measured with Vickers indentation tip using similar loading environment as used for previous CrAlN samples. The microhardness of CrAlN coatings as a function of Al content is shown in **Figure 6.15.** It is observed from this figure that the hardness value increases from 18.28 GPa to 27.9 GPa, for Al/Cr atomic ratio, 0.27 and 1.14, respectively. The linear relation is observed between microhardness and Al/Cr ratio in the CrAlN coatings. The minimum and maximum hardness measured were 18.28 GPa and 27.9 GPa, respectively. The measured hardness values as a function of different Al contents in the coatings is summarized in **Table 6.8.** The trend is quite similar to the results

reported by Ding et al. (2008). However, the hardness achieved in the present work 27.9 GPa, is quite reasonable for industrial application. The increase in hardness of CrAlN coatings is mainly due to solid solution hardening effect. Subsequently, the reduction in grain size as well as higher nitrogen content during deposition (50:50) contributes to the increase in hardness.

6.1.3.2.4 Tribological Properties of CrAlN Coatings Deposited on SA304 Substrate

As discussed in Section 6.1.2.2.3, the hardness of pin and disc material affects its wear behavior. The wear test parameters are given in **Table 6.5**. The friction force produced during pin-on-disc test as a function of sliding distance and time duration is shown in **Figure 6.16**. The coefficient of friction (COF), μ, has been calculated for the coating materials using **Eq. 3.14**. The friction force, hence COF of coating, is summarized in **Table 6.9**. The peaks and valley in the friction force diagrams are mainly attributed to the surface roughness of kinetic pair and the asperity contact of samples as discussed in the previous Section 6.1.2.2.3.

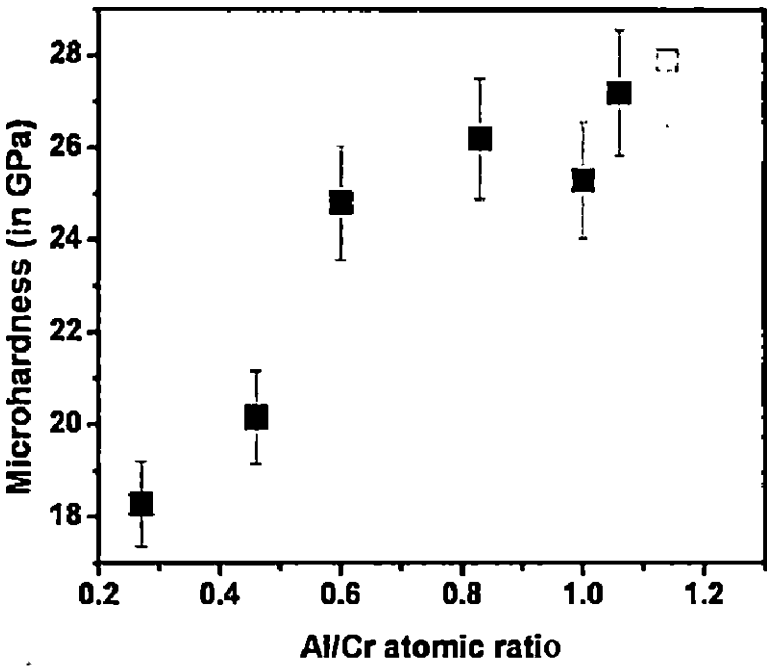

Figure 6.15 Hardness of the as deposited CrAlN coatings on SA304.

For the lower % of Al content (14.40 at%) in the coatings, within around 2.5 to 3 minutes, the friction force is increasing to high value 2- 3 N and with increasing time, it is slowly increased to 5.5 N at a sliding distance of 66 minutes. Similarly, for the CrAlN coatings with 20.77 at% Al content, the friction force versus sliding distance curve follows same trend as in the case of Al

content of 14.40 at% in the coatings. It is reduced here at 58 minutes and then drastically increased from 4.8N and touches the value 7.0N after 66 minutes. The immediate change may indicate the delamination of coatings from the stainless steel substrate and at the same instance; the substrate is touching the disc, causing higher friction force. It can be inferred from the above results that the wear rate is reduced with increase in Al content due to its low mean coefficient of friction (4.8). With increment of Al at% to 14.40 to 33.98, the COF is found to be 0.49 and 0.4, respectively as shown in **Table 6.9**. In the case of CrAlN-coatings, the average friction coefficient has varied from 0.40 to 0.50. The SEM analysis of worn out CrAlN coated pin did not show an adhesive wear mechanism on the countermaterial, disc, which indicates a better adhesion of coating with the substrate. The countermaterial (EN32) exhibits severely worn surface than worn surface by CrN and CrSiN coated pin. It is found that the worn particles from countermaterial, mainly Fe element, get oxidized during the tests and found as wear debris. It gets transferred and stick to the surface of the coated pin. However, the coating material, mainly CrN and CrAlN are not found on counter-material.

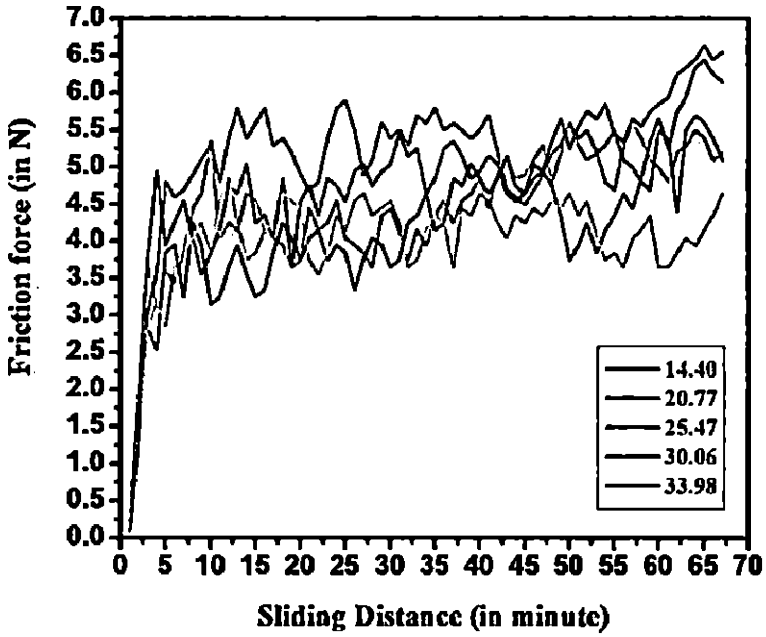

Figure 6.16: Friction force produced during CrAlN coated pin slides against its counterpart disk of steel (with 10N normal force).

Wear debris; in general, are composed of the particles spalling from the pin, a stationary part considered as an upper part, and the disc, a dynamically active part having specific sliding velocity considered as a lower specimens during the wear process. In order to understand the

correlation between wear debris and wear rate of the specimens, the constituents of the debris should be determined first. The mean particle size is naturally related to operating conditions.

Table 6.9 Influence of Al content on coefficient of friction and wear loss of CrAlN coatings studied using Pin on Disc method (50% N_2).

Al/Cr atomic ratio	Al at % in the coating	COF (with EN32 as a counter material)	Wear Lloss of coating K'x10^{-6} (mm^3/ N.m)
0.27	14.40	0.49	7.92
0.46	20.77	0.50	5.85
0.60	25.47	0.44	4.55
0.83	30.06	0.42	3.25
1.0	31.86	--	--
1.06	33.98	0.40	1.38
1.14	34.72	--	--

In the present study, the load applied to wear tests was always constant at 10 N. The micrographs of wear debris reveal that the mean particle size produced at different chemical composition cannot be used as the standard of evaluating specimen's wear rate as it shows same behavior in CrN and CrAlN coatings. The elements of the wear debris generated at the sliding speed of 0.5 m/s are mostly composed of iron and ironic oxides as well as a small amount of hard coating i.e., CrN particles. As the coated specimens become hard by adding the different elements, i.e addition of Al and Si in CrN coating, the wear loss of the upper specimen, different coated pin, is no longer the dominant one. However, wear loss of the lower specimen is actually contributed major part of the debris quantity. During wear test, the transferred materials from the counter material can be compacted and mechanically mixed with the coating material, and the mixture of debris formed a thin layer and stick to the coated surface, which contribute to the reduction in wear (Yang *et al.* 2008). Due to the localized high temperature caused by friction during dry sliding, the surface layer also reacted with oxygen in the ambient room atmosphere forming oxides. This tribo-oxidation plays an important role in controlling friction between the sliding pin and disc surface, therefore affecting the wear behavior of the coatings. It is evident from the wear rates shown in Table 6.9 that the formation of transfer layer in the coating sample with increase in Al content has contributed to the reduced wear rate and COF as explained in Chapter 4 and 5 **(Dey and Biswas, 2009)**.

6.1.4 Conclusion

CrAlN coatings with different Al content (Phase I: < 10% and Phase II: 10% < Al < 35%) were deposited on SA304 and Si substrates by a reactive magnetron sputtering technique. The deposited coatings are highly textured with dominating peak of CrAlN(111), with position being shifted to higher 2θ angle with increasing Al content deposited on SA304. There is no appreciable peak separation found within the range of applied power to the Al target up to 20.77 at% Al. The grain size is reduced to 22 nm at 30.06 at% Al content, which is minimum in all the experiments and then, grain size increases to 48 nm with further increase in Al content up to 34.72%. The surface roughness is comparatively low, between 2 to 10 nm in all the coatings with varying Al content. The low surface roughness and high density of the coating may be due to increasing applied voltage to Al target, which increases mobility of the atoms and results in higher nucleation density leading to denser coating. The linear relation is observed between microhardness and Al content (at%) in the CrAlN coatings. The minimum and maximum hardness measured were 15.28 GPa and 27.90 GPa, respectively, which is quite higher than CrN coatings (13.93 GPa) deposited under similar conditions. The wear resistance of all the CrAlN coatings is better than that of pure CrN coatings deposited under similar conditions, and it is improved gradually with the increase of aluminum incorporation in the coatings. Wear rate is reduced with increase in Al content and hence hardness, leading to the improvement of tribological properties due to reduction in mean coefficient of friction to 0.40 in the case of CrAlN coatings, while in CrN coatings, the COF was found to be 0.644.

6.1.5 Comparison of Present Work with the Existing Literature

The mechanical and tribological properties of CrAlN coatings were evaluated in the present work. For CrAlN coating, the hardness is found to be varying from 18 GPa to 41 GPa, while the COF and wear rate varying from 0.3 to 0.84 and 3.36 X 10^{-6} mm^3/Nm, respectively. The hardness (*H*) and coefficient of friction (COF) were found to be 27.9 GPa and 0.4, respectively. The wear rate of the coatings is 1.38 x 10^{-6} mm^3/Nm. The CrAlN coatings with 33.98 at. % Al content gives best results and the components coated by the CrAlN coating could be better substitute for CrN and CrSiN coatings. The reduction in wear rate and COF indicates the better adhesion of coatings with the substrates, could be potential materials for machining industries. The hardness of CrAlN is found to be almost similar to the CrSiN coatings.

CHAPTER 7

CONCLUSIONS AND FUTURE SCOPE

The present work has been focused to synthesize chromium based hard coatings such as chromium nitride (CrN), chromium silicon nitride (CrSiN), and chromium alumnium nitride (CrAlN) on stainless steel and silicon substrate by DC/RF reactive magnetron sputtering technique. The effects of sputtering parameters on structural, mechanical and tribological properties of these materials were investigated. The following brief conclusions are made based on the results obtained on the aforementioned hard coatings. The suggestions for the future work are proposed at the end.

7.1 Effect of Working Pressure, Temperature, and Target Power on DC Magnetron Sputtered CrN Coatings Deposited on Si(100) and Stainless Steel (SA304) Substrate

The effect of working pressure, temperature, and power on the microstructural characteristics such as texture, grain morphology, and surface roughness of CrN coatings deposited on Sj (100) and SA 304 substrates has been analyzed. It has been observed based on the experimental results that CrN coatings exhibits (111) preferred orientation and it transforms into (200) orientation with the increasing working pressure. The coatings deposited at lower working pressure showed a large grain size with higher crystallinity but it has reduced with increase in working pressure. The preferred orientations of the CrN coatings depend on sputtering conditions, thickness of the coatings, and the induced microstrain in the coatings. Also, the texture coefficient is affected by the working pressure and temperature during deposition. The microstrain in the CrN coatings is decreasing with increasing working pressure for the low deposition temperature of 473K. The columnar grain morphology is observed for the coatings for the chosen deposition conditions. The microhardness of CrN coatings showed an increasing trend due to the combined effect of temperature, working pressure, and power density. The high hardness of the coatings is due to the grain size effect, highly textured grains and compressive residual stress in the coatings.

7.2 Influence of Sputtering Parameters and Reactive Gases on Microstructure, Mechanical, and Tribological Properties of Chromium Nitride Coatings Deposited on SS-304 Substrates by DC-Reactive Magnetron Sputtering

The influence of varying contents of N_2 and Ar gases, variation in deposition conditions ($Ar+N_2$, Pure N_2 and $He+N_2$), and the effect of substrate temperature in pure nitrogen environment on the morphological and microhardness of the CrN coatings were investigated. The micro structural features of coated samples were studied by using XRD, SEM, and AFM. Microhardness, nanoindentation tester, and pin on disc (dry sliding wear) were used to measure the mechanical and tribological properties of the coated sample, respectively. The following conclusions are made based on the above study.

The grain size of CrN coatings is decreasing with increase in nitrogen content in the sputtering chamber. The coatings become denser at higher nitrogen percentage in the gas mixture. The surface roughness of CrN coatings decreases with increasing nitrogen content and substrate temperature. The deposited coatings in pure N_2 and ($He+N_2$) atmosphere lead to lower coating thickness and grain size as compared to coatings deposited in $Ar+N_2$ atmosphere. It may be due to lower sputtering yield of helium ions than argon ions. A mixture of different gases affects the surface morphology, grain size and microhardness of CrN coatings. A mixture of CrN + Cr_2N phase has formed up to 30% nitrogen content in the chamber while at very high N_2 content, there is a phase change and single phase CrN coatings is observed. The microhardness value of CrN +Cr_2N (at 30% N_2 content in the chamber) phase is higher 16.95 GPa than the CrN (above 40% N_2 content) phase. The hardness and modulus of the coatings were influenced by the factors such as grain size, grain morphology, film defects, density, and surface roughness of the coating. The CrN coatings deposited, at 60:40 $Ar:N_2$ content, showed the high hardness value of 21 GPa and lower modulus value of 276 GPa, measured by nanoindentation, which is attributed mainly to the mixture of Cr_2N and CrN phase present in the coatings. The enhancement in hardness may also be due to reduction in surface roughness (RMS) and low film defects (porosity), which increase density of the coatings. The CrN coatings deposited in pure N_2 exhibits a high hardness (27 GPa) and modulus (253 GPa) as compared to that of the coatings deposited in $Ar:N_2$ environment, mainly

due to solid solution hardening of chromium film by nitrogen atoms supported by fine grain size (≈15nm) and comparatively lower surface roughness.

The coefficient of friction (COF) of CrN coatings was found to be varying from 0.63 to 0.68. The coatings deposited in pure N_2 environment show comparatively lower COF (0.64) than CrN coatings deposited with different Ar:N_2 proportion (0.68). The SEM analysis of coated pins revealed that an adhesive wear mechanism manifests in the contact area during the test. During wear test, the transferred materials from the countermaterial get compacted and mechanically mixed with the coating material, and the mixture of debris formed a layer and stick to the coated surface, which contribute to the reduction in wear. The favorable conditions for synthesis of CrN coatings with improved properties are given in the **Table 7.1.**

7.3 Influence of Silicon Content on the Microstructure, Mechanical and Tribological Properties of CrN Coatings Deposited by Reactive Magnetron Sputtering

The surface roughness and grain size of CrSiN coatings decrease with increasing Si conter as observed in the present work. The coatings exhibit a triangular needle-shaped columna morphology, which transform into a finer columnar morphology at higher Si contents of 14.88 at.%. The maximum nanohardness and modulus of CrSiN coatings are found to be 28 GPa and 246 GPa, respectively. The maximum hardness of 28 GPa is observed with 6.33at % Si in the coatings, which is due to size effect caused by grain refinement. However, with the further increase in Si content, the hardness is reduced due to high volume fraction of a-Si_3N_4. The tribological properties of the CrSiN coatings were evaluated by pin-on-disc test. The COF and wear loss of the coatings are found to be 0.49 and 1.93×10^{-6} mm^3/Nm, respectively. The improved wear resistance and reduction in COF of the CrSiN coatings are due to the formation of amorphous SiN_x phase and the oxide layers (silica and chromia) in the coatings.

7.4 Synthesis and Microstructural Characterization of CrSiN Coatings Deposited on Si(100) and SA304 Substrate

The influence of working pressure, deposition time, substrate temperature and argon:nitrogen gas flow proportion on the morphological and structural properties of the CrSiN

coatings were investigated by using XRD, FE-SEM and AFM. The conclusions based on the present study are given below.

The grain size in the CrSiN coatings has increased to 73 nm for the deposition time of 75 min, under the conditions of equal proportion of $Ar+N_2$ atmospheres, but a reduction in grain size to 61 nm occurs with further increase in the deposition time, at 90 minutes. The elemental compositional analysis of the coatings, by EDS, has shown that Si at % content is reduced while the Cr at% content is increased with increase in deposition time. However, the nitrogen concentration remains almost constant with increasing deposition time. The reduction in Si content with time is due to reactivity between Si and N leading to the formation of SiN_x phase at the grain boundary in the coatings. The strain in the coatings has reduced with increasing sputtering pressure during deposition. At temperature 573K, with increasing working pressure, the intensity of preferred orientation (111) has increased due to its lower strain energy.

A small amount of silicon content (3.67at% Si) and the increase in nitrogen content contribute for the formation of CrSiN coatings. A shift in the 2θ value to the higher angle corresponding to the CrN(111) and CrN(200) is observed. The CrSiN coatings consist of nanocrystalline CrN grains, show a columnar growth and become dense, with varying crystallite sizes for the increasing nitrogen content with small amount of Si content (3.67 at%). The morphology of coatings changes from columnar-triangular shape to columnar-needle shape and exhibits a cone growth with a surface roughness of few nanometers at higher nitrogen content (80%). The surface roughness of coatings is decreasing with increasing N_2 content during sputtering. The grain size calculated using XRD, increases from 31 to 45 nm and 41 to 51 nm for the coatings deposited on SA304 and Si(100), respectively, with increase in temperature from 373K to 773K. The RMS values are found to be decreasing from 69 nm and 25 to 28 nm and 11 nm for SA304 and Si(100) substrates, respectively, with increasing substrate temperature from 373 to 773K. The best structural, mechanical, and tribological properties obtained with variation in silicon content in the CrN coatings are given **Table 7.1.**

Table 7.1 Favorable conditions for the deposition of chromium based hard coatings with improved properties.

Process Conditions	Mechanical Properties				Tribological Properties		Possible Hardening Mechanism
	H (GPa)	E (GPa)	E* (GPa)	H^3/E^{*2}	COF	Wear rate (mm^3/Nm)	
CrN coatings deposited with different N_2 gas							
1.33 Pa, 75 W, 573K, 60 min, ≈50 mm, **Ar:N_2 : 60:40**	21	276	303	0.10	--	--	Cr_2N phase with hexagonal structure
CrN coatings deposited in pure N_2 environment							
1.33 Pa, 75 W, **673K**, 60 min, ≈50 mm, **Pure N_2**	27	241	265	0.28	0.64	1.40×10^{-4}	Solid solution hardening supported by dense structure and grain refinement
CrSiN coatings with varying at. % of Si content (6.33 at. % Si content)							
1.33 Pa, 175 W DC / **75 W RF**, 573 K, 60 min, ≈ 50 mm, Ar:N_2 : 50:50	28	246	270	0.30	0.49	1.93×10^{-6}	Grain refinement and formation of denser composite microstructure.
CrAlN coatings with varying at. % of Al content (33.98 at. % Al content)							
0.66 Pa, 60 W DC / **105 W RF**, 573K, 60 min, ≈50 mm, Ar:N_2 : 50:50	27.9	--	--	--	0.40	1.38×10^{-6}	Solid solution hardening supported by grain refinement, dense structure and higher nitrogen content

7.5 Influence of Aluminum (Al) content on the Microstructure, Mechanical and Tribological Properties of CrAlN Coatings Deposited by Reactive Magnetron Sputtering on SA304 and Si(100) Substrates

The CrAlN coatings are highly textured with preferred orientation of CrN(111), which shifts to higher 2θ angle with increasing Al contents in the coatings. The grain size is reduced to 22 nm at 30.06 at% Al content, which is minimum in all the experiments and then, it increases to 48 nm with further increase in Al contents up to 34.72%. The surface roughness is comparatively low, between 2 to 10 nm in all the coatings with varying Al content. The low surface roughness and high density of the coatings may be due to increasing applied voltage to Al target, which increases mobility of the atoms leading to the formation of denser coatings. The minimum and maximum hardness measured were 15.28 GPa and 27.90 GPa, respectively, which is quite higher than CrN coatings (13.93 GPa) deposited under similar conditions. The mean COF and wear rate of CrAlN coatings is found to be to 0.40 and 1.38×10^{-6} mm^3/Nm, respectively, which is less than the CrN coatings, where it is found to be 0.644 and 1.40×10^{-4} mm^3/ Nm, respectively. The analysis of the worn out CrAlN coated pin did not show an adhesive wear mechanism, which indicate better adhesion of coatings with the substrate. The favorable conditions for the deposition of CrAlN coatings with improved properties are summarized in **Table 7.1**.

SUGGESTIONS FOR FUTURE WORK

Based on the present work carried out on the Cr based nitride coatings such as CrN, CrSiN, and CrAlN the following recommendations for the future work are proposed.

1. It is very essential to study the influence of substrate bias and target to substrate distance on the growth of the CrN, CrSiN and CrAlN coatings for obtaining the desirable microstructural characteristics such as fine grain size, textures, and high density in the coatings. The substrate biasing, during deposition of the coatings, is one of the important process parameters to achieve good mechanical properties.
2. The mechanical properties such as bonding strength and scratch resistance of the CrN, CrSiN and CrAlN hard coatings ought to be studied using nanoindentation technique for understanding the failure mechanisms. It would enable to develop superhard and ultrahard coatings hitherto unachieved in the literature.
3. The compositional analysis and bonding nature of the coatings need to be analysed by using XPS for the accurate tailoring of compositions in the coatings as it affects the properties of the coatings significantly.
4. The stresses developed during deposition of CrN, CrSiN and CrAlN coatings by sputtering technique should be measured experimentally as it influence their tribological properties.
5. An attempt can be made for the deposition of multilayer coatings such as CrN/a-SiNx and CrN/AlN for realizing the enhanced hardness and tribological properties of the coatings.
6. A detailed analysis of microstructural and microchemical characterization of the damaged coatings, after pin-on-disc test, using TEM is necessary to understand the tribochemical mechanisms.

REFERENCES

1. **Arzt E.**, "Size effects in materials due to microstructural and dimensional constraints: A comparative review", Acta Matellurgica **46** (1998) 5611-5626.
2. **ASTM standard**, Designation G99-05, "Standard test method for wear testing with a Pin on Disc apparatus", May **2005.**
3. **Aubert A.**, Danroc J., Gaucher A., Terrat, J. P., "Hard chrome and molybdenum coatings produced by physical vapor deposition", Thin Solid Films **126** (1985) 61-67.
4. **Aubert A.**, Gillet R., Gaucher A., Terrat J. P., "Hard chrome coatings deposited by physical vapor deposition", Thin Solid Films **108** (1983) 165-172.
5. **Azzi M.**, Benkahoul M., Szpunar J.A., Klemberg-Sapieha J.E., Martinu L., "Tribological properties of CrSiN-coated 301 stainless steel under wet and dry conditions", Wear **267** (2009) 882–889.
6. **Baker M.A.**, Kench P.J., Joseph M.C., Tsotsos C., Leyland A., Matthews A. , "The nanostructure and mechanical properties of PVD CrCu (N) coatings", Surface and Coatings Technology **162** (2003) 222-227.
7. **Banakh O.**, Schmid P. E., Sanjines R., Levy F., "High-temperature oxidation resistance of CrAlN thin films deposited by reactive magnetron sputtering", Surface and Coatings Technology 163-164 (2003) 57-61.
8. **Barata. A**, Cunha L, Moura C, "Characterisation of chromium nitride films produced by PVD techniques", Thin Solid Films 398-**399** (2001) 501.
9. **Barshilia H. C.**, Rajam K. S, "Reactive sputtering of hard nitride coatings using asymmetric-bipolar pulsed DC generator", Surface and Coatings Technology **201** (2006) 1827-1835.
10. **Barshilia H. C.**, Selvakumar N., Deepthi B., Rajam K. S., "A comparative study of reactive direct current magnetron sputtered CrAlN and CrN coatings", Surface and Coatings Technology **201** (2006) 2193-2201.
11. **Basnyat P.**, Luster B., Kertzman Z., Stadler S., Kohli P., Aouadi S., Xu J., Mishra S. R., Eryilmaz O. L., Erdemir A., "Mechanical and tribological properties of CrAlN-Ag self-lubricating films", Surface and Coatings Technology **202** (2007) 1011–1016.

12. **Basu B,** Sarkar J., and Mishra R, "Understanding Friction and Wear Mechanisms of High-Purity Titanium against Steel in Liquid Nitrogen Temperature", Metallurgical and Materials Transactions A 40A (2009) 472- 480.
13. **Bayer Raymond G,** "Mechanical Wear fundamentals and Testing", ed. **2nd**, Marcel Dekker Inc., NY, (**2004**).
14. **Behrisch R.**, "Sputtering by Particle bombardment", Springer Publication, Berlin, 1981.
15. **Benkahoul M.**, Robin P., Gujrathi S. C., Martinu L., Klemberg-Sapieha J. E., "Microstructure and mechanical properties of Cr–Si–N coatings prepared by pulsed reactive dual magnetron sputtering", Surface and Coatings Technology **202** (2008) 3975–3980.
16. **Benkahoul M.**, Robin P., Martinu L., Klemberg- Sapieha J. E., "Tribological properties of duplex Cr–Si–N coatings on SS410 steel", Surface and Coatings Technology **203** (2009) 934–940.
17. **Bertrand G.**, Savall C., Meunier C., "Properties of reactively RF magnetron-sputtered chromium nitride coatings", Surface and Coatings Technology **96** (1997) 323-329.
18. **Bielawski** M, Seo D., "Residual stress development in UMS TiN coatings", Surface and Coating Technology **200** (2005) 1476-1482.
19. **Binnig, G.**; Quate, C. F.; Gerber, Ch. Physical Review Letter, **56** (1986) 930.
20. **Bobzin K.**, Bagcivan N., Goebbels N., Yilmaz K., Hoehn B. R., Michaelis K., Hochmann M., "Lubricated PVD CrAlN and WC/C coatings for automotive applications", Surface and Coatings Technology **204** (2009) 1097–1101.
21. **Bobzin K.**, Lugscheider E., Nickel R., Bagcivan N., Kramer A., "Wear behavior of $Cr_{1-x}Al_xN$ PVD-coatings in dry running conditions", Wear **263** (2007) 1274-1280.
22. **Bousser E.**, Benkahoul M., Martinu L., Klemberg-Sapieha J. E., "Effect of microstructure on the erosion resistance of Cr–Si–N coatings", Surface and Coatings Technology **203** (2008) 776–780.
23. **Briscoe, B. J.**, Sebastian, K. S. Sinha, S. K. "Application of the compliance method to microhardness measurements of organic polymers", Philosophical Magazine A, 1996, **74**, 1159-1169.
24. **Brizuela** M., Garcia-Luis A., Braceras I., Onate J.I., Sa´nchez-Lo´pez J.C., Martı´nez-Martı´nez D., Lo´pez-Cartes C., Ferna´ndez A., "Corrosion resistance of CrAlN and TiAlN coatings deposited by lateral rotating cathode arc", Surface and Coating Technology **200** (2005) 192-197.

25. **Brizuela M.**, Garcia-Luis A., Braceras I., Onate J.I., Sanchez-Lopez J. C., Martmez-Martınez D., Lopez-Cartes C., Fernandez A., "Magnetron sputtering of Cr(Al)N coatings: Mechanical and tribological study", Surface and Coatings Technology **200** (2005) 192–197.

26. **Brizuelaa M.**, Garcia-Luisa T, A., Bracerasa I., On˜atea J.I., Sanchez-Lopezb J.C.,

27. **Cai F.**, Huang X., Yang Q., Wei R., Nagy D., "Microstructure and tribological properties of CrN and CrSiCN coatings", Surface and Coatings Technology **205** (2010) 182–188.

28. **Castaldi** L., Kurapov D., Reiter A., Shklover V., Schwaller P., Patscheider J., **"High** temperature phase changes and oxidation behavior of Cr-Si-N coatings", Surface and coating Technology **202** (2007) 781.

29. **Cavalerio A.**, Louro C., "Nanocrystalline structure and hardness of thin films", Vacuum **64** (2002) 211-218.

30. **Chandra R,** A. Chawla, D. Kaur, P. Ayyub, "Structural, optical and electronic properties of nanocrystalline TiN films", Nanotechnology **16** (2005) 3053-3056.

31. **Chandra R**, A.Chawla, P. Ayyub, "Optical and Structural Properties of Sputter-Deposited Nanocrystalline Cu2O Films: Effect of Sputtering Gas", Journal of Nanoscience and Nanotechnology **6** (2006) 1119-1123.

32. **Chandra R.**, Kaur D, Chawla A. K., Phinichka N., Barber Z. H., "Texture development in Ti–Si–N nanocomposite thin films", Materials Science and Engineering A **423** (2006) 111–115.

33. **Chang Y. Y.**, Wang D. Y., Hung C. Y., "Structural and mechanical properties of nanolayered TiAlN/CrN coatings synthesized by a cathodic arc deposition process", Surface and Coatings Technology **200** (2005) 1702 – 1708.

34. **Chang Y. Y.**, Wang D. Y., Wu W. T., "Tribological enhancement of CrN coatings by niobium and carbon ion implantation", Surface and Coatings Technology **177 –178** (2004) 441–446.

35. **Chapmann B.**, "Glow Discharge Process: sputtering and plasma etching", John Willey & Sons, New York, 1980.

36. **Chawla V,** "Synthesis and characterization of Titanium based hard coatings", PhD Thesis, Indian Institute of Technology – Roorkee, India, (**2008**).

37. **Chawla V,** Jayaganthan R, Chandra R., 'Structural characterizations of magnetron sputtered nanocrystalline TiN thin films", Materials Characterization 59 (2008) 1015-1020.

38. **Chawla V.**, Jayagnathan R., Chandra R., "Microstructural characteristics and mechanical properties of magnetron sputtered nanocrystalline TiN films on glass substrate", Bulletin of Material Science, **32(2)** (2009) 117-123.

39. **Cheikh L. A. B.**, Tlili B., "Fretting wear of multilayered PVD TiAlCN/TiAlN/TiAl on AISI 4140 steel", Surface and Coatings Technology **201** (2006) 1511–1518.

40. **Chen** H. Y., Han S., Shih H., Materials Letters 58 (2004) 2924. 1

41. **Chim Y. C.**, Ding X. Z., Zeng X. T., Zhang S., "Oxidation resistance of TiN, CrN, TiAlN and CrAlN coatings deposited by lateral rotating cathode arc", Thin Solid Films **517** (2009) 4845–4849.

42. **Choi. J. B.**, Cho K., Lee M. H., Kim K. H., "Effects of Si content and free Si on oxidation behavior of Ti–Si–N coating layers", Thin Solid Films **447–448** (2004) 365-370.

43. **Chopra K. L.**, "Thin Film Phenomena", McGraw-Hill Company, 1969.

44. **Christensen N E**, Gorczyca I, "Calculated structural phase transitions of alumnium nitride under pressure", Physical Review B, **47(08)** (1993) 4307 – 4314.

45. **Christiansen S.**, Albrecht M., Strunk H. P., Veprek S., "Microstructure of novel superhard nanocrystalline-amorphous composites as analyzed by high resolution transmission electron microscopy", Journal of Vacuum Science and Technology B 16 (1998) 19-22.

46. **Chudoba T**, Richter F, "Investigation of creep behaviour under load during indentation experiments and its influence on hardness and modulus results", Surface and Coatings Technology 148 (2001) 191-198.

47. **Chunyan Y.**, Linhai T., Yinghui W., Shebin W., Tianbao L., Bingshe X., "The effect of substrate bias voltages on impact resistance of CrAlN coatings deposited by modified ion beam enhanced magnetron sputtering", Applied Surface Science **255** (2009) 4033–4038.

48. **Chunyan Yu**, Shebin Wang. Linhai Tian, Tianbao Li, Bingshe Xu, Microstructure and mechanical properties of CrAlN coatings deposited by modified ion beam enhanced magnetron sputtering on AISI H13 steel", Journal of Material Science, 44 (2009a) 300–305.

49. **Cosset F.**, Contoux G., Celerier A., Machet J., "Deposition of corrosion-resistant chromium and nitrogen-doped chromium coatings by cathodic magnetron sputtering", Surface and Coatings Technology 79 (1996) 25-34.

50. **Cullity** B. D; "Elements of X-Ray Diffraction", Addison Wesley California, 2001.

51. **Cunha L**, M. Andritschky, K. Pischow, Z. Wang, "Microstructure of CrN coatings produced by PVD techniques", Thin Solid Films **355-356** (1999) 465-471.

52. **Cunha L.**, Andritschky M., "Residual stress, surface defects and corrosion resistance of CrN hard coatings", Surface and Coatings Technology **111** (1999) 158-162.

53. **Dehong H.**, Yingchun L., Kai C., "An investigation of nanoindentation tests on the single crystal copper thin film via an AFM and MD simulation", Proceedings of the IMechE, Part C: Journal of Mechanical Engineering Science **221**(2007) 259-266.

54. **Demaree J. D.**, Fountzoulas C. G., Hirvonen J. K., "Chromium nitride coatings produced by ion beam assisted deposition", Surface and Coatings Technology **87-88** (1996) 309-315.

55. Dey A K, **Biswas K**, "Dry sliding wear of zirconia-toughened alumina with different metal oxide additives", Ceramics International **35** (2009) 997–1002.

56. **Ding X. Z.**, Tan A. L. K., Zeng X. T., Wang C., Yue T., Sun C. Q., "Corrosion resistance of CrAlN and TiAlN coatings deposited by lateral rotating cathode arc", Thin Solid Films **516** (2008) 5716–5720.

57. **Ding X. Z.**, Zeng X. T., "Structural, mechanical and tribological properties of CrAlN coatings deposited by reactive unbalanced magnetron sputtering", Surface and Coatings Technology **200** (2005) 1372-1376.

58. **Ding X. Z.**, Zeng X. T., Liu Y. C., Fang F. Z., Lim G. C., "$Cr_{1-x}Al_xN$ coatings deposited by lateral rotating cathode arc for high speed machining applications", Thin Solid Films **516** (2008) 1710–1715.

59. **Diserens M.**, Patscheider J., Levy F., "Mechanical properties and oxidation resistance of nanocomposite TiN–SiNx physical-vapor-deposited thin films", Surface and Coatings Technology **120-121** (1999) 158 - 165.

60. **Doerner M. F.**, Nix W. D., "A method for interpreting the data from depth-sensing indentation instruments", Journal of Materials Research **1** (1986) 601-609.

61. **Eiper E. ÖAW Leoben, A**; Residual stresses in CrN/Fe structures at high temperature-Experimental Report, BENSC, 2006.

62. **Essen P V**, Hoy H, Kamminga J D, Ehiasarian A P, Janssen G C A M, "Scratch resistance and wear of CrNx coatings", Surface and coatings Technology **200** (2006) 3496 -3502.

63. **Fabis P M**, Cooke R A, McDonough S, "Stress state of chromium nitride films deposited by reactive direct current planar magnetron sputtering", Journal of Vacuum Science and Technology A **8**(5) (1990) 3809-3818.

64. **Fabis P. M**, "Control of reactive d.c. planar magnetron sputtering of chromium nitride", Surface and Coating Technology **52** (1992) 243-250.

65. **Fischer-Cripps** A. C., "Nanoindentation", ed. 2nd , Springer Publication, New York **2004**.

66. **Fleming M.G**, Hashmi M.S.J., "A comparison of the magnetron sputtered and arc evaporated PVD thin-films for wear applications in multipoint cutting tools", Journal of Materials Processing Technology **32** (1992) 481–488.

67. **Fornies E.**, Escobar Galindo R., Sánchez O., Albella J. M., "Growth of CrNx films by DC reactive magnetron sputtering at constant N2/Ar gas flow", Surface and Coatings Technology **200** (2006) 6047 - 6053.

68. **Fuchs** E., Oppolzer H., "Practical Beam Microanalysis", VCH, Weinheim (1990).

69. **Gautier C**, Moussaoui H, Elstner F, Machet J, "Comparative study of mechanical and structural properties of CrN films deposited by D.C. magnetron sputtering and vacuum arc evaporation", Surface and Coatings Technology **86-87 (1996)** 254 – 262.

70. **Gautier** C., Machet J., "Study of the growth mechanisms of chromium nitride films deposited by vacuum ARC evaporation", Thin Solid Films **295** (1997) 43-52.

71. **Glaurt** A M, "Practical methods in electron microscopy", North Holland, Amsterdam, Vol **1** (1972).

72. **Gohil S.**, Banerjee R., Bose S. and Ayyub P., "Influence of synthesis conditions on the nanostructure of immiscible copper–silver alloy thin films", Scripta Materialia, **58** (2008) 842– 845.

73. **Grant W. K.**, Loomis C., Moore J. J., Olsen D. L., Mishra B., Perry A. J., "Characterization of hard chromium nitride coatings deposited by cathodic arc vapor deposition", Surface and Coatings Technology **86-87** (1996) 788-796.

74. **Gregor, A.**, Podgursky V., Adoberg E., Kulu P., "Hard Coatings Manufacturing Technology Used In Tooling", 5th International DAAAM Baltic Conference, 20-22 April 2006, Tallin, Estonia.

75. **Grove W. R.**, Phil. Trans. Roy. Soc. London, **142** (1852) 87.

76. **Grundy P. J.** and Jones G. A., "Electron microscopy in the study of materials", Edward Arnold Limited, London (1976).

77. **Hall E.O.**, "The deformation and ageing of mild steel: III. Discussion of results", Physiological Society, London. **64** (1951) 747–753.

78. **Han Z,**. Tian J, Lai Q., Yu X., Li G., "Effect of N partial pressure on the microstructure and mechanical properties of magnetron sputtered CrNx films", Surface and Coatings Technology **162** (2003) 189-193.

79. **He X -M**, Baker N., Kehler B. A., Walter K. C., Nastási M., "Structure, hardness, and tribological properties of reactive magnetron sputtered chromium nitride films", Journal of Vacuum Science and Technology A **18(1)** (2000) 30-36.

80. **Holleck** H, Material selection for hard coatings, "Material selection for hard coatings", Journal of Vacuum Science and Technology A **4** (1986) 2661-2669.

81. **Hondros E. D.**, Gissler W., Jehn H. A. (eds.), "Advances Techniques for surface Engineering", Kluwer Academic Publishers, Dortrecht 1992.

82. **Hones P.**, Consiglio R., Randall N., Lévy F., "Mechanical properties of hard chromium tungsten nitride coatings", Surface and Coatings Technology **126** (2000) 179 - 184.

83. **Hones** P., Martin N., Regula M., L'evy F., "Structural and mechanical properties of chromium nitride, molybdenum nitride, and tungsten nitride thin films", Journal of Applied Physics D **36** (2003) 1023–1029.

84. **Hones P.**, Ph.D. thesis. EPFL, Lausanne, Switzerland, No 2116 (2000b).

85. **Hones** P., Sanjin'es R., L'evy F., "Sputter deposited chromium nitride based ternary compounds for hard coatings", Thin Solid Films **332** (1998) 240- 246.

86. **Hones** P., Sanjines R., Levy F., "Characterization of sputter-deposited chromium nitride thin films for hard coatings", Surface and Coatings Technology **94-95** (1997) 398-402.

87. **Hones P.**, Zakri C., Schmid P. E., Lévy F., Shojaei O. R, "Oxidation resistance of protective coatings studied by spectroscopic ellipsometry", Applied Physics Letter **76 (22)** (2000a) 3194.

88. **Hosokawa M**, Nogi K, Naito M, Yokoyama T, "Nanoparticle Technology Handbook", Elsevier Publication, Oxford, U.K (**2007**).

89. **Huang Z. P.**, Sun Y., Bell T., "Friction behaviour of TiN, CrN and (TiAl)N coatings", Wear, **173** (1994) 13-20.

90. **Hurkmans T.**, Lewis D.B., Brooks J.S., Munz W.D., "Chromium nitride coatings grown by unbalanced magnetron (UBM) and combined arc/unbalanced magnetron (ABS^{TM}) deposition techniques", Surface and Coatings Technology **86(1-3)** (1996) 192-199.

91. **Hurkmans T.**, Lewis D.B., Paritong H., Brooks J.S., Munz W.D., "Influence of ion bombardment on structure and properties of unbalanced magnetron grown CrNx coatings", Surface and Coatings Technology **114** (1999) 52–59.

92. **Hutchings I M,** "Tribology: Friction and wear of engineering materials", Edward Arnold, London, **(1992).**

93. **Jagielski J,** Khanna A S, Kucinski J, Mishra D S, Racolta P, Sioshansi P, Tobing E, Thereska J, Uglov V, Vilaithong T, Viviente J, Yang S-Z and Zalar A, Applied Surface Science, **156** (2000) 47.

94. Jain Aditya, **Basu B.**, Manoj Kumar B.V., Harshavardhan, Sarkar J., "Grain size–wear rate relationship for titanium in liquid nitrogen environment", Acta Materialia **58** (2010) 2313–2323.

95. **Jedrzejowski P.**, Klemberg-Sapieha J.E., Martinu L., "Quaternary hard nanocomposite TiCxNy/SiCN coatings prepared by plasma enhanced chemical vapor deposition", Thin Solid Films **466** (2004) 189-196.

96. **Jedrzejowski P.**, Klemberg-Sapieha J.E., Martinu L., "Relationship between the mechanical properties and the microstructure of nanocomposite TiNySiN coatings prepared by low temperature plasma enhanced chemical vapor deposition", Thin Solid Films **426** (2003) 150-159.

97. **Jung M J**, Nam K H, Jung Y M, Han J G, "Nucleation and growth behavior of chromium nitride film deposited on various substrates by magnetron sputtering" Surface and Coatings technology **171** (2003) 59.

98. **Kamachi M. U.**, Pujar M.G., Dayal R.K., "Effects of Laser Surface Melting on the Pitting Resistance of Sensitized Nitrogen-Bearing Type 316L Stainless Steel", Journal of Materials Engineering and Performance 7(2) (1998) 214-220.

99. **Karvankova P.**, Karimi A., Coddet O., Cselle T., Morstein M., "Thermal stability of $Cr_{1-x}Al_xSi_yN$ coatings with medium to high aluminium content prepared by arc evaporation", Material Research Society Symposium Proceeding **890** (2006).

100. Kaur M., **Singh H.**, Singh B., Singh Bhupinder, "Studies on the Sliding Wear Performance of Plasma Spray Ni-20Cr and Ni3Al Coatings", Journal of Thermal Spray Technology **19(1-2)** (2010) 378—383.

101. **Kawate M.**, Hashimoto A.K., Suzuki T., "Oxidation resistance of Cr_{1-x} Al_x N and $Ti_{1-x}Al_xN$ films", Surface and Coatings Technology **165** (2003) 163 - 167.

102. **Kelly** A, MacMillan N H, "Strong Solids", Oxford Clarendon Press, London (1986).

103. **Kim G.S.**, Kim B.S., Lee S.Y., "High-speed wear behaviors of CrSiN coatings for the industrial applications of water hydraulics", Surface and Coatings Technology **200** (2005) 1814-1818.

104. **Kim S.K.**, Cha B.C., "Deposition of CrN–MoS_2 thin films by D.C. magnetron sputtering", Surface and Coatings Technology **188–189** (2004) 174–178.

105. **Kim. K.H.**, Choi S.R., Yoon S.Y., "Superhard Ti–Si–N coatings by a hybrid system of arc ion plating and sputtering techniques", Surface and Coatings Technology **161** (2002) 243 - 248.

106. **Knotek O.**, Sffier F. L, Scholl H.-J., "Properties of arc-evaporated CrN and (Cr,Al)N coatings", Surface and Coatings Technology **45** (1991) 53–58.

107. **Kusaka** K, Taniguchi **D**, Hanabusa T, Tominaga K, "Effect of sputtering gas pressure and nitrogen concentration on crystal orientation and residual stress in sputtered AlN films", Vacuum **66** (2002) 441-446.

108. **Lamastra F R**, Leonardi F, Montanari R, Casadei F, Valente T, Gusmano G, "X-ray residual stress analysis on CrN/Cr/CrN multilayer PVD coatings deposited on different steel substrates", Surface and Coatings Technology **200** (2006) 6172-6175.

109. **Lausmann** G.A., "Current industrial practices: Electrolytically deposited hardchrome", Surface and Coatings Technology **86-87** (1996) 814-820.

110. **Lee H.Y.**, Jung W.S., Han J.G., Seo S.M., Kim J.H., Bae Y.H., "The synthesis of CrSiN film deposited using magnetron sputtering system", Surface and Coatings Technology **200** (2005) 1026– 1030.

111. **Lee J. W**, Tien S. K., Kuo Y. C., "The effects of pulse frequency and substrate bias to the mechanical properties of CrN coatings deposited by pulsed DC magnetron sputtering", Thin Solid Films **494** (2006) 161-167.

112. **Lee J. W.**, Chang Y. C., "A study on the microstructures and mechanical properties of pulsed DC reactive magnetron sputtered Cr–Si–N nanocomposite coatings", Surface and Coatings Technology **202** (2007) 831–836.

113. **Lee J.W.**, Tien S K., Kuo Y C, "The Effects of Substrate Bias, Substrate, Temperature, and Pulse Frequency on the Microstructures of Chromium Nitride Coatings Deposited by Pulsed Direct Current Reactive Magnetron Sputtering", Journal of Electronic Materials, **34 (12)** (2005) 1484 – 1492.

114. **Lee S. Y.** , Kim B. S., Kim S. D., Kim G. S., Hong Y. S., "Effect of Si doping on the wear properties of CrN coatings synthesized by unbalanced magnetron sputtering", Thin Solid Films **506– 507** (2006) 192 – 196.

115. **Lee S.-Y.**, Hong Y.-S., "Effect of CrSiN thin film coating on the improvement of the low-speed torque efficiency of a hydraulic piston pump", Surface and Coatings Technology **202** (2007) 1129-1134.

116. **Legg K.O.**, Graham M., Chang P., Rastagar F., Gonzales A., Sartwell B., "The replacement of electroplating", Surface and Coating Technology **81** (1996) 99-105.

117. **Levy F**, P. Hones, P.E. Schmid, R. Sanjines, M. Diserens, C. Wiemer, "Electronic states and mechanical properties in transition metal nitrides", Surface and Coatings Technology **120-121** (1999) 284-290.

118. **Li T.**, Li M., Zhou Y., "Phase segregation and its effect on the adhesion of Cr–Al–N coatings on K38G alloy prepared by magnetron sputtering method", Surface and Coatings Technology **201** (2007) 7692–7698.

119. **Li J. C. M.** "Impression creep and other localized tests", Materials Science and Engineering A, **322** (2002) 23-42.

120. **Li T.**, Zhou Y., Li M., Li Z., "High temperature corrosion behavior of a multilayer CrAlN coating prepared by magnetron sputtering method on a K38G alloy", Surface and Coatings Technology **202** (2008) 1985–1993.

121. **Li, X.** and Bhushan, B. "Micro/nanomechanical characterization of ceramic films for microdevices", Thin Solid Films 340 (1999) 210-217.

122. **Lin C. R.**, Kuo C. T., "High adhesion and quality diamond films on steel substrate", Diamond and Related Materials 7 (1998a) 903-907.

123. **Lin C. R.**, Kuo C. T., Chang Ruey Ming, "Improvement in adhesion of diamond films on cemented WC substrate with Ti–Si interlayers", Diamond and Related Materials **7** (1998) 1628–1632.

124. **Lin J.**, Mishra B., Moore J.J., Sproul W.D., Rees J.A.; "Effects of the substrate to chamber wall distance on the structure and properties of CrAlN films deposited by pulsed-closed field unbalanced magnetron sputtering (P-CFUBMS)", Surface and Coatings Technology **201** (2007) 6960–6969.

125. **Lin J.**, Mishra B., Moore J.J., Sproul W.D.; "A study of the oxidation behavior of CrN and CrAlN thin films in air using DSC and TGA analyses", Surface and Coatings Technology **202** (2008) 3272–3283.

126. **Lin J.**, Moore J. J., Mishra B., Pinkas M., Sproul W. D., Rees J.A., "Effect of asynchronous pulsing parameters on the structure and properties of CrAlN films deposited by pulsed closed field unbalanced magnetron sputtering (P-CFUBMS)", Surface and Coatings Technology **202** (2008a) 1418–1436.

127. **Lin J.**, Moore J. J., Sproul W. D., Mishra B., Wu Z., Wang J., "The structure and properties of chromium nitride coatings deposited using dc, pulsed dc and modulated

pulse power magnetron sputtering", Surface & Coatings Technology **204** (2010) 2230–2239.

128. **Lin J.,** Wu Z.L., Zhang X.H., Mishra B., Moore J.J., Sproul W.D., "A comparative study of CrNx coatings Synthesized by dc and pulsed dc magnetron sputtering", Thin Solid Films 517 (2009) 1887-1894.
129. **Lugscheider E.,** Bobzin K., Barwulf St, Hornig Th., "Oxidation characteristics and surface energy of chromium-based hardcoatings for use in semisolid forming tools", Surface and Coatings Technology **33–134** (2000) 540 - 547.
130. **Lugscheider E.,** Bobzin K., Hornig Th., Maes M., "Investigation of the residual stresses and mechanical properties of (Cr,Al)N arc PVD coatings used for semi-solid metal (SSM) forming dies", Thin Solid Films **420-421** (2002) 318-323.
131. **Luo Q.**, "Origin of Friction in Running-in Sliding Wear of Nitride Coatings", Tribology Letters **37** (2010) 529–539.
132. **Ma** D, Ma S, Xu K,Veprek S, Materials Letter **59** (2005) 838.
133. **Mahan J. E.**, "Physical Vapor Deposition of thin films", John Wiley & Sons; 2000.
134. **Maissel L. I.**, Glang R., "Hand book of Thin Film Technology", McGraw Hill, New York, 1970.
135. **Makino** Y., Nogi K., "Synthesis of pseudobinary CrAlN films with B1 structure by rf – assisted magnetron sputtering method", Surface and Coatings Technology **98** (1998) 1008-1012.
136. **Mannling** H. D., Patil D.S., Moto K., Jilek M., Veprek S., "Thermal stability of superhard nanocomposite coatings consisting of immiscible nitrides", Surface and Coatings Technology **146 – 147** (2001) 263-267.
137. **Mannling H. D.**, Patil D.S., Moto K., Jilek M., Veprek S., Thermal stability of superhard nanocomposite coatings consisting of immiscible nitrides, Surface and Coating Technology, **146 – 147** (2001) 263-267.
138. **Marsh D M,** "Plastic Flow in Glass", Proceeding of Royal Society of London A **279** (1964) 420-435.
139. **Martinez E.,** Sanjine´s R., Banakh O., Levy F., "Electrical, optical and mechanical properties of sputtered CrNy and $Cr_{1-x}Si_xN_{1.02}$ thin films", Thin Solid Films **447 – 448** (2004) 332-336.
140. **Martinez E.,** Sanjines R., Karimi A., Esteve J., Levy F., "Mechanical properties of nanocomposite and multilayered Cr–Si–N sputtered thin films", Surface and Coatings Technology **180 –181** (2004a) 570–574.

141. Martınez-Martınez D., Lopez-Cartesb C., Ferna´ndez A., "Magnetron sputtering of Cr(Al)N coatings: Mechanical and tribological study", Surface and Coatings Technology **200** (2005) 192– 197.

142. **Mayrhofer P H**, Mitterer C, Hultman L, Clemens H, "Microstructural design of hard coatings", Progress in Material Science **51** (2006) 1032-1114.

143. **Mayrhofer P H**, Tischler G, Mitterer C , "Microstructure and mechanical / thermal properties of CrN coatings deposited by reactive unbalanced magnetron sputtering", Surface and Coatings Technology **142-144** (2001) 78-84.

144. **Mayrhofer P.H.**, Music D., Reeswinkel T., Fuß H.G., Schneider J.M., "Structure, elastic properties and phase stability of $Cr_{1-x}Al_xN$", Acta Materialia **56** (2008) 2469–2475.

145. **Mercs D.**, Bonasso N., Naamane S., Bordes J. M., C. Coddet, "Mechanical and tribological properties of Cr–N and Cr–SI–N coatings reactively sputter deposited", Surface and Coatings Technology **200** (2005) 403 – 407.

146. **Mercs D.**, Briois P., Demange V., Lamy S., Coddet C., "Influence of the addition of silicon on the structure and properties of chromium nitride coatings deposited by reactive magnetron sputtering assisted by RF plasmas", Surface and Coatings Technology **201** (2007) 6970-6976.

147. **Meunier C**, S. Vives, G. Bertrand, "X-ray diffractometry analysis of RF -magnetron-sputtered chromium/chromium nitride coatings", Surface and Coatings Technology **107** (1998) 149-158.

148. **Mo J.L.**, Zhu M.H., Lei B., Leng Y.X., Huang N., "Comparison of tribological behaviours of AlCrN and TiAlN coatings—Deposited by physical vapor deposition", Wear **263** (2007) 1423-1429.

149. **Mtlnz W.D.**, Titanium aluminum nitride films: A new alternative to TiN coatings, Journal of Vacuum Science and Technology **4** (1986) 2717-2725.

150. Ambat R, Aung **N. N.**, Zhou **W.**, "Evaluation of microstructural effects on corrosion behaviour of AZ91D magnesium alloy", Corrosion Science 42(8) (2000) 1433-1455.

151. **Musil J.**, "Hard nanostructured and nanocomposite thin films", 3rd Mikkeli International Industrial Coating Seminar Miics-2006, 16-18 March **(2006)** Finland.

152. **Musil J.**, "Physical and mechanical properties of hard nanocomposite films prepared by reactive magnetron sputtering", Invited Chapter 10 in the book "Nanostructured Hard Coatings", (2006a) Kluwer Academic/Plenum Publishers, New York, U.S.A.,

153. **Nam K.H.**, Jung M.J., Han J.G., "A study on the high rate deposition of CrN films with x controlled microstructure by magnetron sputtering", Surface and Coatings Technology **131** (2000) 222–227.

154. **Nam Kyung H.**, Jung Yun M., Han Jeon G., "A comparative study of microstructure and mechanical properties for CrN films with various deposition rates by magnetron sputtering", Surface and Coatings Technology **142-144** (2001) 1012-1016.

155. **Nastasi M.**, D.M. Parkin, Gleiter H., "Mechanical properties and deformation behavior of materials having ultra-fine microstructures", NATO ASI Series, E: Applied Sciences **233** (1993) 3.

156. **Navinsek B.**, Panjan P., Milosev I., "Indistrial applications of CrN (PVD) coatings, deposited at high and low temperatures", Surface and Coatings Technology **97** (1997) 182-191.

157. **Niederhofer A**, Bolom T, Nesladek P, Moto K, Eggs C, Patil D S, Veprek S, "The role of percolation threshold for the control of the hardness and thermal stability of super- and ultrahard nanocomposites", Surface and Coating Technology **146-147** (2001) 183.

158. **Niederhofer A.**, Nesl´adek P., M¨annling H.D., Veprek S., Jılek M., "Structural properties, internal stress and thermal stability of nc-TiN/a-Si_3N_4, nc-TiN/$TiSi_x$ and nc-$(Ti_{1-y}Al_ySi_x)N$ superhard nanocomposite coatings reaching the hardness of diamond", Surface and Coating Technology **120- 121** (1999) 173-178.

159. **North B.**, "Six issues for the hard coatings community", Surface and coatings Technology **106** (1998) 129–134.

160. **Nose M**, Chiou W A, Zhou M, Mae T, Meshii M, "Microstructure and mechanical properties of Zr-Si-N films prepared by rf-reactive sputtering", Journal of Vacuum Science Technology A **20** (2002) 823.

161. **Ohring M**, "Material science of Thin films: Deposition and structure", ed 2, Academic Press Inc. Elsevier, California, USA **(2002)**.

162. **Olaya J.J**, S.E. Rodil, S. Muhl, E. Sanchez, "Comparative study of chromium nitride coatings deposited by unbalanced and balanced magnetron sputtering", Thin Solid Films **474** (2005) 119-126.

163. **Oliver W C** and Pharr G M, "An improved technique for determining hardness and elastic modulus using load and displacement sensing indentation experiments", Journal of Material Research, 7 (1992) 1564-1583.

164. **Oliver, W.C.,** Pharr, G.M.. "An Improved Technique for Determining Hardness and Elastic Moduli using Load and Displacement Sensing Indentation Experiments", Journal of Materials Research, 7 (1992) 1564-1583.

165. **Ong H. C.**, Zhu A. X. E., Du G. T., "Dependence of the excitonic transition energies and mosaicity on residual strain in ZnO thin films", Applied Physics Letter **80** (2002) 941-943.

166. **Ortmann S**, Savan A, Gerbig Y, Haefke H, "In-process structuring of CrN coatings, and its influence on friction in dry and lubricated sliding" Wear **254** (2003) 1099.

167. **Ouyang J.H.**, Sasaki S., "Tribo-oxidation of cathodic arc ion-plated (V, Ti)N coatings sliding against a steel ball under both unlubricated and boundary-lubricated conditions" Surface and Coatings Technology **187** (2004) 343.

168. **PalDey S**, Deevi S C. "Structure of Material Properties: Microstruct and Process", Material Science and Engineering A **58** (2002) 342.

169. **Pandey R.**, Sutjianto A., Seel M., Jaffe J. E., Journal of Materials Research **8** (1993) 1922.

170. **Park I. W.**, Kang D. S., Moore J. J., Kwon S. C., Rha J. J., Kim K. H., "Microstructures, mechanical properties, and tribological behaviors of Cr–Al–N, Cr–Si–N, and Cr–Al–Si–N coatings by a hybrid coating system", Surface and Coatings Technology **201** (2007) 5223–5227.

171. **Park J H**, Chung W S, Cho Y R, Kim K H, "Synthesis and mechanical properties of CrSiN coatings deposited by a hybrid system of arc ion plating and sputtering techniques", Surface and Coatings Technology **188-189** (2004) 425-530.

172. **Paternoster C**, Fabrizi A., Cecchini R., Mehtedi M. El, Choquet P, "Thermal stability of CrN_x nanometric coatings deposited on stainless steel", Journal of Material Science **43** (2008) 3377-3384.

173. **Paulitsch J.**, Schenkel M., Zufra Th., Mayrhofer P.H., Münz W.-D., "Structure and properties of high power impulse magnetron sputtering and DC magnetron sputtering CrN and TiN films deposited in an industrial scale unit", Thin Solid Films **518** (2010) 5558–5564.

174. **Pelleg J.**, Zevin L. Z., Lungo S., Croitoru N., "Reactive sputter deposited TiN films on glass substrates", Thin Solid Films **197** (1991) 117-128.

175. **Petch N.J.**, "The cleavage strength of polycrystals", Journal of Iron and Steel Institute **174** (1953) 25–28.

176. **Pethica J.B.**, R. Hutchings, W.C. Oliver, "Hardness measurements at penetration depths as small as 20 nm", Philosophical Magazine (A) **48** (1983), pp. 593–606.

177. **Pethica, J. B.**, Huntchings, R. and Oliver, W. C. "Hardness measurements at penetration depths as small as 20 nm". Philosophical Magazine A **48** (1983) 593-606.

178. **Petrov. I,** Myers A, Green J E, Abelson J R, Journal of Vacuum Science and Technology A **12** (1994) 2846.

179. **Polcar T**, N.M.G. Parreira, R. Novák, "Friction and wear behaviour of CrN coating at temperatures up to 500 °C", Surface and Coatings Technology **201** (2007) 5228-5235.

180. **Pulugurtha S. R.**, Bhat D. G., "A study of AC reactive magnetron sputtering technique for the deposition of compositionally graded coating in the Cr–Al–N system", Surface and Coatings Technology **201** (2006) 4411–4418.

181. **Pulugurtha S.R.**, Bhat D.G., Gordon M.H., Shultz J., Staia M., Joshi S.V., Govindarajan S., "Mechanical and tribological properties of compositionally graded CrAlN films deposited by AC reactive magnetron sputtering", Surface and Coatings Technology 202 (2007) 1160–1166.

182. Ravi Kumar, Calis Acikbas N., Kara Ferhat, Mandal Hasan, **Basu B,** Microstructure–Mechanical Properties–Wear Resistance Relationship of SiAlON Ceramics, Metallurgical and Material Transactions A, 40A (2009) 2319 – 2332.

183. **Rebholz C.**, Ziegele H., Leyland A., Matthews A., "Structure, mechanical and tribological properties of nitrogen-containing chromium coatings prepared by reactive magnetron sputtering", Surface and Coatings Technology, **115** (1999) 222-229.

184. **Reid J.S.**, Sun X., Kolawa E., Nicolet M.A., "Ti-Si-N Diffusion Barriers between Silicon and Copper", IEEE Electronic Device Letter **15** (1994) 298-300.

185. **Romero J.**, Gómez M.A., Esteve J., Montalà F., Carreras L., Grifol M., Lousa A., "CrAlN coatings deposited by cathodic arc evaporation at different substrate bias", Thin Solid Films **515** (2006) 113-117.

186. **Safi I,** "Recent aspects concerning DC reactive magnetron sputtering of thin films: a review", Surface and Coatings Technology **127** (2000) 203-219.

187. **Sanchez J.E.**, Sanche´z O.M., Ipaz L., Aperador W., Caicedo J.C., Amaya C., Herna´ndez Landaverde M.A., Espinoza Beltran F., Munoz-Saldana J., Zambrano G., "Mechanical, tribological, and electrochemical behavior of CrAlN coatings deposited by RF reactive magnetron co-sputtering method", Applied Surface Science **256** (2010) 2380–2387.

188. **Sanchez-Lopez** J. C., Martínez M D., López-Cartes C., Fernández A., Brizuela M., García- Luis A., Oñate J. I., "Mechanical behavior and oxidation resistance of Cr.Al.N coatings", Journal of Vacuum Science and Technology **A 23** (2005) 681-686.

189. **Sandu C.S.**, Sanjinés R., Benkahoul M., Medjani F., Lévy F., "Formation of composite ternary nitride thin films by magnetron sputtering co-deposition", Surface and Coatings Technology **201** (2006a) 4083-4089.

190. **Sandu C.S.**, Sanjines R., Benkahoul M., Parlinska-Wojtan M., Karimi A., Levy F., "Influence of Ge addition on the morphology and properties of TiN thin films deposited by magnetron sputtering", Thin Solid Films **496** (2006) 336-341.

191. **Sang G B**, Yong K C, Kyoung I M, Sang Gweon Kim, Sung Wan Kim, Material Research Society Symposium Proceeding Vol. **890** (2006) 17.1.

192. **Sanjines R.**, Benkahoul M., Sandu C.S., and Lévy F., "Relationship between the physical and structural properties of NbSiN thin films by dc reactive magnetron sputtering", Journal of Applied Physics, **98** (2005) 123511-1.

193. **Sarakinos K**, Kassavetis S, Patsalas P, Logothetidis S, "Structural factors determining the nanomechanical performance of transition metal nitride films", Materials Research Society Symposium Proceeding, **843** (2005) T.7.8.1.

194. **Schell N.**, Petersen J.H., Bøttiger J., Mucklich A., Chevallier J., Andr easen K.P., Eichhorn F., "On the development of texture during growth of magnetron-sputtered CrN" Thin Solid Films **436** (2003) 100-110. 6

195. **Schneider J.M.**, Rhode S.L., Sproul W.D., and Matthews A., "Recent developments in plasma assisted physical vapour deposition", Journal of Physics- D, Applied Physics, **33** (2000) R173–R186. 1

196. **Schulz H.**, Bergmann E., "Properties and applications of ion-plated coatings in the system Cr–C–N", Surface and Coatings Technology **50** (1991) 53–56.

197. Schulz H., Bergmann E., Properties and applications of ion-plated coatings in the system Cr–C–N, Surface and Coatings Technology **50** (1991) 53–56.

198. **Seok J. W**, Jadeed N. M., Lin R. Y, "Sputter-deposited nanocrystalline Cr and CrN coatings on steels", Surface and Coatings Technology **138** (2001) 14-22.

199. **Shah H. N.**, Jayaganthan R., Kaur D., Synthesis and microstructural characterization of CrSiN thin films deposited on Si(100) substrate, Surface Engineering, **DOI:** 10.1179 /026708410 X 12459349720097 (**2009**).

200. **Shah H. N.**, Jayaganthana R., Kaur D., "Influence of silicon content on the microstructure and hardness of CrN coatings deposited by reactive magnetron sputtering", Materials Chemistry and Physics **121** (2010) 567–571.

201. **Shah H.N.**, Jayaganthan R., Kaur D., Chandra R., "Influence of sputtering parameters and nitrogen on the microstructure of chromium nitride thin films deposited on steel substrate by direct-current reactive magnetron sputtering", Thin Solid Films **515** (2010) 5762 -5768.

202. **Shankar Ravi**, Kamachi M U., Sole Ravikumar, Khatak H.S., Raj Baldev, "Plasma-sprayed yttria-stabilized zirconia coatings on type 316L stainless steel for pyrochemical reprocessing plant", Journal of Nuclear Materials 372 (2008) 226–232.

203. **Shi Y.**, Long S., Fang L., Pan F., and Liao H., "Effects of N_2 content and thickness on CrNx coatings on Mg alloy by the planar DC reactive magnetron sputtering", Applied Surface Science, **255** (2009) 6515-6524.

204. **Sigmund P.**, Nucl. Instr. Meth. Phys. Res. B, **27** (1987) 1.

205. **Singh H,** Grewal M S, Sekhon H S, Rao R G, "Sliding wear performance of high-velocity oxy-fuel spray Al_2O_3/TiO_2 and Cr_2O_3 coatings", Proceeding of IMechE, Journal of Engineering Tribology : J **222** (2008) 601-610.

206. **Singh P**, Kumar A, Deepak, Kaur D, Growth and characterization of ZnO nanocrystalline thin films and nanopowder via low-cost ultrasonic spray pyrolysis Journal of Crystal Growths **306** (2007) 303.

207. **Singh P.**, Kaur D, "Influence of film thickness on texture and electrical and optical properties of room temperature deposited nanocrystalline V_2O_5 thin film", Journal of Applied Physics. **103** (2008) 043507-1 -9.

208. **Smith P.M**, and Custer J.S., "Chemical vapor deposition of titanium-silicon-nitride films", Applied Physics Letter, **70** (1997) 3116.

209. **Sneddon, I. N.**, "The relation between load and penetration in the axisymmetric boussinesq problem for a punch of arbitrary profile", International Journal of Engineering Science, 3 (1965) 47-57.

210. **Sneddon, I.N.** "The Relation between load and penetration in the axisymmetric boussinesq problem for a punch of arbitrary profile", International Journal of Engineering Science, **3** (1965) 47.

211. **Spain E.**, Avelar-Batista J.C., Letch M., Housden J., and Lerga B., "Characterisation and applications of Cr–Al–N coatings", Surface and Coating Technology, **200** (2005) 1507-1513.

212. **Srakinos K**, Alami J, Karimi P M, Severin D, Wuttig M, Journal of Physics- D: Applied Physics. **40** (2007) 778.

213. Srivastav Sangeeta, Jain Amitabh, **Kanjilal D.**, Improvement of adhesion of TiN coatings on stainless steel substrates by high energy heavy ion irradiation, Nuclear Instruments and Methods in Physics Research B **101** (1995) 400-405.

214. **Su** Y.L., Yao S.H., Leu Z.L., Wei C.S., Wu C.T., "Comparison of tribological behavior of three films-TiN, TiCN and CrN-grown by physical vapor deposition", Wear **213** (1997) 165–174.

215. **Su Y.L.**, Yao S.H., Leu Z.L., Wei C.S., Wu C.T., "Comparison of tribological behavior of three films-TiN, TiCN and CrN-grown by physical vapor deposition", Wear **213** (1997) 165–174.

216. **Sue J. A.**, and Chang T. P., "Friction and wear behavior of titanium nitride, zirconium nitride and chromium nitride coatings at elevated temperatures", Surface and Coatings Technology 76**(1-3)** (1995) 61-69.

217. **Sumi** H, H. Inoue, M. Taguchi, Y.Sugano, H.Masuya, N. Ito, S. Kishida, H. Tokutaka, Journal of Applied Physics **36** (1997) 595.

218. **Sun C. C.**, Lee S. C., Dai S. B., Fu Y. S., Wang Y. C., and Lee Y. H., "Surface free energy of CrNx films deposited using closed field unbalanced magnetron sputtering", Applied Surface Science **252** (2006) 8295–8300.

219. **Sun X.**, Reid J., Kolawa E., Nicolet M.A., and Ruiz R., "Reactively sputtered Ti-Si-N films. I. Diffusion barriers for Al and Cu metallizations on Si", Journal of Applied Physics **81(2)** (1997) 664-671.

220. **Sun** Y., Wang Y. H., Seow H. P., "Effect of substrate material on phase evolution in reactively sputtered Cr-Al-N films", Journal of Materials Science **39** (2004) 7369 – 7371.

221. **Takadoum J**, Houmid Bennani, Mairey D, "The wear characteristics of silicon nitride", Journal of European Ceramic Society, **18** (1998) 553-556.

222. **Tan S.**, Zhang X., **Wu** X., Fang F., Jiang J., "Effect of substrate bias and temperature on magnetron sputtered CrSiN films", Applied Surface Science (2010), **doi:10.1016/j.apsusc.2010.08.114.**

223. **Terrat J.P.**, Gaucher A., Hadj-Rabah H., and Fillit R.Y., "Structure and mechanical properties of reactively sputtered chromium nitrides", Surface and Coatings Technology **45** (1991) 59-65.

224. **Thobor-Keck, F.** Lapostolle,T, A.S. Dehlinger, D. Pilloud, J.F. Pierson, C. Coddet, Influence of silicon addition on the oxidation resistance of CrN coatings, Surface and Coatings Technology **200** (2005) 264– 268.

225. **Thornton J A**, "Hexagonal nitride coatings: electronic and mechanical properties of V_2N, Cr_2N and d-MoN", Annual Review of Material Science 7 (1977) 239-299.

226. **Tillmann W**, Vogli E., Mohapatra S., "A new approach to improve SCC resistance of austenitic stainless steel with a thin CrN film, deposited by cathodic vacuum arc deposition technique", Surface and Coating Technology **202** (2007) 750-754.

227. **Tlili B.**, Mustapha N., Nouveau C., Benlatreche Y., Guillemot G., Lambertin M., "Correlation between thermal properties and aluminum fractions in CrAlN layers deposited by PVD technique", Vacuum **84** (2010) 1067–1074.

228. **Tu J.**-N., Duh J.-G., and Tsai S.-Y., "Morphology, mechanical properties, and oxidation behavior of reactively sputtered CrN films", Surface and Coatings Technology **133**. (2000) 181-185.

229. **Tua Jui-Neng**, Duha Jenq-Gong, Tsai Shu-Yueh, "Morphology, mechanical properties, and oxidation behavior of reactively sputtered CrN films", Surface and Coatings Technology **133-134** (2000) 181-185.

230. **Uchida** M., Nihira N., Mitsuo A., Toyoda K., Kubota K., Aizawa T., "Friction and wear properties of CrAlN and CrVN films deposited by cathodic arc ion plating method", Surface and Coatings Technology **177–178** (2004) 627–630.

231. **Ueno M**, Onodera A, Shimomura O, Takemura K, "X-ray observation of the structural phase transition of aluminum nitride under high pressure", Physical Review B, **45(17)** (1992) 10123- 10126.

232. **Ulrich S.**, Holleck H., Ye J., Leiste H., Loos R., Stuber M., Pesch P., Sattel S., "Influence of low energy ion implantation on mechanical properties of magnetron sputtered metastable (Cr,Al)N thin films", Thin Solid Films **437** (2003) 164-169.

233. **Van E. P**, R. Hoy, J. D. Kamminga, A. P. Ehiasarian, G. C. A. M. janssen, "Scratch resistance and wear of CrNx coatings", Surface and Coating Technology **200** (2006) 3496-3502.

234. **Vaz F.**, Rebouta L., Goudeau P., Rivier J.P., Schaffer E., Kleer G., Bodmann M., "Physical, structural and mechanical characterization of $Ti_{1-x}Si_xNy$ films", Thin Solid Films **402** (2002) 195–202.

235. **Vaz F.**, Rebouta L., Ramos S., de Silva M.F., Soares J.C., "Structure, mechanical and tribological properties of nitrogen-containing chromium coatings prepared by reactive magnetron sputtering", Surface and Coating Technology 108–109 (1998) 236–240.

236. **Veprek S**, Haussmann M and Reiprich S, "Superhard nanocrystalline W_2N/amorphous Si_3N_4 composite materials", Journal of Vacuum Science and Technology **A 14** (1996) 46.

237. **Veprek S**, Niederhofer A, Moto K, Bolom T, Mannling H-D, Nesladek P, Dollinger G and Bergmaier A , "Composition, nanostructure and origin of the ultrahardness in nc-TiN/a-Si_3N_4/a- and nc-$TiSi_2$ nanocomposites with H_V=80 to 105 GPa" Surface and Coating Technology **133/134** (2000) 152.

238. **Veprek S.**, Haussmann M., Reiprich S., Schzhi Li, and Dian J., "Novel thermodynamically stable and oxidation resistant superhard coating materials", Surface and Coatings Technology, **86–87** (1996a) 394-401 .

239. **Veprek S.**, Reiprich S., "A concept for the design of novel superhard coatings", Thin Solid Films **268** (1995) 64-71.

240. **Veprek S.**, Veprek-Heijman M.G.J., "The formation and role of interfaces in superhard nc-MenN/a-Si3N4 nanocomposites", Surface and Coating Technology **201** (2007) 6064-6070.

241. **Veprek S** , "The search for novel, superhard materials", Journal of Vacuum Science and Technology A **17 (1999)** 2401.

242. **Vossen J.L**, W.Kern, "Thin Film Processes", Academic Press, New York, 1978.

243. **Wang D.**, and Oki T., "The morphology and orientation of Cr-N films deposited by reactive ion plating", Thin Solid Films, **185(2)** (1990) 219-230.

244. **Wang** L., Nie X., Housden J., Spain E., Jiang J.C., Meletis E.I., Leyland A., Matthews A., "Material transfer phenomena and failure mechanisms of a nanostructured Cr–Al–Ncoating in laboratory wear tests and an industrial punch tool application", Surface and Coatings Technology **203** (2008) 816–821.

245. **Wang Q. M.**, and Kim K. H., "Microstructural control of Cr–Si–N films by a hybrid arc ion plating and magnetron sputtering process", Acta Materialia **57** (2009) 4974-4987.

246. **Wang Z**, Cohen S A, Ruzic D N, Goeckner M J, **"**Nitrogen atom energy distributions in a hollow-cathode planar sputtering magnetron", Physical Review E **61** (2000) 1904.

247. **Warcholiniski B**, Gilewicz A, Myslinski P, "Tribologica properties oc TiAlCrN thin films", Reviews on Advance Material Science, 22 (2009) 81-88.

248. **Wasa K.**, and S. Hayakawa in Hand Book of Sputter Deposition Technology: principles, technology and applications, Noyes Publications, New Jersy, 1992.

249. **Weblink 1:** http://brycoat.com/pvd-crn.html (access on 22/06/2010).
250. **Weblink 2:** http://commons.wikimedia.org/wiki/File:Chromium(III)-nitride-xtal-3DvdW.png, (access on 13/07/2010).
251. **Weblink 3,** http://www.ntmdt.com/spm-principles/view/dc-contact-techniques (access date: 25th June 2010).
252. **Weblink 4:** http://www.gordonengland.co.uk/hardness/microhardness.htm (access date: 26th June 2010).
253. **Wei G,** Rar A., Barnard J.A., "Composition, structure, and nanomechanical properties of DC-sputtered CrN ($0 \leq x \leq 1$) thin films", Thin Solid Films **398-399** (2001) 460-464.
254. **Weng K.-W.,** Chen Y.-C., Han S., Hsu C.-S., Chen Y.-L., Wang D.-Y., "Effects of ion implantation on the microstructure and residual stress of filter arc CrN films", Thin Solid Films 516 (2008) 5330-5333.
255. **Willmann H.,** Mayrhofer P. H., Hultman L., Mitterer C., "Hardness evolution of Al–Cr–N coatings under thermal load", Journal of Material Research **23**(11) (2008) 2880 – 2885.
256. **Willmann H.,** Beckers M., Birch J., Mayrhofer P.H., Mitterer C., Hultman L., "Epitaxial growth of Al–Cr–N thin films on MgO(111)", Thin Solid Films **517** (2008a) 598–602.
257. **Willmann H.,** Mayrhofer P.H., Persson P.O.A., Reiter A.E., Hultman L., Mitterer C., "Thermal stability of Al–Cr–N hard coatings", Scripta Materialia **54** (2006) 1847–1851.
258. **Wilson** S and Alpas A T, Wear **245** (1996) 223.
259. **Wu F.B,** J.J. Li, J.G. Duh, "Evaluation of the mechanical properties and tribological behavior of the CrN coating deposited on mild steel modified with electroless Ni interlayer", Thin Solid Films **377-378** (2000) 354-359.
260. **Wuhrer R.,** Yeung W.Y., "A comparative study of magnetron co-sputtered nanocrystalline titanium aluminum and chromium aluminum nitride coatings", Scripta Materialia, **50** (2004) 1461–1466.
261. **Xu J.,** Kato K., "Formation of tribochemical layer of ceramics sliding in water and its role for low friction", Wear **245** (2000) 61-75.
262. **Xue J.M.,** Ezhilvalavan S., Gao X.S. and Wang J., "Strontium titanate doped lead metaniobate ferroelectric thin films", Applied Physics Letters, 81 (2002) 877-879.
263. **Yang** Q., Zhao L.R., Cai F., Yang S., Teer D.G., "Wear, erosion and corrosion resistance of CrTiAlN coating deposited by magnetron sputtering", Surface and Coatings Technology **202** (2008) 3886-3892.

264. Yang S. M., **Chang Y. Y.**, Lin D. Y, Wang Da-Y., Wu W., "Mechanical and tribological properties of multilayered TiSiN/CrN coatings synthesized by a cathodic arc deposition process", Surface and Coatings Technology **202** (2008) 2176–2181.

265. **Yoo Y H**, Hong J.H., Kim J.G., Lee H.Y., J.G. Han, "Effect of Si addition to CrN coatings on the corrosion resistance of CrN/stainless steel coating/substrate system in a deaerated 3.5 wt.% NaCl solution", Surface and Coating Technology, **201** (2007) 9518-9523.

266. **Yu C.**, Linhai T., Yinghui W., Wang S., Li T., and Xu B., "The effect of substrate bias voltages on impact resistance of CrAlN coatings deposited by modified ion beam enhanced magnetron sputtering", Applied Surface Science, **255** (2009) 4033–4038.

267. **Yu C.**, Wang S., Tian L., Li T., and Xu B., "Microstructure and mechanical properties of CrAlN coatings deposited by modified ion beam enhanced magnetron sputtering on AISI H13 steel", Journal of Material Science, **44** (2009a) 300–305.

268. **Yuji E**, Takashi Y, "New materials in automotive tribology", Tribology Letters, **5** (1998) 13–24.

269. **Zhang G. A**, P. X. Yan, P. Wang, Y. M. Chen, Y. J. Zhang, "Influence of nitrogen content on the structural, electrical and mechanical properties of CrNx thin films", Material Science and Engineering A **460-461** (2007) 301-305.

270. **Zhang G.**, Wang L., Wang S.C., Yan P., Xue Q., "Structure and mechanical properties of reactive sputtering CrSiN films", Applied Surface Science **255** (2009) 4425–4429.

271. **Zhang G.A.**, Yan P.X., Wang P., Chen Y.M., Zhang J.Y., "The structure and tribological behaviors of CrN and Cr–Ti–N coatings", Applied Surface Science **253** (2007) 7353–7359.

272. **Zhang Z.G.**, Rapaud O., Bonasso N., Mercs D., Donga C., and Coddet C., "Control of microstructures and properties of dc magnetron sputtering deposited chromium nitride films", Vacuum, **82** (2008) 501-509.

273. **Zhao Z. B**, Rek Z.U, Yalisove S.M, Bilello J.C., "Nanostructured chromium nitride films with a valley of residual stress", Thin Solid Films **472** (2005) 96-104.

274. **Zhou M.**, Makino Y., Nose M., Nogi K., "Phase transition and properties of T i-Al-N thin films prepared by r.f.-plasma assisted magnetron sputtering", Thin Solid Films, **339** (1999) 203-208.